School of Mathematical, Physical and Computational Sciences

The molecular dynamics and rheology of polymer melts near the flat surface

by

Jack Kirk

Thesis submitted for the degree of Doctor of Philosophy

February 2018

Abstract

This thesis is concerned with the molecular dynamics and rheology of polymer melts in the vicinity of a hard flat surface. One initial motivation is the desire to better understand the phenomenon of slip between flowing molten polymer and a bounding solid wall. Alternation between sticking and slipping boundary conditions is suspected to be the cause of 'spurt flow', widely observed in polymer extrusion. A related aim is to investigate the nature of chain entanglements at surfaces, which also has important consequences for the material properties of nano-composites and thin films. In addition more general effects of confinement are considered.

The primary method of investigation is observation, using Molecular Dynamics (MD) computer simulations of relevant systems. Single-chain models are fitted to the 'fundamental' multi-chain MD simulations, and the simplifying assumptions of this coarse-graining are then examined.

Declaration of Authorship

I confirm that this is my own work and the use of all material from other sources has been properly and fully acknowledged.

Jack Kirk

Contents

Acknowledgements

The help of many people has been essential to this thesis. Most importantly I thank my two primary supervisors, Dr Patrick Ilg, and Professor Alexei E. Likhtman.
Patrick's input has significantly enhanced the quality of every part of this work. There is no doubt that my ability to do science has been greatly improved thanks to his patient supervision over the past four years. I have learnt a great deal and enjoyed working with him.
In every chapter the importance of Alexei's body of work is evident. I frequently think about the things that he told me, and the questions that he emphasized have remained a road-map for my PhD since his death. Essentially this thesis could not exist at all without Alexei, and I hope that he would be interested to see where his ideas have led. I am deeply saddened that I cannot speak to him again, but I am very grateful for the time that I knew him.

Dr Zuowei Wang has also made an important contribution as a secondary supervisor. His wide knowledge of the polymer literature and careful suggestions have led to new ideas and prevented many mistakes.
Much of this thesis depended on the years of previous work on Molecular Dynamics code in the polymer physics group at Reading. Dr Dipesh Amin in particular wrote a large amount of code that has been employed in this thesis, and helped me to get started in using CUDA. Thanks to Dr Pawel Stasiak for technical advice and his important role in maintaining the computer cluster which enables the rest of us to work.
Thanks to Professor Martin Kröger for adapting his Z1 code for use in chapters 4 and 5, and for a great deal of help and interesting discussion. Thanks to Professor Peter Olmsted for introducing me to soft matter physics, and for much interesting discussion and guidance at Leeds. Thanks to Professor Jean-Louis Barrat and Dr. Jochen Bröcker for acting as my examiners.
Lastly, special thanks to my parents for the books when I was young, among other things.

For the thrill of the exploit, and for Alexei

I say to these students who have to spend a year, two years, writing theses about one book: "There is only one way to read, which is to browse in libraries and bookshops, picking up books that attract you, reading only those, dropping them when they bore you, skipping the parts that drag–and never, never reading anything because you feel you ought

Doris Lessing

Study hard what interests you the most in the most undisciplined, irreverent and original manner possible

Richard Feynman

Notation

In this thesis only scalars, vectors and second rank tensors are used. Second rank tensors are bold and double underlined, e.g. $\underline{\underline{\boldsymbol{\sigma}}}$ is a second rank tensor: the stress tensor. Vectors are bold, and unit vectors have hats, e.g. $\hat{\boldsymbol{y}}$ is a unit vector. Elements of tensors and other scalars do not have bond font, e.g. an element of the stress tensor, $\sigma_{\alpha\beta}$, is a scalar.
Tensor contractions are indicated via dot-product notation, e.g. $\boldsymbol{v} = \underline{\underline{\boldsymbol{H}}} \cdot \boldsymbol{F}$, where $v_\alpha = \sum_\beta H_{\alpha\beta} F_\beta$.
Subscripts α and β are used to indicate tensor components and subscripts i and j are particle identifiers. Both are placed as lower indices, and are separated by a comma if they are simultaneously used: e.g. $f_{ij,\alpha}$ indicates the α component of the force acting on particle j from particle i.

The squared norm of a vector, $\boldsymbol{u} \cdot \boldsymbol{u}$ is shortened to $\boldsymbol{u}^2$.

Sometimes in this thesis linear maps are used that do not have transformation rules with respect to changes to the coordinate system. Such an object is referred to as 'matrix' in the text, in contrast to 'tensors' which do have transformation rules with respect to changes in the coordinate system. Only two-dimensional matrices are considered in this thesis and they are referred to using non bold double underlined symbols, e.g. $\underline{\underline{M}}$.

Temperature, T, is given in units of the Boltzmann constant, k_b, throughout this thesis.

log() always refers to the natural logarithm.

All other notation is defined within context in the text at the first occurrence.

Chapter 1

Introduction to the rheology of polymer melts

Rheology is the branch of physics describing the relationship between stress and deformation in a material. The material may be classified as a solid, characterised by a 'yield stress': the minimum stress necessary for irreversible (plastic) deformation to occur; or a fluid, which flows when subjected to an arbitrarily small shear stress. Elastic solids may be deformed macroscopically and yet still approximately return to their original shape once the stress is removed. Some fluids, such as liquids whose constituents include large macromolecules, can behave like an elastic solid on small time-scales following deformation, and only display classical fluid behaviour after a characteristic relaxation time has elapsed. A go-to example is silly putty, a polymer melt, which may be bounced off the ground providing the impact velocity is sufficiently high; but, in the limit of being simply placed in a container and left for a long time, will eventually flow and take the form of its container. Such fluids are called 'visco-elastic', and also usually come under the more general umbrella term of 'complex fluids'. Depending on the conditions and time-scale of an experiment, many materials that are usually sorted into the well known terms: solids, liquids, and gases, can still have 'complex' properties, such that a simple three phase picture may only describe idealized materials, not necessarily real ones [88].

Macromolecules are constructed from polymers. A polymer is a molecule consisting of many (poly-) repeat units (mers). The wide range of possible polymer topology and chemistry provides a building block for a variety of materials, allowing for a vast range of phenomena. Organic polymers (with carbon back-bones) are the main building blocks of

life and in the past century synthetic polymers have been created with widespread applications.

This thesis is particularly interested in the properties and rheology of molten polymer interacting with a flat confining solid surface. An example of the importance of such systems is discussed in 1.0.4. Chapter 1 introduces the tools and concepts that are used in later chapters to model polymers at a surface, focusing on existing relevant knowledge of bulk behaviour. Chapter 1 relies heavily on the material as it is presented in the first five chapters of the book *'The Theory of Polymer Dynamics'* [39] by Masao Doi and Sam Edwards, and references therein. Features relevant for the purposes of this work are expanded upon.

Definition of material deformation

An instantaneous affine deformation applied uniformly to a material is completely characterised by the affine transformation taking a vector $\boldsymbol{q}^-$ embedded in the material at a time t^- before the deformation is applied, to a new vector $\boldsymbol{q}^+$ after the deformation at time t^+:

$$\boldsymbol{q}^+ = \boldsymbol{q}^- \cdot \underline{\underline{\boldsymbol{F}}}^{-1} \tag{1.1}$$

$\boldsymbol{q}^-$ may denote, for example, the vector connecting any two particles in the material before the deformation. Where the affine transformation (usually called the inverse deformation gradient tensor [87, 70]) is:

$$\underline{\underline{\boldsymbol{F}}}^{-1} = \begin{bmatrix} \frac{\partial q_x^+}{\partial q_x^-} & \frac{\partial q_y^+}{\partial q_x^-} & \frac{\partial q_z^+}{\partial q_x^-} \\ \frac{\partial q_x^+}{\partial q_y^-} & \frac{\partial q_y^+}{\partial q_y^-} & \frac{\partial q_z^+}{\partial q_y^-} \\ \frac{\partial q_x^+}{\partial q_z^-} & \frac{\partial q_y^+}{\partial q_z^-} & \frac{\partial q_z^+}{\partial q_z^-} \end{bmatrix} \tag{1.2}$$

An affine transformation allows for the stretch and rotation of material lines. An important type of deformation that is investigated in this thesis is shear. The following tensor corresponds to a shear deformation that leaves material lines orthogonal to the $\hat{\boldsymbol{y}}$ direction unchanged:

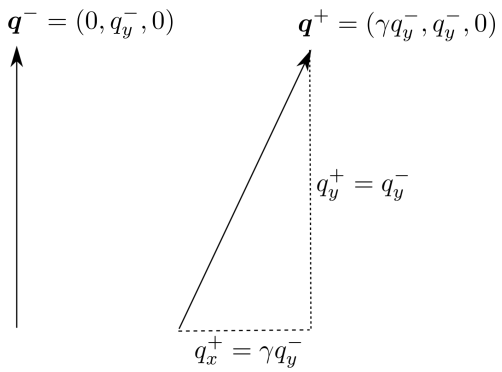

Figure 1.1: Vector $\boldsymbol{q}^-$ is transformed to vector $\boldsymbol{q}^+$ by the shear deformation $\underline{\underline{\boldsymbol{F}}}^{-1}_{\text{shear}}$, eqn (1.3). Material lines in the $\hat{\boldsymbol{y}}$ direction are stretched and rotated.

$$\underline{\underline{\boldsymbol{F}}}^{-1}_{\text{shear}} = \begin{bmatrix} 1 & 0 & 0 \\ \gamma & 1 & 0 \\ 0 & 0 & 1 \end{bmatrix} \tag{1.3}$$

The resulting transformation of a vector that is parallel to $\hat{\boldsymbol{y}}$ is illustrated in figure 1.1. Shear is a volume-preserving deformation, [110] such that material constituents may re-arrange their orientations subject to the deformation without the breaking of covalent bonds.

Definition of the material stress tensor

In order to have a microscopic understanding of rheology we must work with a microscopic definition of the material stress tensor. A stress tensor is defined by the property that when acted upon with the gradient operator it returns the rate of change of the momentum flux vector. This definition does not lead to a unique microscopic stress tensor. Varnik et al. [162] have compared different definitions whilst investigating the properties of a simulated polymer melt. In this thesis a well established definition for the planar stress vector derived by Todd et al. [160] is primarily used, which assumes only two body interactions exist between constituent particles. This 'method of planes' (MOP) expression gives the α component of the stress vector acting through the plane with normal unit vector $\hat{\boldsymbol{y}}$ and

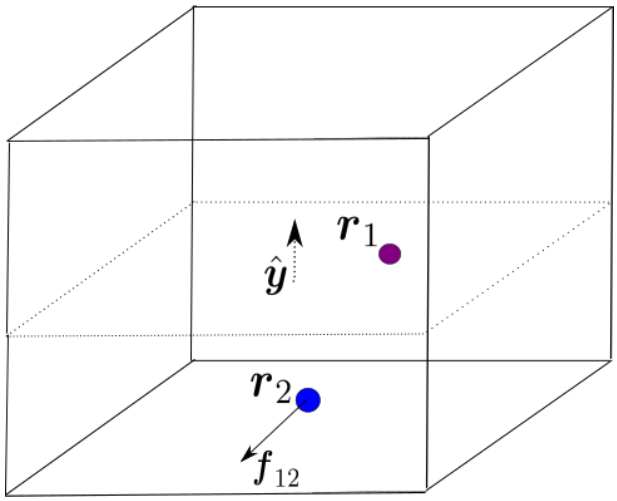

Figure 1.2: Particle 1 (purple) lies above the plane with unit vector $\hat{\boldsymbol{y}}$ and equation $y = \mathcal{Y}$, and particle 2 (blue) lies below it. The two Heaviside functions in eqn (1.4) are therefore both equal to unity, so the force component, $f_{12,\alpha}$, contributes to the stress $\sigma_{\alpha y}$.

equation of plane $y = \mathcal{Y}$, as:

$$\sigma_{\alpha y}(\mathcal{Y}) = \frac{1}{\mathscr{A}} \sum_{i,j} f_{ij,\alpha}\, \Theta(y_i - \mathcal{Y})\Theta(\mathcal{Y} - y_j) + \frac{1}{\mathscr{A}} \sum_i \frac{p_{i,\alpha} p_{i,y}}{m_i} \delta(y_i - \mathcal{Y}) \tag{1.4}$$

$\mathscr{A}$ is the total area of the plane. $\boldsymbol{p}_i$ and $\boldsymbol{r}_i$ are respectively the peculiar momentum and position of the ith particle with mass m_i. The first term on the right hand side of eqn (1.4) is a sum over forces, $\boldsymbol{f}_{ij}$, acting on particle j from particle i under certain constraints imposed on their positions via Heaviside step functions, denoted by $\Theta(y)$. An example force contribution to $\sigma_{\alpha y}$ is illustrated in figure 1.2. At equilibrium, the second term on the right hand side of eqn (1.4) is the ideal gas pressure; more generally it is often termed the 'kinetic stress'. In dense polymeric material it is usually assumed that away from equilibrium the shear stress contribution from this term is negligible compared to the 'configurational stress' contribution given by the first term.

Eqn (1.4) may be integrated over a range of positions, $\mathcal{Y}$, of the plane: this integral would then coincide with the classical virial stress [39] once the integrated volume coincides with that of the complete material. The MOP form is useful for calculating the stress tensor in Molecular Dynamics simulations of inhomogeneous fluids such as thin films. In chapter 3 we shall use a MOP algorithm integrated over small volume slabs to calculate equilibrium

time correlation functions of the stress within inhomogeneous MD simulations of thin polymer films.

Small deformation rheology: linear response

If we apply a small shear deformation to a fluid, previously at equilibrium, the fluid is deformed away from equilibrium, leading temporarily to non-equilibrium restoring forces in eqn (1.4), which result in a non-zero fluid averaged shear stress. The mean material shear stress at time t, following a small instantaneous shear deformation that is completely characterized by $\gamma = \partial q_x^+ / \partial q_y^-$, performed at time t', depends generally on the stress relaxation function, $G(t-t')$, of the material, which is an ensemble averaged function over all possible initial configurations and relaxation pathways:

$$\sigma_{xy}(t) = G(t-t')\gamma(t') \tag{1.5}$$

If the decay time of $G(t-t')$ is finite it is said to describe a visco-elastic material. For example, the form of $G(t-t')$ used in the simplest phenomenological model of a visco-elastic material, the single-mode Maxwell model, is:

$$G(t-t') = \exp\left(-\frac{(t-t')}{\tau}\right) \tag{1.6}$$

with characteristic material relaxation time τ. A contribution to the shear stress at time t due to a small deformation performed in the past around time t' over a time interval dt' is defined:

$$d\sigma_{xy}(t) = G(t-t')\frac{d\gamma(t')}{dt'}dt' \tag{1.7}$$

The Boltzmann superposition principle [70], a phenomenological law, states that such contributions to the stress are additive:

$$\sigma_{xy}(t) = \int_{-\infty}^{t} G(t-t')\dot{\gamma}(t')dt' \tag{1.8}$$

When there is a large separation of time-scales in the relaxation modes of the material- e.g. there may be solvent (fast) and polymer (slow) phases, eqn (1.8) may be split into two contributions relating to polymer-like and solvent-like stresses:

$$\sigma_{xy}(t) = \dot{\gamma}(t)\eta_{\text{solv}} + \int_{-\infty}^{t} G_{\text{poly}}(t-t')\dot{\gamma}(t')dt' \tag{1.9}$$

Here η_{solv} is the solvent viscosity and $G_{\text{poly}}(t-t')$ is the part of the stress relaxation function attributed to polymer modes. We see that the relaxation function for the solvent contribution is:

$$G_{\text{solv}}(t-t') = \eta_{\text{solv}}\delta(t-t') \tag{1.10}$$

Therefore the solvent is considered purely viscous. However, the concept of visco-elasticity depends upon the nature of the experiment. That the solvent is considered purely viscous simply means that over the shortest characteristic time scale of the experiment, $\tau_{\text{experiment}}$, $G_{\text{solv}}(\tau_{\text{experiment}})$ has already decayed to zero. The material shear viscosity may be generally defined as:

$$\eta = \int_{0}^{\infty} G(t)dt \tag{1.11}$$

Beyond weak shear, $\dot{\gamma} \gtrsim 1/\tau$, where τ is a longest molecular relaxation time, the dynamic shear viscosity may generally differ from eqn (1.11), and becomes a function of shear-rate, $\eta(\dot{\gamma}) = \sigma_{xy}/\dot{\gamma}$.

Slip boundary conditions in polymer melts

In polymer processing a final product shape is realized by forcing molten polymer through a die. This process is called extrusion, and the polymer exiting the die is called the extrudate. Figure 1.3 illustrates a simplified extrusion experimental setup. Flow instabilities are a serious problem for the plastic extrusion process. The reviews by Denn [37] and Hatzikiriakos [59] cover effects found in industry and experimental studies, including a summary of theoretical models. The 'stick-slip' instability, which is of interest in the present work, is one such example: for a variety of materials it has been found that, at a sufficiently high fixed pressure, the flow rate of the polymer in the die alternates between

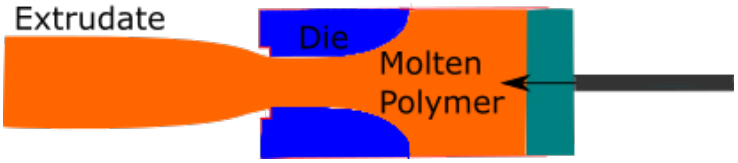

Figure 1.3: A very simple example of the extrusion process: a piston pushes molten polymer through a die. Swelling of the extrudate with respect to the die diameter may occur due to normal stresses in the extrudate. *Note: not to scale.*

high and low rates, which are thought to correspond with slip and stick boundary conditions. If instead the die flow rate is held fixed then oscillations in the pressure occur [166]. These oscillations are further associated with varying degrees of 'die swelling', in which upon exiting the die the extrudate diameter increases. Oscillations in the extrudate diameter follow the pressure oscillations [166]. At sufficiently high flow rates this effect may lead to fracture of the extruded polymer melt.

In most extrusion setups the die channel dimension is much greater than the molecular dimension. Assuming that there is no bulk instability associated with boundary effects [4], in wide channels the importance of the surface is relegated to a boundary condition for the fluid velocity and molecular state. In the following we will consider the effect of the boundary conditions on the velocity field in the sliding plate geometry (also known as simple Couette flow) which is a drag flow - one surface plate, the 'rotor', slides relative to a stationary plate, the 'stator': see figure 1.4. The sliding plate flow is generally simpler than pressure driven flow: in the bulk it results in a uniform shear-rate. Polymer melts are effectively incompressible and most flow situations correspond to the limit of low Reynolds number, so that the Navier-Stokes equation reduces to 'creeping flow' over relevant time-scales:

$$\nabla \cdot \underline{\underline{\boldsymbol{\sigma}}} = 0 \tag{1.12}$$

where $\underline{\underline{\boldsymbol{\sigma}}}$ is the stress tensor. In the sliding plate geometry, assuming that the material stress is invariant with respect to translations parallel to the surface, eqn (1.12) leads to the condition:

$$\frac{\partial \sigma_{xy}}{\partial y} = 0 \tag{1.13}$$

Under this condition the shear stress at the fluid-solid interface that is 'slipping' must be

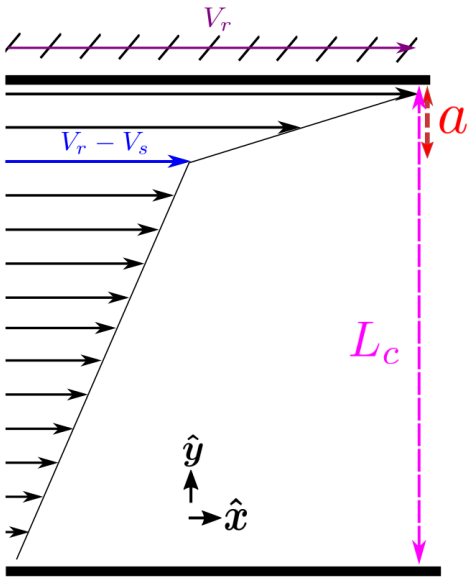

Figure 1.4: Sliding plate flow geometry. The rotor (top wall) slides relative to the stator (bottom wall) with velocity $V_r\hat{\boldsymbol{x}}$. This induces a rectilinear shear flow across the channel. In this particular illustration, there is a high shear-rate region ('apparent slip') within a distance a from the rotor, whereas the stator is a no slip boundary.

matched by the bulk value:

$$\sigma_{xy} = \sigma_{yx} = \eta_{\text{bulk}}\dot{\gamma}_{\text{bulk}} = \xi_s V_s \tag{1.14}$$

where η_{bulk} and $\dot{\gamma}_{\text{bulk}}$ are the bulk viscosity and shear-rate respectively. ξ_s is an interfacial friction constant and V_s is the 'slip velocity'. The condition that the stress tensor must be symmetric if there is torque balance in the material has been used in eqn (1.14). Figure 1.4 depicts the case where slip only occurs at the rotor. For the purposes of this discussion we define the edge of a surface region at the rotor, at a distance a from the surface, as the point at which the shear-rate deviates appreciably from the bulk value. Then the slip velocity may be defined by subtracting the fluid velocity at the edge of the surface region (depicted by the blue arrow in figure 1.4) from the rotor velocity, V_r. The stick-slip (shear flow) instability implies that for a given steady state shear stress, there are two or more solutions of the average channel shear-rate:

$$\dot{\gamma} = V_r/L_c \tag{1.15}$$

where L_c is the channel width. Assuming that the bulk flow curve (the relationship between bulk shear-rate and stress) is monotonic, this means that the surface region flow curve is not, i.e. at some point $\partial\xi_s/\partial V_s < 0$ such that the surface friction force, $\xi_s V_s$, does not increase with increasing slip velocity.

An effective surface region shear-rate can be defined:

$$\dot{\gamma}_{\text{surface}} = \frac{V_s}{a} \tag{1.16}$$

The width of the surface region, a, may be identified as a characteristic monomer size in the case of 'true slip', such that the slip occurs between the surface and the monomers in the first fluid layer. If a is much greater than the monomeric length then 'apparent slip' is said to occur. In this case there exists a lubricating fluid layer at the surface with a viscosity that is lower than the bulk viscosity. For example, even near to equilibrium this may occur in polydisperse polymer melts if the lower molecular weight component wets the surface, or in monodisperse entangled melts if there is a depletion of entanglements near the surface. Chapter 5 investigates surface slip that is due to a non-equilibrium shear-flow induced 'coil-stretch' transition of surface adsorbed chains. Note that 'apparent slip' is also sometimes used to refer to bulk instabilities [17] which may be misinterpreted as wall slip in experiments.

A common measure of the degree of slip: the 'slip length', gives the distance beyond the surface at which an extrapolation of the bulk fluid velocity profile reaches the plate velocity:

$$L_{\text{slip}} = \frac{V_s}{\dot{\gamma}_{\text{bulk}}} - a = \frac{\eta_{\text{bulk}}}{\xi_s} - a \tag{1.17}$$

The slip length is often defined experimentally by assuming that $a/L_{\text{slip}} \approx 0$, so that eqn (5.3) becomes simply $L_{\text{slip}} = V_s/\dot{\gamma}_{\text{bulk}}$. For a review of the seminal experiments investigating surface slip in polymer melts see Léger et al [104].

De Gennes [33] pointed out that if true slip occurs in entangled polymer melts, the effective surface viscosity, $\eta_{\text{surface}} = a\xi_s$, could be orders of magnitude lower than the bulk viscosity, assuming that the monomeric surface friction is similar to that of a corresponding simple fluid. The effect of fluid-surface interactions on slip has since been well studied using

simulation [132, 131, 122]. Niavarani and Priezjev [122] investigated the slip behaviour of rectilinear flows of very short non-entangled linear chains (comprising $n = 19$ bonds) in a channel with width $L_c \approx 7\sqrt{\langle \boldsymbol{u}_{\text{bulk}}{}^2 \rangle}$, where $\langle \boldsymbol{u}_{\text{bulk}}{}^2 \rangle$ is the bulk mean square end-to-end distance of the chains. Their study found that the slip length scaling depended on the same parameters as for simple Lennard-Jones particle fluids [129]:

$$L_{\text{slip}} \propto \left[\frac{T}{S(\boldsymbol{G}_1)\rho_c} \right]^{\zeta} \tag{1.18}$$

The exponent was found to be $\zeta = 1.44$ for simple fluids and $\zeta = 0.9$ for the polymer study. Here T is the temperature, $\boldsymbol{G}_1$ is the first reciprocal lattice vector in the flow direction; ρ_c is the 'contact density', which is defined as the maximum value of the particle density in the first fluid layer. $S(\boldsymbol{G}_1)$ is the structure factor in the first fluid layer defined as:

$$S(\boldsymbol{G}_1) = \frac{1}{N_l} \left| \sum_j \exp(i\boldsymbol{G}_1 \cdot \boldsymbol{r}_j) \right|^2 \tag{1.19}$$

where here $i = \sqrt{-1}$, $\boldsymbol{r}_j$ is the two-dimensional position vector of particle j in the surface plane, and the sum is over all N_l particles in the first fluid layer. Eqn (1.18) is found to be valid near to equilibrium providing that the wall fluid energy is weak, e.g. for the simple fluid the condition is: $0.3 \leq \epsilon_{wf}/\epsilon_{ff} \leq 1.1$ [122], where ϵ_{wf} and ϵ_{ff} are fluid-wall and fluid-fluid interaction energies respectively.

As opposed to this true slip phenomenology, this thesis is interested in systems in which a is of order a molecule size. For entangled polymers that do not have macroscopically slipping boundaries, the De Gennes argument suggests that the dominant contribution to surface friction results from topological interactions between adsorbed and non-adsorbed molecules. Resultantly, when investigating the shear induced transition to slip in an entangled melt in chapter 5, the contribution of monomeric friction, to the transfer of stress across the surface, is explicitly neglected, through the application of a flat reflective boundary. The stress across the surface is transferred via the interactions between chains that are free with those that are permanently grafted by one end to the surface.

Statistical methods for rheology

We consider classical mechanical systems [55] comprising n particles, whose state is determined by a complete set of particle positions and momenta; where for example $\{\boldsymbol{r}^n\} = \{\boldsymbol{r}_0, \boldsymbol{r}_1, .., \boldsymbol{r}_{n-1}\}$ represents a complete set of n particle positions and correspondingly $\{\boldsymbol{p}^n\}$ a complete set of particle momenta.

The usefulness of a statistical description of physics depends primarily upon the assumption that on experimental time-scales, $\tau_{\text{experiment}}$, the phase space of the system of interest has been sufficiently well sampled such that the mean over the time of observation of a phase space function, $B(\{\boldsymbol{r}^n\}, \{\boldsymbol{p}^n\})$, gives a result that is equal to the limit of infinite observation time. The ergodic hypothesis states that for $t \to \infty$, where t is the time of observation, the time average coincides with the ensemble average:

$$\langle B \rangle = \lim_{t\to\infty} 1/t \int_0^t dt' B(\{\boldsymbol{r}^n(t')\}, \{\boldsymbol{p}^n(t')\}) = \int \{d\boldsymbol{r}^n\}\, \{d\boldsymbol{p}^n\}\, \psi(\{\boldsymbol{r}^n\}, \{\boldsymbol{p}^n\}) B(\{\boldsymbol{r}^n\}, \{\boldsymbol{p}^n\}) \tag{1.20}$$

where $\psi(\{\boldsymbol{r}^n\}, \{\boldsymbol{p}^n\})$ represents the occupational probability density around the phase space point $(\{\boldsymbol{r}^n\}, \{\boldsymbol{p}^n\})$, such that the total occupational probability within the infinitesimal hypervolume bounded by $(\{\boldsymbol{r}^n\}, \{\boldsymbol{p}^n\})$ and $(\{\boldsymbol{r}_0 + d\boldsymbol{r}, \boldsymbol{r}_1 + d\boldsymbol{r}, .., \boldsymbol{r}_{n-1} + d\boldsymbol{r}\}, \{\boldsymbol{p}_0 + d\boldsymbol{p}, \boldsymbol{p}_1 + d\boldsymbol{p}, .., \boldsymbol{p}_{n-1} + d\boldsymbol{p}\})$ is $(d\boldsymbol{r}\, d\boldsymbol{p})^n\, \psi(\{\boldsymbol{r}^n\}, \{\boldsymbol{p}^n\})$. $\int \{d\boldsymbol{r}^n\}\, \{d\boldsymbol{p}^n\}$ represents an integration over the complete $6n$ dimensional phase space.

According to the ergodic hypothesis, at macroscopic time-scales long compared to the fundamental microscopic dynamics, we only observe ensemble average material properties. In this case it is convenient to use a statistical description of material properties.

Some materials, such as polymeric ones, may show time-dependent properties on relevant time-scales since the decay of fluctuations away from mean behaviour can be slow. This is characterised by the Deborah number: $De = \tau_T/\tau_{\text{experiment}}$ where τ_T is a characteristic longest system relaxation time. At small De, fluid-like behaviour is observed. The Deborah number [137] is named after the prophetess Deborah, who in Judges 5:5[1] sings:

" The mountains melted from before the Lord"

[1]King James Bible version. Many more modern translations such as the English Standard Version replace "melted from", with "quaked".

An interpretation of the particular meaning of this verse is that solids may behave like fluids on sufficiently long experimental time-scales (accessible only to God). The classification of fluids, solids, and visco-elastic fluids that we employ is a reflection of the time-scales of human experience.

In the case of macroscopic systems comprising an extremely large number of constituent particles, simple considerations suggest that even over very short time-scales (large De) the time-average global material properties often deviate little from the ensemble average. This is due to the fact that relative fluctuations in global material properties decrease proportionally with the square root of the system size, providing that they are additive properties (scale with the system size - e.g. the total surface stress scales with surface area): consider any physical system (either closed or in contact with a secondary 'environment') that is sufficiently large so that one may imagine splitting it into a large number of sub-systems which themselves are sufficiently large that physical properties of the complete system can be written to a good approximation as a sum of the physical properties of its sub-systems. This is equivalent to the statement that the surface interactions of the sub-systems are negligible compared to bulk contributions. Then, on sufficiently short time-scales, the interactions between each sub-system remain negligible (exchange of matter and energy). In this case the sub-systems are considered to be 'quasi-closed'. Provided the sub-systems remain quasi-closed over the time of observation, they cannot be correlated with one another. Then the mean square fluctuation of the global observable can be written as a sum over every sub-systems, and therefore for the relative fluctuation we get:

$$\frac{\sqrt{\langle (B - \langle B \rangle)^2 \rangle}}{\langle B \rangle} = \frac{\sqrt{\sum_i \langle (B_i - \langle B_i \rangle)^2 \rangle}}{\sum_i \langle B_i \rangle} \propto 1/\sqrt{N} \tag{1.21}$$

Resultantly, even without invoking the ergodic hypothesis, the global instantaneous properties of macroscopic systems are, for all intents and purposes, equivalent to the ensemble average for all time: fluctuations may decay slowly in time as in the case of some polymeric materials, but for sufficiently large systems the fluctuations are so small that they do not matter. For further discussion, including a quantitative example of the incredible minuteness of fluctuations in macroscopic systems, see Landau [85].

Even materials with a global dimension of order nano-metres: for example thin films, often also have a macroscopic dimension (the film is only 'thin' in one direction). Therefore we may in principle predict properties of such systems via time-averages of much smaller systems which may be simulated using computer models on reasonable time-scales.

Stress Optical Rule (SOR)

Which are the microscopic properties that dictate the macroscopic rheology of polymeric materials?

A general experimental observation for polymer melts is that, under deformations which are not too large, the instantaneous melt stress is proportional to the sum over all bond orientation tensors of the N_c polymer chains constituting the material:

$$\boldsymbol{\sigma}(t) \propto \sum_{l=1}^{N_c} \boldsymbol{O}^l(t) \tag{1.22}$$

where the bond orientation tensor of a chain is given by the sum over all dyadic products formed from each of the n bond vectors within the chain with themselves:

$$O_{\alpha\beta}(t) = \sum_{j=1}^{n} q_{j,\alpha} q_{j,\beta} \tag{1.23}$$

where the jth bond vector is $\boldsymbol{q}_j = \boldsymbol{r}_j - \boldsymbol{r}_{j-1}$.

Eqn (1.22) is generally known as the 'Stress Optical Rule' (SOR), since the bond orientation tensor is proportional to the index of refraction tensor in polymer melts [39]. This means that stresses may be inferred via optical measurements, which may be simpler to perform compared with directly measuring stress [96]. When eqn (1.22) is satisfied [82], the instantaneous stress in the material is completely dictated by the mean orientation of the polymer constituents. Resultantly it is important to understand the statistical distribution of the bond orientation tensor at equilibrium, and its evolution subject to deformation, in order to have a microscopic understanding of melt rheology. These subjects will be discussed in sections 1.1 and 1.2.

Chain orientations in polymer melts at equilibrium

Markoff chain models

For polymer melts it has for a long time [53] been postulated that chain orientations are well described by the Markoff (random-walk) property at sufficiently large length-scales. A chain model is Markoff if the probability distributions of all bond vectors in the chain are uncorrelated. Then the probability distribution of the complete set of bond vectors in the chain, $\{\boldsymbol{q}^n\}$, is given by the products of all individual bond vector probability weights:

$$\Psi(\{\boldsymbol{q}^n\}) = \prod_{j=1}^{n} P(\boldsymbol{q}_j) \tag{1.24}$$

A simple example of such a chain model is the freely jointed model in which the chain traces out an off-lattice random walk with fixed bond-length b_0. The bond vectors then satisfy:

$$\langle \boldsymbol{q}_j \cdot \boldsymbol{q}_k \rangle = b_0^2 \delta_{jk} \tag{1.25}$$

The absence of correlations leads to a simple expression for the mean square end-to-end vector of the polymer chain consisting of n bonds:

$$\left\langle \boldsymbol{u}^2 \right\rangle = \left\langle \sum_{j,k} \boldsymbol{q}_j \cdot \boldsymbol{q}_k \right\rangle = n b_0^2 \tag{1.26}$$

where $\boldsymbol{u} = \boldsymbol{r}_n - \boldsymbol{r}_0$ is the chain end-to-end vector. It can be further demonstrated that the probability distribution of the chain end-to-end vector for this model is Gaussian in the limit $n \to \infty$ [39]:

$$\psi(\boldsymbol{u}) = \sqrt{\frac{3}{2\pi n b_0^2}} \exp\left(-\frac{3(\boldsymbol{u} \cdot \boldsymbol{u})}{2 n b_0^2} \right) \tag{1.27}$$

Generally eqn (1.27) follows for any Markoff model and is a consequence of the central-limit theorem [174]. In the case that $\langle \boldsymbol{q}_j \cdot \boldsymbol{q}_k \rangle$ does not always vanish for $j \neq k$ (chain not Markoff), then provided that correlations decay sufficiently rapidly with respect to $|j - k|$ compared to the total number of segments in the chain, the Gaussian distribution, eqn (1.27), is recovered in a rescaled form. This can be shown quite easily in the case

of a freely-rotating chain model where a fixed bond length and one fixed bond angle are prescribed [39]. The general case is discussed by Yamakawa [174].

What is the effect of non-bonded interactions?

For polymers in solution, non-bonded self-interactions break the Markoff condition; although under special 'theta' temperature conditions [174] the interactions between solvent and solute cancel and the Markoff condition is satisfied.

However in polymer melts, sufficiently long bulk chains are expected to have universal Gaussian statistics independent of temperature. This now experimentally examined idea [176] was first hypothesised by Flory - see De Gennes for a discussion [34]. Edwards [39] performed a self consistent field calculation (SCF) to predict that bond correlations decay exponentially in the melt over a characteristic length of density fluctuations $\xi = (b_0^2/(12cv))^{1/2}$, where c is the polymer concentration and v is the excluded volume parameter. The SCF calculations used harmonic bonded potentials with spring constant $3T/b_0^2$, where T is the temperature, and delta point 'excluded volume' non-bonded interactions. According to Edwards, for bond index separations, $|j-k| \gg (\xi/b_0)^2$, the self-chain excluded volume interaction is cancelled by the surrounding chains, satisfying the Markoff condition. More recently, a correction to the calculation of Edwards has been given by Wittmer et al. [172], which predicts a slower, power-law decay of correlations. These predictions have been corroborated by both lattice (Bond Fluctuation Model (BFM)) [54] and off-lattice multi-chain simulation models (Kremer-Grest Molecular Dynamics (KG MD)) [96]. Compared to the case of a polymer chain in a dilute theta solution the total number of allowable single chain conformations is much fewer in the melt, but the distribution of segment vectors also tends to a Gaussian for sufficiently long segments. Such chains are said to be 'ideal'.

A summary of the existing literature regarding the influence of strong confinement on the decay in bond correlations of melt chains is made in chapter 2, and in appendix B.1 the influence of weak confinement is examined.

Dynamics of polymer melt chains near equilibrium

In 1953 Rouse [140] used the assumption of ideal Gaussian chain statistics as the basis for a simple model describing the segmental dynamics of bulk polymer chains near equilibrium. Rouse originally created the model to describe chains in dilute solutions but it was later understood to be more appropriate for non-entangled melts and concentrated solutions. Being a general description of polymer conformations, the Rouse model may be compared to a large number of different polymer melt experiments [51].

This section describes the general formulation of a statistical dynamical model for a system near equilibrium: the Smoluchowski equation, which has the irreversible property of reaching the system equilibrium distribution function for long time, $t \to \infty$, satisfies Onsager's reciprocal relations [36] with respect to the coarse-grained thermodynamic degrees of freedom, and reproduces Fick's phenomenological law for diffusion. For the case that the non-equilibrium thermodynamic state of interest is completely determined from the distribution function of a complete set of coarse-grained degrees of freedom of a polymer chain, using the Flory hypothesis of chain ideality, a class of dynamical single chain models is found, of which the Rouse model is a particular case.

The Smoluchowski equation and the Rouse model

We consider the dynamics of a sub-system consisting of a single polymer chain, forming a small part of a large system comprising a fluid of many *similar* [34] chains. A complete description of the composite system can be given by solving the fundamental equations of motion for every degree of freedom of every chain. Later in this thesis the fundamental system of interest will be a Molecular Dynamics model where the equations of motion for the complete set of particle positions and momenta follow classical mechanics. This fundamental model may be compared directly with the predictions of any single-chain model which aims to be a coarse-grained description of the fundamental model.

Apart from the sub-system, the other much larger part of the composite system we call the reservoir (or heat-bath). The sub-system may exchange energy in the form of heat with the reservoir. The number of particles, $n + 1$, in the sub-system, and its volume, V_0, are

prescribed and maintained such that there is a well defined monomer (or coarse-grained bead) density. The exact energy of the sub-system is unknown but fluctuates about a mean value $\langle E_0 \rangle$ due to interactions with the reservoir. The reservoir is maintained at a constant temperature, defined as the derivative of the total system entropy with respect to its energy, with volume and total particle number held fixed:

$$1/T = \left.\frac{\partial S}{\partial E}\right|_{V_{\text{tot}}, n_{\text{tot}}} \tag{1.28}$$

where S, E, V_{tot}, and n_{tot} are the total system entropy, energy, volume and number of particles respectively.

This situation was first described by Gibbs [85] in 1902, who derived the corresponding equilibrium probability distribution of sub-system states: the 'Canonical Ensemble'. The key result of Gibbs gives the sub-system equilibrium distribution function in terms of the total sub-system potential energy, $\mathscr{U}$, and kinetic energy, $\mathscr{K}$:

$$\psi_{\text{eq}}(\{\boldsymbol{r}^{n+1}\}, \{\boldsymbol{p}^{n+1}\}) = \frac{\exp\left(-\frac{\mathscr{U}(\{\boldsymbol{r}^{n+1}\}) + \mathscr{K}(\{\boldsymbol{p}^{n+1}\})}{T}\right)}{Z^{n+1}} \tag{1.29}$$

where Z^{n+1} is the sub-system partition function:

$$Z^{n+1} = \int \{d\boldsymbol{r}^{n+1}\}\{d\boldsymbol{p}^{n+1}\} \exp\left(-\frac{\mathscr{U}(\{\boldsymbol{r}^{n+1}\}) + \mathscr{K}(\{\boldsymbol{p}^{n+1}\})}{T}\right) \tag{1.30}$$

Note that here we have already made the assumption that the chain energy only depends on the positions and momenta of its monomers, and is independent of the surrounding chains.[2]

The form of eqn (1.29) means that the distribution functions of particle positions and momenta are uncorrelated. The distribution of momenta is generally given by the Maxwell-Boltzmann distribution [85].

When the system ensemble is driven out of equilibrium via a deformation applied at

[2]It is a standard assumption of the Gibbs formulation that the energy of the sub-system and reservoir is additive, i.e. there is no contribution to the total system energy due to interaction terms involving both reservoir and sub-system degrees of freedom. As an aside it is noted that this assumption appears questionable when the sub-system is a single chain which pervades a volume containing many similar chains forming the reservoir.

the system boundaries or otherwise, the faster dynamical modes (describing for example relaxation of covalent bonds) in the chain quickly relax to equilibrium, but some 'slow' modes may be kept in a steady non-equilibrium state. This concept of partial equilibrium is widely used in statistical physics [85]. Resultantly, in a simple description of chain dynamics weakly perturbed from equilibrium, one may replace the complete set of chain degrees of freedom with a coarse-grained set of thermodynamic degrees of freedom which from now on will be referred to as the chain 'beads'. Many different prescriptions for the coarse-grained variables are possible, and choosing suitable ones is a non-trivial problem. A good choice should lead to an accurate description of non-equilibrium dynamical properties of interest.

Given a matrix $\underline{\underline{M}}$ of size $[N+1, n+1]$ that maps from microscopic to coarse-grained degrees of freedom:

$$\boldsymbol{R}_i = \sum_{j=0}^{n} \underline{\underline{M}}_{ij} \boldsymbol{r}_j \tag{1.31}$$

the equilibrium probability distribution of the set of $N+1$ ($N < n$) coarse-grained bead positions, $\{\boldsymbol{R}^{N+1}\}$, may then be uniquely defined:

$$\Psi_{\mathrm{eq}}(\{\boldsymbol{R}^{N+1}\}) = \int \{d\boldsymbol{r}^{n+1}\} \psi_{\mathrm{eq}}(\{\boldsymbol{r}^{n+1}\}) \prod_{i=0}^{N} \delta(\boldsymbol{R}_i - \sum_{j=0}^{n} M_{ij} \boldsymbol{r}_j) \tag{1.32}$$

Eqn (1.32) is known in statistical mechanics as the 'restricted partition function'. It allows calculation of ensemble averages of functions of the coarse-grained variables.

The set of probabilities, eqn (1.32), may be calculated from MD simulations of the fundamental model, for which the microscopic probability distribution, $\psi_{\mathrm{eq}}(\{\boldsymbol{r}^{n+1}\})$, is assumed to be given by the canonical ensemble, eqn (1.29). See Voth [124] and Noid et al. [123] for details and examples using this methodology. Finding a coarse-grained probability distribution in this way is particular to the exact formulation of the fundamental model, and since the integration cannot be performed analytically the functional form is usually unknown. An alternative inexact method is to define a form for the probability distribution of the coarse-grained degrees of freedom which comes from a guiding principle such as that of Gaussian statistics, as applied by Rouse for the case of flexible polymers. In the inexact approach the distribution of microscopic variables cannot generally be mapped to

the particular coarse-grained distribution via a linear transformation. Instead, generally at least one moment can be matched; then if the form of the distribution is meaningful a whole class of microscopic models can be coarse-grained in this way reasonably accurately. This thesis is interested in understanding the dynamics of polymer molecules in contact with a flat surface in a general way, not just for a specific system, therefore the inexact method is the appropriate one. For the purpose of this discussion we may assume that the mapping satisfies eqn (1.32) exactly; for an example of the inexact methodology see 2.1.4.

Writing eqn (1.32) in the form of Boltzmann statistics:

$$\Psi_{\text{eq}}(\{\boldsymbol{R}^{N+1}\}) = \frac{\exp\left(-\frac{U(\{\boldsymbol{R}^{N+1}\})}{T}\right)}{Z^{N+1}} \tag{1.33}$$

defines the coarse-grained effective potential, $U(\{\boldsymbol{R}^{N+1}\})$; Z^{N+1} is the partition function of the coarse-grained system. If, as discussed in section 1.1, the distribution function may be written in terms of a product of Gaussian distributions for the set of coarse-grained bonds, $\{\boldsymbol{Q}^N\}$, where $\boldsymbol{Q}_i = \boldsymbol{R}_i - \boldsymbol{R}_{i-1}$, the Rouse bonded potential is found from writing the Gaussian distribution, eqn (1.27) in the form of eqn (1.33):

$$U(\{\boldsymbol{Q}^N\}) = U_{\text{Rouse}} = \sum_i^N k\boldsymbol{Q}_i^2 \tag{1.34}$$

Here $k = 3T/b^2$ is an effective bond spring constant, where b is the characteristic length of the Gaussian chain. Each chain segment has mean-square length b^2.

We define a non-equilibrium free energy density as:

$$\mathcal{F}(\{\boldsymbol{R}^{N+1}\}) = U(\{\boldsymbol{R}^{N+1}\}) + T\log(\Psi(\{\boldsymbol{R}^{N+1}\})) \tag{1.35}$$

where the distribution $\Psi(\{\boldsymbol{R}^{N+1}\})$ may generally be a non-equilibrium distribution, different to eqn (1.33). As a basic model for the dynamics away from equilibrium, we can match the gradient in the free energy density to a force. We define a thermodynamic force

$\boldsymbol{F}_j$ acting on coarse-grained bead j as:

$$\boldsymbol{F}_j(\{\boldsymbol{R}^{N+1}\}) = -\frac{\partial \mathcal{F}(\{\boldsymbol{R}^{N+1}\})}{\partial \boldsymbol{R}_j} \tag{1.36}$$

At equilibrium, solving eqn (1.33) for $U(\{\boldsymbol{R}^{N+1}\})$ and inserting into eqn (1.35) gives:

$$\mathcal{F}_{\text{eq}} = -T\log(Z^{N+1}) \tag{1.37}$$

so that the thermodynamic force vanishes. Eqn (1.37) is the equilibrium free energy from statistical mechanics. A more general non-equilibrium free energy will be defined in eqn (1.44).

We now derive an evolution equation for a non-equilibrium coarse-grained distribution using the thermodynamic force, assuming that the traced over modes whose information has been lost in the reductive transformation, eqn (1.31), remain at equilibrium. We assume that on time-scales of interest the flux velocity of particle i, $\boldsymbol{v}_i^f$, is related to the thermodynamic force acting on particle j via a mobility matrix (which is generally a tensor), $\underline{\underline{\boldsymbol{H}}}$, by:

$$\boldsymbol{v}_i^f = \sum_j \underline{\underline{\boldsymbol{H}}}_{ij} \cdot \boldsymbol{F}_j \tag{1.38}$$

In the case $N = 0$: beads do not form a chain, taking the potential as a constant and the mobility matrix to be: $\underline{\underline{\boldsymbol{H}}}_{ij} = \delta_{ij}\underline{\boldsymbol{I}}/\xi$, where ξ is the bead friction constant and $\underline{\boldsymbol{I}}$ is the identity tensor; we find:

$$\boldsymbol{J}_i = \Psi \boldsymbol{v}_i^f = -\frac{T}{\xi}\frac{\partial \Psi}{\partial \boldsymbol{R}_i} \tag{1.39}$$

where $\boldsymbol{J}_i$ is the probability flux of particle i. Thus equations (1.35), (1.36) and (1.38) lead directly to Fick's phenomenological law of diffusion, eqn (1.39), relating a particle flux to a gradient in concentration via a diffusion constant. Eqn (1.38) gives the diffusion constant as:

$$D = \frac{T}{\xi} \tag{1.40}$$

This is a non-trivial result first derived by Einstein [42], relating the diffusion constant of a large particle (or coarse-grained coordinate) to the product of the temperature and a

particle mobility.

In the general case we get for the probability flux of the ith bead:

$$\boldsymbol{J}_i = -\sum_j \underline{\underline{\boldsymbol{H}}}_{ij} \cdot \left(T\frac{\partial \Psi}{\partial \boldsymbol{R}_j} + \Psi \frac{\partial U}{\partial \boldsymbol{R}_j} \right) \tag{1.41}$$

The Smoluchowski equation is then found from the continuity equation for the probability flux:

$$\frac{\partial \Psi}{\partial t} = -\sum_i \frac{\partial}{\partial \boldsymbol{R}_i} \cdot \boldsymbol{J}_i \tag{1.42}$$

The Smoluchowski equation is a partial differential equation for the distribution function:

$$\frac{\partial \Psi}{\partial t} = \sum_{i,j} \frac{\partial}{\partial \boldsymbol{R}_i} \cdot \underline{\underline{\boldsymbol{H}}}_{ij} \cdot \left(T\frac{\partial \Psi}{\partial \boldsymbol{R}_j} + \Psi \frac{\partial U}{\partial \boldsymbol{R}_j} \right) \tag{1.43}$$

Extending the concept of entropy beyond equilibrium, a dynamical free energy functional is defined [39]:

$$\mathcal{A}[\Psi] = \int \{d\boldsymbol{R}^{N+1}\} \Psi(\{\boldsymbol{R}^{N+1}\}) \left(U(\{\boldsymbol{R}^{N+1}\}) + T\log(\Psi(\{\boldsymbol{R}^{N+1}\})) \right) \tag{1.44}$$

using the definition of the non-equilibrium Boltzmann-Gibbs entropy of the ensemble of the coarse-grained beads:

$$\mathcal{S}[\Psi] = -\int \{d\boldsymbol{R}^{N+1}\} \Psi(\{\boldsymbol{R}^{N+1}\}) \log(\Psi(\{\boldsymbol{R}^{N+1}\})) \tag{1.45}$$

The dynamics, eqn (1.43), have the important irreversible characteristic that the dynamical free energy is a monotonically decreasing function (proven in Doi and Edwards [39]) providing that $\underline{\underline{\boldsymbol{H}}}$ is positive semi-definite: $\sum_{i,j} \boldsymbol{F}_i \cdot (\underline{\underline{\boldsymbol{H}}}_{ij} \cdot \boldsymbol{F}_j) \geq 0$ for any set of vectors, $\{\boldsymbol{F}^{N+1}\}$. At equilibrium the dynamical free energy coincides with the equilibrium free energy, eqn (1.37), and therefore the dynamics, eqn (1.43), tend to the equilibrium distribution for $t \to \infty$.

The Smoluchowski equation tells us how the distribution function evolves and can therefore be amenable to analytic calculation of equilibrium ensemble averaged dynamical observables which we shall employ in section 2.1.6 and appendix A. The Onsager regression

hypothesis [36] states that the *macroscopic* relaxation of a system that has been driven (weakly) away from equilibrium, as discussed in section 1.0.3, is identical to the mean regression of *microscopic* fluctuations at equilibrium. This statement can be formally demonstrated for some special observables under idealized conditions via the Fluctuation-Dissipation-Theorem (appendix C).

Having defined the set of coarse-grained thermodynamic variables, $\{\boldsymbol{R}^{N+1}\}$, in eqn (1.31), and their effective potential (conformational free energy) via eqn (1.33), a dynamical model describing the evolution of the distribution function of the thermodynamic variables close to equilibrium was defined, eqn (1.43), via the definition of the free energy density, eqn (1.35), the thermodynamic force, eqn (1.36), and its relation to the flux velocity eqn (1.38). This model is irreversible and correctly predicts Fick's law. In addition to the constraint that the phenomenological mobility tensor must be positive semi-definite, beginning with an alternative phenomenological law, Onsager showed that time-reversibility of the microscopic equations of motion enforce the constraint that $\underline{\underline{\boldsymbol{H}}}$ is generally symmetric in the absence of a magnetic field (See de Groot and Mazur [36] chapter 7 section 4). Some additional assumptions then lead again to the Smoluchowski equation, eqn (1.43); this time with the symmetric constraint acting on the mobility matrix (See de Groot and Mazur [36] chapter 7 section 6). Generally other constraints may exist for the form of the mobility matrix, however all these considerations are beyond the scope of this work since we only ever consider the simple form: $\underline{\underline{\boldsymbol{H}}}_{ij} = \delta_{ij}\underline{\boldsymbol{I}}/\xi$.

In the case of polymer solutions, hydrodynamic interactions are frequently modelled using the $i \neq j$ elements of $\underline{\underline{\boldsymbol{H}}}_{ij}$, to give the contribution to the flux of one bead due to the force acting on another bead via eqn (1.38) [39].

Finally, at this level of description the planar stress tensor may be defined via the thermodynamic forces, eqn (1.36), that act on the beads, in an identical way to the microscopic case, eqn (1.4), except that there is no term involving velocities; there is only the 'configurational' term. This coarse-grained definition of the stress is consistent with the thermodynamic definition [39].

For the Rouse model, the average material stress in a volume V that contains N_c chains

is given by:

$$\begin{aligned}\sigma_{\alpha\beta}(t) &= \frac{1}{V}\sum_{l=1}^{N_c}\frac{3T}{b^2}\sum_{i=0}^{N-1}\left(R^l_{i+1,\alpha}-R^l_{i,\alpha}\right)\left(R^l_{i+1,\beta}-R^l_{i,\beta}\right)\\ &= \frac{N_c}{V}\frac{3T}{b^2}\left\langle O_{\alpha\beta}(t)\right\rangle\end{aligned} \tag{1.46}$$

which predicts the Stress Optical Rule (at least applied to coarse-grained Gaussian bonds). We now describe the corresponding dynamical equations for the micro-states of the ensemble. This equivalent description, termed Brownian Dynamics (BD), consists of stochastic equations of motion for the coarse-grained degrees of freedom. When quantities are not amenable to analytic solution an alternative method is to solve them via numerical integration of the stochastic equations of motion.

Brownian Dynamics

The $N+1$ dimensional Langevin equation subject to the potential $U(\{\boldsymbol{R}^{N+1}\})$ in contact with a heat bath at temperature T is:

$$\frac{d\boldsymbol{R}_i}{dt} = \sum_{j=0}^{N}\underline{\underline{\boldsymbol{H}}}_{ij}\cdot\left(-\frac{\partial U(\{\boldsymbol{R}^{N+1}\})}{\partial \boldsymbol{R}_j}+\boldsymbol{f}^r_j(t)\right)+\frac{T}{2}\sum_{j=0}^{N}\frac{\partial}{\partial\boldsymbol{R}_j}\cdot\underline{\underline{\boldsymbol{H}}}_{ij} \tag{1.47}$$

$\boldsymbol{f}^r_i(t)$ is a Gaussian white-noise random variable connecting the particle to the heat-bath:

$$\begin{aligned}&\left\langle \boldsymbol{f}^r_i(t)\right\rangle = 0\,;\\ &\left\langle \boldsymbol{f}^r_i(t)\boldsymbol{f}^r_j(t')\right\rangle = 2T\delta(t-t')(\underline{\underline{\boldsymbol{H}}}^{-1})_{ij}\end{aligned} \tag{1.48}$$

where $\underline{\underline{\boldsymbol{H}}}^{-1}$ denotes the inverse matrix of $\underline{\underline{\boldsymbol{H}}}$. The justification for using eqn (1.47) is that the evolution of the probability distribution for position which results from using an ensemble of systems described by eqn (1.47) is given by the corresponding Smoluchowski equation, eqn (1.43), with the same system potential, mobility matrix and temperature (for a complete discussion of the relation between the Langevin and Smoluchowski descriptions see de Groot and Mazur [36] chapter 7 section 7).

In the simple case that we consider: $\underline{\underline{\boldsymbol{H}}}_{ij} = \delta_{ij}\underline{\underline{\boldsymbol{I}}}/\xi$, eqn (1.47) becomes:

$$\frac{d\boldsymbol{R}_i}{dt} = \frac{1}{\xi}\left(\boldsymbol{f}_i^r(t) - \frac{\partial U(\{\boldsymbol{R}^{N+1}\})}{\partial \boldsymbol{R}_i}\right) \tag{1.49}$$

Eqn (1.49) gives the standard Brownian Dynamics of a system of $N+1$ particles in a potential U. Note that U is an effective potential that depends upon the state point of the fundamental system via eqn (1.32). If the temperature or density of the fundamental system is changed then the effective potential must be reformulated, and there is no guarantee that a previous definition of coarse-grained variables will remain a good one. In section 2.1 we will use numerical integration of the Langevin equation for a single-chain 'Brownian Dynamics' model interacting with a flat reflective surface.

Molecular Dynamics

Eqn (1.49) may alternatively be found as the zero inertia limit ($m_i \to 0$, where m_i is the mass of the ith particle) of Newton's second law:

$$m_i \frac{d^2\boldsymbol{r}_i}{dt^2} = \boldsymbol{F}_i^{\text{tot}} \tag{1.50}$$

which, in addition to the thermodynamic force, includes the friction force $-\xi\frac{d\boldsymbol{r}_i}{dt}$, and the stochastic force, $\boldsymbol{f}_i^r(t)$:

$$m_i \frac{d^2\boldsymbol{r}_i}{dt^2} = -\frac{\partial U}{\partial \boldsymbol{r}_i} - \xi\frac{d\boldsymbol{r}_i}{dt} + \boldsymbol{f}_i^r(t) \tag{1.51}$$

where again the friction constant is related to the variance of the random force via $\left\langle \boldsymbol{f}_i^r(t)\boldsymbol{f}_j^r(t')\right\rangle = 2T\xi\delta(t-t')$. The inertial term becomes negligible over time-scales $\Delta t \gg m_i/\xi$.

The loss of information associated with coarse-graining necessitates the introduction of the dissipative and random terms. The accuracy of the assumption that the random force in eqn (1.49) satisfies a Gaussian distribution can then be understood to depend on the validity of the assumption that the forces acting from traced over microscopic degrees of freedom can be considered uncorrelated on time-scales in which inertia is negligible, so that their sum, represented by $\boldsymbol{f}_i^r(t)$, is Gaussian.

Eqn (1.51) is also often used as a form of 'thermostating' Molecular Dynamics solutions of Newton's equations of motion for the microscopic degrees of freedom. In this case we designate the thermostat friction constant as ξ_{MD}. Although unphysical, thermostat methods are used to counteract the increase in temperature resulting from cumulative errors in the numerical integration scheme, or to simulate quasi-isothermal non-equilibrium processes. Various alternative velocity renormalization schemes have been developed to counteract these heating effects [9]. In the Molecular Dynamics simulations reported in this thesis, the so called Langevin thermostat described by eqn (1.51) is employed. A problem with this thermostat method is that it does not conserve momentum, which may lead to unphysical behaviour if inertia is important over time-scales longer than those in which momentum is approximately conserved using the thermostat. Once an MD system has been properly equilibrated (via preparation using a thermostat or otherwise), it is possible to solve Newton's equations without the addition of a thermostat providing that the simulation is run for a sufficiently short time at a given time-step such that temperature is maintained throughout. In Section 2.2, in order to assess the effect of the thermostat on the dynamics of polymer chains near a surface, we carry out identical simulations using two values of the friction constant; a high value (the literature standard) and a much lower value. Observables using the lower value correspond closely to the limit $\xi_{\mathrm{MD}} = 0$, since for this value hydrodynamics is not important after the timescale $\Delta t \approx m_i/\xi_{\mathrm{MD}}$ for the chain length investigated.

In Molecular Dynamics simulations reported in this thesis, the Verlet algorithm [9] has been used to solve the equations of motion. The Verlet algorithm eliminates the velocity from the evolution equation for particle position by summing the second order expansion of the position at previous and future incremental time-steps:

$$\begin{aligned} \boldsymbol{r}(t+\Delta t) &= \boldsymbol{r}(t) + \boldsymbol{v}(t)\Delta t + \frac{\boldsymbol{a}(t)}{2}\Delta t^2 + \ldots \\ \boldsymbol{r}(t-\Delta t) &= \boldsymbol{r}(t) - \boldsymbol{v}(t)\Delta t + \frac{\boldsymbol{a}(t)}{2}\Delta t^2 - \ldots \end{aligned} \tag{1.52}$$

leading to:

$$\boldsymbol{r}(t+\Delta t) = 2\boldsymbol{r}(t) - \boldsymbol{r}(t-\Delta t) - \frac{1}{m}\left.\frac{\partial U}{\partial \boldsymbol{r}}\right|_t \Delta t^2 \tag{1.53}$$

To second order the velocity can be written in terms of position using eqn (1.52):

$$\frac{\boldsymbol{r}(t+\Delta t)-\boldsymbol{r}(t-\Delta t)}{2\Delta t}=\boldsymbol{v}(t) \tag{1.54}$$

Hence the instantaneous velocity is not available until a time-step later. This means that the velocity term in the Langevin thermostat, eqn (1.51), must be approximated using:

$$\frac{d\boldsymbol{r}(t)}{dt}\approx\frac{\boldsymbol{r}(t+\Delta t)-\boldsymbol{r}(t)}{\Delta t} \tag{1.55}$$

which introduces an error of order Δt into the frictional force in eqn (1.51). As an alternative, the Velocity-Verlet algorithm [9] is often used, for which the velocities are evolved along with the positions. However we find that both algorithms give effectively identical results at all time-steps used.

Molecular dynamics boundary conditions

Although the majority of MD simulations employ periodic boundary conditions in all directions in order to avoid explicit boundary effects and directly simulate bulk systems, there have been a number of studies using explicit boundaries, e.g. to investigate surface friction in both simple and polymeric fluids [159, 131, 132, 122]. We employ similar methods in order to bound the fluid using Lennard-Jones beads, and/or place surface end-tethered chains. In both cases a Face Centred Cubic (FCC) lattice is used which is oriented such that the plane bounding the fluid has Miller indices (111) [181] and unit vector $\hat{\boldsymbol{y}}$. A view normal to the lattice plane is shown in figure 1.5.

The relative dimensions of the periodic widths in the $\hat{\boldsymbol{x}}$ and $\hat{\boldsymbol{z}}$ directions depend upon the orientation of the lattice. The nearest neighbour distance between lattice sites is denoted by r_{nnd}. In the (111) orientation an infinite lattice conformation is invariant with respect to translations of r_{nnd} in the $\hat{\boldsymbol{x}}$ direction and $\sqrt{3}r_{\text{nnd}}$ in the $\hat{\boldsymbol{z}}$ direction. For this reason, in order to produce an isotropic surface environment care must be taken that the periodic width in the $\hat{\boldsymbol{x}}$ direction be a multiple of r_{nnd}, whereas in the $\hat{\boldsymbol{z}}$ direction a multiple of $\sqrt{3}r_{\text{nnd}}$ is required. The grafting density is $\rho_g = 1/r_{\text{nnd}}^2$.

As an alternative to a physical boundary constructed with lattice beads, a reflective bound-

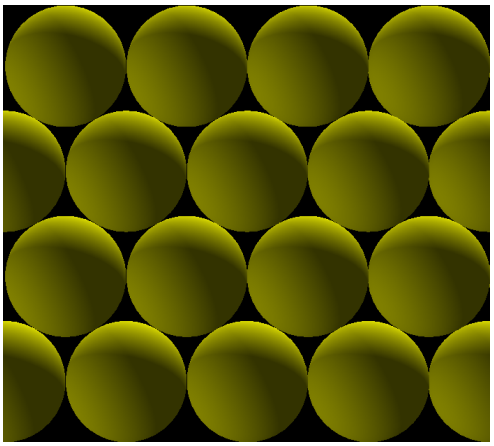

Figure 1.5: View of the cross section of the lattice placement (lattice beads are placed at centres of yellow spheres with radius r_{nnd}) in a simulation box with periodic width $4r_{\mathrm{nnd}}$ in the $\hat{\boldsymbol{x}}$ direction (horizontal) and $2\sqrt{3}r_{\mathrm{nnd}}$ in the $\hat{\boldsymbol{z}}$ direction (vertical). The view into the page is looking onto the surface plane in the surface normal ($\hat{\boldsymbol{y}}$) direction. The surface plane has Miller indices (111).

ary may be employed (in isolation or in addition to a lattice placement of tethered chain ends). Using a reflective boundary, if a bead in the fluid crosses the surface boundary its current and previous positions are reflected in the surface plane. This simultaneously reflects the bead velocity, defined in eqn (1.55).

The Generic Polymer Simulation (GPS) MD code written at the University of Reading [101, 95, 22] is used in this thesis. When necessary, additions, such as the explicit boundaries described here, are made to the package.

Computer simulation using realistic polymer models is a modern method, complementary to experiment, for testing theory and making observation. However, no matter how detailed the models are, they must be subject to validation via experiment.

Plan of the thesis, and summary of the principal results

The content of chapter 2 has been published in 'Macromolecules' (in collaboration with Patrick Ilg) [78]. The content of chapter 4 has been submitted for publication (in collaboration with Patrick Ilg and Zuowei Wang). The content of chapter 5 has been submitted

for publication (in collaboration with Patrick Ilg and Martin Kröger).

In chapter 2 we will investigate, by extensive Molecular Dynamics simulations as well as a simplified single-chain model, the influence of steric hindrance on the dynamic properties of non-entangled chains in polymer melt due to confining surfaces. Non-entangled descriptions are also relevant for the dynamic correlations of longer entangled polymers over a duration of time that is short with respect to a characteristic time, τ_e (often termed the 'equilibration time'), for which dynamic correlations become aware of topological constraints. We extend the Rouse model to also include wall effects, using an additional potential that results from the assumption that chain conformations have reflected random-walk statistics, as first advocated by Silberberg. Results for end-to-end vector and Rouse mode correlation functions of chains end-tethered to the surface compare well with those obtained from Molecular Dynamics simulations of a multi-chain system using the Kremer-Grest bead-spring model (KG MD). Even though the additional single-chain potential is parameter-free, we show that the accuracy of the model for surface chains is comparable to that of the Rouse model for bulk chains. An analytic dumbbell model accurately describes the longest Rouse mode correlation function of surface-tethered 'mushroom' chains immersed in a polymer melt at low grafting density.

Chapter 2 looks at dynamical behaviour of individual chains in the melt, whereas chapter 3 investigates the behaviour of inter-chain correlations of segmental motions under confinement using boundaries with different degrees of roughness on a monomeric scale, and compares the results to the case using periodic boundaries [24].
The most important conclusion from chapter 3 is that global rheological properties (stress relaxation) of polymer melts that are confined in a channel are strongly dependent upon the structure of the surface (the boundary condition). This remains true even when the dimension of the channel considerably exceeds a characteristic size of the surface structure (surface roughness).
Systems that are relevant to the industrial application of polymer extrusion will have interfacial regions that are very narrow compared to their bulk region. However, for

computational reasons we are limited to simulating channel widths which, although often defined as 'weakly confining', are still no greater than ten times the bulk radius of gyration. Although the chain conformations in the interfacial region of such weakly confined films do not differ from the infinite channel limit, the degree of rheological coupling between different regions of a film is not well understood. Therefore the non-local stress correlations between different parts of a film are also investigated. This chapter sheds light on the finite-size effects of our simulations and also has relevance with respect to the surface rheology of thin films and polymer composites with large filler particles.

The success of the non-entangled model investigated in chapters 2 and 3 motivates its extension to entangled systems via the introduction of slip-springs [94]. Chapter 4 investigates this model.

First, the dynamics of an entangled polymer melt confined in a channel by parallel plates is investigated by Molecular Dynamics (MD) simulations of a detailed, multi-chain model. A Primitive Path Analysis predicts that the density of entanglements remains approximately constant throughout the gap and drops to lower values only in the immediate vicinity of the surface. Based on these observations, we propose a coarse-grained, single-chain slip-spring model with a uniform density of slip-spring anchors and slip-links. In order to evaluate the value of a theoretical model it is necessary to compare its predictions with unambiguous dynamical observations using a well defined and physically relevant system. Molecular Dynamics provides an ideal platform for such observations, in addition to initially motivating the choice of slip-spring density profile. The slip-spring model is compared to the Kremer-Grest MD bead-spring model via equilibrium correlation functions of chain orientations. Reasonably good agreement between the single-chain model and the detailed multi-chain model is obtained for chain relaxation dynamics, both away from the surface and for chains whose center of mass positions are at a distance from the surface that is less than the bulk chain radius of gyration, without introducing any additional model parameters. Our results call into question the widely held assumption of a drop in topological interactions in the vicinity of a surface. We infer from the slip-spring model that the experimental plateau modulus of a confined polymer melt may be less than a corresponding

unconfined system even if there is no drop in topological interactions for the confined case.

In chapter 5, we perform non-equilibrium Molecular Dynamics shear-flow simulations of an entangled polymer melt consisting of flexible linear chains. A steady-state rectilinear shear-flow is developed by sliding explicit walls with permanently grafted chains in a simple planar Couette flow geometry. As the channel average shear-rate is increased, a rapid coil-stretch transition of the surface end-grafted chains is observed. The corresponding primitive path network properties are investigated, revealing a disentanglement between surface grafted and non-grafted chains during the coil-stretch transition. Changes in slip length and surface friction are also measured. Grafted chains develop a trumpet like conformation at high shear-rates, which correlates with an increased relative density of entanglements near the free ends, a phenomenon that has already been considered by scaling models. The same mechanisms leading to slip in the investigated system may remain relevant for polymer melts of much higher (and more experimentally relevant) molecular weights. Therefore we use the simulation results to examine the predictions and assumptions of some existing theoretical models. The conclusions drawn from the simulation may be used in the future to further develop theoretical models for the surface rheology of polymer melts.

Chapter 2

Chain dynamics in a non-entangled polymer melt confined by a flat surface

In this chapter we employ the Smoluchowski, Brownian Dynamics and Molecular Dynamics (MD) formalisms presented in the previous chapter in order to study the dynamics of polymer melts near to surfaces. The content of this chapter has been published in Macromolecules (with Patrick Ilg) [78]. Some superficial changes have been made with respect to the published article to allow for thesis integration. In addition, the text refers to some results that were not originally included in the paper, which are included in appendix B. Section 2.3 has an updated discussion involving these appendices.

Current interest in polymer dynamics at surfaces can be separated into two general system categories. In the first category, the size of the region in which chains are influenced by the surface is comparable to a bulk size. Examples of such systems are polymer melts or solutions in thin films or narrow pores [163]. Also, systems with filler particles much larger than the size of polymer coils, and sufficiently high filler concentration, belong to this category [170, 164]. The global rheological properties will be strongly influenced by the chain behaviour near to the filler surfaces. Strong confinement occurs when there is no bulk region and any given chain may interact with more than one surface simultaneously, leading to different chain statics and dynamics compared to weak confinement, which is the focus of this thesis, where chains only interact with a single surface and at least the

static behaviour of chains in the surface vicinity coincides with an asymptotically wide channel.

In the second category, the only chain bounding surface lies at the system extremities, and the boundary layer is small compared to the bulk dimension. Then surface chain behaviour is relegated to a dynamic boundary condition, as discussed in 1.0.4, which can be important for shear flows [15, 158].

For high molecular weight melts or dense solutions, a likely surface effect will be a change in the behaviour of entanglements. At the time of writing, investigations into the dynamics of entangled polymers in interfacial regions have concentrated on using equilibrium Molecular Dynamics simulations [63, 146, 157] to find an 'entanglement molecular weight' parameter as a function of position relative to the surface. Theories for entangled polymers are typically built upon the Rouse model [140], which in addition to low molecular weight systems, describes the dynamics of long entangled polymers on short time-scales before they are aware of the topological constraints formed from neighbouring chains. It is therefore to some degree fundamentally important to investigate how the non-entangled dynamics change near to surfaces, in order to identify the corresponding changes in entangled dynamics and the crossover between the two regimes. Therefore before investigating entangled dynamics at surfaces in chapter 4, the purpose of this chapter is to investigate the corresponding non-entangled dynamics.

In addition to entanglements, many recent Molecular Dynamics studies of surface chain dynamics have been motivated by experimental observations that the glass transition temperature can change near to a surface [152, 80, 120, 175, 165, 151]. Both atomistically detailed [152, 80, 175] and coarse-grained [165, 151] simulation models have been used. Methods of investigation include probing changes in Rouse mode correlation functions or monomer layer occupation survival functions [175, 165], and observing rates of diffusion parallel to and normal to the surface [165, 151]. A quite comprehensive review of older work was made by Mischler et al. [120].

In atomistic models, microscopic details not present in the coarse-grained descriptions, such as torsional potentials, may influence the particular wall interaction. However, even coarse-grained models, such as the Kremer-Grest Molecular Dynamics (KG MD) [81] poly-

mer melt model that we investigate in this work, may conserve important dynamic mechanisms occurring over the length scale of a single coarse-grained bond, whose strength depends on the particular choice of surface interaction and the parameters used in the interaction potentials. One such example which could be important at temperatures approaching the glass transition is 'layer-exchange dynamics', [175] occurring between the identifiably ordered monomer layers induced by smooth surfaces [159]. A recurrent issue which we aim to settle is the distinction between such microscopic surface effects, which depend strongly on chemical detail, and larger scale dynamics which are universal for all flexible polymers. Chain relaxation at long time scales is entropic in origin and depends more generally on how global chain orientation statistics differ near to a surface due to steric hindrance.

It has already been identified that the conformations of chains near a flat confining surface in a wide channel using the KG MD model are reasonably well described using reflected random walk statistics [144]. In this chapter we construct a modified-Rouse model for the Brownian dynamics of reflected random walks which reduces to the Rouse model in the bulk. Within this model we explore the dynamics of chains that are either end-tethered at the surface, or non-tethered but in the proximity of it, and compare the results with those of the KG MD model.

We also consider how the inaccuracies of the Rouse model crossover to the modified-Rouse model. In recent years it has become more clear for exactly which observables and to what extent the Rouse model gives accurate predictions for general polymer melt systems [51, 111, 125, 126, 72]. A joint experimental and simulation study of a $C_{100}H_{202}$ melt revealed deviations from the Rouse prediction for the dynamic structure factor in the high momentum transfer end of the considered spectrum [126], corresponding to the first three Rouse modes. In the simulation portion of the same study, correlation functions of even the longest Rouse modes displayed stretched exponentials, instead of the single exponential modes predicted by Rouse. Despite such discrepancies, the Rouse model can reasonably describe the bulk linear stress relaxation function of a wide variety of non-entangled polymer melts when the effects of glassy modes are taken account of [51].

The Rouse model assumes the validity of Flory's hypothesis [53], which states that in the

melt, chain orientations satisfy random-walk statistics. Wittmer et al. [171, 172] have described theoretically how the correlations of bond vectors within melt chains decay more slowly along the chain contour than predicted by Edwards. [39]. Resultantly, even in bulk there are non-negligible deviations from Gaussian statistics up to length scales which may extend into the entanglement regime, as is the case for the KG MD model. There have been attempts to understand the relative success of the Rouse model despite this observation [50]. In turn, the accuracy of other key Rouse assumptions have been considered: screening of hydrodynamic interactions [47, 48], and the 'phantom-chain' picture in which topological interactions between neighbouring chains are neglected [95, 49]. Under strong confinement, approaching the two-dimensional and one-dimensional limit in polymer films [145, 27] and nano-tubes [90] respectively, the Strasbourg group and co-workers have demonstrated much stronger deviations from ideality. These papers have shown that for ultra thin films of width comparable to a chain 'blob' length, there is a logarithmic correction to the surface parallel chain dimension. Correspondingly it may be conjectured that a similar correction may occur in a wide channel for chains whose centre of mass falls within a single blob length from the surface. In this work we find that short flexible chains near to the surface are only weakly swollen in the surface parallel direction, and that this effect also has a contribution from a weak nematic interaction which occurs even for the 'fully-flexible' KG MD model. Although the ratio of confined radius of gyration to bulk radius of gyration is an increasing function of chain length in the surface parallel direction [27], in weak confinement the distance from the surface to the centre of mass of surface chains scales with the bulk radius of gyration [144]; therefore in wide channels corrections to ideality near the surface may be of even less importance for longer chains.

The multi-chain 'soft MD' model, which allows bond crossings and therefore explicitly satisfies the phantom-chain picture of the Rouse model, has been shown to fail to match the Rouse prediction for mid-bead mean square displacement [96]. In the same work, the more realistic KG MD model, which does not allow bond crossings but has very similar conformation statistics to soft MD, showed improved agreement. This suggested that topological interactions play a dynamical role even before the onset of the entanglement regime, which for certain observables may even improve agreement with the Rouse model.

In section 2.3 we compare results for mid-monomer and centre of mass mean square displacement near the surface using the soft MD and KG MD models.

This chapter is organized as follows: in section 2.1 we review the structure of the Rouse model and the ideas of Silberberg relating to the conformations of polymer chains in melt at a surface. These ideas motivate a modification of the Rouse model to include surface effects. We shall be interested primarily in the behaviour of the resulting model for chains consisting of a large number of bonds, analogous to the continuous Rouse model, which may be compared with the behaviour of reasonably long but non-entangled KG MD chains. Generally, the modified-Rouse model is solved numerically, although the longest relaxation behaviour of a surface-tethered chain is accurately modelled using a dumbbell, tethered by one end to a reflective surface. We derive an analytic expression for the end-to-end vector correlation function of the dumbbell in the wall normal direction. We show that the functional form of the dumbbell end-to-end vector correlation function closely matches the first Rouse mode auto-correlation function of a chain consisting of many bonds, and that the correspondence between the two functions matches that of the standard analytic Rouse model, applicable to chains without boundary constraints.

In section 2.2, the modified-Rouse model is compared to KG MD, via the end-to-end vector and individual Rouse mode (mode numbers $p > 0$) correlation functions of surface-tethered chains. We investigate chain lengths spanning the non-entangled regime (comprising 32, 64 or 128 bonds). Whilst we find that the choice of thermostat friction constant has little effect on the end-to-end correlation function, which is dominated by the longest Rouse modes, Farago et al. [47, 48] have shown that the zeroth Rouse mode, i.e., the centre of mass motion, deviates strongly from simple diffusion at times shorter than the Rouse time, and is strongly dependent on the coupling between chain elasticity and hydrodynamics. In section 2.3 we show that the surface parallel component of the zeroth mode motion has an enhanced diffusion rate in the presence of a perfectly smooth flat surface. Final conclusions are made in section 2.4.

The Rouse model with a reflective boundary condition

A simple class of single-chain model assumes that the dynamics of a polymer chain, consisting of $N+1$ connected beads, may be described via a set of $N+1$ Langevin equations, which without external force are of form (from 1.2.2):

$$\frac{d\boldsymbol{R}_i}{dt} = \sum_{j=0}^{N} \underline{\underline{\boldsymbol{H}}}_{ij} \cdot \left(-\frac{\partial U}{\partial \boldsymbol{R}_j} + \boldsymbol{f}_j^r(t) \right) + \frac{T}{2} \sum_{j=0}^{N} \frac{\partial}{\partial \boldsymbol{R}_j} \cdot \underline{\underline{\boldsymbol{H}}}_{ij} \tag{2.1}$$

for $i = 0, 1, ..., N$. The position vector of bead i is denoted by $\boldsymbol{R}_i$. In this work we consider such a model of a single polymer chain in a channel bounded in only one direction such that $y_{w1} < y_i < y_{w2}$, where the positions of the channel walls are denoted by y_{w1} and y_{w2}; we resolve $\boldsymbol{R}_i$ into surface normal and surface parallel components, $\boldsymbol{R}_i = \boldsymbol{R}_{i,\parallel} + y_i \hat{\boldsymbol{e}}_\perp$, where $\hat{\boldsymbol{e}}_\perp$ is the wall normal direction unit vector.

In the case of the Rouse model, the assumption that hydrodynamic interactions are screened led to a simple form for the mobility tensor:

$$\underline{\underline{\boldsymbol{H}}}_{ij} = \frac{\delta_{ij} \underline{\underline{\boldsymbol{I}}}}{\xi} \tag{2.2}$$

This assumption is usually considered valid for the melt or concentrated solution. $\boldsymbol{f}_i^r(t)$ is then a Gaussian white-noise random variable:

$$\begin{aligned} &\langle \boldsymbol{f}_i^r(t) \rangle = 0\,; \\ &\left\langle \boldsymbol{f}_i^r(t) \boldsymbol{f}_j^r(t') \right\rangle = 2T\xi\delta(t-t')\delta_{ij}\underline{\underline{\boldsymbol{I}}} \end{aligned} \tag{2.3}$$

The equilibrium probability distribution of a given set of bead positions specifying a system state is related to the potential U by eqn (1.33).

As discussed in the previous chapter, using the assumption that sub-segments of polymer chains satisfy Gaussian statistics on all length scales, Rouse found a harmonic potential acting between beads, eqn (1.34). In this chapter we investigate whether the assumptions of the Rouse model are equally accurate near the surface. Namely that:

1. Hydrodynamic interactions are screened: beads experience isotropic friction, eqn (2.2).
2. Time dependent topological constraints are not considered.

Under these assumptions, eqns (2.1), (2.2) and (2.3) remain valid, but with a modified potential U, corresponding to a different probability distribution of segment orientations. We determine the modified potential by requiring that the equilibrium probability distribution corresponds to a random walk with a particular boundary condition. Crucially, any such model reduces to the Rouse model far from surfaces. In 1982 Silberberg advocated that the reflective boundary condition is appropriate to describe melt statistics at a flat surface [148].

Silberberg's hypothesis: surface chain conformations are reflected random walks

Silberberg's hypothesis is an extension of the Flory hypothesis [53] for polymer melts at a flat surface. As a result of the effective incompressibility of the melt state, the monomer density remains almost uniform up to an interface. Silberberg argued that since monomers experience an isotropic environment right up to the surface, Flory's argument should hold equally well in this region. Then the probability distribution for the orientation of a chain bond near (but not in direct contact with) a flat impenetrable surface is identical to the bulk distribution, having no preferred direction.

In the simplified case of a random walk lattice chain model, the hypothesis means that locally the polymer melt at a flat surface looks the same as the unconfined melt. The only difference being that steps beginning at the surface are constrained to move away from it, therefore satisfying reflective boundary conditions. Silberberg showed that a method of images like conformation swap procedure conserves the unconfined segment partition function and respects the boundary constraint. Since the random walk uncouples in directions parallel and normal to the surface, the conformation swap only affects the wall normal probability distribution.

Sussman et al. [157] have noted that the conformation swap procedure of Silberberg may be generalized to the case of chains bounded by two surfaces in a channel of width L_c.

The total partition function (number of walks) of a chain with fixed start position inside the channel is conserved irrespective of the channel width, as must be the case under reflective boundary conditions. If the ith segment is near to one of the surfaces, and we allow the channel width to go arbitrarily large, $L_c \to \infty$, the probability weight for the wall normal end position of the segment, y_i, under the conditions of segment start position, y_{i-1}, and wall position, y_w, reduces to the form found by Silberberg, given by a sum of two unbounded walk weights (in the continuous limit):

$$\begin{aligned} P(y_i|y_{i-1}, y_w) &= P(y_i|y_{i-1}) + P(\bar{y}_i|y_{i-1}) \\ &= \frac{1}{\sqrt{2\pi {\sigma_1}^2}} \exp\left(-\frac{(y_i - y_{i-1})^2}{2{\sigma_1}^2}\right) + \frac{1}{\sqrt{2\pi {\sigma_1}^2}} \exp\left(-\frac{(\bar{y}_i - y_{i-1})^2}{2{\sigma_1}^2}\right) \end{aligned} \tag{2.4}$$

where $\bar{y}_i$ is the surface reflected end position $\bar{y}_i = y_w - (y_i - y_w)$, and ${\sigma_1}^2 = b^2/3$. In appendix A.1 we find eqn (2.4) directly by solving the formal boundary value problem with a pair of reflective boundaries in the limit $L_c \to \infty$.

Modified-Rouse potential

We propose a potential for eqn (2.1) when a chain segment is close to a flat impenetrable surface in a wide channel, using eqn (2.4) and the general relation, eqn (1.33). The final potential comprises the Rouse potential, eqn (1.34), and an additional term due to the surface which depends on the set, $\{y^{N+1}\}$, of bead positions in the wall normal direction, relative to the surface position:

$$U(\{\boldsymbol{R}^{N+1}\}) = U_{\text{Rouse}}(\{\boldsymbol{R}^{N+1}\}) + \sum_{i=1}^{N} A(y_i, y_{i-1}, y_w) \tag{2.5}$$

where the additional term is:

$$A(y_i, y_{i-1}, y_w) = -T \log\left(1 + \exp\left(-\frac{2(y_i - y_w)\,(y_{i-1} - y_w)}{{\sigma_1}^2}\right)\right) \tag{2.6}$$

Woo et al. [173] similarly derived a potential using absorbing boundary conditions. Absorbing boundaries are considered appropriate for an ideal polymer chain in dilute solution.

The reader is referred to appendix A.2 for a derivation of the resulting potential in both cases.

If the channel width, L_c, is very large compared to the characteristic chain segment length, b, the contribution to the partition function corresponding to segment conformations which are reflected at both surfaces is negligible. This is certainly the case for the weakly confined simulations that we study in this work; therefore we neglect the finite channel corrections [157] to eqn (2.4) and use a system potential consisting of two wall interaction terms of the form given in eqn (2.6), corresponding to the two surfaces.

Single chain (modified-Rouse) model numerical scheme

Using the potential given by eqn (2.5), adapted to a system with two parallel walls, we solve the set of equations (2.1), (2.2) and (2.3) numerically, using a two-stage predictor-corrector algorithm for the conservative force, the simplest Euler scheme for the random force [182] and reflective boundary conditions. The algorithm is:

$$\begin{aligned}\bar{\mathbf{R}}_i(t+\Delta t) &= \mathbf{R}_i(t) + \frac{\Delta t}{\xi}\mathbf{f}_i^c(\mathbf{R}(t)) + \sqrt{\frac{2T\Delta t}{\xi}}\mathbf{n}_t \\ \mathbf{R}_i(t+\Delta t) &= \bar{\mathbf{R}}_i(t+\Delta t) + \frac{\Delta t}{2\xi}(\mathbf{f}_i^c(\bar{\mathbf{R}}(t+\Delta t)) - \mathbf{f}_i^c(\mathbf{R}(t)))\end{aligned} \tag{2.7}$$

where $\mathbf{f}_i^c(\mathbf{R}(t)) = -\frac{\partial U(\{\mathbf{R}^{N+1}\})}{\partial \mathbf{R}_i}\Big|_t$ is the conservative force, and $\mathbf{n}_t$ is a normally distributed random vector with unit variance in each direction. If the particle crosses a boundary its position is reflected in the boundary plane. We are aware of numerical errors in this scheme and more advanced algorithms have been proposed [128]. For the present case, we have confirmed convergence of the numerical scheme, and validated agreement with static and dynamic analytic results where available. In the bulk, the natural length unit is b. We find the shortest natural time unit, τ_b, from the bead diffusion for very small t:

$$\tau_b = \frac{\xi b^2}{6T} \tag{2.8}$$

Accurate results are found using a time-step $\Delta t = \tau_b/10$. Smaller time-steps yield nearly identical results.

Mapping to the single-chain (modified-Rouse) model

While a number of detailed studies on coarse-graining interacting many-chain systems exist [124], much less is known about mapping a many-chain system to an effective single-chain model [67]. In order to investigate the usefulness of the modified-Rouse model for describing polymer dynamics of non-entangled melts near surfaces, we study two multi-chain bead-spring 'fundamental' models as references; both described in more detail in section 2.2.

We restrict ourselves to fundamental systems with chains containing an even number, n, of bonds, such that we can define a mapping ratio $m : 1$ to the modified-Rouse model comprising $N = n/m$ bonds and $N+1$ beads, where m is a divisor of n. The only constraint within our mapping is that we pick b such that the chain mean square end-to-end distance matches the fundamental model in the bulk:

$$b = \sqrt{\frac{\langle \boldsymbol{u}_{\mathrm{bulk}}{}^2 \rangle}{N}} \tag{2.9}$$

where $\langle \boldsymbol{u}_{\mathrm{bulk}}{}^2 \rangle$ is the mean square end-to-end distance of bulk chains within the fundamental model using periodic boundaries. Then the degree to which other system observables, such as more general internal square distances, are successfully mapped, depends upon the accuracy of reflected random walk statistics on all length scales. Results presented in section 2.2 will test the extent of this agreement. Within the modified-Rouse model we keep $T = 1$. This leaves two unknown parameters in the model: the mapping ratio m which decides N, and the friction coefficient ξ. These two parameters are chosen from the best simultaneous fit of the auto-correlation functions of the longest Rouse modes of surface-tethered chains. For a more systematic derivation of single-chain friction coefficients using projection operator techniques, see e.g. Akkermans et al. [7] and Ilg et al. [66].

Before mapping the fundamental models, we first investigate the general dynamical behaviour of chains end-tethered at the surface using the modified-Rouse model.

Dynamics of the modified-Rouse model

For a chain connected by harmonic bonds, the dynamic equations of the Rouse normal coordinates (modes) uncouple for all possible chain conformations. However, for such a chain experiencing confinement, the real space description of dynamics cannot be replaced by uncoupled Rouse modes, since they are effectively coupled via the boundary conditions. We are left then with a complicated system of coupled equations and boundary conditions even without the additional potential, eqn (2.6). Despite this, the Rouse mode correlation functions remain important general observables, since they describe the decay of chain structure correlations with characteristic segment number 'wavelength' $m_p \approx 2N/p$, where p is the mode number. All correlation functions which depend solely on chain bond orientations can be written as a function of Rouse mode auto- and cross-correlation functions. Should the mapped modified-Rouse model predict these correlation functions well, all orientation correlation functions must be well described.

In a different approach to Vladkov et al. [165], in which Rouse mode analysis was performed over a limited time duration on free chains binned from chain positions in the channel at $t = 0$, we first investigate the dynamics of chains which have a constraint keeping them in the surface region for all time. We choose to make the constraint by fixing one of the end beads at the surface. Surface-adsorbed chains themselves strongly influence rheological properties [168, 149]. In section 2.3 we use a similar binning method to Vladkov et al. to investigate the mean square displacement behaviour of free chains at different points in the channel.

We analyse the orientational relaxation of the surface-tethered chains in terms of the normal modes of unbounded Rouse chains with one end fixed. These coordinates differ slightly from those usually referred to by 'Rouse modes' (this term is usually reserved for the normal modes of Rouse chains with free ends), and are derived for finite N in A. Likhtman's short course: 'Entangled Polymer Dynamics': [93]

$$\boldsymbol{X}_p = \frac{1}{N+1/2} \sum_{j=1}^{N} \boldsymbol{R}_j \sin\left(\frac{\pi j(p-1/2)}{N+1/2}\right) \tag{2.10}$$

For simplicity we refer to the set of coordinates, $\boldsymbol{X}_p$, as 'Rouse modes', to emphasize that they correspond to the normal modes of tethered chains within the Rouse model.
We now show that the functional form of the longest Rouse mode correlation function within a modified-Rouse model of a surface-tethered chain can be accurately modelled by an analytic dumbbell model.

End-to-end vector correlation function of a surface-tethered dumbbell

The dynamics of the modified-Rouse model uncouple in Cartesian coordinates providing that one axis coincides with the surface normal direction. Since the dynamical equations in each parallel direction coincide, we define dynamic functions for directions normal, $\perp$, and parallel, $\|$, to the surface. In this chapter, when we label functions using the subscripts $\perp$ and $\|$, this always refers to functions of surface-tethered chains unless otherwise stated. The end-to-end vector correlation function is an experimentally accessible observable for type-A dipolar polymers, being proportional to the correlation function of the chain electric dipole in this case. For end-tethered chains, in the α direction it may be generally written in terms of the Rouse coordinates, eqn (2.10), as: [93]

$$\langle u_\alpha(t)u_\alpha(0)\rangle = 4\sum_{p,q=1}^{N}(-1)^{p+q}\cos\left(\frac{\pi(p-1/2)}{2(N+1/2)}\right)\cos\left(\frac{\pi(q-1/2)}{2(N+1/2)}\right)\langle X_{p,\alpha}(t)X_{q,\alpha}(0)\rangle \tag{2.11}$$

where u_α are components of the end-to-end vector. We define a normalized end-to-end vector correlation function with respect to the mean in each direction:

$$\Phi_\alpha(t) = \frac{\langle(u_\alpha(t)-\langle u_\alpha\rangle)\,(u_\alpha(0)-\langle u_\alpha\rangle)\rangle}{\langle u_\alpha^2\rangle - \langle u_\alpha\rangle^2} \tag{2.12}$$

For a dumbbell, the normalized end-to-end correlation function, $\Phi_{\mathrm{db},\alpha}(t)$, coincides with the first normalized Rouse mode auto-correlation function, $A_{1,\alpha}(t)$. The $A_{p,\alpha}(t)$ are:

$$A_{p,\alpha}(t) = \frac{\langle(X_{p,\alpha}(t)-\langle X_{p,\alpha}\rangle)\,(X_{p,\alpha}(0)-\langle X_{p,\alpha}\rangle)\rangle}{\left\langle {X_{p,\alpha}}^2\right\rangle - \langle X_{p,\alpha}\rangle^2} \tag{2.13}$$

Within the modified-Rouse model for an end-tethered chain, the surface normal component of the end-to-end vector is described by a half Gaussian distribution where the first two moments are:

$$\begin{aligned} \langle u_\perp \rangle &= \sqrt{\frac{2\left\langle {u_\perp}^2 \right\rangle}{\pi}} \\ \left\langle {u_\perp}^2 \right\rangle &= \left\langle {u_\parallel}^2 \right\rangle = \frac{Nb^2}{3} \end{aligned} \tag{2.14}$$

where $u_\parallel$ is a component of the end-to-end vector in a surface parallel direction. Resultantly, in the case of a surface-tethered dumbbell, the corresponding potential has a simple harmonic form and therefore corresponds to an Ornstein-Uhlenbeck process [39, 182] with a reflective boundary at the potential minimum. For details of the analytic solution of the end-to-end vector correlation function of this dumbbell model, $\Phi_{\mathrm{db},\perp}(t)$, we refer the reader to appendix A.3. The final expression is:

$$\Phi_{\mathrm{db},\perp}(t) = \frac{1}{\pi/2 - 1}\left(\arctan\left(\mathrm{e}^{-\frac{t}{\tau_{\mathrm{db},\parallel}}}\frac{1}{\sqrt{1-\mathrm{e}^{-\frac{2t}{\tau_{\mathrm{db},\parallel}}}}}\right)\mathrm{e}^{-\frac{t}{\tau_{\mathrm{db},\parallel}}} + \sqrt{1-\mathrm{e}^{-\frac{2t}{\tau_{\mathrm{db},\parallel}}}} - 1\right) \tag{2.15}$$

where $\tau_{\mathrm{db},\parallel}$ is the relaxation time of $\Phi_{\mathrm{db},\parallel}(t)$ which is simply the standard Ornstein-Uhlenbeck process position correlation function.

Regimes of $\Phi_{\mathrm{db},\perp}(t)$

Expanding the dumbbell end-to-end vector correlation function to leading order around $t = 0$ gives:

$$\begin{aligned} \left\langle \left(u_{\mathrm{db},\perp}(t) - \langle u_{\mathrm{db},\perp}\rangle\right)\left(u_{\mathrm{db},\perp}(0) - \langle u_{\mathrm{db},\perp}\rangle\right)\right\rangle &\approx \frac{b^2}{3}\left(1 - \frac{t}{\tau_{\mathrm{db},\parallel}}\right) - \frac{2b^2}{3\pi} \\ &\approx \left\langle u_{\mathrm{db},\parallel}(t)u_{\mathrm{db},\parallel}(0)\right\rangle - \langle u_{\mathrm{db},\perp}\rangle^2 \end{aligned} \tag{2.16}$$

so that in the limit $t/\tau_{\mathrm{db},\parallel} \to 0$ ($\Phi_{\mathrm{db},\perp}(t)$ is not analytic at $t = 0$), the derivative of the dumbbell end-to-end vector correlation function in the wall normal direction is identical to the parallel direction. The dumbbell relaxes as if it were in the unbounded direction, since it has not yet interacted with the surface.

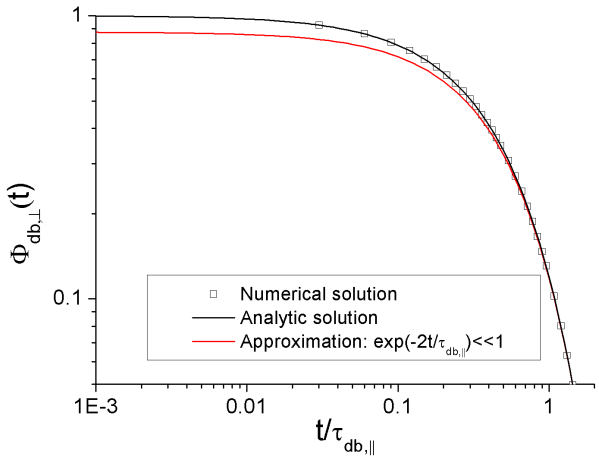

Figure 2.1: Comparison of $\Phi_{\mathrm{db},\perp}(t)$, eqn (2.15), with its long time asymptotic expansion, eqn (2.17), and numerical solution.

For $\exp(-2t/\tau_{\mathrm{db},\parallel}) \ll 1$, expanding eqn (2.15) in $\epsilon = \exp(-2t/\tau_{\mathrm{db},\parallel})$ to leading order gives:

$$\Phi_{\mathrm{db},\perp}(t) \approx \frac{1}{\pi - 2} \exp\left(-\frac{2t}{\tau_{\mathrm{db},\parallel}}\right) \tag{2.17}$$

In figure 2.1, eqn (2.17) is compared to the exact form, eqn (2.15), revealing that for $t \gtrsim \tau_{\mathrm{db},\parallel}/2$, $\Phi_{\mathrm{db},\perp}(t)$ is well approximated by a single exponential with relaxation time $\tau_{\mathrm{db},\parallel}/2$. In the intermediate regime between eqn (2.16) and eqn (2.17), there is a stronger decay, well described by a power-law, $\Phi_{\mathrm{db},\perp}(t) \propto 1/\sqrt{t}$.

In addition, figure 2.1 compares the analytic and numeric solutions for $\Phi_{\mathrm{db},\perp}(t)$. This presents one validation of our numerical Brownian dynamics method.

Correspondence between $\Phi_{\mathrm{db},\perp}(t)$ and $A_{1,\perp}(t)$ (for $N \to \infty$)

For the modified-Rouse model the Rouse modes completely uncouple parallel to the surface, so that the functions $A_{p,\parallel}(t)$ remain single exponential irrespective of N [93]. Since for a dumbbell we have: $\Phi_{\mathrm{db},\alpha}(t) = A_{1,\alpha}(t)$, for $N \to \infty$, $A_{1,\parallel}(t)$ matches $\Phi_{\mathrm{db},\parallel}(t)$ exactly providing we use the correct correspondence between the bead friction coefficient in each model: $\xi \to \xi_{\mathrm{db}}$ (In addition to matching the mean square end-to-end distance of the dumbbell and the chain) where ξ_{db} is the corresponding free bead dumbbell friction. This correspondence is found from equating the longest relaxation times of the models:

$\tau_{1,\parallel} = \tau_{\mathrm{db},\parallel}$. For an unbounded end-tethered Rouse chain, the expression for the mode relaxation times are [93]:

$$\tau_{p,\parallel} = \frac{\xi b^2}{12T \sin^2\left(\frac{\pi(p-1/2)}{2(N+1/2)}\right)} \tag{2.18}$$

For $N \gg 1$, the longest relaxation time $\tau_{1,\parallel}$ is well approximated by its limit $\tau_{R,\parallel}$ ($N \to \infty$):

$$\tau_{R,\parallel} = \frac{4\xi N^2 b^2}{3\pi^2 T} \tag{2.19}$$

Equating $\tau_{R,\parallel}$ with the corresponding relaxation time for a fixed dumbbell gives the limiting relation between ξ and ξ_{db}:

$$\xi_{\mathrm{db}} = \frac{4\xi N}{\pi^2} \tag{2.20}$$

Then if the same correspondence applies in the wall normal direction, the asymptotic ratio of longest relaxation times in directions normal and parallel to the surface, must match the dumbbell ratio which we already know:

$$\frac{\tau_{R,\perp}}{\tau_{R,\parallel}} = \frac{\tau_{\mathrm{db},\perp}}{\tau_{\mathrm{db},\parallel}} = \frac{1}{2} \tag{2.21}$$

Figure 2.2 compares $A_{1,\perp}(t)$ for a modified-Rouse chain comprising 32 bonds with the analytic solution of $\Phi_{\mathrm{db},\perp}(t)$, eqn (2.15). The time axis is normalized assuming the relationship eqn (2.21), where $\tau_{1,\parallel}$ is given by eqn (2.18). As for the parallel direction, described by standard Rouse theory, the large N converged behaviour of $A_{1,\perp}(t)$ is reached by $N \approx 32$. In appendix A.4 we explore the convergence of $\Phi_{\perp}(t)$ as more bonds are used to model a chain.

Figure 2.2 implies that the asymptotic relation, eqn (2.20), remains appropriate in the wall normal direction, and that the form of $A_{1,\perp}(t)$ is very close to being conserved from a dumbbell to a chain consisting of many bonds. Specifically, we see the same power-law crossover from the initial decay, eqn (2.16), to the final single exponential behaviour, eqn (2.17), with relaxation time very close to half that of the unbounded case.

For intermediate modes we see the same qualitative behaviour: for modes $p = 2, 3$, $A_{p,\perp}(t)$ (plotted and compared with the KG MD model in section 2.2) may be fitted to the form of the dumbbell end-to-end correlation function reasonably well, although at very long

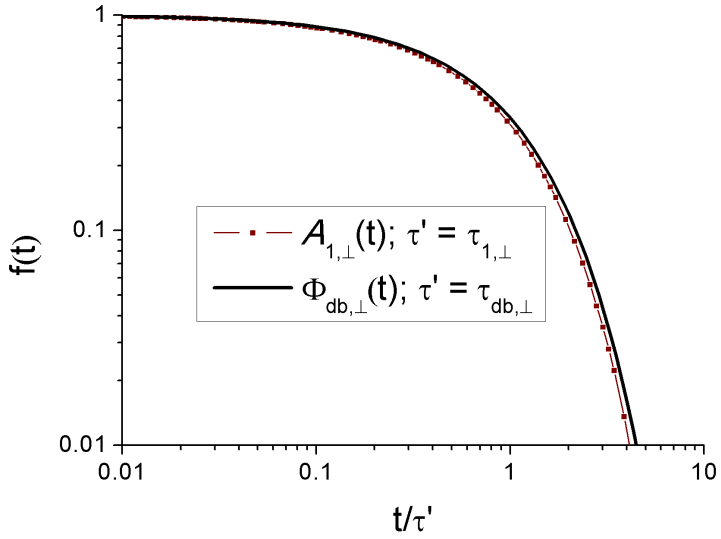

Figure 2.2: Comparison of the analytic solution of $\Phi_{\mathrm{db},\perp}(t)$, eqn (2.15), with $A_{1,\perp}(t)$ using a chain of 32 bonds within the modified-Rouse model. We assume $\tau_{1,\perp} = \tau_{1,\parallel}/2$.

times there are stronger deviations from the single-exponential form. The faster modes mostly decay without interacting with the surface, and therefore we see a return to the unbounded behaviour for $A_{p,\perp}(t)$; $p \gg 1$. Resultantly, the mode relaxation times in the wall normal direction approach those of the wall parallel direction for $p \gg 1$. From eqn (2.18), taking $N \to \infty$, the relationship between successive mode relaxation times in the parallel direction becomes:

$$\frac{\tau_{p,\parallel}}{\tau_{p+1,\parallel}} = \frac{(p+1/2)^2}{(p-1/2)^2} \tag{2.22}$$

In figure 2.3 we compare the first six Rouse relaxation times in the wall parallel direction, $\tau_{p,\parallel}$, found from eqns (2.19) and (2.22), with the corresponding relaxation times in the normal direction, $\tau_{p,\perp}$, which are found by fitting the functions $A_{p,\perp}(t)$ to a single exponential using the Reptate software [133]. The relaxation times, $\tau_{p,\perp}$, are found using a modified-Rouse model consisting of 256 bonds. For this chain bond number and $p < 7$, $\tau_{p,\parallel}$ has effectively asymptotic behaviour: eqn (2.22). Figure 2.3 shows that already at $p = 4$, $\tau_{p,\perp}/\tau_{p,\parallel} > 0.9$.

In appendix A.4.1, the behaviour of the Rouse mode cross-correlation functions is investigated. Contrary to the unbounded Rouse model, cross-correlations do not vanish in the

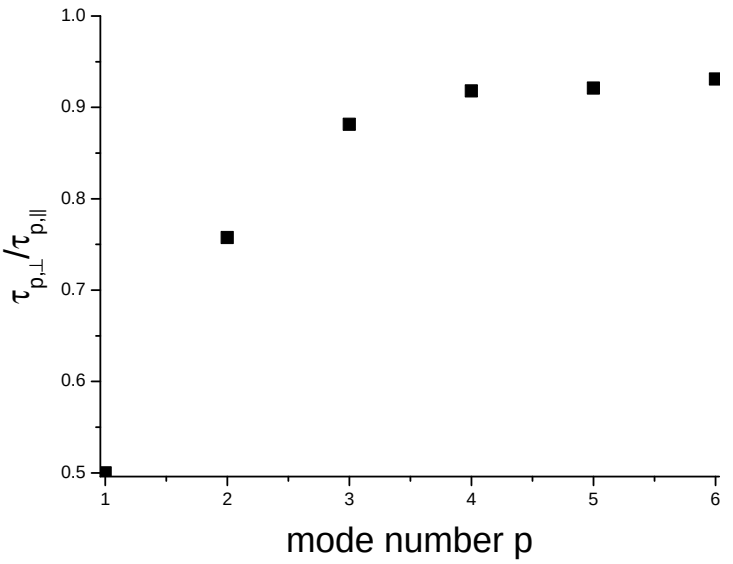

Figure 2.3: The ratio, $\tau_{p,\perp}/\tau_{p,\parallel}$, of relaxation times of the first six Rouse mode correlation functions for a chain end-tethered to the surface ($N = 256$), using the modified-Rouse model.

modified normal direction. Although non-negligible, the influence of cross-correlations is small. Resultantly $A_{1,\perp}(t)$ still dominates the terminal behaviour of $\Phi_\perp(t)$.

Comparing the modified-Rouse model to multi-chain models

The purpose of the following two sections is to compare the modified-Rouse model with interacting multi-chain models which are coarse-grained descriptions that nevertheless exhibit the most important features of flexible polymer melts at the time and length scales of interest. The primary model we will use is the well-studied KG MD model [81]. This model has the realistic characteristic that bonds may not cross one another. We also investigate a second model, soft MD, which comprises soft bonded and non-bonded potentials, with parameters chosen such that, in the bulk, the mean square internal distances along a chain, $\left\langle (\boldsymbol{r}_i - \boldsymbol{r}_j)^2 \right\rangle / |i-j|$, match almost exactly those of KG MD; whilst simultaneously allowing bond crossing events. Making a comparison between these two models may help to elucidate the importance of chain topology in dynamics. The soft MD model has previously been used to examine the effect of entanglements on chain orientation

coupling [24], and as a means for faster equilibration of KG MD systems [22]; details of soft MD and the parameters we use are given in these references. All MD simulations with confinement use periodic boundaries in the $\hat{\boldsymbol{x}}$ and $\hat{\boldsymbol{z}}$ directions and reflective boundaries in the $\hat{\boldsymbol{y}}$ direction, whereby particle positions and velocities are reflected if they pass the surface plane. The box dimensions in the periodic directions were set as $L_z, L_x \approx 2\sqrt{\langle \boldsymbol{u}_{\text{bulk}}{}^2 \rangle}$. In order to test against finite periodic box dimension effects, some simulations were doubled in size by cloning all polymer chains and displacing the cloned chains by L_x, then resetting the box dimension in the $\hat{\boldsymbol{x}}$ direction to $2L_x$. After re-equilibration, the larger systems showed no significant deviation from the original ones in typical static or dynamic observables. Bulk simulations use periodic boundaries in all directions.

The KG MD model consists of Lennard-Jones (LJ) beads connected via a FENE bonded potential:

$$U_{\text{LJ}}(r) = 4\epsilon\left((\sigma/r)^{12} - (\sigma/r)^{6} + 1/4\right), \quad r/\sigma < 2^{1/6}$$
$$U_{\text{FENE}}(r) = -\frac{KR_0^2}{2}\log\left(1 - (r/R_0)^2\right)$$

where the FENE parameters are $R_0 = 1.5\sigma$ (corresponding to the maximum bond extension) and $K = 30\epsilon/\sigma^2$ (spring constant). σ is the LJ bead radius and ϵ is the LJ energy. The shortest natural time unit is set by the Lennard-Jones potential: $\tau_{\text{LJ}} = \sqrt{\sigma^2 m_{\text{b}}/\epsilon}$, where m_{b} is the bead mass. The LJ potential we use is purely repulsive, corresponding to a cut-off at $2^{1/6}\sigma$. The temperature is maintained via a Langevin thermostat. In all plots, unless otherwise stated, we use a thermostat friction constant $\xi_{\text{MD}} = 0.5 m_b/\tau_{\text{LJ}}$ at $T = \epsilon$. This is the most common value for the friction constant in the literature [81, 101, 62, 144, 11]. Under these parameters the maximum time-step implemented is $\Delta t = 0.012\tau_{\text{LJ}}$ using periodic boundaries and $\Delta t = 0.01\tau_{\text{LJ}}$ using reflecting boundaries. Correlation functions generated using a smaller time-step produce negligibly different results. We also present some results using a much weaker friction constant, $\xi_{\text{MD}} = 0.05 m_b/\tau_{\text{LJ}}$, in order to explore the influence of momentum conservation on the dynamics. For the lower friction constant we use $\Delta t = 0.002\tau_{\text{LJ}}$. We have verified that a uniform temperature profile is maintained across the channel under these conditions. Lit-

tle difference in dynamical behaviour is found if ξ_{MD} is reduced beyond $\xi_{\mathrm{MD}} = 0.05 m_b/\tau_{\mathrm{LJ}}$ for all observables considered, using chains with $n = 64$ bonds (appendix B.2 makes further comparison using a yet lower friction constant). For the chain lengths of interest, the larger, most standard friction constant, $\xi_{\mathrm{MD}} = 0.5 m_b/\tau_{\mathrm{LJ}}$, is itself an intermediate value for which there remain non-negligible effects due to inertia. Our comparison between the high and low friction cases is therefore not a comprehensive study of the influence of momentum conservation on the chain dynamics near surfaces, but should be sufficient to observe the main trends. Importantly, for soft MD the dimensionless friction constant we use is close to the high friction KG MD value.

The equations of motion are solved using the Verlet algorithm [9]. We calculate all correlation functions using the multiple-tau correlator code developed by Ramirez et al. [136]. For the mean square displacement observable the block averaging is not performed, in order to avoid all systematic error.

Molecular dynamics equilibration procedure

Within this work, all chain lengths (except $n = 128$) are below the threshold at which entanglement effects become important in the bulk [81, 96], which greatly reduces the time of equilibration. Free chains are initially placed in the simulation box with random start positions. The other beads are then grown with mean equilibrium bond length and bond angles that correspond closely to the equilibrium distribution. Tethered chain orientations are similarly generated, but the start beads are ordered into a periodic face-centred cubic lattice with Miller indices: (111). An example system snapshot including tethered chains is given in figure 2.4. The interaction potentials are gradually turned on ('push-off') over a single Lennard-Jones time unit [11]. The boundary condition leads to a small increase in density at the surface relative to the channel centre. The initial volume is estimated such that the density in the middle of the channel is close to the melt density, $\rho = 0.85\sigma^{-3}$, that we use for simulations with periodic boundaries in all directions. Then, during a second equilibration step, the simulation box is affinely compressed or extended very slowly until the middle channel density reaches $0.85 \pm 0.001\sigma^{-3}$. This equilibration step is typically quick, since the initially chosen density is itself very close to the desired value. The

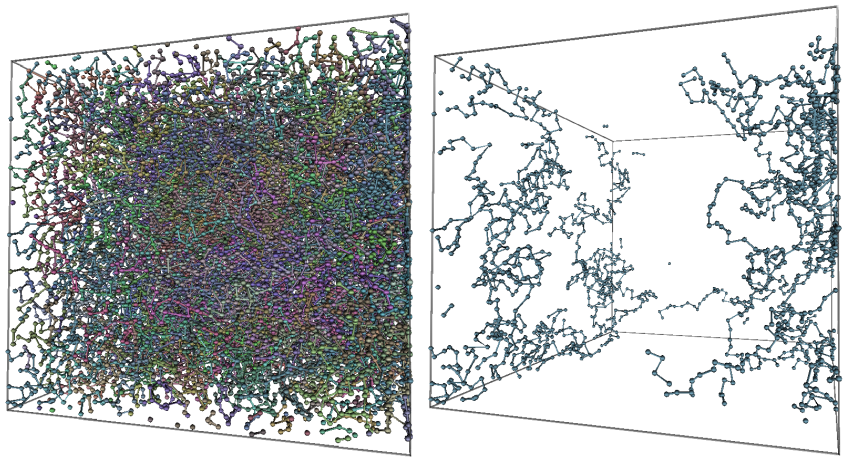

Figure 2.4: A typical simulation box snapshot for the surface-tethered system. Left: all chains included. Right: only surface-tethered chains shown.

simulation then runs for several longest system relaxation times before any observations are made. The mean square internal distances are also monitored as a means to check that the systems are well equilibrated.

Mean square internal distances

Sarabadani et al. [144] have already compared the static behaviour of an almost identical KG MD variant to the one we use, with reflected random walks, including the cases of attractive and repulsive surface interactions. Their results were in agreement with those of Skvortsov et al. [150], who compared the Self Consistent Field (SCF) calculations of a wall tethered chain immersed in a melt at different wall-fluid interaction strengths. The results confirmed that static properties of a melt at a surface are largely unaffected by changes in boundary interactions. All cases universally agreed well with a single-chain under critical conditions, of which there are analytic expressions for bead density profiles [43]. The MD simulations did however reveal some deviations from the Silberberg picture: the entropic surface interaction of chain ends [108] is not described, and the mean field description cannot take into account the surface induced ordering of monomers [159].
We now present some additional static results for the multi-chain models, which show that the dominant deviations from reflected random walk statistics at the surface are similar to known deviations from random walk statistics in the bulk [171].

In figure 2.5 we plot the wall normal component of the mean square end-to-end distance of chain sub-segments consisting of m bonds, such that at least one end be a distance y from the surface, which we refer to as $\langle {u_{m,\perp}}^2(y)\rangle$. For reflected random walks, the internal distance profile is [148]:

$$\frac{\langle {u_{m,\perp}}^2(y)\rangle}{\left\langle u^2_{m,\perp}(\infty)\right\rangle} = 1 - \left(\frac{4\nu}{\sqrt{\pi}}\right)\exp(-\nu^2) + 4\nu^2(1-\mathrm{erf}(\nu)) \tag{2.23}$$

where $\nu = y/\sqrt{2{\sigma_m}^2}$ is a characteristic dimensionless distance and ${\sigma_m}^2 = (mb^2)/3$. Figure 2.5d shows that if we map KG MD and soft MD multi-chain models to a reflected random walk, such that the mean square end-to-end distances match in the bulk, they also match closely across the whole channel. Agreement between soft MD and KG MD for the chain internal distances remains good at all points in the channel and at all length scales ($\langle {u_{m,\perp}}^2(y)\rangle$ for $m = 8, 16$, and 32 are plotted in figures 2.5a, 2.5b, and 2.5c respectively). The most notable difference between the two models is that soft MD has smaller wall normal mean square end-to-end distances for segments with ends very close to the surface. Across the channel, the mapped reflected random walks tend to predict larger mean square internal distances than are found for sub-segments of multi-chain models, since segments are progressively more swollen as the bond number increases. However, at around $\nu = 1$, the reflected random walk end-to-end distances approach, and actually become slightly smaller than the corresponding multi-chain model values. That upon approaching the surface the internal distances of the reflected random walks decrease at a faster rate compared to the real chain segments they are mapped from, can be understood easily; they are more extended and therefore more likely to come into contact with the surface, reducing the end-to-end distance. The oscillations that are apparent for short segments are associated with the wall ordering phenomenon influenced by our choice of boundary condition [159]. We have performed additional simulations using lattices of Lennard-Jones beads acting as an explicit boundary. Increasing the roughness of the lattice reduces surface ordering of monomers. At the density in question, $\rho = 0.85\sigma^{-3}$, we find that the degree of bead ordering has no significant effect on chain dynamics near to the surface for all observables considered in this section. However as will be discussed in section 2.3, the

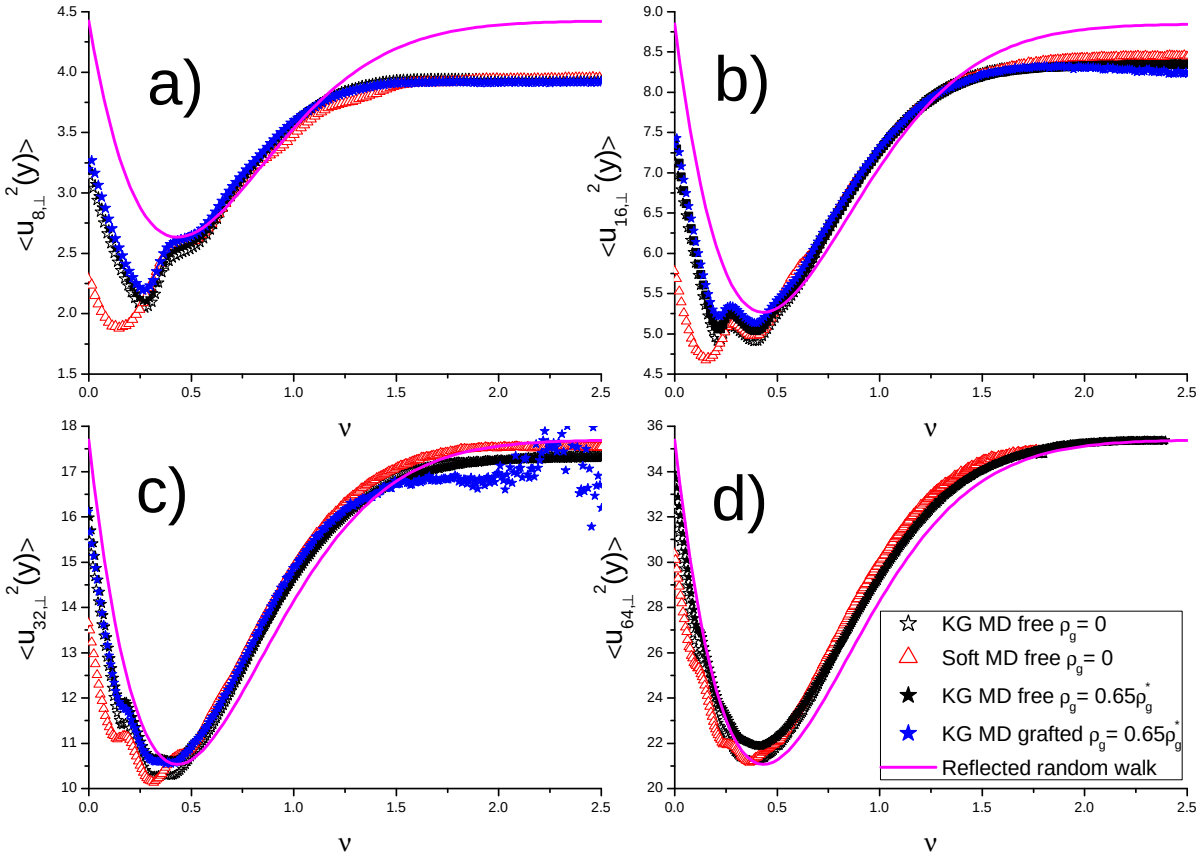

Figure 2.5: Comparison of KG MD with the mapped reflected random-walk prediction, eqn (2.23), for mean square internal distances, $\langle {u_{m,\perp}}^2(y)\rangle$, as a function of the reduced distance $\nu = y/\sqrt{2{\sigma_m}^2}$, where y is the distance from an end bead to the surface, for sub-chains consisting of m bonds. **a)** $m = 8$, **b)** $m = 16$, **c)** $m = 32$, **d)** $m = 64$. The chains consist of $n = 64$ bonds.

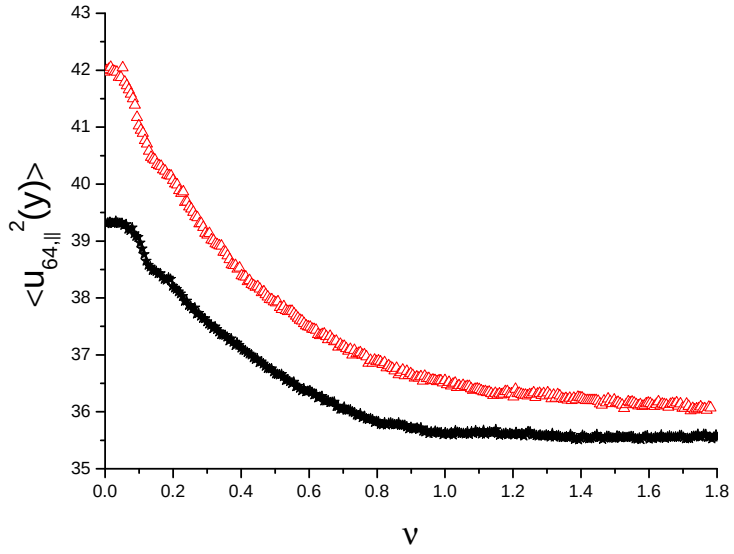

Figure 2.6: Complete chain mean square end-to-end distance in the surface parallel direction for chains with one end at distance y from the surface. $\nu = y/\sqrt{2\sigma_{64}{}^2}$. Red: soft MD, black: KG MD. The chains consist of $n = 64$ bonds.

degree of roughness does influence centre of mass motion. Chapter 3 also demonstrates that surface roughness influences global film properties via cross-chain correlations.

Sarabadani et al. [144] have also shown that surface chains become swollen in the surface parallel direction. We find that in the surface parallel direction the mean square end-to-end distance of complete KG MD chains comprising $n = 64$ bonds is around 10% larger for chains beginning with one end at the surface, compared to bulk chains, as shown in figure 2.6. The chains do not appear swollen in the perpendicular direction at the surface (figure 2.5); in fact, the end-to-end dimension is slightly shrunk with respect to the reflected random walk prediction. This suggests that the surface induces a weak nematic chain alignment which we investigate in appendix B.1. For soft MD chains the corresponding swelling and contraction effect is slightly more pronounced.

We are also interested in systems with identical chain properties and architecture but which are subject to constraints. These are our tethered chain systems, whose microstates coincide with a sub-ensemble of the confined free-chain system, whereby there are chains with an end-bead fixed at regular lattice sites on the reflective surface. Figures 2.5a-c includes a comparison of $\langle u_{m,\perp}{}^2(y)\rangle$ for free and tethered chains, within a system at surface grafting density of end-tethered chains, $\rho_g = 0.65\rho_g^*$, where we define an approx-

imate 'overlap density', ρ_g^*, which gives correct scaling for the grafting density at which neighbouring tethered chains begin to interact and stretch:

$$\rho_g^* = \frac{1}{\langle \boldsymbol{u}_{\text{bulk}}{}^2 \rangle} \tag{2.24}$$

The grafting density we use is sufficiently low such that the square internal distances of both the tethered and free chains almost exactly coincide with the completely free chain system. We therefore expect very similar dynamical behaviour of tethered chains compared to free chains with one end bead at the surface.
The free chain system used a smaller channel height of $3\sqrt{\langle \boldsymbol{u}_{\text{bulk}}{}^2 \rangle}$, compared to $4\sqrt{\langle \boldsymbol{u}_{\text{bulk}}{}^2 \rangle}$ for the tethered system. This increases computational speed and only leads to a very small difference in the mean square end-to-end distance of the complete chain in the middle of the channel (figure 2.5d). For channel heights smaller than $3\sqrt{\langle \boldsymbol{u}_{\text{bulk}}{}^2 \rangle}$, there is no bulk region and the surface chain behaviour begins to deviate from weak confinement.

Rouse mode correlation functions of surface-tethered chains

We map to the modified-Rouse model from surface-tethered chains immersed in a free chain matrix using the KG MD system. Both free and tethered chains consist of the same number, n, of bonds. The two free parameters, m and ξ, are determined by ensuring the best simultaneous agreement between the models for the first four Rouse mode correlation functions, $A_{p,\perp}(t); p = 1, 2, 3, 4$, of the tethered chains, which are plotted in figure 2.7a. For $n = 64$, at grafting density $\rho_g = 0.65\rho_g^*$, we find $m = 2$ and $\xi/m = 22 m_{\text{b}}/\tau_{\text{LJ}}$, where the mapping ratio is $m : 1$. The longest parallel tethered-chain Rouse time may then be defined in Lennard-Jones time units as, e.g. for $n = 64$:

$$\tau_{1,\parallel} \approx \frac{4(\xi/m)n \langle \boldsymbol{u}^2 \rangle}{3\pi^2 T} \approx 20200\tau_{\text{LJ}} \tag{2.25}$$

Using this mapping, $A_{1,\perp}(t)$ is very well matched between the models. As the mode number increases, the corresponding correlation functions in the KG MD system gain stronger stretched exponential behaviour, but the dominant contribution is universally

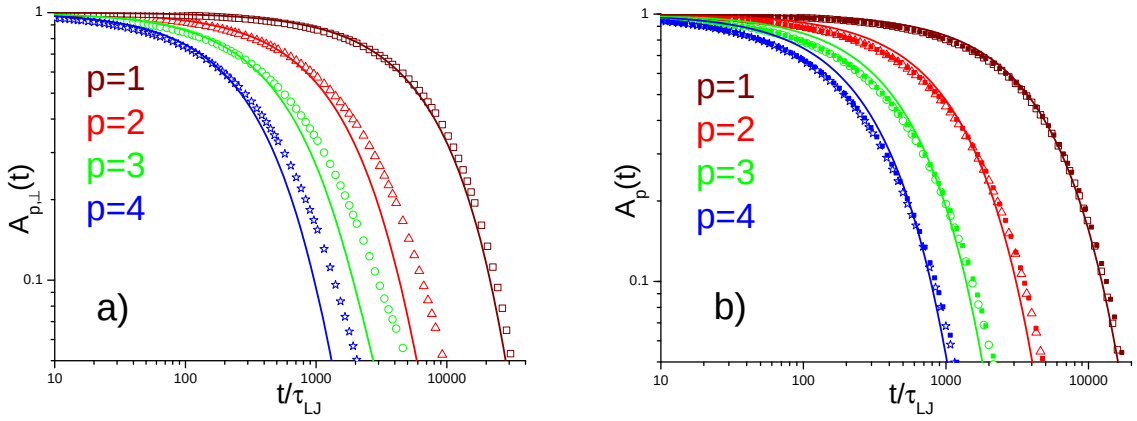

Figure 2.7: For chains consisting of $n = 64$ bonds and mode number $p = 1, 2, 3, 4$ from right to left. Open symbols and lines correspond to the KG MD model and mapped modified-Rouse model respectively. **a)** First four Rouse mode correlation functions, $A_{p,\perp}(t)$, eqn (2.13), in the surface normal direction, for surface-tethered chains at grafting density $\rho_g = 0.65\rho_g^*$. **b)** First four Rouse mode correlation functions of free chains, using periodic boundaries for the KG MD model, compared to the analytic Rouse model. Filled squares correspond to KG MD using the reduced friction, $\xi_{\mathrm{MD}} = 0.05 m_b/\tau_{\mathrm{LJ}}$, plotted in reduced time units, $\tau_{\mathrm{reduced}} = 0.86\tau_{\mathrm{LJ}}$.

well described by the modified-Rouse model. In figure 2.7b we see the same behaviour for free chains in periodic boundaries, using correlation functions of the Rouse modes of free chains, and the same mapping parameters as for the fixed chains. Figure 2.7b includes plots for the low thermostat friction, $\xi_{\mathrm{MD}} = 0.05 m_b/\tau_{\mathrm{LJ}}$, with the time axis corresponding to these plots given in reduced units, $\tau_{\mathrm{reduced}} = 0.86\tau_{\mathrm{LJ}}$, which takes into account the simulation speed-up resulting from the change in friction constant. With this rescaling of time we see close agreement for all Rouse modes using both high and low friction constants. However, the zeroth mode describing the centre of mass diffusion is more strongly dependent on the thermostat friction [48] (see section 2.3 for further discussion). Figure 2.8 shows that the good agreement with reflected random walk statistics on large length-scales corresponds with good agreement for the Rouse mode amplitudes at small p. Resultantly, since the small p modes (particularly the first mode) dominate $\Phi_\alpha(t)$ (and Rouse mode cross-correlations are also small for KG MD), we get excellent agreement between the models for $\Phi_\perp(t)$. For $p \gg 4$ the modified-Rouse model fails to predict $A_{p,\perp}(t)$ accurately within the KG MD model using this mapping.

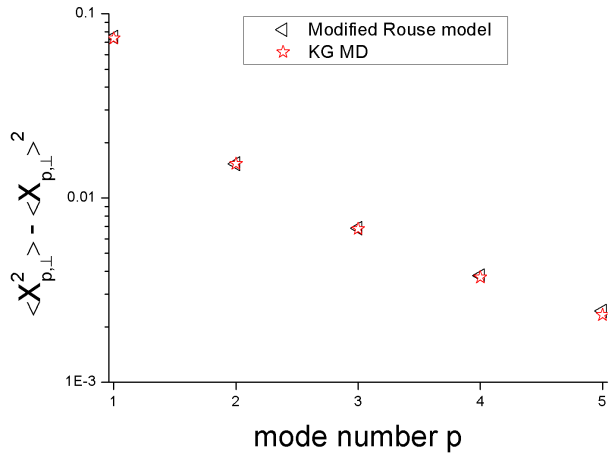

Figure 2.8: Surface normal amplitudes (variance) of Rouse modes for surface-tethered KG MD chains at grafting density $\rho_g = 0.65\rho_g^*$, compared to the mapped reflected random walk (modified-Rouse) prediction using mapping ratio $2:1$. The amplitudes are normalized by the bulk chain mean square end-to-end distance in one direction. $n = 64$.

We see that $\Phi_\perp(t)$ (figure 2.9a), described by the modified-Rouse model, predicts the corresponding KG MD correlation functions as accurately as the analytic Rouse model does for $\Phi_\parallel(t)$ (figure 2.9b) and the end-to-end vector correlation function of free chains in the bulk (figure 2.9c) using periodic boundaries. In figures 2.9a and 2.9b, plots corresponding to the low friction system in units of τ_{reduced} are given for $n = 32$, which match the high friction plots well. We find that Rouse mode correlation functions of tethered chains are also well matched between the high and low friction cases for $n = 32$, upon renormalization of time-scales using $\tau_{\text{reduced}} = 0.86$ (not plotted). In figure 2.9 we use a bond mapping ratio of $2:1$ up to a maximum of $N = 32$. The friction coefficients used are: for $n = 32 : \xi/m = 20m_{\text{b}}/\tau_{\text{LJ}}$; for $n = 64, 100, 128, 200 : \xi/m = 22m_{\text{b}}/\tau_{\text{LJ}}$. In all cases, the same friction coefficients and mapping ratios are used in both the periodic and bounded simulations, meaning that the modified-Rouse model can simultaneously give a good description of both bulk and surface chains. That we also use the same friction coefficients in parallel and normal directions means that the theoretical prediction for the ratio of relaxation times, eqn (2.21), is valid within the KG MD system.

The plots corresponding to tethered chains consisting of $n = 32$ or 64 bonds have a grafting density $\rho_g = 0.65\rho_g^*$. The plots for $n = 128$ used a higher grafting density,

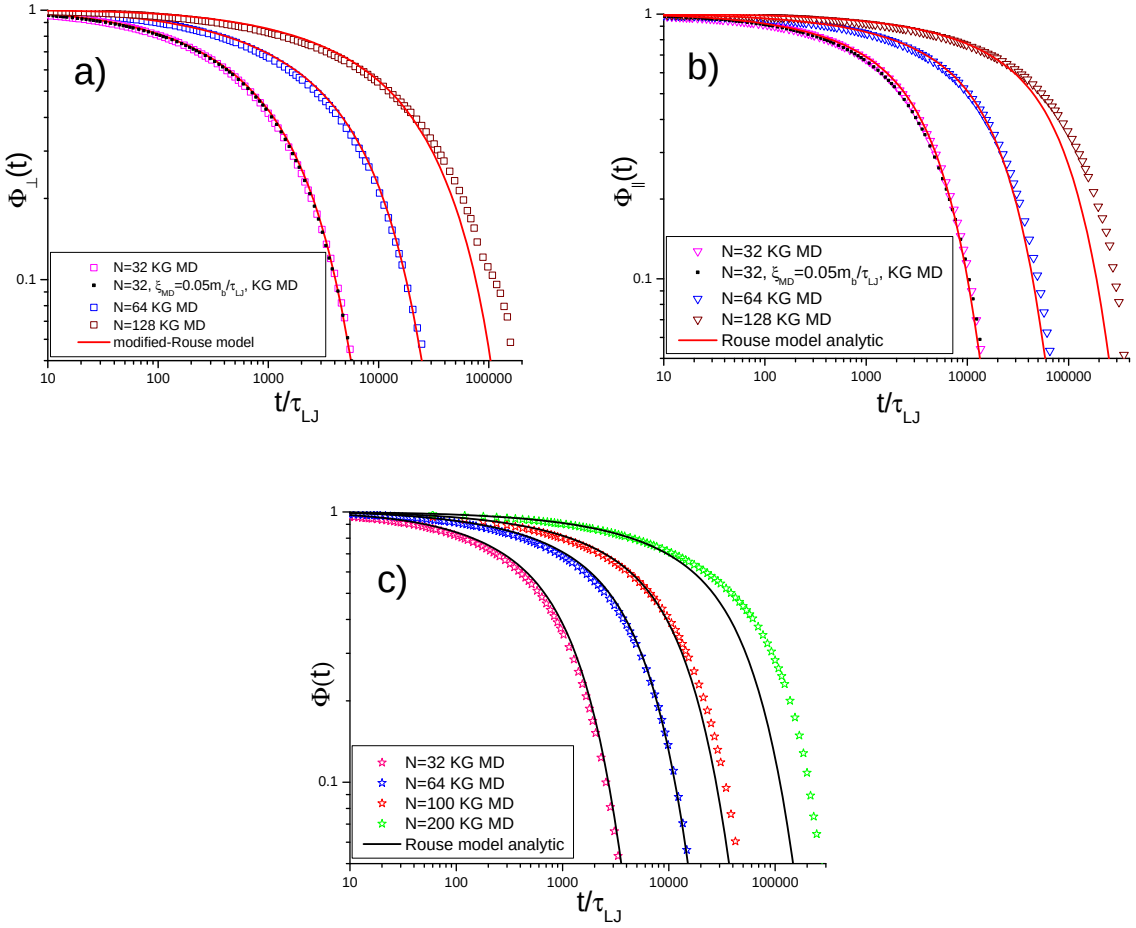

Figure 2.9: Normalized end-to-end vector correlation function in directions normal to, **a)**, and parallel to, **b)**, the surface, for surface-tethered KG MD chains mapped to the modified-Rouse model and analytic Rouse respectively. The tethered chains consist of $n = 32, 64$, or 128 bonds. For $n = 32$, KG MD using reduced friction, $\xi_{\mathrm{MD}} = 0.05 m_b/\tau_{\mathrm{LJ}}$, is plotted in reduced time units, $\tau_{\mathrm{reduced}} = 0.86\tau_{\mathrm{LJ}}$. **c)** End-to-end vector correlation function for free bulk chain systems consisting of $n = 32, 64, 100$ or 200 bonds, mapped to the analytic Rouse prediction.

$\rho_g = 1.3\rho_g^*$; however, chain stretching due to 'brush' interactions remains minimal. We therefore associate the deviations from the single-chain model prediction at $n = 128$ bonds with the onset of entanglements, which may be compared with the analogous deviations of free chains comprising $n = 100$ and 200 bonds, shown in figure 2.9c.

Influence of the flat boundary condition on mean square displacement

In simulation, a widely used observable is the mid-bead mean square displacement $g_{1,\mathrm{mid}}(t)$. For a chain consisting of an even number of bonds, $g_{1,\mathrm{mid}}(t)$ can be written in a particularly simple form in terms of the normal coordinates of free Rouse chains [96]:

$$g_{1,\mathrm{mid}}(t) = \sum_{p,q=0,\mathrm{even}}^{N} (-1)^{(p+q)/2} \left(2 - \delta_{p0}\right) \left(2 - \delta_{q0}\right) \left\langle \left(\boldsymbol{X}_p(t) - \boldsymbol{X}_p(0)\right) \cdot \left(\boldsymbol{X}_q(t) - \boldsymbol{X}_q(0)\right) \right\rangle \tag{2.26}$$

$g_{1,\mathrm{mid}}(t)$ generally encompasses motion of the chain on all length scales, unlike the end-to-end vector correlation function, eqn (2.11). In the Rouse model, cross-correlations do not contribute, and eqn (2.26) may be written as:

$$g_{1\mathrm{Rouse,mid}}(t) = \frac{6Tt}{(N+1)\xi} + \frac{b^2}{(N+1)} \sum_{p=2,\mathrm{even}}^{N} \frac{\left[1 - \exp\left(-\frac{t}{\tau_p}\right)\right]}{\sin^2\left(\frac{\pi p}{2(N+1)}\right)} \tag{2.27}$$

The first term is the centre of mass mean square displacement:

$$g_{3\mathrm{Rouse}}(t) = \frac{6Tt}{(N+1)\xi} \tag{2.28}$$

Eqn (2.28) results immediately for any stochastic model only comprising bonded forces. Upon a transformation to the centre of mass coordinate, all forces are pairwise and cancel. This leaves a sum of uncorrelated Wiener processes acting on the $N + 1$ beads in the chain. Even in the bulk, $g_3(t)$ of real chains is not diffusive on short time scales. Both experiment and simulation find a sub-diffusive regime, which for $t < \tau_R$ has characteristic

scaling $g_3(t) \propto t^{\nu_3}$, $\nu_3 \approx 0.8$ [49]. τ_R is the Rouse time for free chains:

$$\tau_R = \frac{\xi N^2 b^2}{3\pi^2 T} \tag{2.29}$$

so that $\tau_R = \tau_{R,\parallel}/4$ where $\tau_{R,\parallel}$ is given in eqn (2.19).

This sub-diffusive regime has been attributed to hydrodynamic-viscoelastic couplings, [47, 48] and soft sphere like interactions between nearest neighbour chains [49].

In figure 2.10 we plot the centre of mass diffusion of free chains in both wall parallel, $g_{3,\parallel}(t)/(t/\tau_R)$, and normal, $g_{3,\perp}(t)/(t/\tau_R)$, directions, for chains with different start positions relative to the surface in a channel of width $3\sqrt{\langle \boldsymbol{u}_{\rm bulk}{}^2 \rangle}$. Chains are assigned to narrow bins of wall normal width $0.25\sqrt{\langle \boldsymbol{u}_{\rm bulk}{}^2 \rangle}$ at $t = 0$, depending on the distance, $y_{\rm cm}$, from the centre of mass to the nearest wall at that time. For example, the bin closest to the surface corresponds to chains that at $t = 0$ have centre of mass position located within a distance $0.25\sqrt{\langle \boldsymbol{u}_{\rm bulk}{}^2 \rangle}$ from the surface. Then the correlation functions are calculated for a duration $\approx 1.7\tau_R$. In this time the chains move a distance normal to the surface of approximately the bin diameter.

Note that for all such spatially dependent correlation functions, such as those plotted in figure 2.10, the horizontal axis corresponds to the time interval, t, between correlations, $f(t')f(t'+t)$, such that $t' \geq 0$ (section 4.4 describes such correlation functions in greater detail). It is possible to consider a second type of correlation function using the constraint $t' = 0$ for all time correlations. Such a correlation function should give a more exact comparison between two different models since in the first type of function the initial constraint that all chains at time zero in both models have centre of mass positions within a certain region is blurred out. However at long time there is little difference between both types of correlation function. For computational simplicity and efficiency we stick to the first type.

For soft MD, τ_R is found from the centre of mass mean square displacement in the diffusive limit, using a simulation box with periodic boundaries, assuming the relation, eqn (2.28); whereas for KG MD τ_R is found directly from our previously fitted friction value, $\xi/m = 22m_b/\tau_{\rm LJ}$ (this also applies to mid-bead mean square displacement in the next

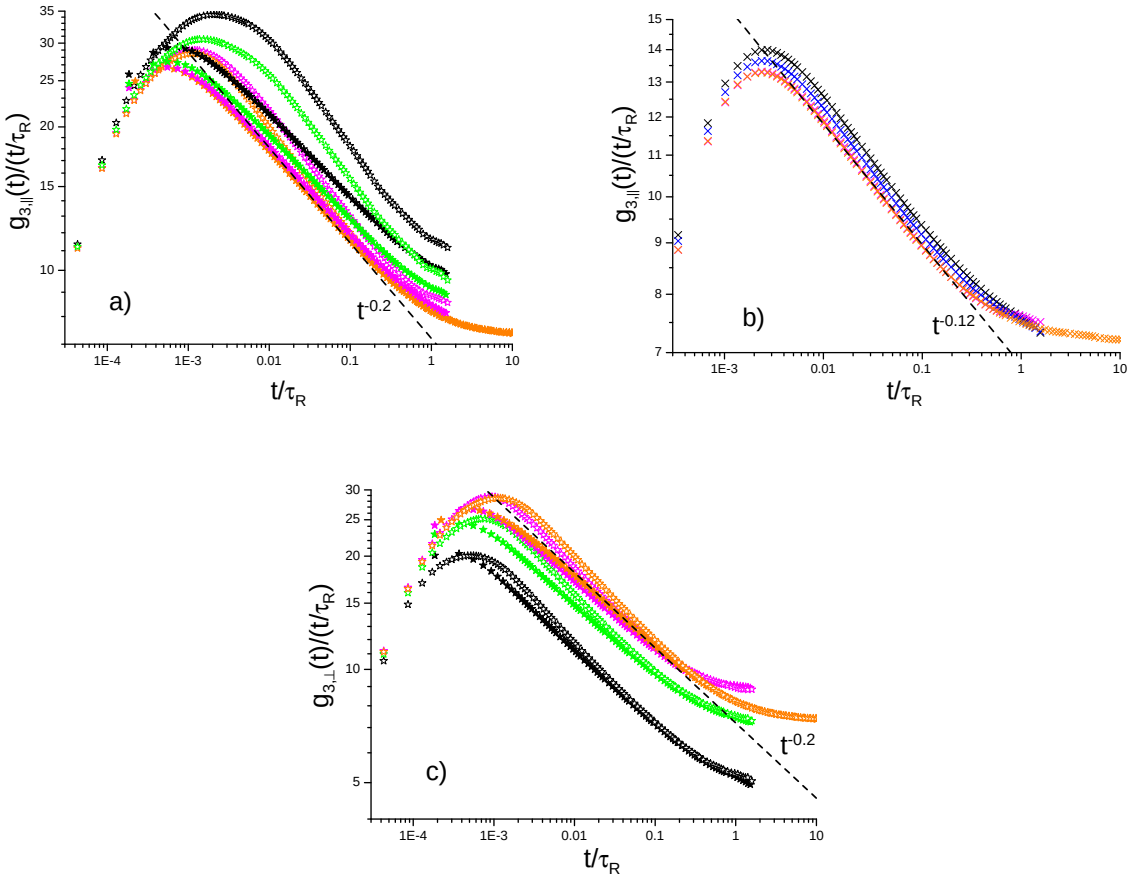

Figure 2.10: Centre of mass time dependent diffusion rate in the wall parallel direction: **a**) KG MD, **b**) soft MD; and wall normal direction: **c)** KG MD. Black: $y_{\rm cm} < 0.25\sqrt{\langle \boldsymbol{u}_{\rm bulk}{}^2\rangle}$; blue: $0.25\sqrt{\langle \boldsymbol{u}_{\rm bulk}{}^2\rangle} < y_{\rm cm} < 0.5\sqrt{\langle \boldsymbol{u}_{\rm bulk}{}^2\rangle}$; green: $0.5\sqrt{\langle \boldsymbol{u}_{\rm bulk}{}^2\rangle} < y_{\rm cm} < 0.75\sqrt{\langle \boldsymbol{u}_{\rm bulk}{}^2\rangle}$; magenta: $1.25\sqrt{\langle \boldsymbol{u}_{\rm bulk}{}^2\rangle} < y_{\rm cm}$; orange: periodic boundaries. Filled stars are KG MD using $\xi_{\rm MD} = 0.5 m_b/\tau_{\rm LJ}$ and open stars are KG MD using $\xi_{\rm MD} = 0.05 m_b/\tau_{\rm LJ}$. $\tau_{R,\xi_{\rm MD}=0.05} = 0.86\tau_{R,\xi_{\rm MD}=0.5}$.

sub-section). For each model, the simulation was repeated more than 100 times. The resulting statistics are good enough to ensure that in a corresponding simulation of the modified-Rouse model using the same total number of chains, the relative error in the final correlation point for the mid-bead mean square displacement observable with respect to the analytic Rouse expression is less than 1%. Again we use chains consisting of $n = 64$ bonds within the fundamental models, and mapping ratio 2 : 1. We also include plots corresponding to systems using periodic boundaries which are in good agreement with similar simulations from an existing study [48], whose theory predicts an enhanced super-diffusive regime at early time followed by the sub-diffusive regime until $t \approx \tau_R$. We find that for KG MD chains beginning with centre of mass in the channel centre, for $g_{3,\parallel}(t)/(t/\tau_R)$, figure 2.10a, the results match closely to the periodic simulations except that the sub-diffusive regime has a weaker slope. Although in the channel centre it appears that the high and low friction cases tend to the same diffusive limit, which matches closely to the periodic simulation, it appears that this is not the case closer to the surface. It is clear that the final diffusion rate is generally faster closer to the surface. This is in contrast to the parallel centre of mass diffusion using the soft MD model, figure 2.10b. In this case all regions appear to tend to the same diffusive limit, although, at early time, the increase in the super-diffusion near to the surface is similar to KG MD ($\approx 10\%$). However it is only for the two bins closest to the surface that deviations from the channel centre behaviour become discernible. It is interesting to note that the sub-diffusive decay of the diffusion constant for soft MD using periodic boundaries scales with $t^{-0.12}$, whereas for KG MD the scaling follows $t^{-0.2}$: see dashed lines in figure 2.10.

Preliminary simulations investigating $g_3(t)$ using boundaries formed from Lennard-Jones beads with varying degrees of roughness (see appendix B.3) have also been performed. We find that in the limit of zero roughness the results tend to the flat reflective surface case. Increasing the roughness reduces the strength of the super-diffusive regime near the surface, and thus appears to counteract hydrodynamic effects, such that at sufficiently large surface roughness the parallel centre of mass diffusion is actually reduced near the surface compared to the channel centre. At an intermediate surface roughness we find that the HI effect is close to constant across the channel so that $g_{3,\parallel}(t)$ is almost independent of

channel position. However, in all cases investigated the centre of mass parallel diffusion is generally faster in the bounded channel compared to periodic boundary conditions. More details are given in appendix B.3. We find that $g_{3,\perp}(t)$ is close to independent of surface roughness.

The comparison of KG MD with soft MD may appear suggest that to some degree the increased rate of diffusion occurring for KG MD surface chains is associated with a decrease in topological interactions at the surface. However it must be noted that the viscoelastic-hydrodynamic effect could behave differently for soft MD, and we have not sufficiently investigated this in order to unambiguously associate the qualitative differences between KG MD and soft MD with the topological interaction, independently of hydrodynamics and the effects of surface roughness. The influence of the surface on topological interactions will be investigated in more detail in chapter 4.

In the surface normal direction, figure 2.10c, we find that both high and low friction cases appear to tend to the same diffusive limit and that in contrast to the surface parallel direction there appears to be little difference in the behaviour of HI effects closer to the surface. Interestingly the channel centre diffusion in the normal direction appears to tend to a higher diffusive limit compared to periodic simulations (We observe the same feature using soft MD - not plotted).

It is clear that at the surface, as in the bulk, the simple centre of mass diffusion on all time scales predicted by the Rouse model parallel to the surface, eqn (2.28), is strongly inaccurate.

Chain mid-monomer mean square displacement

The deviations from Rouse behaviour due to hydrodynamic-viscoelastic couplings are not expected to be as strong for individual bead diffusion [48], which is instead dominated by the bonded forces and expected to follow the Rouse scaling more closely. For $\tau_N < t < \tau_R$, $g_{1\text{Rouse,mid}}(t)$ is well approximated by [110]:

$$g_{1\text{Rouse,mid}}(t) \approx 2b\sqrt{\frac{3tT}{\pi\xi}} \approx \frac{2\left\langle \boldsymbol{u}^2 \right\rangle}{\pi^{3/2}}\sqrt{\frac{t}{\tau_R}} \tag{2.30}$$

where the second relation in eqn (2.30) uses $N+1 \approx N$. The physical origin of the $\sqrt{t}$ scaling in eqn (2.30) is traced to an increasing effective drag that the bead experiences as its displacement becomes correlated with other beads along the chain. Here we repeat this argument as laid out by McLeish [110]. Over time-scales in which a bead becomes aware of its connection to other beads in the chain, the sum of all forces acting along the correlated section of chain contour must balance on average, so that $g_1(t)$ only depends on the sum of uncorrelated random forces acting on the correlated beads. The mean number of other beads that a labelled bead is correlated with, N_{corr}, can be approximated in terms of its mean square displacement:

$$N_{\mathrm{corr}}(t) = \frac{g_1(t)}{b^2} \tag{2.31}$$

Approximating $g_1(t)$ with the mean square displacement resulting from a sum of N_{corr} uncorrelated forces described by three dimensional Wiener processes with variance $6T\xi$ gives:

$$g_1(t) = \frac{6Tt}{N_{\mathrm{corr}}(t)\xi} = \sqrt{\frac{6Tb^2t}{\xi}} \tag{2.32}$$

This matches eqn (2.30) up to the pre-factor. Since melt chains are not strictly ideal but experience swelling, if we wish to map the KG MD and soft MD models onto $N_{\mathrm{corr}}(t)$ in eqn (2.31), b^2 becomes a time dependent increasing function. For this reason we can expect that for these models, at least in the bulk, $g_1(t) \propto t^{\nu_1}$ with $\nu_1 > 0.5$ for $\tau_N < t < \tau_R$. Likhtman [96] has compared the Rouse model prediction of $g_{1,\mathrm{mid}}(t)$ to soft MD and KG MD using periodic boundaries and free chains comprising $n = 64$ bonds. Here we investigate the same observable for free chains confined in the channel of width $3\sqrt{\langle \boldsymbol{u}_{\mathrm{bulk}}{}^2 \rangle}$. Figure 2.11 includes plots of mid-bead mean square displacement in the wall normal direction ($g_{1,\mathrm{mid},\perp}(t)$), for chains with different start positions relative to the surface. For this observable the chains are assigned to bins at $t = 0$ depending on the distance, y_{mid}, from the mid-bead to the nearest wall at that time. Then the correlation functions are again calculated for a duration $\approx 1.7\tau_R$. The data is presented to test the scaling regime of eqn (2.30), normalized such that the Rouse model (in the limit $N \to \infty$) gives the value $2/\pi^{3/2}$, for $\tau_N \lesssim t \lesssim \tau_R$. For $N = 32$ the analytic Rouse solution has not yet met this limit, as

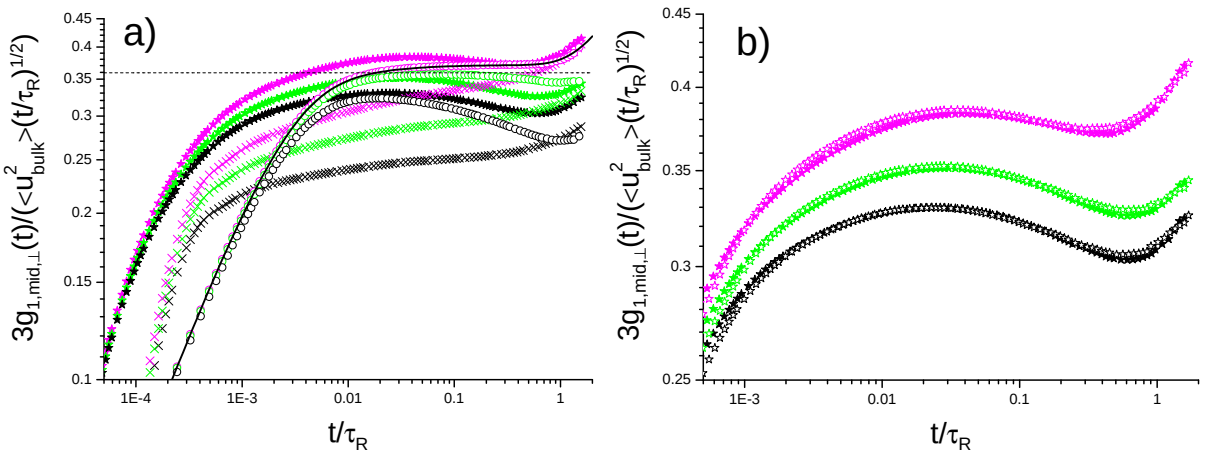

Figure 2.11: **a)** Mid-bead mean square displacement in the wall normal direction normalized to test the $\sqrt{t}$ scaling. Black: $y_{\mathrm{mid}} < 0.25\sqrt{\langle \boldsymbol{u}_{\mathrm{bulk}}{}^2 \rangle}$; green: $0.5\sqrt{\langle \boldsymbol{u}_{\mathrm{bulk}}{}^2 \rangle} < y_{\mathrm{mid}} < 0.75\sqrt{\langle \boldsymbol{u}_{\mathrm{bulk}}{}^2 \rangle}$; magenta: $1.25\sqrt{\langle \boldsymbol{u}_{\mathrm{bulk}}{}^2 \rangle} < y_{\mathrm{mid}}$. Circles are modified-Rouse, crosses are soft MD, and filled stars are KG MD using $\xi_{\mathrm{MD}} = 0.5 m_b/\tau_{\mathrm{LJ}}$; dashed line is $2/\pi^{3/2}$ and solid black line is analytic Rouse. **b)** plots for KG MD using $\xi_{\mathrm{MD}} = 0.5 m_b/\tau_{\mathrm{LJ}}$ are compared with KG MD using $\xi_{\mathrm{MD}} = 0.05 m_b/\tau_{\mathrm{LJ}}$ (open stars). $\tau_{R,\xi_{\mathrm{MD}}=0.05} = 0.86\tau_{R,\xi_{\mathrm{MD}}=0.5}$.

apparent in figure 2.11a. The analytic Rouse solution matches the modified-Rouse model in the centre of the channel, indicating that in this region the modified-Rouse chains are not influenced by the surface. The KG MD plot in figure 2.11a which represents chains satisfying $1.25\sqrt{\langle \boldsymbol{u}_{\mathrm{bulk}}{}^2 \rangle} < y_{\mathrm{mid}}$, matches closely to the Rouse plot for $t \gtrsim \tau_R$.

In figure 2.11a we observe that, before the first Rouse time is reached, $t < \tau_N$, $g_{1,\mathrm{mid}}(t)$ for the MD models is not captured well by modified-Rouse since Rouse has no super-diffusive regime. For $t \gtrsim 0.01\tau_R$ the soft MD chains in the centre of the channel exhibit a scaling exponent $\nu_1 > 0.5$ as expected; however, the KG MD model matches the Rouse scaling more closely. This difference between KG MD and soft MD appears to suggest [96] that adding chain topology slows down $g_{1,\mathrm{mid}}(t)$ in such a way that the time-dependence of the speed-up due to the effect of chain swelling is counteracted.

Closer to the surface, for $0.5\sqrt{\langle \boldsymbol{u}_{\mathrm{bulk}}{}^2 \rangle} < y_{\mathrm{mid}} < 0.75\sqrt{\langle \boldsymbol{u}_{\mathrm{bulk}}{}^2 \rangle}$, all models are still in reasonable agreement at $t \approx \tau_R$; However, for chains beginning immediately at the surface, $y_{\mathrm{mid}} < 0.25\sqrt{\langle \boldsymbol{u}_{\mathrm{bulk}}{}^2 \rangle}$, the values of the soft MD and modified-Rouse plots in figure 2.11a are less than KG MD, indicating that the relative drop in mobility from the channel centre to the surface is less for KG MD compared to the other two models. Analogous behaviour

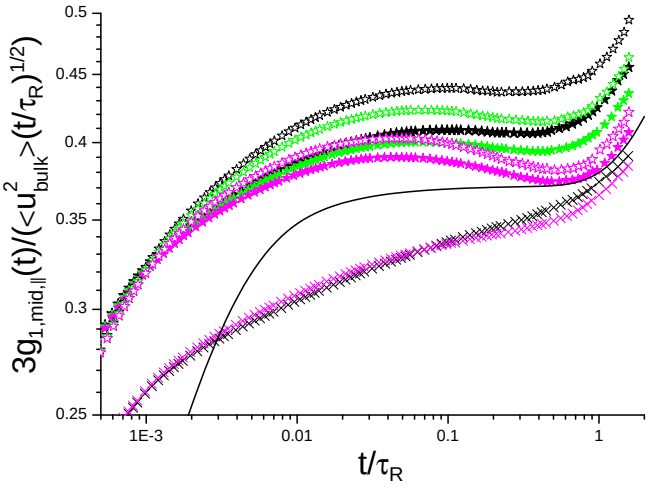

Figure 2.12: Mid-bead mean square displacement in the wall parallel direction normalized to test the $\sqrt{t}$ scaling. Black: $y_{\rm mid} < 0.25\sqrt{\langle \boldsymbol{u}_{\rm bulk}{}^2\rangle}$; green: $0.5\sqrt{\langle \boldsymbol{u}_{\rm bulk}{}^2\rangle} < y_{\rm mid} < 0.75\sqrt{\langle \boldsymbol{u}_{\rm bulk}{}^2\rangle}$; magenta: $1.25\sqrt{\langle \boldsymbol{u}_{\rm bulk}{}^2\rangle} < y_{\rm mid}$. Solid black line is analytic Rouse, crosses are soft MD, filled stars and open stars are KG MD using $\xi_{\rm MD} = 0.5 m_b/\tau_{\rm LJ}$ and $\xi_{\rm MD} = 0.05 m_b/\tau_{\rm LJ}$ respectively. $\tau_{R,\xi_{\rm MD}=0.05} = 0.86\tau_{R,\xi_{\rm MD}=0.5}$.

occurs for the surface parallel mid-bead mean square displacement shown in figure 2.12; for soft MD, the surface parallel diffusion is effectively constant across the channel, agreeing with the simple modified-Rouse model in this regard; whereas the KG MD model displays a weak increase in parallel mobility, and a slope which matches more closely to the Rouse plot for $t \gtrsim 0.1\tau_R$, for chains near to the surface.

In figure 2.12 it is apparent that the KG MD model using the low thermostat friction has progressively faster surface parallel mid-bead diffusion for chains approaching the surface, with respect to the high friction model. In figure 2.11b the corresponding comparison is made in the wall normal direction. Here the difference between the high and low friction cases is very small (this small difference matches closely to the results of periodic boundary conditions). A simple approximate characterization of the chain diffusion in a channel parallel to the walls may be now given: the centre of mass motion experiences a lower friction near the surface when the surface is perfectly smooth. The mid-monomer diffusion, eqn (2.27), crosses over from a channel independent rate at early time to an enhanced rate near the surface at later time when it must coincide with the zeroth Rouse

mode. This characterization can change quite dramatically depending on the particular structure at the surface (see appendix B.3).

Conclusion

This chapter has investigated the accuracy of a Brownian dynamics of reflected random walks as a model to describe the motion of polymer chains in melts near a flat surface. As for the Rouse model there are only two phenomenological parameters: the number of bonds forming a chain, and the bead friction coefficient. We map to this single-chain 'modified-Rouse' model from multi-chain MD models which capture the dominant behaviour of flexible chains. The same mapping parameters are used across all bulk and surface observables, in order to test the generality of the modified-Rouse description. Within the MD models, near a flat surface the deviations of chain orientation statistics from reflected random walks are similar to those of chains in bulk from unbounded random walks. In turn, we find that modified-Rouse describes the end-to-end vector correlation function of non-overlapping surface-tethered chains within KG MD as well as the Rouse model does for unconfined free chains. This success follows from the fact that the model accurately describes the correlation functions of the longest Rouse modes, which dominate the end-to-end vector correlation function. The longest Rouse mode correlation function of a surface-tethered chain at low grafting density is well modelled by a reflected Ornstein-Uhlenbeck process, and the ratio of longest relaxation times in wall normal (bounded) and wall parallel (unbounded) directions is $\tau_\perp/\tau_\parallel = 1/2$. We have demonstrated that this good agreement remains when momentum-conservation is approximately restored, by reducing the thermostat friction coefficient by an order of magnitude.

As has been widely observed with the Rouse model, the modified-Rouse model does not describe so well the correlation functions of faster modes. Despite this, far from a surface, the mid-bead mean square displacement of free chains, which depends more strongly on the faster mode dynamics, is reasonably well described by the Rouse model. Using a perfectly smooth flat surface, modified-Rouse simultaneously predicts the mid-bead mean square displacement at $t \approx \tau_R$ for both soft MD chains in the immediate surface vicinity

and in the channel centre. However the KG MD model predicts a weaker relative drop in bead mobility at the surface compared to the modified-Rouse mapping. These results may appear to suggest a weakened topological interaction at the surface compared to in bulk, even before the onset of the entanglement regime [21]. However, further investigation, made in appendix B.3 using rough lattice surfaces, strongly questions such a conclusion. We find that the most important deviation from the simple Rouse picture near to the surface is the neglection of hydrodynamic interactions (HI). However, the influence of HI are only very strong for the zeroth mode dynamics, already described theoretically and investigated with simulation by Farago et al. [48]. For a smooth flat surface we observe an increase in the centre of mass surface parallel diffusion rate for chains close to the surface with respect to those in the channel centre; whereas for a roughened surface the opposite effect is observed. In the wall normal direction there is no discernible influence of boundary condition on centre of mass motion.

Despite the failure to describe centre of mass motion, since the simple modified-Rouse picture does a reasonable job of describing the correlation functions of Rouse modes for $p > 0$, the model is still useful for several interesting quantities. This suggests that the simple modified-Rouse description of surface dynamics may be experimentally relevant. The most straightforward test might be to compare the dynamic structure factor of chains in a thin (but weakly confined) film with the prediction of modified-Rouse.

As a single-chain model, the modified-Rouse will not necessarily describe stress relaxation of films, since this generally necessitates a complete description of how contributions to the stress due to orientation cross-correlations between chains at different relative surface positions decay, although for bulk blends Cao et al. [24] have shown that the decay of cross-correlations between different polymer species may be understood in terms of the decay of auto-correlations. A similar phenomenological attempt at adapting a single chain model to include the cross-correlations between surface and bulk chains was recently made by Abberton et al. [3]. The relevance of the simple modified-Rouse description may be useful to this end. The behaviour of cross-correlations of bond orientations of different chains, and their influence on stress correlation functions of thin films, are investigated in the following chapter.

Additionally, there is a lot of interest in the dynamics of tethered chains at higher grafting densities [138, 149]. At higher grafting densities eqns (2.1), (2.2), and (2.3) may give a good description using an appropriate potential [35, 116, 98, 107]. However, it is expected that entanglements between neighbouring grafted chains, and therefore deviations from this simple single chain picture, will occur at lower molecular weights in this case [86].

Chapter 3

Stress correlation functions in thin films: influence of the boundary condition

> God made the bulk; the surface was invented by the devil.
>
> Wolfgang Pauli

In the previous chapter, using a particular model well above the glass-transition temperature, it was shown that the changes in equilibrium auto-correlation functions of individual chain orientations in weak confinement can be quite well described by only taking into account the changes in the equilibrium probability distribution for chains near the surface. What about the cross-correlations between the orientations of different chains under confinement?

The most important conclusion from this chapter is that, for polymer melts confined in a channel, global rheological properties (stress relaxation) are highly dependent upon the structure of the surface (boundary condition), even when the dimension of the channel greatly exceeds a characteristic size of the surface structure (surface roughness). This means that the choice of boundary structure in molecular simulations is highly non-trivial. It is identified that the surface structure strongly influences the behaviour of cross-chain orientation correlation functions. Results are compared with a previous study [3], where the influence of the boundary structure on stress relaxation *may* not have been properly

taken into account.

Introduction

Recent studies [95, 24] have demonstrated that cross-chain correlations make a large contribution to the total bulk bond orientation correlation function. Applying the Stress Optical Rule (section 1.0.6) implies that they are also important for the material stress relaxation. This chapter examines stress correlation functions in confined films, in addition to corresponding auto- and cross- chain bond orientation correlation functions.
One important motivation is the possibility that cross-chain orientation correlations play a role in the strain hardening effects frequently found under confinement. There were a series of experiments performed in the 1990s investigating the shear rheology of thin films of non-entangled or weakly entangled close to monodisperse polymer melts, spanning both strong and weak confinement. Both weakly attractive [127] and strongly attractive [65, 57, 103] surfaces were investigated. For strong attraction, the presence of very slowly relaxing 'pinned' surface chains was hypothesized. Contrasting behaviour between total film di-electric spectroscopy [31] and rheology of thin films of type A dipolar Cis-polyisoprene with molecular weight 14500g mol^{-1} using smooth mica surfaces pointed towards the possibility of non-local collective dynamics dominating the terminal linear stress response. Reducing the film thickness led to a broadening of the peak in the di-electric response frequency. For sufficiently thin films the frequency of the di-electric peak exceeded greatly that of the peak of mechanical loss. In the words of the authors [31]:

'*this suggests the interesting possibility that the rheological measurements at low frequency either were dominated by a subpopulation of confined chains, or reflected slow collective motions.*'

A general limitation of many older experiments is that the molecular structure near the surface was not completely characterized, which, in addition to the challenging experimental procedures, may have contributed to some contradictions in the literature [109]. Very

recently, Lee et al. [89] investigated the effect of covalently grafting polystyrene chains with molecular weight $M_n = 28000\text{g mol}^{-1}$ to a flat epoxide functionalized layer. This molecular weight is below the critical entanglement molecular weight in the bulk. Then a melt of close to monodisperse non-grafted polystyrene with $M_n = 2200\text{g mol}^{-1}$ was incorporated into the samples via spin coating, forming a free surface opposite the functionalized boundary. Different amounts of the low molecular weight polystyrene melt were added to the samples in order to create films with different thicknesses. The grafting density was approximately $0.1nm^{-2}$ for every sample, which is more than ten times the characteristic overlap density, eqn (2.24), of the tethered chain species, but still allowed for good interpenetration of the free species inside the brush layer. It was found that even for a film more than 20 times thicker than the radius of gyration of the tethered species, the characteristic film relaxation times at all frequencies were around twice as long with respect to a reference film of the same thickness comprising only the free low molecular weight species. Most notably, when the film thickness was reduced under around 10 radii of gyration of the tethered species, the film relaxation times increased by several orders of magnitude.

In this chapter, polymer melts confined in channels both with and without permanently grafted surface chains are considered. In section 3.2 the auto-chain bond orientation correlation functions of chains that are in the vicinity of a surface are investigated. The results from Molecular Dynamics are compared with predictions of the modified-Rouse model, showing good qualitative agreement. In section 3.3 cross-chain bond orientation correlation functions are investigated and compared to the auto-chain correlation functions via orientation coupling parameters [24]. In section 3.4 stress correlation functions of the confined melts are examined. The applicability of the Stress Optical Rule under confinement is discussed, and examined via comparison of the total film stress correlation functions with total film bond orientation correlation functions. The influence of cross-chain correlations on the total film stress relaxation is considered, via the results from section 3.3.

In addition to the important subject of thin film rheology, within the scope of this thesis it would be useful to know how important finite channel width effects are with respect to

non-local stress correlations between a surface region and the rest of the film; this is relevant for the surface slip behaviour that will be investigated in chapter 5. Clearly molecular simulations are limited to quite narrow channels even if the experimental interest is that of effectively asymptotically large channels. In section 3.4 total film, regional, and non-local stress correlation functions are defined, and the relationships between these correlation functions and non-equilibrium material stress relaxation functions are considered. Section 3.4.5 investigates the non-local stress correlation coupling in the film comprising both free and surface end-tethered chains.

Bond orientation auto-chain correlations in weakly confined polymer melts

Bond orientation auto-chain correlation function of tethered chains

Within the modified-Rouse single chain model where cross chain correlations do not exist by definition, we can calculate the stress contribution from the tethered chains using a single chain and eqn (1.46). Since from section 2.2 we know about the correlation functions of the normal modes of tethered chains in directions both normal and parallel to the surface, it will be ideal to formulate the correlation function of eqn (1.46) in terms of these functions. The bond orientation tensor of a chain, eqn (1.23) is (in terms of our coarse-grained chain notation introduced in chapter 2):

$$O_{\alpha\beta}(t) = \sum_{i=0}^{N-1} \left(R_{i+1,\alpha}(t) - R_{i,\alpha}(t)\right)\left(R_{i+1,\beta}(t) - R_{i,\beta}(t)\right) \tag{3.1}$$

where N is the number of bonds in the chain. Transforming to the normal modes of tethered chains (eqn (2.10)), eqn (3.1), becomes:

$$O_{\alpha\beta}(t) = 4\sum_{p=1}^{N}\sum_{q=1}^{N} H_{pq}(N) X_{p,\alpha}(t) X_{q,\beta}(t) \tag{3.2}$$

where the function $H_{pq}(N)$ is:

$$H_{pq}(N) = \sum_{j=0}^{N-1} \left(\sin\left(\frac{\pi(j+1)(p-\frac{1}{2})}{N+\frac{1}{2}} \right) - \sin\left(\frac{\pi j(p-\frac{1}{2})}{N+\frac{1}{2}} \right) \right) \times \left(\sin\left(\frac{\pi(j+1)(q-\frac{1}{2})}{N+\frac{1}{2}} \right) - \sin\left(\frac{\pi j(q-\frac{1}{2})}{N+\frac{1}{2}} \right) \right) \tag{3.3}$$

Taking $p = q$, according to Maple™[1] $H_{pp}(N)$ simplifies to:

$$\begin{aligned} H_{pp}(N) &= \sum_{j=0}^{N-1} \left(\sin\left(\frac{\pi(j+1)(p-\frac{1}{2})}{N+\frac{1}{2}} \right) - \sin\left(\frac{\pi j(p-\frac{1}{2})}{N+\frac{1}{2}} \right) \right)^2 \\ &= \left(1 - \cos\left(\frac{\pi}{2N+1} \right) \right) N + \frac{\sin\left(\frac{\pi}{2N+1}\right) \sin\left(\frac{\pi N}{2N+1}\right) \cos\left(\frac{\pi N}{2N+1}\right)}{\cos\left(\frac{\pi}{2N+1}\right) + 1} \end{aligned} \tag{3.4}$$

We consider correlation functions of the bond orientation tensor averaged over all tethered chains: $\left\langle O_{\parallel\perp}(t) O_{\parallel\perp}(0) \right\rangle_T$. The notation: $\parallel\perp$ indicates that the average is taken over xy and zy components which are found to be effectively identical for the flat boundary case considered here. Note that in principle they could be different using the chain grafted surface since the graft lattice is not invariant with respect to the transformation $x \to z$. Considering at the moment the modified-Rouse model in the terminal relaxation regime, $t \gtrsim \tau_{1,\perp}$, $\left\langle O_{\parallel\perp}(t) O_{\parallel\perp}(0) \right\rangle_T$ may be approximated by the time correlation of a single term in eqn (3.2): $p = q = 1$ (assuming for the moment that the other terms involving the longest mode correlation functions are negligible):

$$\begin{aligned} \left\langle O_{\parallel\perp}(t) O_{\parallel\perp}(0) \right\rangle_T &\approx 16 H_{11}^2(N) \left\langle X_{1,\perp}(t) X_{1,\perp}(0) \right\rangle_T \left\langle X_{1,\parallel}(t) X_{1,\parallel}(0) \right\rangle_T ; t \gtrsim \tau_{1,\perp} \\ &\propto \exp(-t/\tau_{1,\parallel})(2 + (\pi - 2)\exp(-2t/\tau_{1,\parallel}))/\pi \end{aligned} \tag{3.5}$$

where in the second line the results of section 2.1 have been applied.

The numerical solution of eqn (3.5), using $N = 32$ and the modified-Rouse model is plotted in figure 3.1 alongside $\left\langle O_{\parallel\perp}(t) O_{\parallel\perp}(0) \right\rangle_T$ (using a chain with $N = 32$: $H_{11}(N) \approx 0.038$). There is effectively exact agreement at $t \gtrsim \tau_{1,\parallel}$.

[1] Version 18

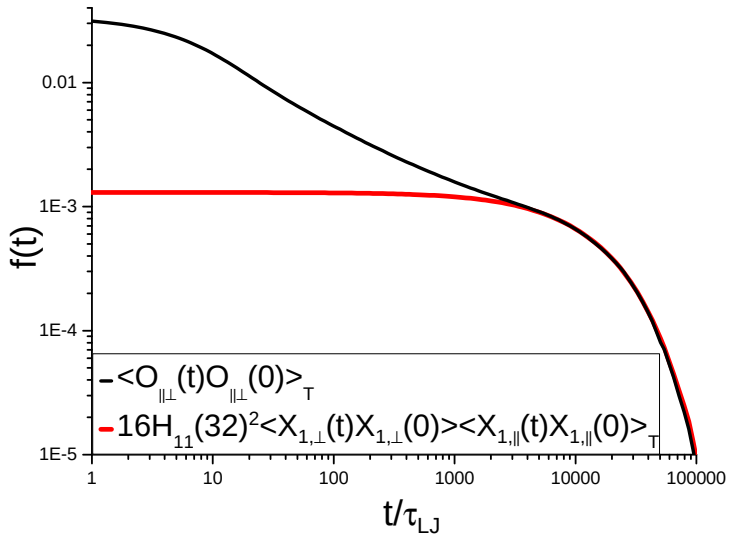

Figure 3.1: Comparison between the shear orientation correlation function, $\left\langle O_{\parallel\perp}(t)O_{\parallel\perp}(0)\right\rangle_T$, and its term with the longest relaxation - eqn (3.5); using the modified-Rouse model for a chain with $N = 32$ bonds. Note that the y axis values are normalized by N^2. For example the black line plots the quantity $\bar{A}_T(t) = \left\langle O_{\parallel\perp}(t)O_{\parallel\perp}(0)\right\rangle_T / N^2$

An important point is that since $\lim_{t\to\infty} \langle X_{1,\perp}(t)X_{1,\perp}(0)\rangle_T = \langle X_{1,\perp}\rangle_T^2$ is large ($\langle X_{1,\perp}\rangle_T^2 / \left\langle {X_{1,\perp}}^2\right\rangle_T \approx 2/3$ for this long chain - close to $2/\pi$ for the exact dumbbell case, eqn (2.14)), there would be a non-negligible contribution to the shear modulus of the tethered chain Rouse model from a single exponential with relaxation time $\tau_{1,\parallel}$. This is twice the longest relaxation time of the stress correlation function corresponding to a bulk end tethered Rouse model, and eight times longer than the standard longest Rouse stress mode for a free chain. For a free Rouse chain model the longest stress relaxation time is half the longest Rouse mode relaxation time, τ_R, eqn (2.29). The Rouse time, τ_R, is often referred to as the 'rotational relaxation time' [39]. For the surface tethered chain we can then conclude that the longest stress relaxation time matches the rotational relaxation time of a surface end-tethered chain, $\tau_{1,\parallel}$.

Figure 3.2a compares the mapped modified-Rouse prediction for $\left\langle O_{\parallel\perp}(t)O_{\parallel\perp}(0)\right\rangle_T$, now using $N = 64$ bonds, with the KG MD model films of chains comprising $n = 64$ bonds (so mapping ratio 1:1; using the Langevin thermostat with $\xi_{\mathrm{MD}} = 0.5m_b/\tau_{\mathrm{LJ}}$. Mapping parameters are as in chapter 2.) at two grafting densities, $\rho_g = 0.00625\sigma^{-2} = 0.65\rho_g^*$ and $\rho_g = 0.025\sigma^{-2} = 2.6\rho_g^*$. The moment $\left\langle {O_{\parallel\perp}}^2\right\rangle$ is around 7.5 times smaller for the KG MD

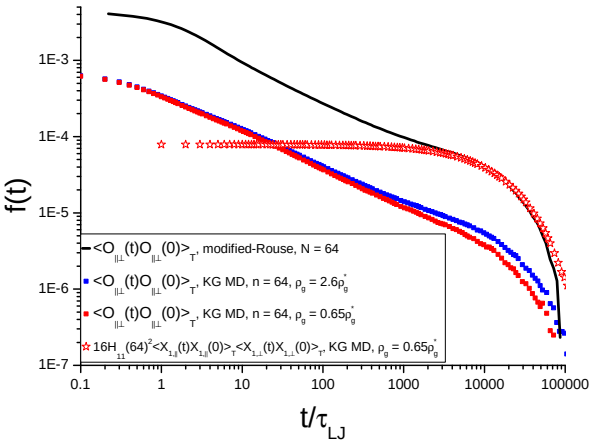

(a)

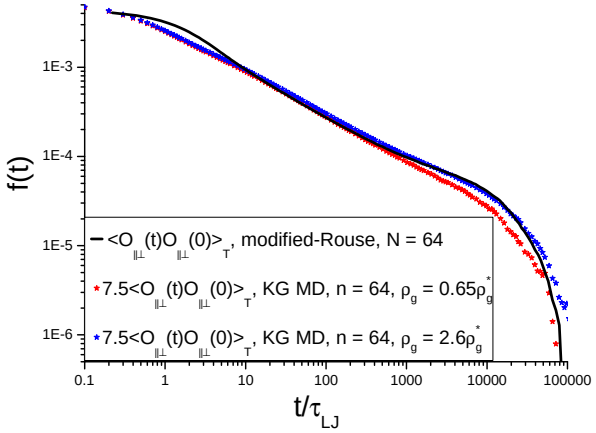

(b) The solid square plots in (a) have been multiplied by a factor of 7.5

Figure 3.2: $\left\langle O_{\parallel\perp}(t)O_{\parallel\perp}(0)\right\rangle_T$: Black line: mapped modified-Rouse and $N = 64$; KG MD at grafting densities $\rho_g = 0.00625\sigma^{-2} = 0.65\rho_g^*$ (filled red symbols) and $\rho_g = 0.025\sigma^{-2} = 2.6\rho_g^*$ (filled blue symbols). Open red stars plot the function $16H_{11}^2(64)\left\langle X_{1,\perp}(t)X_{1,\perp}(0)\right\rangle_T\left\langle X_{1,\parallel}(t)X_{1,\parallel}(0)\right\rangle_T$ using the lower grafting density KG MD model. Note that the y axis values are normalized by N^2. For example the black line plots the quantity $\bar{A}_T(t) = \left\langle O_{\parallel\perp}(t)O_{\parallel\perp}(0)\right\rangle_T/N^2$

chains compared to the Rouse model when the end-to-end square distances match by construction, and this ratio is uniform for all chains across the channel; this disagreement is due to the swelling of the KG MD chains that was discussed in 2.2.1. Figure 3.2a also plots the long time prediction for $\left\langle O_{\parallel\perp}(t)O_{\parallel\perp}(0)\right\rangle_T$, eqn (3.5), calculated numerically using the KG MD model at the lower grafting density. For this KG MD case, the actual long time $\left\langle O_{\parallel\perp}(t)O_{\parallel\perp}(0)\right\rangle_T$ is very different from eqn (3.5). However figure 3.2a also shows that, using KG MD, eqn (3.5) is very similar to the mapped modified-Rouse prediction (This must be the case since the Rouse correlation functions which compose eqn (3.5) match the modified-Rouse prediction - see section 2.2). For KG MD, if $\left\langle O_{\parallel\perp}(t)O_{\parallel\perp}(0)\right\rangle_T$ is multiplied by a factor 7.5 (see figure 3.2b), then both grafting densities agree reasonably well with the mapped modified-Rouse model, showing that at least the form of $\left\langle O_{\parallel\perp}(t)O_{\parallel\perp}(0)\right\rangle_T$ matches closely across the models, and that $\tau_{1,\parallel}$ is a good prediction for the longest relaxation time. This implies that there are additional negative long time terms contributing to $\left\langle O_{\parallel\perp}(t)O_{\parallel\perp}(0)\right\rangle_T$ for the KG MD model, which decay on the same time-scale as eqn (3.5); this has yet to be verified explicitly. For grafting densities far beyond the overlap

density $\left\langle O_{\parallel\perp}(t)O_{\parallel\perp}(0)\right\rangle_T$ is not investigated.

It has already been shown in chapter 2 that agreement between the long Rouse mode correlation functions of modified-Rouse and KG MD is maintained when using approximately momentum conserving thermostats. This means that the long time agreement in figure 3.2b must also be maintained even if we used e.g. a lower thermostat friction. However the effect of the thermostat friction at earlier time is not yet clear. In the next section we validate that it does not strongly influence this observable on all time-scales using free chains.

Bond orientation auto-correlation functions of free chains near the surface

In figure 3.3 $\left\langle O_{\parallel\perp}(t)O_{\parallel\perp}(0)\right\rangle$ is plotted using free chains whose centre of masses at time zero are at different positions relative to the surface. As in section 2.3, the correlation functions are calculated for a duration $\approx 1.7\tau_R$. In this time the chains move a distance normal to the surface of approximately the bin diameter. Note that as for $\left\langle O_{\parallel\perp}(t)O_{\parallel\perp}(0)\right\rangle_T$ using the grafted chains, the factor of 7.5 in front of $\left\langle O_{\parallel\perp}(t)O_{\parallel\perp}(0)\right\rangle$ is used to scale the KG MD functions to the modified-Rouse predictions (figure 3.3). The qualitative differences between the two models are very similar to the grafted chain case. The modified-Rouse model simultaneously fits free KG MD chains reasonably well at different channel positions, although the fit to chains in the channel centre is better than the fit to chains close to the surface. Near to the surface $\left\langle O_{\parallel\perp}(t)O_{\parallel\perp}(0)\right\rangle$ decays more quickly with respect to bulk chains. The KG MD model in figure 3.3 uses thermostat friction coefficient, $\xi_{\mathrm{MD}} = 0.5m_b\tau_{\mathrm{LJ}}^{-1}$, and a flat reflective surface. Figure 3.4 compares corresponding plots for the lower thermostat friction simulation using $\xi_{\mathrm{MD}} = 0.05m_b\tau_{\mathrm{LJ}}^{-1}$ (again using a flat reflective surface) and simulations with two different rough surfaces (both use $\xi_{\mathrm{MD}} = 0.5m_b\tau_{\mathrm{LJ}}^{-1}$). The first rough surface has random Gaussian displacements with variance, $Var = 0.3\sigma$, in the surface normal direction with respect to the FCC lattice. The second rough surface uses an ordered rough lattice texture that will be described in section 3.3.

Figure 3.4 shows no discernible dependence on the thermostat friction strength. There

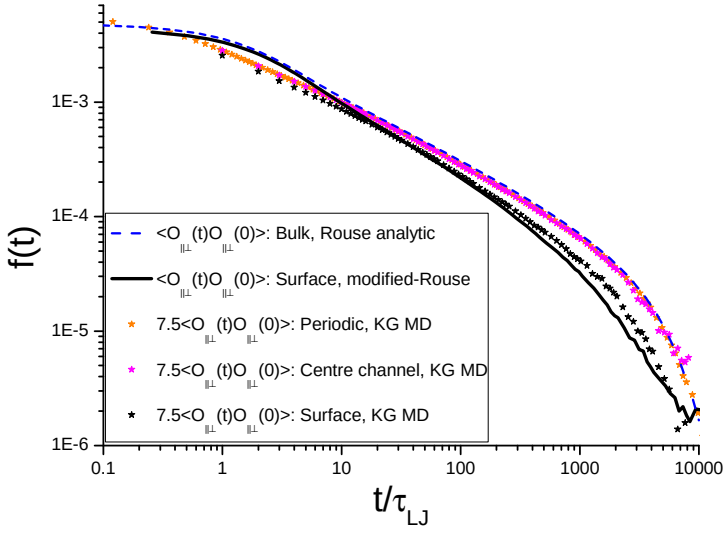

Figure 3.3: $\left\langle O_{\parallel\perp}(t)O_{\parallel\perp}(0)\right\rangle$ for free chains. Comparison between KG MD and the mapped modified-Rouse model. Black line: modified-Rouse; orange stars: KG MD using periodic boundaries; magenta stars: KG MD in the channel with centre of mass position: $1.25\sqrt{\langle \boldsymbol{u}_{\text{bulk}}{}^2\rangle} < y_{\text{cm}}$; black stars: chains in the channel with $y_{\text{cm}} < 0.25\sqrt{\langle \boldsymbol{u}_{\text{bulk}}{}^2\rangle}$; dashed blue line: analytic (bulk) Rouse model. Note that the y axis values are normalized by N^2. For example the black line plots the quantity $\bar{A}(t) = \left\langle O_{\parallel\perp}(t)O_{\parallel\perp}(0)\right\rangle / N^2$ (for chains in the surface region).

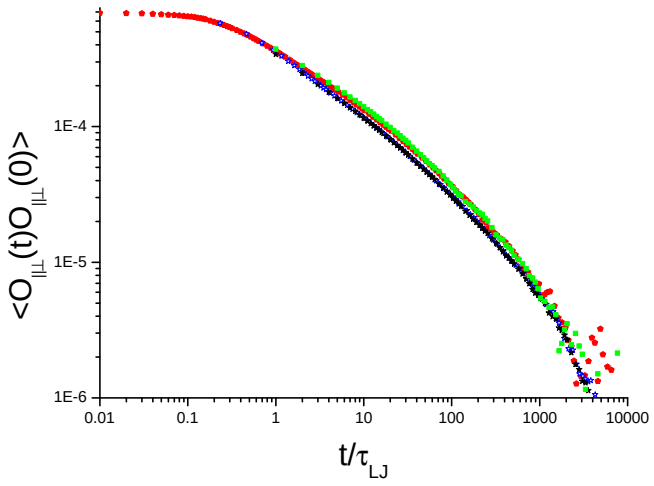

Figure 3.4: $\left\langle O_{\parallel\perp}(t)O_{\parallel\perp}(0)\right\rangle$ for free chains near the surface using KG MD: $y_{\text{cm}} < 0.25\sqrt{\langle \boldsymbol{u}_{\text{bulk}}{}^2\rangle}$. Filled symbols use thermostat friction $\xi_{\text{MD}} = 0.5 m_b/\tau_{\text{LJ}}$. Open stars uses thermostat friction $\xi_{\text{MD}} = 0.05 m_b/\tau_{\text{LJ}}$. Stars use a flat reflective surface. Green squares use the uniform pattern 'rough' lattice that was used in sections 3.3 and 3.4.4; red hexagons use the random rough surface with $Var = 0.3\sigma$ that is also used in appendix B.3. Note that the y axis values are normalized by N^2.

is a small discernible difference between the rough and smooth surfaces. The effect of roughness on the auto-chain bond orientation correlation behaviour is clearly very weak.

Bond orientation cross-chain correlations in confined melts

For binary blends in the bulk, consisting of slow relaxing and fast relaxing linear chains, it has been shown that there exist cross-chain time correlations of bond orientations between the slow and fast species which do not decay completely until the slow component auto-chain correlations have also decayed [24]. A simple mixing law, valid across a range of binary blend composition, was found to describe the total blend bond shear orientation correlation function, $S(t)$, in terms of the total monodisperse bond orientation correlation functions of each species, providing that there is the same total number of bonds, N_b, in both the blend and monodisperse melt systems. The mixing law was:

$$S(t) = \varphi_S S_S^{\text{mono}}(t) + \varphi_F S_F^{\text{mono}}(t) \tag{3.6}$$

where e.g. φ_S is the slow species volume fraction and $S_S^{\text{mono}}(t)$ is the total bond shear orientation correlation function in the monodisperse melt of slow species. Generally the total bond shear orientation correlation function in a binary blend is:

$$S(t) = \frac{N_b}{T} \sum_{l \in S+F} \sum_{m \in S+F} \frac{1}{N_b^2} \left\langle O_{xy}^l(t) O_{xy}^m(0) \right\rangle \tag{3.7}$$

where $O_{xy}^l(t)$ is a shear component of the bond orientation tensor, eqn (3.1), of the lth chain. The simple mixing law, eqn (3.6), leads to a universal relationship between the cross-species correlation function and the total monodisperse correlation functions of each species, assuming that the auto-correlation functions of each component in the blend match the same functions in the monodisperse phase. Then the cross species orientation

correlation function [24]:

$$C_{SF}(t) = \frac{N_b}{T}\frac{1}{N_b^2\varphi_S\varphi_F}\sum_{l\in S}\sum_{m\in F}\left\langle O_{xy}^l(t)O_{xy}^m(0)\right\rangle \tag{3.8}$$

and single species cross-chain orientation correlation functions, e.g. $C_{FF}(t)$:

$$C_{FF}(t) = \frac{N_b}{T}\frac{1}{N_b^2\varphi_F^2}\sum_{l\in F}\sum_{m\in F, m\neq l}\left\langle O_{xy}^l(t)O_{xy}^m(0)\right\rangle \tag{3.9}$$

were found to satisfy:

$$\begin{aligned} 2C_{SF}(t) &= \kappa(t)(S_S^{\text{mono}}(t) + S_F^{\text{mono}}(t)) \\ C_{SS}(t) &= \kappa(t)S_S^{\text{mono}}(t) \\ C_{FF}(t) &= \kappa(t)S_F^{\text{mono}}(t) \end{aligned} \tag{3.10}$$

where:

$$\begin{aligned} \kappa(t) &= C(t)/S(t) \\ &= \frac{\varphi_S^2 C_{SS}(t) + \varphi_F^2 C_{FF}(t) + 2\varphi_S\varphi_F C_{SF}(t)}{S(t)} \\ &= \frac{S(t) - \varphi_S A_S(t) - \varphi_F A_F(t)}{S(t)} \end{aligned} \tag{3.11}$$

is a 'coupling parameter' that gives the relative importance of cross-chain correlations, which was found to have a universal form irrespective of melt composition. In eqn (3.11) $A_S(t)$ and $A_F(t)$ are the bond orientation auto-correlation functions of the slow and fast species respectively, e.g.:

$$A_S(t) = \frac{N_b}{T}\frac{1}{N_b^2\varphi_S}\sum_{l\in S}\left\langle O_{xy}^l(t)O_{xy}^l(0)\right\rangle \tag{3.12}$$

An initial question to investigate is the behaviour of the coupling parameter, $\kappa(t)$, in confinement: i.e. how important are cross-chain bond orientation correlations in a film, relative to the auto-chain correlations investigated in the previous section, compared to in bulk? For films consisting of tethered species, $S_T^{\text{mono}}(t)$ is not well defined (from now

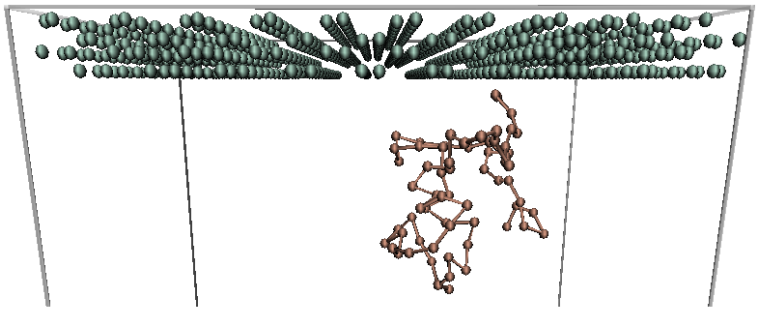

Figure 3.5: The ordered roughened FCC surface using two lattice layers. View facing the $\hat{\boldsymbol{z}}$ direction. Note that the view can give the impression that lattice beads are displaced in pairs, but this is a trick of the perspective. An example free chain conformation is also shown. Wall lattice particles are green.

on the notation is specialized for the film blends consisting of tethered, T, and free, F, species, $S_{\text{film}}(t)$ refers to $S(t)$, eqn (3.7), using a film), such that the generalization of the relations (3.10) to the film cannot be tested for this grafted blend case; considerations of confined blends of polydisperse free chains are not made here. We will later compare the behaviour of alternative time dependent coupling parameters which give the relative weight of cross-chain contributions to the uniquely tethered or the uniquely free species contributions to $S_{\text{film}}(t)$. These coupling parameters are respectively defined by eqn (3.13) and eqn (3.14).

First we compare the total cross-correlation coupling parameter, $\kappa(t)$ (eqn (3.11)) using different films with and without surface grafted chains, in addition to a periodic simulation of free chains. All chains in every simulation contain $n = 64$ bonds. The grafted film uses grafting density: $\rho_g = 2.6\rho_g^*$, and has channel width: $L_c \approx 4\sqrt{\langle \boldsymbol{u}_{\text{bulk}}{}^2 \rangle}$, whereas the films, without grafted chains have $L_c \approx 3\sqrt{\langle \boldsymbol{u}_{\text{bulk}}{}^2 \rangle}$. Two different types of boundary structure are used to investigate the coupling parameter: a flat reflective surface or a 'rough' lattice surface consisting of Lennard-Jones beads. In section 3.4.4 we will also investigate a 'smooth' lattice surface using the stress observable. The rough wall consists of an ordered lattice texture instead of the random texture used in appendix B.3. For the non-roughened ('smooth') lattice with Miller indices (111), each lattice bead has nearest neighbours at displacements $\pm\sigma\hat{\boldsymbol{x}}$ from its own position. The configuration of the roughened lattice is shown in figure 3.5. In the roughened lattice every second bead in the $\hat{\boldsymbol{x}}$ direction is

displaced with respect to its non-roughened lattice position by $0.5\sigma\hat{\boldsymbol{y}}$ (the non-roughened lattice is represented in figure 1.5). The $\hat{\boldsymbol{z}}$ direction also has a degree of roughness using the lattice surface, in the sense that it is not generally true that $\frac{\partial U_{\text{Latt}}}{\partial z_i} = 0$, where U_{Latt} is the contribution to the potential energy from all lattice particles, and z_i is the $\hat{\boldsymbol{z}}$ component of the ith bead position. However, the $\hat{\boldsymbol{z}}$ component of all lattice positions are the same for both the 'smooth' and 'rough' displaced lattices. The Lennard-Jones potentials of the lattice use the same cutoff distance as the fluid Lennard-Jones interaction which is $r_c = 2^{1/6}\sigma$. The lattice particles have fixed positions and only interact with fluid particles. Two different thermostat conditions are investigated: a Langevin thermostat using $\xi_{\text{MD}} = 0.5 m_b \tau_{\text{LJ}}^{-1}$ or $\xi_{\text{MD}} = 0.05 m_b \tau_{\text{LJ}}^{-1}$, as in chapter 2. Other details are identical to the specification in section 2.2.

Figure 3.6 plots the total coupling parameter, $\kappa(t)$ - eqn (3.11) for each case. First we comment on the simulations that use a Langevin thermostat with friction constant, $\xi_{\text{MD}} = 0.5 m_b \tau_{\text{LJ}}^{-1}$. For the case without grafted chains using a flat reflective surface, $\kappa(t)$ is negative for $t \gtrapprox 1000\tau_{\text{LJ}}$, so that $S_{\text{film}}(t)$ must decay more quickly than the chain bond orientation auto-correlation function. The coupling parameter is also slightly lower in the film compared to the periodic simulation when the flat reflective boundary is used with grafted chains, at least for $t \lessapprox 10000\tau_{\text{LJ}}$. Figure 3.7 plots a tethered chain time dependent coupling parameter given by the ratio of the uniquely tethered species cross-chain and total contributions to $S_{\text{film}}(t)$:

$$\kappa_T(t) = C_{TT}(t)/(A_T(t)/\varphi_T + C_{TT}(t)) \tag{3.13}$$

At $t \approx 10000\tau_{\text{LJ}}$, the tethered coupling parameter is: $\kappa_T(t) \approx -1$, indicating that the contribution to $S_{\text{film}}(t)$ due to cross-correlations between tethered chains is negative and has a magnitude around half that of the corresponding auto-correlation contribution. However, note that a corresponding free species coupling parameter:

$$\kappa_F(t) = C_{FF}(t)/(A_F(t)/\varphi_F + C_{FF}(t)) \tag{3.14}$$

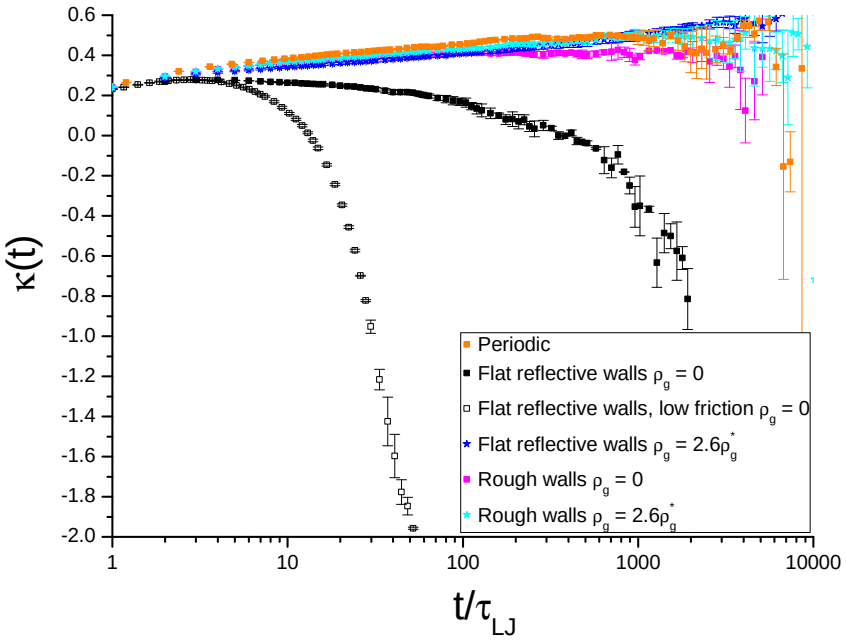

Figure 3.6: $\kappa(t)$, eqn (3.11), using a variety of films or a periodic simulation. All chains consist of $n = 64$ bonds and a Langevin thermostat is used with $\xi_{\mathrm{MD}} = 0.5 m_b {\tau_{\mathrm{LJ}}}^{-1}$, unless otherwise stated. Orange squares: periodic boundaries; magenta squares: rough walls, $\rho_g = 0$; black squares: flat reflective walls $\rho_g = 0$; open black squares: flat reflective walls, $\rho_g = 0$, $\xi_{\mathrm{MD}} = 0.05 m_b {\tau_{\mathrm{LJ}}}^{-1}$; cyan stars: rough walls $\rho_g = 2.6\rho_g^*$; blue stars: flat reflective walls $\rho_g = 2.6\rho_g^*$.

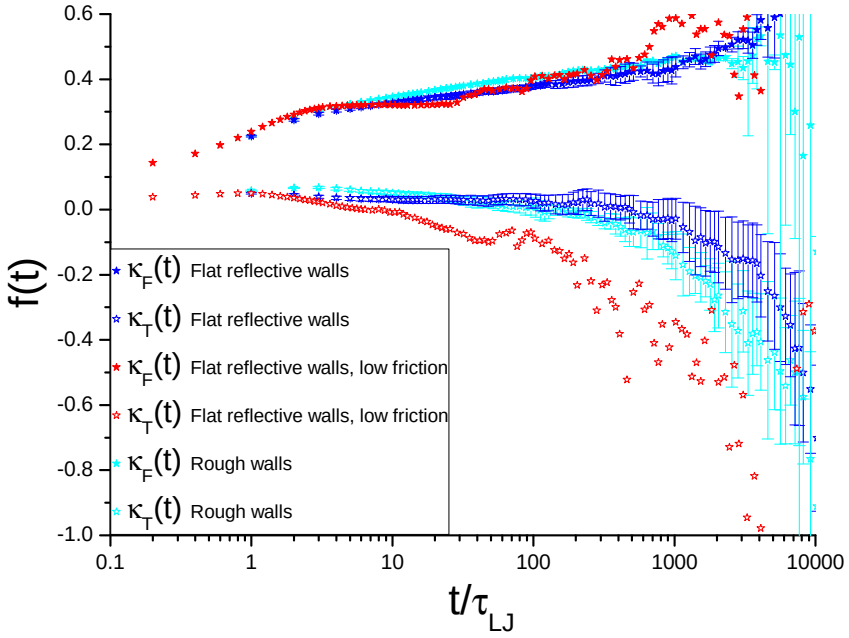

Figure 3.7: $\kappa_T(t)$, eqn (3.13), and $\kappa_F(t)$, eqn (3.14). $\rho_g = 2.6\rho_g^*$. Filled stars: $\kappa_F(t)$; Open stars: $\kappa_T(t)$. Blue: flat reflective walls, Langevin thermostat using $\xi_{\mathrm{MD}} = 0.5 m_b {\tau_{\mathrm{LJ}}}^{-1}$; red: flat reflective walls, Langevin thermostat using $\xi_{\mathrm{MD}} = 0.05 m_b {\tau_{\mathrm{LJ}}}^{-1}$; cyan: Rough wall, Langevin thermostat using $\xi_{\mathrm{MD}} = 0.5 m_b {\tau_{\mathrm{LJ}}}^{-1}$.

also plotted in figure 3.7, is similar to the complete coupling parameter, $\kappa(t)$, in the periodic simulation using only free chains.

Figure 3.7 also reveals that replacing the flat surface with a rough lattice leads to little discernible change in $\kappa_T(t)$ or $\kappa_F(t)$, and figure 3.6 shows that there is also little change in $\kappa(t)$. The influence of the rough lattice is much more pronounced for the zero grafting density case. Generally the addition of the relatively low number of grafted chains greatly increases $\kappa(t)$ at $t \gtrapprox 10\tau_{\mathrm{LJ}}$ with respect to a film only consisting of free chains. For the zero grafting density case, introducing roughness at the boundary also leads to a total coupling parameter with similar behaviour to the periodic simulation.

Figure 3.8 shows that the weak confinement, or the addition of tethered chains, both have little effect on the average bond orientation auto-correlation function of all free chains in the sample, with respect to a periodic simulation. Note however that this applies to the film average.

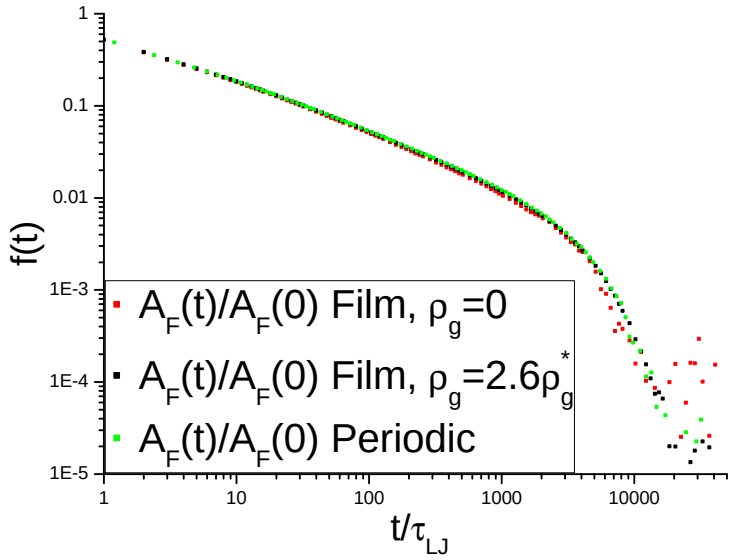

Figure 3.8: Bond orientation auto-correlation functions of free chains under different conditions; all using a Langevin thermostat with $\xi_{\mathrm{MD}} = 0.5 m_b \tau_{\mathrm{LJ}}{}^{-1}$. Red: flat reflective walls, $\rho_g = 0$; black: flat reflective walls, $\rho_g = 2.6\rho_g^*$; green: periodic boundaries.

Effect of lowering the thermostat friction

If the flat wall is instead used in conjunction with the Langevin thermostat with a lower friction constant: $\xi_{\mathrm{MD}} = 0.05 m_b \tau_{\mathrm{LJ}}^{-1}$, then $\kappa_T(t)$ (open red stars in figure 3.7) becomes negative more rapidly with respect to the case of the higher thermostat friction, but the behaviour is qualitatively similar. Note that error bars were not available in this case since only a single simulation run was used; it is clear that the error is much larger in this low friction simulation compared to the other two cases, which were averaged over several uncorrelated simulations which also ran for a much longer time.

Reducing the thermostat friction leads to little or no discernible change using the rough walls. However the thermostat has a notable influence in the flat wall case: using the low friction Langevin thermostat we find a negative $\kappa(t)$ at $t \gtrapprox 10\tau_{\mathrm{LJ}}$, two orders of magnitude earlier than the simulation using a thermostat friction constant that is an order of magnitude larger. As in chapter 2, when the lower thermostat friction is used, the effective Lennard-Jones time is always rescaled as: $\tau_{\mathrm{LJ},\xi_{\mathrm{MD}}=0.05} = 0.86\tau_{\mathrm{LJ},\xi_{\mathrm{MD}}=0.5}$. In the following section film stress correlation functions are introduced, and are compared to the chain bond orientation correlation functions that were investigated in this section.

Global and local stress correlations in confined melts

Recently Abberton et al. [3] performed non-equilibrium shear deformation simulations of a Kremer-Grest model bounded by repulsive, flat, featureless walls, using free chains in varying degrees of confinement. A sudden start-up affine shear deformation was prescribed uniformly across the channel for a short duration. Following this, the shear deformation was switched off and the relaxation of the total stress in the film was recorded. For one particular film width the non-equilibrium results were compared with the equilibrium correlation function of the total film stress. From the mechanical Fluctuation-Dissipation Theorem (FDT) [44] (appendix C), the equilibrium stress correlation function is equal to the linear stress relaxation function following an isotropic infinitesimal deformation under isothermal conditions:

$$G(t) = \frac{V}{T} \langle \sigma_{xy}(t)\sigma_{xy}(0) \rangle \tag{3.15}$$

where V is the total material volume and here $\sigma_{xy}(t)$ is the mean material shear stress at time t. Abberton et al. found that the film stress relaxation function did not match the equilibrium stress correlation function exactly. They came to the conclusion that their applied deformation went beyond the linear regime.

It is important to acknowledge that realistic deformations are usually boundary driven. Such a boundary driven flow is called a 'thermal process' by Evans and Morriss [44]. Whereas the FDT links equilibrium correlation functions to the linear response following a uniform mechanical process under isothermal conditions, there is no analogous theorem for a thermal process. An example of a thermal process is a film that responds to motion of the sliding boundary wall with a weak steady state shear-flow that may generally be non-uniform across the channel.

Evans and Morriss have argued that if a thermal process results in a uniform deformation field then there exists a 'congruent' system that is driven by an idealized uniform mechanical field that is an equivalent physical description. Such a mechanical description is given by the SLLOD equations of motion [44]. If the sliding plate flow leads to a non-uniform shear-flow in the channel, then there does not exist a hypothetical equivalent mechanical

process that applies a uniform deformation rate. Without such a correspondence, the FDT may not be invoked, and the equivalence between the non-equilibrium shear relaxation function and the equilibrium stress correlation function given by eqn (3.15) is not valid. Therefore even though eqn (3.15) may be satisfied in the case of the simulations of Abberton et al., since they used a uniform deformation (providing the step shear is sufficiently weak), for more realistic non-equilibrium models (surface driven flow) the relation may fail.

Definitions of stress correlation functions

Despite the uncertainty in the exact meaning of the stress correlation function in inhomogeneous materials, the FDT has been heuristically applied in other studies: for example to define a local viscosity in a polymer brush solvent system [38]: the fluid is first split up into regions with equal volume that are bounded in the surface-normal direction (see e.g. Fig. 3.9). Then a total regional stress correlation function is defined for region k which is bounded by wall normal positions $\mathcal{Y}_k$ and $\mathcal{Y}_{k+1}$:

$$G_{k,\text{total}}(t) = \frac{V}{T}\left\langle \int_{y'=\mathcal{Y}_k}^{\mathcal{Y}_{k+1}} \frac{\sigma_{xy}(y',t)}{\mathcal{Y}_{k+1}-\mathcal{Y}_k} dy' \int_{y''=\mathcal{Y}_0}^{\mathcal{Y}_0+L_c} \frac{\sigma_{xy}(y'',0)}{L_c} dy'' \right\rangle \tag{3.16}$$

where $\mathcal{Y}_0$ is the position of the first wall and V is the complete film volume; the local shear stress, $\sigma_{xy}(y,t)$, is defined in eqn (1.4). It also follows from the FDT, appendix C, that eqn (3.16) may be equated with the *local* stress relaxation function following a mechanical process. More generally a heuristic local viscosity is defined as the time integral of eqn (3.16) [38].

In this section we make similar investigations. In particular, section 3.4.5 makes detailed investigations of stress correlation functions using a film with chains grafted to flat reflective surfaces immersed in a melt of free chains. Both tethered and free species have the same bond number, $n = 64$, identical to one of the tethered systems investigated in section 2.2 except that here a higher grafting density is used ($\rho_g = 2.6\rho_g^*$). The static properties of the grafted chains for this case are almost identical to the lower grafting density case. For this grafted film we make detailed observations of both the total film stress and total

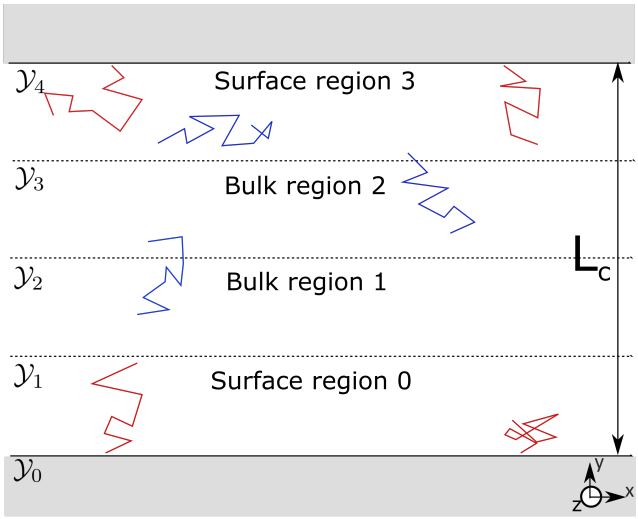

Figure 3.9: In this section, the time correlation of the stress in one region of a bounded channel with the stress in another region is calculated, to give a measure of the degree of non-local rheological coupling. The channel width is L_c. Four regions with equal volume are defined - two 'bulk' regions and two 'surface' regions. The channel is completely symmetric for all simulations considered. For the simulation containing surface grafted chains, the grafted chains (a few are illustrated in red) are almost competely located in the surface regions. There are free chains (a few are illustrated in blue) in all regions.

film orientation correlation functions, in addition to total regional correlation functions and regional cross-correlation functions (to be defined shortly).

Whereas Abberton et al. proposed a phenomenological model describing the non-local coupling of the stress relaxation in different parts of the film, here the approach is to use MD to directly observe the behaviour of both local and non-local equilibrium stress time correlations in different parts of the confined films. The simulations use symmetric channels. Four regions in the channel are considered, corresponding to two surface regions and two bulk regions, each with height $L_c/4$, such that for the system including tethered chains ($L_c \approx 4\sqrt{\langle \boldsymbol{u}_{\text{bulk}}{}^2 \rangle}$), tethered chains are almost always completely located in the surface region. See Fig. 3.9 for a schematic of the simulation channel. Then the total film in-surface plane shear stress is an average over every region:

$$\sigma_{\text{film},xy}(t) = \frac{1}{4}\left(\sigma_{0,xy}(t) + \sigma_{1,xy}(t) + \sigma_{2,xy}(t) + \sigma_{3,xy}(t)\right) \tag{3.17}$$

where:

$$\sigma_{k,xy}(t) = \frac{1}{\mathcal{Y}_{k+1} - \mathcal{Y}_k} \int_{y'=\mathcal{Y}_k}^{\mathcal{Y}_{k+1}} \sigma_{xy}(y', t) dy' \tag{3.18}$$

where the region index k corresponds with the regions illustrated in Figure 3.9. The total regional stress correlation functions, eqn (3.16), may be decomposed into six different local (auto) and non-local (cross) correlation functions. For example, a total surface region stress correlation function, $G_{S,\text{total}}(t)$, may be decomposed as:

$$\begin{aligned} G_{S,\text{total}}(t) &= \frac{V}{2T}\left(\langle \sigma_{0,xy}(t)\sigma_{\text{film},xy}(0)\rangle + \langle \sigma_{3,xy}(t)\sigma_{\text{film},xy}(0)\rangle\right) \\ &= \left(G_S(t) + G_{SB1}(t) + G_{SB2}(t) + G_{SS}(t)\right) \end{aligned} \tag{3.19}$$

where the surface auto-region stress correlation function, $G_S(t)$, is:

$$G_S(t) = \frac{1}{4}\frac{V}{2T}\left(\langle \sigma_{0,xy}(t)\sigma_{0,xy}(0)\rangle + \langle \sigma_{3,xy}(t)\sigma_{3,xy}(0)\rangle\right) \tag{3.20}$$

the first surface-bulk cross-region stress correlation function, $G_{SB1}(t)$, is:

$$G_{SB1}(t) = \frac{1}{4}\frac{V}{2T}\left(\langle \sigma_{0,xy}(t)\sigma_{1,xy}(0)\rangle + \langle \sigma_{2,xy}(t)\sigma_{3,xy}(0)\rangle\right) \tag{3.21}$$

the second surface-bulk cross-region stress correlation function, $G_{SB2}(t)$, is:

$$G_{SB2}(t) = \frac{1}{4}\frac{V}{2T}\left(\langle\sigma_{0,xy}(t)\sigma_{2,xy}(0)\rangle + \langle\sigma_{1,xy}(t)\sigma_{3,xy}(0)\rangle\right) \tag{3.22}$$

and the surface-surface cross-region stress correlation function, $G_{SS}(t)$, is:

$$G_{SS}(t) = \frac{1}{4}\frac{V}{T}\langle\sigma_{0,xy}(t)\sigma_{3,xy}(0)\rangle \tag{3.23}$$

Note that all correlations between distinct regions are found to approximately satisfy time-reversal invariance: $\langle\sigma_{l,xy}(t)\sigma_{m,xy}(0)\rangle = \langle\sigma_{l,xy}(-t)\sigma_{m,xy}(0)\rangle$. Correspondingly, the total bulk region stress correlation function, $G_{B,\text{total}}(t)$, is:

$$\begin{aligned} G_{B,\text{total}}(t) &= \frac{V}{2T}\left(\langle\sigma_{1,xy}(t)\sigma_{\text{film},xy}(0)\rangle + \langle\sigma_{2,xy}(t)\sigma_{\text{film},xy}(0)\rangle\right) \\ &= \left(G_B(t) + G_{SB1}(t) + G_{SB2}(t) + G_{BB}(t)\right) \end{aligned} \tag{3.24}$$

In eqn (3.24) there are also contributions from the bulk-bulk cross-region stress correlation function, $G_{BB}(t)$:

$$G_{BB}(t) = \frac{1}{4}\frac{V}{T}\langle\sigma_{1,xy}(t)\sigma_{2,xy}(0)\rangle \tag{3.25}$$

and the bulk auto-region stress correlation function, $G_B(t)$:

$$G_B(t) = \frac{1}{4}\frac{V}{2T}\left(\langle\sigma_{1,xy}(t)\sigma_{1,xy}(0)\rangle + \langle\sigma_{2,xy}(t)\sigma_{2,xy}(0)\rangle\right) \tag{3.26}$$

Then the total film stress correlation function is formed from the sum over every total local function:

$$\begin{aligned} G_{\text{film}}(t) &= \frac{V}{T}\langle\sigma_{\text{film},xy}(t)\sigma_{\text{film},xy}(0)\rangle \\ &= \frac{1}{2}\left(G_{S,\text{total}}(t) + G_{B,\text{total}}(t)\right) \\ &= \frac{1}{2}\left(G_S(t) + G_B(t) + G_{BB}(t) + G_{SS}(t)\right) + \left(G_{SB1}(t) + G_{SB2}(t)\right) \end{aligned} \tag{3.27}$$

Computational implementation

For systems without lattice boundaries we average over both shear components of the stress in the surface plane (the systems with FCC wall lattice particles are not completely invariant with respect to rotations in the plane with normal unit vector: $\hat{\boldsymbol{y}}$ - see figure 1.5), so that eqn (3.27) for example becomes:

$$G_{\text{film}}(t) = \frac{V}{2T}\left(\langle\sigma_{\text{film},xy}(t)\sigma_{\text{film},xy}(0)\rangle + \langle\sigma_{\text{film,zy}}(t)\sigma_{\text{film,zy}}(0)\rangle\right) \tag{3.28}$$

When it is necessary to distinguish shear components of the stress tensor we use the notation e.g.:

$$G_{\text{film,zy}}(t) = \frac{V}{T}\langle\sigma_{\text{film,zy}}(t)\sigma_{\text{film,zy}}(0)\rangle \tag{3.29}$$

The algorithm used to calculate the stress in the kth film region, $\sigma_{k,\alpha y}$, is found from integrating the MOP expression, eqn (1.4), over the kth region:

$$\begin{aligned}\sigma_{k,\alpha y} = &\frac{1}{2\mathscr{A}(\mathcal{Y}_{k+1}-\mathcal{Y}_k)}\sum_{i,j} f_{ij,\alpha}(y_i - y_j)\,\Theta(\mathcal{Y}_{k+1}-y_i)\Theta(y_i-\mathcal{Y}_k)\Theta(\mathcal{Y}_{k+1}-y_j)\Theta(y_j-\mathcal{Y}_k)\\ &+\frac{1}{\mathscr{A}(\mathcal{Y}_{k+1}-\mathcal{Y}_k)}\sum_{i,j} f_{ij,\alpha}(\mathcal{Y}_{k+1}-y_j)\,\Theta(y_i-\mathcal{Y}_{k+1})\Theta(\mathcal{Y}_{k+1}-y_j)\Theta(y_j-\mathcal{Y}_k)\\ &+\frac{1}{\mathscr{A}(\mathcal{Y}_{k+1}-\mathcal{Y}_k)}\sum_{i,j} f_{ij,\alpha}(y_i-\mathcal{Y}_k)\,\Theta(\mathcal{Y}_k-y_j)\Theta(\mathcal{Y}_{k+1}-y_i)\Theta(y_i-\mathcal{Y}_k)\end{aligned} \tag{3.30}$$

Note that the factor of $1/2$ is necessary in the first sum to prevent over-counting. For the second and third sums there is an implicit constraint that $y_i > y_j$ which prevents over-counting. In eqn (3.30) the kinetic stress contribution to eqn (1.4) has been neglected for simplicity since it makes a negligible contribution to shear stress correlations in all parts of the film and neglecting it does not change any qualitative aspects of the correlation functions for all time, for all cases considered (including simple fluids). The algorithm used by Dimitrov et al. [38] appears to correspond with eqn (3.30) although they formulate it starting from the Irving-Kirkwood [68] expression for the stress. If all particles are located within any one region; e.g. if the region width corresponds with the film width, then we

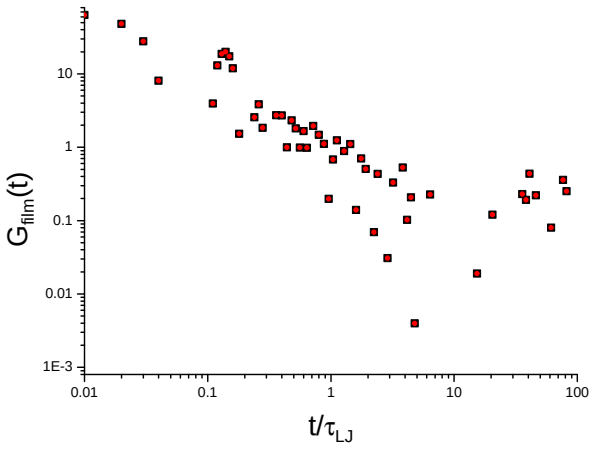

(a) Red circles - instantaneous stress is found from eqn (3.30) and eqn (3.17);
black squares - instantaneous stress is found from eqn (3.31).

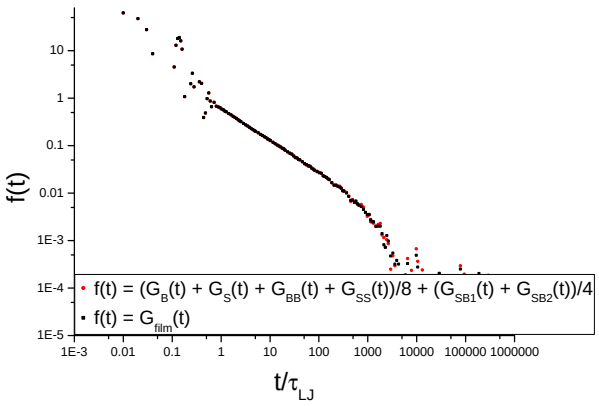

(b) Comparison of the sum - eqn (3.27) - red circles, with the total film stress correlation function calculated using eqn (3.31) - black squares.

Figure 3.10: (a) Test for the consistency of the stress algorithm, eqn (3.30), via the film stress correlation function. (b) Test of the decomposed stress correlation functions.

get the standard 'virial' stress expression (e.g. see Doi and Edwards [39]).

$$\sigma_{\text{film},\alpha y} = \frac{1}{2V} \sum_{i,j} f_{ij,\alpha} \left(y_i - y_j \right) \tag{3.31}$$

An algorithm corresponding to eqn (3.30) which may be run in parallel using OpenMP [2] has been implemented in GPS. An algorithm corresponding to eqn (3.31) was previously implemented in GPS. It has been verified that using eqn (3.30) to find the regional stress, then summing over the stress from each region, as in eqn (3.17), gives identical results for the total film stress as those found from the algorithm corresponding to eqn (3.31). As an example, figure 3.10a compares the total film stress correlation function using both methods. Additionally it is verified that the time average of every normal component of the stress is identical for every bin in the fluid: a constraint which is determined by the film geometry in the creeping flow limit, eqn (1.12).

The correlation functions $G_S(t)$, $G_B(t)$, $G_{SB1}(t)$, $G_{SB2}(t)$, $G_{BB}(t)$, and $G_{SS}(t)$ are calculated in GPS using new correlator classes, 'StressCorrelatorFilm' and 'StressCrossCorrelatorFilm'. This code is verified by checking eqn (3.27). In this case the systematic error introduced by the block averaging used in the on-the-fly calculation of the correlator [136]

means that the total film correlator and its construction from the sum of its decomposed correlation functions do not give exactly identical results. However as seen in figure 3.10b, this is only evident at long time.

Stress Optical Rule (SOR) near the surface

Let us consider whether we expect that the SOR (see 1.0.6) will be valid near to the surface. We start by recalling the widely accepted postulate that the stress in a polymer melt is determined by the short-time chain dynamics (One argument given by Doi and Edwards justifying this is that the elastic stress following an instantaneous deformation is given by the (observably) instantaneous change in the free energy - which whether for entangled or non-entangled melts is Rouse like). Extending this postulate to the surface model, the instantaneous stress is then expected to be completely determined by the modified-Rouse potential, eqn (2.5), to a good approximation. Now for chain sub-segments with characteristic length $\approx b$ (Kuhn length), for which the dynamical potential, eqn (2.5), becomes appropriate, the additional wall dependent contribution to the potential is only non-negligible when the segment is within a distance from the surface of $\approx b$. We then expect that very strong confinement will be necessary in order to break the SOR. In sections 3.4.4 and 3.4.5 the proportionality between $G_{\text{film}}(t)$ and the total film bond orientation correlation function, $S_{\text{film}}(t)$, will be tested. Assuming this proportionality, we can meaningfully examine stress-correlation functions in terms of bond orientation correlation functions.

Total (film volume averaged) stress correlation functions in confined melts

Figure 3.11 plots the total film shear stress correlation function, $G_{\text{film},xy}(t) = \langle \sigma_{\text{film},xy}(t)\sigma_{\text{film},xy}(0)\rangle$ using the weakly confined free chain films with $L_c \approx 30\sigma \approx 3\sqrt{\boldsymbol{u}_{\text{bulk}}{}^2}$. Figure 3.11 reveals that using the low friction thermostat with the flat wall leads to a negative stress correlation function for $10\tau_{\text{LJ}} \lessapprox t \lessapprox 100\tau_{\text{LJ}}$. Next we investigate a much more confined channel: Figure 3.12a plots $G_{\text{film,xy}}(t)$ using a film

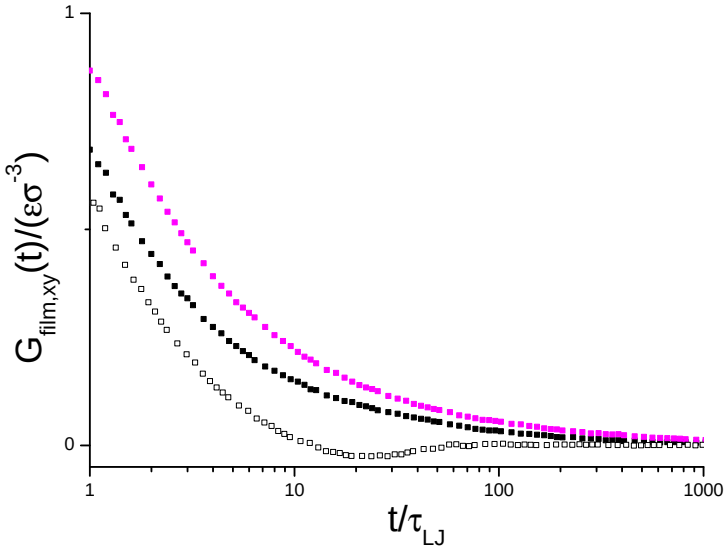

Figure 3.11: $G_{\mathrm{film,xy}}(t)$. Black: flat reflective surface; magenta: rough lattice. Filled squares: Langevin thermostat with $\xi_{\mathrm{MD}} = 0.5 m_b \tau_{\mathrm{LJ}}^{-1}$; Open squares: Langevin thermostat with $\xi_{\mathrm{MD}} = 0.05 m_b \tau_{\mathrm{LJ}}^{-1}$.

with $L_c \approx 10\sigma \approx \sqrt{\boldsymbol{u}_{\mathrm{bulk}}{}^2}$, which may be compared to a $\log_{10}$-$\log_{10}$ scale representation of the corresponding wide channel plots (figure 3.11) in figure 3.12b. The channel width, $L_c \approx 10\sigma$, coincides very closely to the second thinnest channel used by Abberton et al. [3] with a perfectly flat boundary. In their supporting material [3] they include $G_{\mathrm{film,xy}}(t)$ (the correlation function) for $t > 10\tau_{\mathrm{LJ}}$. Their results match quite closely to a plot in figure 3.12a ($\xi_{\mathrm{MD}} = 0.5 m_b/\tau_{\mathrm{LJ}}$ - filled black squares), suggesting the possibility that their purely flat repulsive Lennard-Jones wall potential gives very similar results to the purely flat reflective wall case we consider. Note however that Abberton et al. used the full Lennard-Jones potential (cutoff distance: $r_c = 2.5\sigma$), for both the surface and non-bonded potentials, and a higher monomer density ($\rho = 0.8867\sigma^{-3}$); they used a Langevin thermostat with an unspecified friction constant.

For the perfectly flat surface, lowering the friction constant to $\xi_{\mathrm{MD}} = 0.05 m_b/\tau_{\mathrm{LJ}}$ results in $G_{\mathrm{film,xy}}(t)$ being negative at $1 \lessapprox t \lessapprox 10\tau_{\mathrm{LJ}}$ under the strong confinement (compare this with the corresponding wider channel plots in figure 3.12b: in this wider channel the behaviour is qualitatively similar but $G_{\mathrm{film,xy}}(t)$ is negative at $10 \lessapprox t \lessapprox 100\tau_{\mathrm{LJ}}$). Figure 3.12a also includes a plot for $G_{\mathrm{film,zy}}(t)$ using the rough lattice which appears to be slightly different to $G_{\mathrm{film,xy}}(t)$ for this (rough lattice) case only. For the flat lattice $G_{\mathrm{film,xy}}(t) \approx G_{\mathrm{film,zy}}(t)$

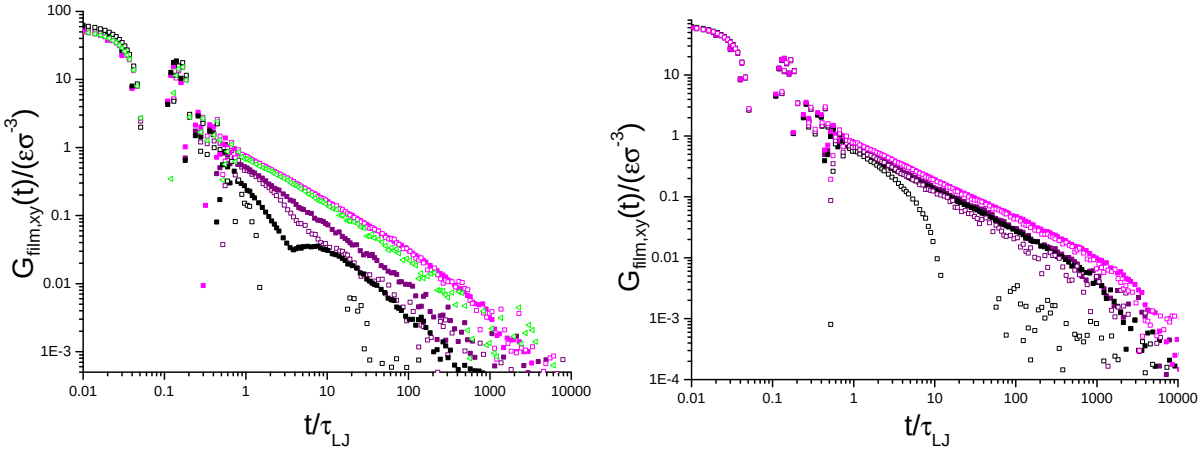

(a) $L_c \approx 10\sigma$ (b) $L_c \approx 30\sigma$

Figure 3.12: $G_{\text{film,xy}}(t)$ under **(a)** strong and **(b)** weak confinement. Filled symbols: Langevin thermostat with $\xi_{\text{MD}} = 0.5m_b/\tau_{\text{LJ}}$; open symbols: Langevin thermostat with $\xi_{\text{MD}} = 0.05m_b/\tau_{\text{LJ}}$. Black: flat reflective walls; purple: 'smooth' (non-displaced) lattice; magenta: 'rough' (displaced) lattice; green triangles: $G_{\text{film,zy}}(t)$ using the rough lattice and $\xi_{\text{MD}} = 0.05m_b/\tau_{\text{LJ}}$.

and for the perfectly flat wall they must be identical by symmetry.

Figure 3.13 shows corresponding plots for the bond orientation correlation function, $S_{\text{film}}(t)$ ($S_{\text{film}}(t) = S_{\text{film,xy}}(t)$ always) - eqn (3.7), using the strongly confined channel, which has similar behaviour: smoother surfaces/reduced thermostat friction lead to faster decay. However $G_{\text{film,xy}}(t)$ and $S_{\text{film}}(t)$ are clearly not proportional for $t < 100\tau_{\text{LJ}}$ using the smooth surface and low thermostat friction. Despite this we may still note the correlation between the negative bond orientation coupling constant that was observed in figure 3.6 (using the flat boundary film) and the negative stress correlation observed in figure 3.12.

Next we look at figure 3.14 which plots the out of surface plane shear stress correlation function, $G_{\text{film,xz}}(t)$, which in contrast to $G_{\text{film,xy}}(t)$ and $G_{\text{film,zy}}(t)$ is apparently independent of surface roughness and thermostat friction. $G_{\text{film,xz}}(t)$ also has very little channel width dependence, consistent with the findings of Abberton et al [3].

Since the time-scale of the negative $G_{\text{film,xy}}(t)$ is of order τ_{LJ} using the strong confinement, we now consider a simple fluid consisting of Lennard-Jones dimers - $n = 1$, using the channel width, $L_c \approx 10\sigma$. Figure 3.15a plots $G_{S,\text{total}}(t)$, eqn (3.19), and $G_{B,\text{total}}(t)$, eqn (3.24), for dimers and chains with $n = 64$. It is striking that corresponding curves in both cases agree quite closely despite the large difference in chain length. A fluid using single

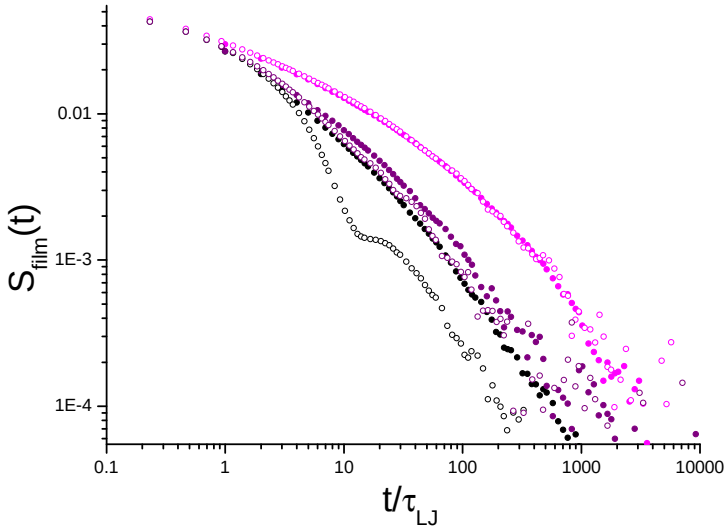

Figure 3.13: $S_{\text{film}}(t)$ - eqn (3.7): $L_c \approx 10\sigma$.
Filled circles: Langevin thermostat with $\xi_{\text{MD}} = 0.5m_b/\tau_{\text{LJ}}$; open circles: Langevin thermostat with $\xi_{\text{MD}} = 0.05m_b/\tau_{\text{LJ}}$. Black: flat reflective walls; purple: 'smooth' (non-displaced) lattice; magenta: 'rough' (displaced) lattice.

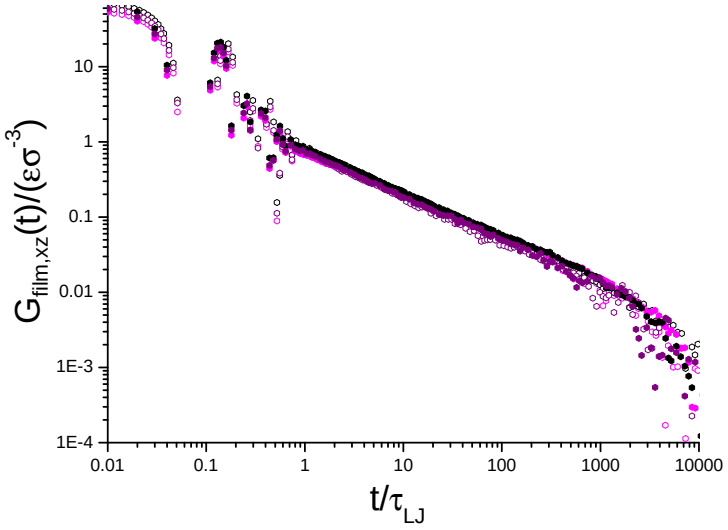

Figure 3.14: $L_c \approx 10\sigma$.
The out of surface plane stress correlation function, $G_{\text{film,xz}}(t)$. Filled hexagons: Langevin thermostat with $\xi_{\text{MD}} = 0.5m_b/\tau_{\text{LJ}}$; open hexagons: Langevin thermostat with $\xi_{\text{MD}} = 0.05m_b/\tau_{\text{LJ}}$. Black: flat reflective surface; purple: 'smooth' (non-displaced) lattice; magenta: 'rough' (displaced) lattice.

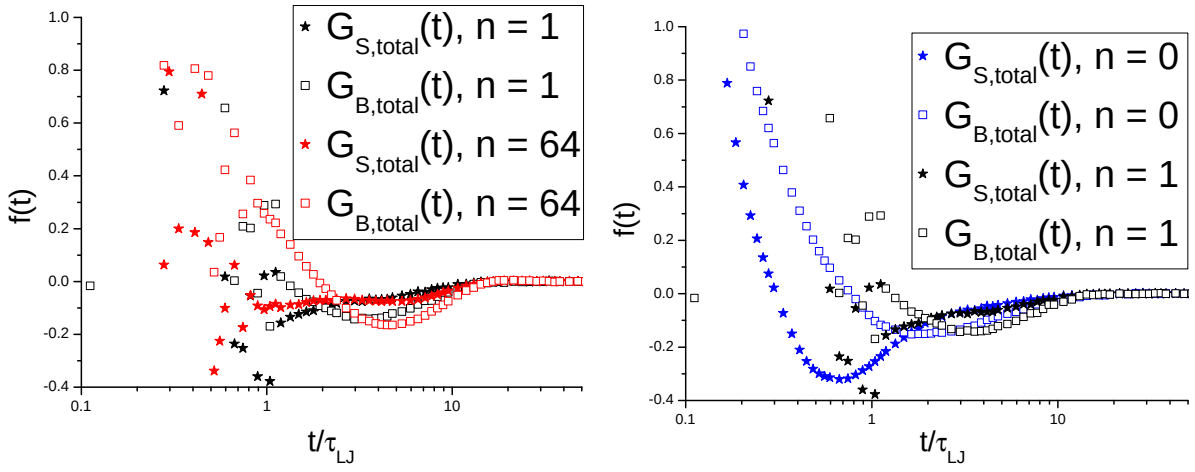

(a) (b)

Figure 3.15: $G_{S,\text{total}}(t)$ (stars) and $G_{B,\text{total}}(t)$ (squares), $L_c \approx 10\sigma$: (**a**) Comparison between dimers (black) and chains with $n = 64$ bonds (red). (**b**) Comparison between dimers (black) and single Lennard-Jones beads (blue). All simulations use a flat reflective surface and Langevin thermostat with $\xi_{\text{MD}} = 0.05 m_b/\tau_{\text{LJ}}$.

Lennard-Jones beads also matches the dimer plots very well for $t > \tau_{\text{LJ}}$: see figure 3.15b, indicating that the negative stress correlations at $t > \tau_{\text{LJ}}$ is not a bonded phenomena. The simulations using FENE bonds display additional stress correlation oscillations for $t < \tau_{\text{LJ}}$. Beyond the conclusion that the negative stress correlations are traced to monomeric dynamics, that inertia is important, and that the phenomena occurs using a flat (momentum reflecting) boundary, a precise understanding is still lacking. A further step could be to examine whether a similar effect occurs using a film with a free surface. It may also be relevant to note that the addition of a rough surface has a reasonably large effect on the bead density profiles of the films which are plotted in figure 3.16.

Finally figure 3.17 shows that, adding a relatively low density of surface grafted chains, $G_{\text{film},xy}(t)$ is much more invariant with respect to the considered changes in surface structure. Note that the open blue stars using the low thermostat friction corresponds with the red coupling parameter plots in figure 3.7. The faster decay of $\kappa_T(t)$ compared to the high thermostat friction cases suggests that the terminal behaviour of $G_{\text{film},xy}(t)$ may also be different with respect to the high friction simulations, however there is too much noise in the low friction plot in figure 3.17 to tell whether any notable difference exists. In the following section the terminal stress relaxation in a film with surface grafted chains is

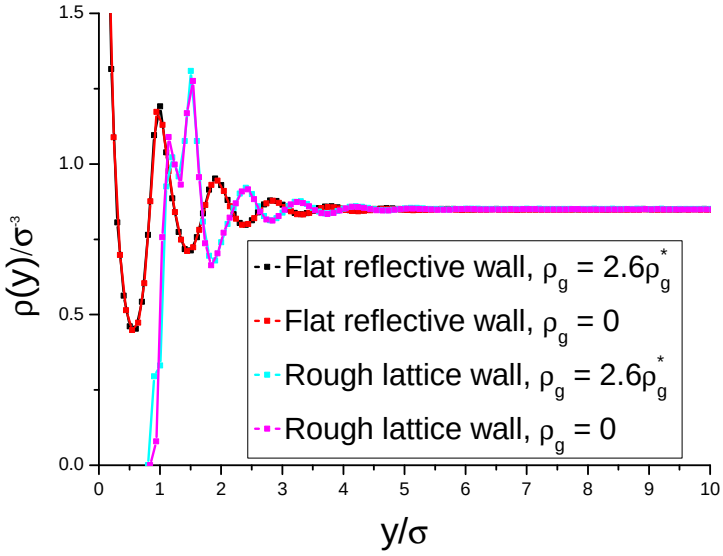

Figure 3.16: Total bead densities as a function of distance from the reflective surface or lattice plane. Note that for the rough tethered plot (blue), the grafted end beads of tethered chains are located 0.9σ from the lattice plane which coincides with the minimum distance of free beads from the surface.

investigated in more detail for the single case of a film with flat reflective boundaries.

Non-local stress correlations in a tethered 'blend'

Here we examine in more detail the tethered 'blend' consisting of surface end-tethered chains with $n = 64$ bonds at grafting density, $\rho_g = 0.025\sigma^{-2} = 2.6\rho_g^*$, immersed in a melt of free chains of the same length. We examine whether the terminal decay of the film stress correlation function of the tethered 'blend' corresponds to the single chain model prediction, eqn (3.5). The data was averaged over seven independent simulations that ran for $10^7\tau_{\rm LJ}$. Figure 3.18a plots the different functions that contribute to the total film stress correlation function, eqn (3.27). It is striking that at $t \approx 10000\tau_{\rm LJ}$ every function is similar in magnitude and form. Figure 3.18b plots $G_{S,\rm total}(t)$, $G_{B,\rm total}(t)$, and compares both to the total stress correlation function using periodic boundaries and only free chains with $n = 64$: $G_{\rm periodic}(t)$. The terminal decay of $G_{\rm periodic}(t)$ is well fitted to a single exponential with relaxation time, $\tau_R/2$ (orange line), as predicted by the Rouse model. For both $G_{S,\rm total}(t)$ and $G_{B,\rm total}(t)$, the terminal relaxation decays proportionally to eqn (3.5) for $\tau_{1,\perp} < t < \tau_{1,\parallel}$ (magenta line in figures 3.18b and 3.18c), which has characteristic

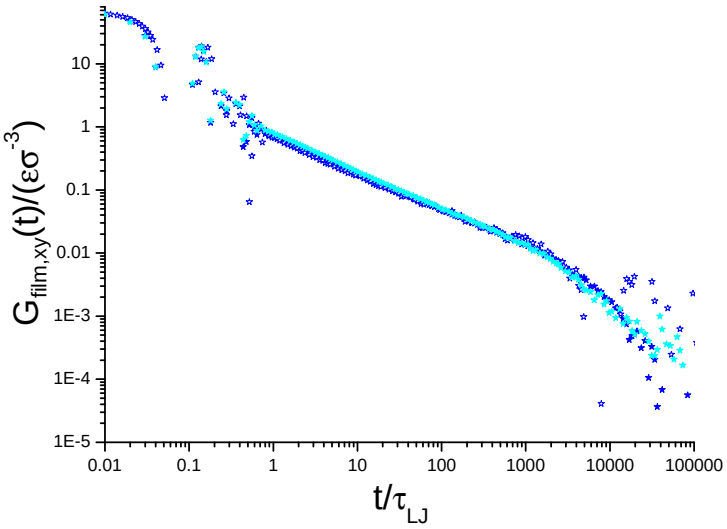

Figure 3.17: $G_{\mathrm{film,xy}}(t)$ in a simulation with surface grafted chains: $L_c \approx 40\sigma$ and $\rho = 2.6\rho_g^*$. Filled blue stars: flat reflective surface, Langevin thermostat with $\xi_{\mathrm{MD}} = 0.5m_b/\tau_{\mathrm{LJ}}$; open blue stars: flat reflective surface, Langevin thermostat with $\xi_{\mathrm{MD}} = 0.05m_b/\tau_{\mathrm{LJ}}$; cyan stars: rough surface, Langevin thermostat with $\xi_{\mathrm{MD}} = 0.5m_b/\tau_{\mathrm{LJ}}$;.

relaxation time $1/(1/\tau_{1,\perp} + 1/\tau_{1,\parallel}) = \tau_{1,\parallel}/3$. $\tau_{1,\parallel} \approx 20220\tau_{\mathrm{LJ}}$ - as for the lower grafting density case - eqn (2.25). Figure 3.18c plots $G_{\mathrm{film}}(t)$ and demonstrates the proportionality with $S_{\mathrm{film}}(t)$ for $t \gtrapprox 10\tau_{\mathrm{LJ}}$. $G_{\mathrm{film}}(t)$ remains proportional to a single exponential with relaxation time $\tau_{1,\parallel}/3$ at $t \approx \tau_{1,\parallel}$. At $t > \tau_{1,\parallel}$ the error is sufficiently small so that any contribution from a mode with relaxation time $\tau_{1,\parallel}$, as predicted by eqn (3.5) must be very small. The delayed terminal relaxation of the centre channel region, $G_{B,\mathrm{total}}(t)$, which only contains free chains, with respect to the periodic case indicates that there may be a finite channel effect on the centre channel rheology for the channel length used.

We now return to the chain bond orientation correlations in the film. Figure 3.18d shows the decomposition of $S_{\mathrm{film}}(t)$:

$$S_{\mathrm{film}}(t) = (\varphi_F A_F(t) + \varphi_F^2 C_{FF}(t)) + (\varphi_T A_T(t) + \varphi_T^2 C_{TT}(t)) + 2\varphi_T\varphi_F C_{TF}(t) \qquad (3.32)$$

in terms of contributions from the free chain (first bracketed term in eqn (3.32)) and tethered chain (second bracketed term) correlations and the inter-species cross-correlations (final term). The cross-correlations are responsible for most of the error in figure 3.18d; error bars included for $2\varphi_T\varphi_F C_{TF}(t)$ demonstrate the magnitude of error. Each of these

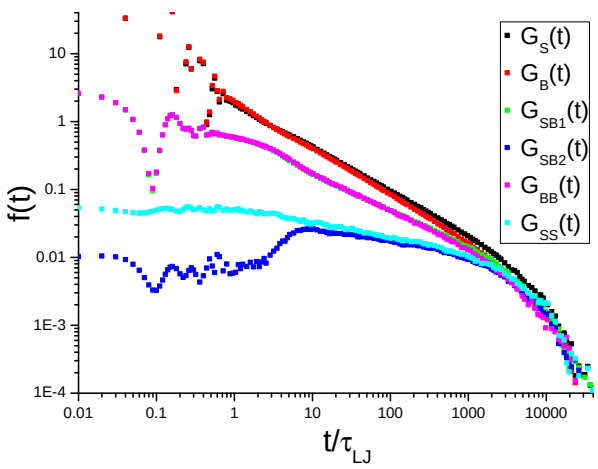

(a) Every function that contributes to the total film stress correlation function, eqn (3.27).

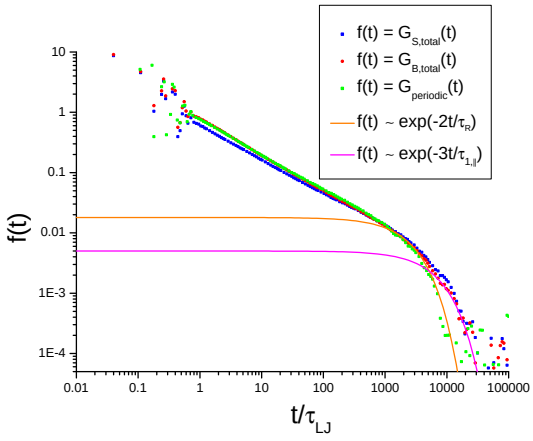

(b) Total surface and bulk region stress correlation functions compared with a periodic free chain system.

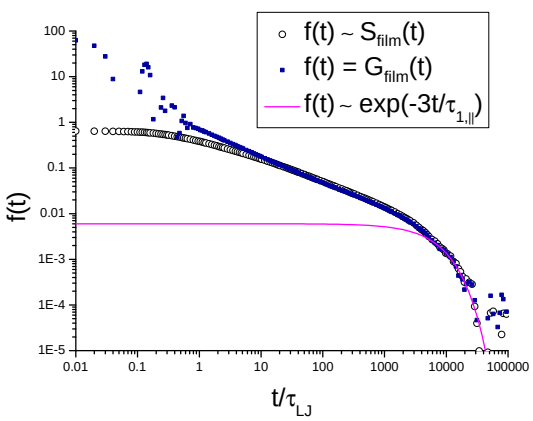

(c) Total film stress correlation function compared to the total film bond orientation correlation function.

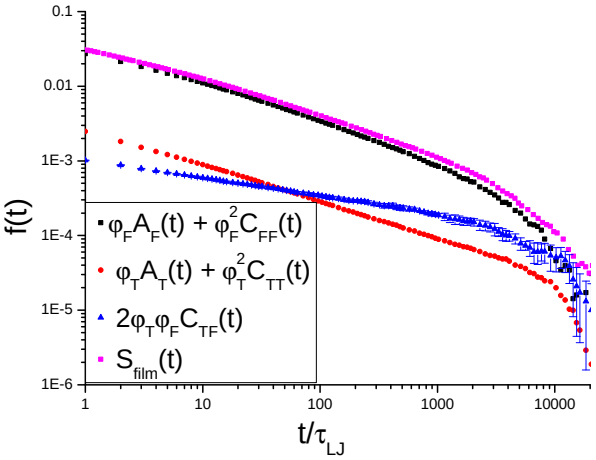

(d) Decomposition of $S_{\text{film}}(t)$, eqn (3.32).

Figure 3.18: Various bond orientation and stress correlation functions of the tethered 'blend' film. Orange line is proportional to the longest stress correlation mode for free chains: $\tau_R/2$. Magenta line is proportional to eqn (3.5) at early time which has characteristic relaxation time: $1/(1/\tau_{1,\perp} + 1/\tau_{1,\|}) = \tau_{1,\|}/3$.

three contributions appear to approximately share the same terminal relaxation time: $\approx \tau_{1,\parallel}/3$. Since the auto-correlation part of the tethered chain contribution is known to have a longer relaxation time than this: $\tau_{1,\parallel}$, we can deduce that the negative cross-correlation term ($C_{TT}(t)$) that was identified in section 3.3 acts to cancel out this longest relaxation mode. Figure 3.3 indicates that the free chain auto-correlation function has longest relaxation time $\tau_R/2 \approx \tau_{1,\parallel}/8$. This means that the free chain cross correlation function, $C_{FF}(t)$, must account for the slower relaxation of $(\varphi_F A_F(t) + \varphi_F^2 C_{FF}(t))$ at $t \approx \tau_{1,\parallel}/3$. Note that this particular phenomenon also occurred in periodic conditions [24]: The fast component cross-correlation function was proportional to the slowest component correlation function in the terminal regime. However this 'secondary' coupling appears to be stronger in this film case, since in the periodic case the magnitude of the contribution to $C_{FF}(t)$ that was proportional to $A_F(t)$ dominated even for a 50% blend.

Regional bond orientation correlation functions of the tethered 'blend'

We define regional averages of shear bond orientations, $O_{k,\parallel\perp}$, where bonds are designated a region using their centre of mass position:

$$O_{k,\parallel\perp} = \frac{1}{\mathscr{A}(\mathcal{Y}_{k+1} - \mathcal{Y}_k)} \sum_{l=1}^{N_c} \sum_{i=0}^{N-1} (r^l_{i+1,\parallel} - r^l_{i,\parallel})(r^l_{i+1,\perp} - r^l_{i,\perp})\, \Theta(\mathcal{Y}_{k+1} - (r^l_{i+1,\perp} + r^l_{i,\perp})/2) \times \Theta((r^l_{i+1,\perp} + r^l_{i,\perp})/2 - \mathcal{Y}_k) \tag{3.33}$$

Note that eqn (3.33) sums over all N_c chains in the film and that different bonds forming a single chain can be in different regions.

We now examine bond orientation auto-region correlation functions: $S_S(t)$, $S_B(t)$ and cross-region correlation functions: $S_{SB1}(t)$, $S_{SB2}(t)$, $S_{BB}(t)$, and $S_{SS}(t)$. These regional bond orientation correlation functions are defined from eqn (3.33) in an identical manner to how the regional stress correlation functions, eqns (3.20)-(3.23) and eqns (3.25)-(3.26),

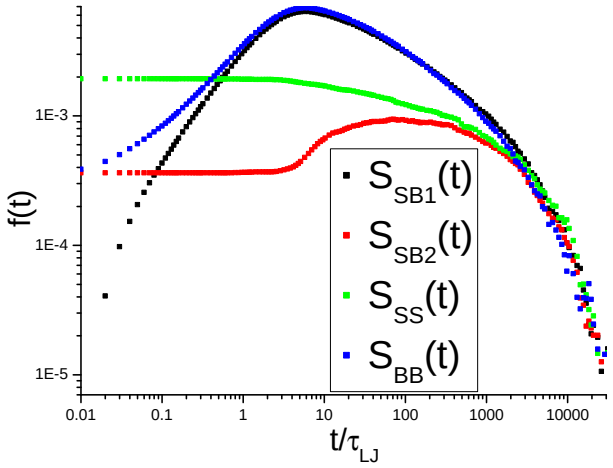

Figure 3.19: Each cross-region bond orientation correlation function in the film. Note that for long time every function has similar (but not matching) magnitude. Their behaviour is demonstrated more clearly by the regional coupling parameters which are plotted in figure 3.20.

are defined from the regional shear stresses, eqn (3.30). In particular we have the relations:

$$\begin{aligned} S_{S,\text{total}}(t) &= \frac{V}{2T}\left(\left\langle O_{0,\parallel\perp}(t)O_{\text{film},\parallel\perp}(0)\right\rangle + \left\langle O_{3,\parallel\perp}(t)O_{\text{film},\parallel\perp}(0)\right\rangle\right) \\ &= (S_S(t) + S_{SB1}(t) + S_{SB2}(t) + S_{SS}(t)) \end{aligned} \tag{3.34}$$

and

$$\begin{aligned} S_{B,\text{total}}(t) &= \frac{V}{2T}\left(\left\langle O_{1,\parallel\perp}(t)O_{\text{film},\parallel\perp}(0)\right\rangle + \left\langle O_{2,\parallel\perp}(t)O_{\text{film},\parallel\perp}(0)\right\rangle\right) \\ &= (S_B(t) + S_{SB1}(t) + S_{SB2}(t) + S_{BB}(t)) \end{aligned} \tag{3.35}$$

where:

$$O_{\text{film},\parallel\perp}(t) = \frac{1}{4}(O_{0,\parallel\perp}(t) + O_{1,\parallel\perp}(t) + O_{2,\parallel\perp}(t) + O_{3,\parallel\perp}(t)) \tag{3.36}$$

Every cross-region correlation function is plotted in figure 3.19. In figure 3.18a only one stress cross-region correlation function, $G_{SB2}(t)$, has a notable positive time dependence, however all bond orientation cross-region correlation functions are increasing functions of time on some time-scale. We define regional time coupling parameters, which give the relative weight of $S_S(t)$, $S_B(t)$, $S_{SB1}(t)$, $S_{SB2}(t)$, $S_{BB}(t)$, and $S_{SS}(t)$ with respect to

the total regional bond orientation correlation functions, eqn (3.34) and eqn (3.35). The surface region bond orientation coupling parameters are:

$$\begin{aligned} \kappa_S(t) =& S_S(t)/S_{S,\text{total}}(t) \\ \kappa_{SB1,S}(t) =& S_{SB1}(t)/S_{S,\text{total}}(t) \\ \kappa_{SB2,S}(t) =& S_{SB2}(t)/S_{S,\text{total}}(t) \\ \kappa_{SS}(t) =& S_{SS}(t)/S_{S,\text{total}}(t) \end{aligned} \tag{3.37}$$

and the bulk region bond orientation coupling parameters are:

$$\begin{aligned} \kappa_B(t) =& S_B(t)/S_{B,\text{total}}(t) \\ \kappa_{SB1,B}(t) =& S_{SB1}(t)/S_{B,\text{total}}(t) \\ \kappa_{SB2,B}(t) =& S_{SB2}(t)/S_{B,\text{total}}(t) \\ \kappa_{BB}(t) =& S_{BB}(t)/S_{B,\text{total}}(t) \end{aligned} \tag{3.38}$$

Similarly, regional coupling parameters are defined for the stress correlation functions, eqns (3.20)-(3.23) and eqns (3.25)-(3.26). The surface region stress coupling parameters are:

$$\begin{aligned} \iota_S(t) =& G_S(t)/G_{S,\text{total}}(t) \\ \iota_{SB1,S}(t) =& G_{SB1}(t)/G_{S,\text{total}}(t) \\ \iota_{SB2,S}(t) =& G_{SB2}(t)/G_{S,\text{total}}(t) \\ \iota_{SS}(t) =& G_{SS}(t)/G_{S,\text{total}}(t) \end{aligned} \tag{3.39}$$

and the bulk region stress coupling parameters are:

$$\begin{aligned} \iota_B(t) =& G_B(t)/G_{B,\text{total}}(t) \\ \iota_{SB1,B}(t) =& G_{SB1}(t)/G_{B,\text{total}}(t) \\ \iota_{SB2,B}(t) =& G_{SB2}(t)/G_{B,\text{total}}(t) \\ \iota_{BB}(t) =& G_{BB}(t)/G_{B,\text{total}}(t) \end{aligned} \tag{3.40}$$

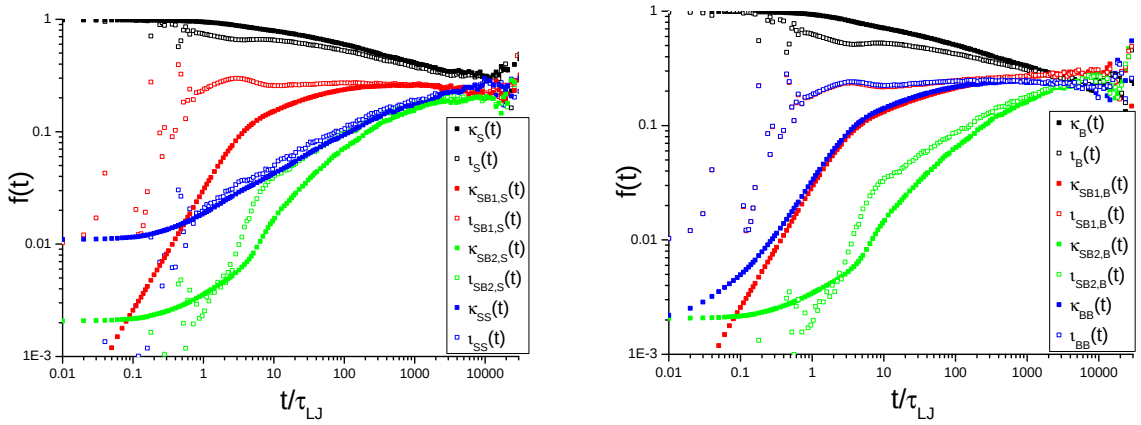

(a) Surface region

(b) Bulk region

Figure 3.20: Time dependent regional stress (open squares) and regional bond orientation (filled squares) coupling parameters.
(a) Surface region: eqns (3.37) and (3.39)
(b) Bulk region: eqns (3.38) and (3.40)

These coupling parameters are plotted in figure 3.20. At $t \approx \tau_{1,\parallel}/3 \approx 7000\tau_{\mathrm{LJ}}$, every regional coupling parameter has a similar magnitude. Although figure 3.18c shows that $G_{\mathrm{film}}(t)$ and $S_{\mathrm{film}}(t)$ are proportional at $t \gtrapprox 10\tau_{\mathrm{LJ}}$, figure 3.20 demonstrates that regional coupling parameters for stress and orientation only match closely at $t \gtrapprox 1000\tau_{\mathrm{LJ}}$. Although all coupling parameters tend to similar values at $t \approx \tau_{1,\parallel}/3$, for the surface region, figure 3.20a, $\kappa_S(t)$ and $\kappa_{SS}(t)$ appear to have a greater magnitude than $\kappa_{SB1,S}(t)$ and $\kappa_{SB2,S}(t)$. For the bulk region, figure 3.20b, $\kappa_{SB1,B}(t)$ and $\kappa_{SB2,B}(t)$ appear to have a greater magnitude than $\kappa_B(t)$ and $\kappa_{BB}(t)$.

Conclusion

This chapter has demonstrated that making what may be considered quite subtle changes to the boundary structure (topology) of films leads to very different stress correlation functions using the KG MD model. It was found that the degree of surface roughness on a monomeric length-scale strongly influences the behaviour of cross-chain bond orientation correlations, although the auto-chain bond orientation correlation function was found to

be effectively identical across the range of boundary and thermostat conditions explored. Corresponding changes in film stress correlation functions were also found. In particular, the limiting case of a perfectly smooth, momentum reflecting surface, used in approximately momentum conserving simulations, led to a negative total film shear stress time correlation for $t \gtrapprox \tau_{\mathrm{LJ}}$. Very similar behaviour was observed using either single monomers or dimers instead of polymers. When a large value of the thermostat friction is used in conjunction with the flat surface, the negative stress correlation is not observed. However, much faster shear-stress relaxation with respect to films with roughened surfaces is still observed. Films with rough surfaces have stress time correlation behaviour that is invariant with respect to the choice of thermostat friction constant. These observations may explain the recently observed effect of confinement induced accelerated relaxation made by Abberton et al. [3] using similar simulations. We find that a relatively low grafting density of tethered chains can counteract these flat surface effects.

It has also been demonstrated that, in weak confinement, the modified-Rouse model can reasonably describe auto-chain bond orientation correlation functions for chains both near and far from the surface (figure 3.3), as well as for end-tethered chains in the mushroom regime (figure 3.2b).

The presence of around 10% by volume of tethered chains leads to a global slowing down of film stress relaxation, which has been characterised in detail in section 3.4.5. However the degree of strain hardening found in the presence of tethered chains by Lee et al. [89] is not observed here, even though the width of their thinnest film was very similar to the one we investigate ($\approx$ 10 radii of gyration of the grafted species). Note that the grafting density used by Lee et al. was around four times larger than that which was used in section 3.4.5.

The terminal stress relaxation time of the tethered chain blend does not coincide with the tethered chain rotational relaxation time, as predicted by the modified-Rouse model. This phenomenon has not yet been fully understood, although the change in terminal relaxation time with respect to the single chain model prediction has been associated with negative cross-chain orientation correlations between chains of the tethered species. This phenomena could be investigated further in the following way: the tethered chains may be distinguished by which wall they are grafted to - we split the tethered chains into two

'species'. Then we may investigate their interspecies cross correlations: is it the correlations between tethered chains on the same surface, or those between chains of opposing surfaces, which become negative? It would also be desirable to make more detailed checks regarding the impact of thermostat friction for films with grafted chains, since figures 3.7 and 3.17 have a non-negligible degree of error at long time for the low thermostat friction simulation.

For films comprising both tethered and free species, the coupling of stress correlations between the surface region containing the slowly relaxing tethered species and the centre channel region which only contains the more quickly relaxing free chains has been investigated. Even in the weakly confined film investigated, the total local centre channel stress correlation function, $G_{B,\text{total}}(t)$, matches the total local surface stress correlation function, $G_{S,\text{total}}(t)$, in the terminal regime, indicating that the centre channel rheology may be influenced by the finite size of the channel. The non-local coupling of bond orientations in different regions of the film has also been measured and compared to corresponding stress couplings.

The main conclusion of this chapter is that the choice of boundary condition is non-negligible, even when the film channel width greatly exceeds the length-scale of the surface structure. Since the KG MD model is a theoretical coarse-grained model, it would be desirable that future work examines how meaningful the simple surfaces explored in this chapter are, with respect to both more detailed simulations and experiment. It would also be very interesting to investigate free-standing films corresponding directly to the experiments by Lee et al. [89]. Could the results of a free surface be similar to a flat reflective surface?

Another future direction could compare the behaviour of polydisperse films with the bulk phenomenology [24] of orientation coupling described at the beginning of section 3.3.

Chapter 4

Chain dynamics in an entangled polymer melt confined by a flat surface

Introduction

The dynamics of confined polymers is an interesting subject that is particularly important for the behaviour of nanocomposite materials [8, 153] and the phenomenon of surface slip in polymer melts [59, 104]. However the dynamics are difficult to characterise and predict. A key concept is the behaviour of entanglements between different polymer molecules in the vicinity of a confining surface. There has been much interest in the changes in properties and density of entanglements for such systems [14, 165, 157, 91, 16, 170, 74, 165]. Ever since the seminal work by Fetters et al. [52], the success of the Lin-Noolandi conjecture [117, 102, 77] has been cited in predictions of an increase in the entanglement molecular weight for polymer melts under steric confinement [21]. Generally the justification for this prediction is the expectation that confined chains will be less inter-penetrating than their bulk counterparts. Examples of relevant systems are polymer melts that are confined in a channel or filled with large particles. Despite much investigation, even under weak confinement there is no clear consensus regarding the magnitude and characteristic length of any depletion in the density profile of entanglements at a flat surface. For example, looking towards experiment, Bodiguel and Fretigny [16] suggested that the density of entanglements at the surface might only deviate from the bulk value within approximately a tube diameter (entanglement spacing) from the surface, using polystyrene films. Weir et al. [170] studied nano-composite systems comprising polymer melts filled with very high

aspect ratio Graphene Oxide nano-particles. The authors suggest that the entanglement density could be reduced within roughly a chain radius of gyration from a surface.

Several studies using computer simulation have examined the system average 'entanglement length', N_e, of confined melts, found from Primitive Path Analysis (PPA) [45]. In some cases an 'S-coil' [64] definition of entanglement length was employed [74, 165] that makes an assumption of Gaussian chain statistics. This assumption is usually considered appropriate in the bulk melt but appears questionable for confined systems. See appendix D and for further discussion on generalized S-coil measures and how they may be applied to confined systems. Alternative measures for the entanglement length that count the number of kinks in primitive paths which are generated using Kröger's Z1 algorithm [147] have also been investigated under confinement [73, 75, 156]. One such measure, the 'modified S-kink' estimator, is:

$$\mathscr{N}_e^{\text{topo}}(n) = \frac{n+1}{\langle Z \rangle} \tag{4.1}$$

where n is the number of bonds in a chain and $\langle Z \rangle$ is the mean number of kinks in a primitive path which separate straight line segments, such that:

$$\lim_{n\to\infty} \mathscr{N}_e^{\text{topo}}(n) = N_e^{\text{topo}} \tag{4.2}$$

Eqn (4.1) is sometimes referred to as a 'topological length' [46]. For a range of flexible polymer melts, eqn (4.1) underestimates the most widely used rheological definition of the entanglement length, N_e^{rheo}, by a factor of $N_e^{\text{rheo}}/N_e^{\text{topo}} \approx 2$ [147]. A comparison with the S-coil measure, which agrees closely with the rheological definition, indicates that the primitive path, defined in this way, is not fully flexible. Everaers [46] has argued that the ratio, $N_e^{\text{rheo}}/N_e^{\text{topo}}$, may be used to measure the functionality of the entanglement network using an analogy with phantom network theory. The observed ratio implies that entanglements are predominately binary events, roughly in agreement with a detailed investigation using Molecular Dynamics which nevertheless showed that a smaller but significant number of entanglements involve three chains [99]. There is also evidence for the dominance of binary entanglements in simulations of star [23] and ring [25] chain architectures. Here a relevant question is whether the binary picture is also valid for confined melts. It should

be stressed that it is not a priori known how any entanglement measure found from microscopic simulation should correspond to the number of topological constraints used in a theoretical coarse-grained model (e.g. tube or slip-spring models). For bulk melts, the relationships between PPA generated entanglement measures and the parameters controlling entanglements in theoretical models have been tested and are quite well understood [45, 147, 154, 169, 46]. In inhomogeneous systems the correspondence is not known since up till now no direct quantitative comparison between microscopic and coarse-grained models of inhomogeneous polymer systems has been made for dynamic observables. Furthermore one cannot assume that the concepts of topological constraints ('entanglements') that are well defined in e.g. slip-spring models (slip-springs) or tube models (tube persistence length) may be extended to an inhomogeneous confined system.
Simply put, we must ask the following general question:

Is an entanglement near a surface similar to an entanglement in the bulk?

To consider this question our approach is to generalize a theoretical bulk model with well defined topological constraints to a confined system. Then quantitative comparison with a detailed MD model tests whether such a generalized entanglement model can accurately predict dynamical observables, and if so, for which choice of density profile of topological constraints across the inhomogeneous confined system.
This chapter focuses on the relatively simple case of a polymer melt of linear and flexible chains that is weakly confined in a channel bounded by two parallel surfaces. We compare the predictions of a single-chain slip-spring model with well defined topological constraints to a much more detailed many-chain molecular model. The channel width is large compared to the size of a chain. The distributions of the topological constraint (slip-spring) lifetimes are shown to be very similar for all slip-spring positions relative to a surface. Topological interactions are not an emergent phenomena within the single-chain model but are explicitly introduced via slip-springs. It is therefore more straightforward to investigate how topological constraints affect chain dynamics near the surface within this model compared to detailed Molecular Dynamics where the definition of an entanglement

is unclear. The single-chain slip-spring model is also vastly less computationally expensive than a corresponding MD simulation.

Since confinement influences chain statistics and dynamics irrespective of whether topological interactions also exist, it is important that the slip-spring model also incorporates these effects. A detailed comparison of a simplified version of the model without slip-springs, to MD, has already been made in chapter 2. This non-entangled 'modified-Rouse' model agrees reasonably well with the behavior of sufficiently short Kremer-Grest (KG MD) model [81] chains near the surface. Deviations from the modified-Rouse model predictions, which emerge using longer KG MD model chains, are expected to be due to emergent topological interactions. This means that when we decorate the non-entangled modified-Rouse model with slip-springs, the degree of agreement of the resulting dynamics of the model with the entangled KG MD chains should give an indication of how well the slip-springs model the emergent effects of topological interactions at the surface.

It is necessary to prescribe a density profile of slip-links and slip-spring anchors in the channel. Simulation has also been employed to investigate entanglement depletion. Since primitive path kinks have a well defined spatial position, a kink density may be calculated as a description for an 'entanglement point' density profile. This has been carried out by Sussman [156] for the case of free standing films using two different channel widths: $L_c \approx \sqrt{\left\langle \boldsymbol{R}_e^{\,2} \right\rangle_{\text{bulk}}}$ and $L_c \approx \sqrt{\left\langle \boldsymbol{R}_e^{\,2} \right\rangle_{\text{bulk}}}/3$, for very long chains ($n = 2000$ bonds), where $\left\langle \boldsymbol{R}_e^{\,2} \right\rangle_{\text{bulk}}$ is the mean square end-to-end distance of chains in the bulk. In both cases, a very narrow depletion layer of kinks of width $\approx 4\sigma$ was observed, where σ is the Lennard-Jones length that is characteristic of a monomer size. A small maximum in the kink density profile at the border of the depletion layer was also observed. This observation is not well understood. Note that although the MD model of Sussman used a similar bead density to us, very stiff harmonic bonded potentials were used instead of the FENE springs of the standard KG MD model [81]. We think that this should have only a small influence on chain statistics however.

It has been noted [46] that for bulk systems the number of slip-springs per chain used in the slip-spring model to fit dynamical data of Molecular Dynamics simulations of KG MD model chains [154, 169] is very similar to the number of kinks per chain found using PPA.

It is then tempting to heuristically associate a kink in a primitive path with a slip-spring in the slip-spring model. By associating kinks with slip-springs, as a working assumption, the relevant quantity that we would like to extract from MD is the kink density profile at the surface.

This chapter is organized as follows: in section 4.2 we perform a PPA using the $Z1$ algorithm, adapted for channel confinement, on a KG MD model of a melt confined in a channel by two parallel flat reflective surfaces. We generate a kink density profile as a function of distance to a surface analogous to the free film case carried out by Sussman. The kink density profile motivates the study of a simple single-chain slip-spring model under parallel plate confinement that assumes a uniform density of slip-links and anchors across the channel. Section 4.3 presents the slip-spring model. Finally, in section 4.4 we compare the slip-spring model with the KG MD model using dynamical correlation functions of chains at equilibrium. Conclusions are made in section 4.5.

Molecular Dynamics model

We use the same confined KG MD model and parameters for flexible chains as in chapter 2, which is very similar to other models in the literature [13, 3]. There are two parallel reflective surfaces bounding the fluid in one dimension so that the channel is symmetric, and periodic boundaries in the other two dimensions. The choice of reflecting surfaces is made for simplicity. Using simulations of melts comprising short chains, we saw in chapter 3 that, for all auto-chain correlation function observables considered in this chapter, this choice leads to no difference with respect to a surface formed by a rough lattice wall. However we found in chapters 2 and 3 that the choice of surface structure is very important for global observables such as the channel average stress correlation function [3] and cross-chain orientation correlation functions [24].

We investigate a monodisperse melt comprising $N_{ch} = 357$ chains, each with $n = 256$ bonds. A Langevin thermostat with friction constant $\xi_{\mathrm{MD}} = 0.5 m_b/\tau_{\mathrm{LJ}}$ was used, where m_b is the bead mass and $\tau_{\mathrm{LJ}} = \sqrt{\sigma^2 m_b/\epsilon}$ is the shortest natural time unit of the simulation

('Lennard-Jones time'); ϵ and σ are the Lennard-Jones interaction energy and length respectively. The simulation box size was chosen to ensure the standard bulk density of $\rho = 0.85\sigma^{-3}$ for a Kremer-Grest melt. We choose a channel width normal to the confining surfaces of $L_c \approx 3.4\sqrt{\left\langle \boldsymbol{R}_e{}^2 \right\rangle_{\text{bulk}}}$, where $\left\langle \boldsymbol{R}_e{}^2 \right\rangle_{\text{bulk}}$ is the mean square end-to-end distance of chains in the bulk. This choice ensures that there is a centre channel region with width $0.5\sqrt{\left\langle \boldsymbol{R}_e{}^2 \right\rangle_{\text{bulk}}}$ that only comprises chains whose segment mean square end-to-end distances match those of bulk chains [78].

Equilibration procedure

In addition to the confined channel system preparation for shorter chains described in section 2.2, additional equilibration steps for the entangled system with $n = 256$ are necessary. We here follow the procedure of Cao and Likhtman [22] by first preparing the system using soft non-bonded and harmonic bonded potentials which allow bond-crossing events. This set of soft interaction potentials has been termed 'soft MD' [96]. In chapter 2 it was demonstrated that in the presence of a flat reflective surface the soft MD model has very similar static properties to KG MD [78]. Simulations using the soft MD model ran for several Rouse times. Following this the potentials were switched to the KG MD model using a 'push-off' over the first Lennard-Jones time, τ_{LJ}. The system then ran for several longest KG MD system relaxation times, τ_{F}, (defined from the longest Maxwell mode of a spectrum fitted to the surface parallel end-to-end vector correlation function (where in τ_{F} 'F' denotes that all chains have two free ends in this system)) before any data presented here was collected. For $n = 256$ we find that $\tau_{\text{F}} \approx 2.5 \times 10^5 \tau_{\text{LJ}}$. Several independent runs were carried out and the results were obtained by an ensemble average. Checking that the data recorded in consecutive runs was consistent acted as an additional check that the system was properly equilibrated. For every observable, error bars are calculated based on the assumption that recorded data generated from conformations which are separated by $2.4\tau_{\text{F}}$ are uncorrelated.

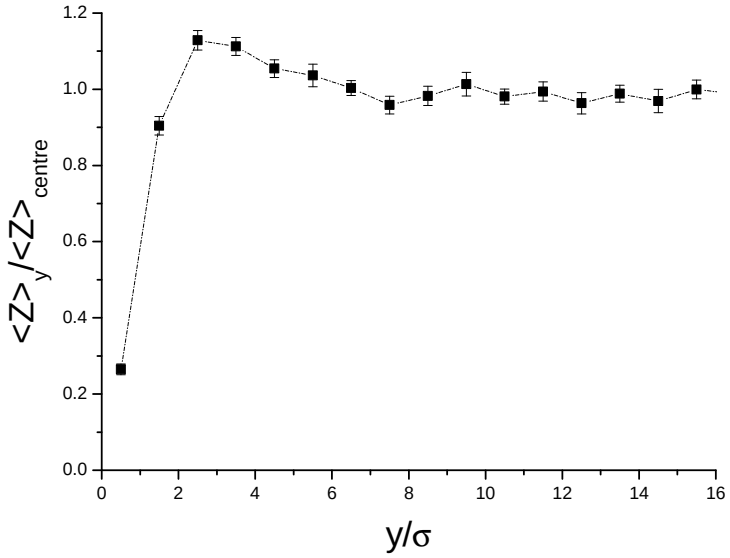

Figure 4.1: Kink density profiles as a function of distance from the kink to the nearest surface, normalized by the centre channel density. Kinks are obtained via the Z1 algorithm [147] applied to the KG MD melt using chains comprising $n = 256$ bonds.

A Primitive Path Analysis of a confined polymer melt

We use the Z1 algorithm of Kröger [147] in order to determine the spatial locations of kinks in the primitive paths of polymer chains. Figure 4.1 plots the kink density as a function of distance from the nearest wall, normalized by the mean kink density in the channel centre. There is a depletion layer of kinks until approximately 2σ from the surface, immediately followed by a moderate excess of kinks before the bulk behaviour is reached at approximately $5 - 6\sigma$ from the surface. 5σ is similar to the spatial distance between consecutive kinks along a primitive path, and is correspondingly also similar to the spatial distance separating slip-links when we map to the slip-spring model in section 4.3.

Taking into account the region with increased kink density, the mean density in the surface region (of width $\approx 5\sigma$) is only a little less than in the channel centre (approximately 10% less). Primitive paths may also be found by 'non-destructive' methods such as the Isoconfigurational Ensemble (ICE) method [14]. ICE defines a primitive path, that is consistent with the classical picture of tube models, by averaging chain conformations over a time interval of order the equilibration time, τ_e: the time at which topological constraints become important for dynamic correlations so that a 'phantom chain' description

such as the Rouse model becomes insufficient. Several simulations with identical initial spatial configurations but different initial bead velocities are averaged over. Alternative definitions of 'entanglement points' have been proposed using ICE [26], and a comparison between the primitive paths that are generated using either a Z1 type algorithm or ICE has been made, demonstrating good qualitative agreement between the two methods [14]. Since the particular form of a density profile for 'entanglement points' is expected to depend to some degree on their particular definition, we consider that the mean kink density in the surface region is the most important quantity to extract with regard to informing an appropriate slip-link density profile, and that further analysis using a range of chain-lengths is necessary in order to establish a good understanding for the scaling of the size of any 'entanglement point' surface depletion, preferably using more than one definition of 'entanglement point'. It has been postulated [1], that the drop in kinks at the surface could be due to the weak nematic interaction for segments close to the surface (see appendix B.1), but this possibility has not been tested. We also note that figure 4.1 is qualitatively similar to the density profile of the chain centre of mass near the surface (see figure B.2). Figure 4.1 shows that the magnitude of any depletion in kinks is very small for the chain length studied. However we must note that although we do not have a surface density profile of 'entanglement points' that is generated using a 'non-destructive' method, the ICE methodology applied to ring polymers concluded that the tube diameter is larger than in the bulk within two or three bulk tube diameters from the surface of a free-standing film by a maximum factor of $15-20\%$. Finally we note that the Z1 algorithm ignores self entanglements. A previous PPA investigation concluded that the number of self-entanglements is negligible in the bulk [155]. In the future it would be useful to also examine the importance of self-entanglements at the surface.

In the following section we present an extension of the the original single-chain slip-spring model, developed by Likhtman [94], to include confinement effects. We investigate the effect that surface proximity has on chain dynamics under the assumption that there is a uniform density of slip-links and anchors at all points in the channel. Since the average kink density near the surface is only slightly less than in the channel centre, this

assumption appears to be a reasonable initial guess.

A slip-spring model with parallel plate confinement

The single-chain slip-spring model presented here aims to describe entangled chains in a polymer melt at flat and completely non-adsorbing surfaces. It is an adaptation of the original model by Likhtman [94] with no additional parameters, and a natural extension of a non-entangled modified-Rouse model for surface chain dynamics in weak confinement [78].

In the same spirit as the original work [94] where slip-links are added to the standard Rouse model to capture entanglement effects, we here add slip-links to the modified-Rouse model [78] to include entanglement and confinement effects. The slip-links are connected to anchors via a 'spring' potential that is modified with respect to the Hookean spring used in the original slip-spring model. The total chain potential in the presence of a single wall at position $y_w\hat{\boldsymbol{e}}_\perp$, including the sets of interactions due to N real 'springs' connecting the modified-Rouse beads and Z virtual 'springs' acting between slip-links at positions $\boldsymbol{s}_j$ and anchors at positions $\boldsymbol{a}_j$, is given by:

$$\begin{aligned} U_{SS} &= U_N(\{\boldsymbol{R}^{N+1}\}, y_w) + U_Z(\{\boldsymbol{s}^Z\}, \{\boldsymbol{a}^Z\}, y_w) \\ &= \sum_{i=1}^{N}\left(\frac{k}{2}{\boldsymbol{Q}_i}^2 + A(y_i, y_{i-1}, y_w)\right) \\ &+ \sum_{j=1}^{Z}\left(\frac{k}{2N_s}(\boldsymbol{s}_j - \boldsymbol{a}_j)^2 + A(s_{j,y}, a_{j,y}, y_w)\right) \end{aligned} \tag{4.3}$$

where $\boldsymbol{R}_i$ and $\boldsymbol{Q}_i = \boldsymbol{R}_i - \boldsymbol{R}_{i-1}$ are the real chain bead and bond vectors respectively, $k = T/{\sigma_1}^2$, ${\sigma_1}^2 = b^2/3$, and b^2 is equal to the mean square bond length far from the surface. Temperature, T, is written in units of the Boltzmann constant, k_b. $a_{j,y} = \boldsymbol{a}_j \cdot \hat{\boldsymbol{e}}_\perp$ and $y_i = \boldsymbol{R}_i \cdot \hat{\boldsymbol{e}}_\perp$. Tildes indicate relative wall positions, e.g. $\tilde{s}_{j,y} = s_{j,y} - y_w$. N_s is the 'number of monomers per virtual spring' [94] which controls the mean square virtual bond length far from the surface, ${b_v}^2$, via the relation: ${b_v}^2 = N_s b^2$. The first part of eqn (4.3) is the standard modified-Rouse potential previously investigated in chapter 2 (eqn (2.5)).

The modified-Rouse potential leads to reflected-Gaussian bond statistics and a uniform bead density at all points in the channel, such that the fluid is considered incompressible. To this is added the virtual-spring potential, $U_Z(\{\boldsymbol{s}^Z\},\{\boldsymbol{a}^Z\},y_w)$, which differs from the original slip-spring potential via the additional surface dependent term:

$$A(s_{j,y},a_{j,y},y_w) = -T\log\left(1+\exp\left(-\frac{2\tilde{s}_{j,y}\tilde{a}_{j,y}}{N_s{\sigma_1}^2}\right)\right) \tag{4.4}$$

In the surface parallel direction the probability distribution of the complete set of real and virtual bond orientations is identical to the original slip-spring model. In the wall normal direction the probability distribution becomes:

$$\begin{aligned}&\Psi(\{y^{N+1}\},\{s_y^Z\},\{a_y^Z\},y_w) \propto \\ &\exp\left(-\sum_{i=1}^{N}\left(\frac{\left(y_i-y_{i-1}\right)^2}{2{\sigma_1}^2}+\frac{\left(-\tilde{y}_i-\tilde{y}_{i-1}\right)^2}{2{\sigma_1}^2}\right)\right)\times \\ &\exp\left(-\sum_{j=1}^{Z}\left(\frac{\left(s_{j,y}-a_{j,y}\right)^2}{2N_s{\sigma_1}^2}+\frac{\left(-\tilde{s}_{j,y}-\tilde{a}_{j,y}\right)^2}{2N_s{\sigma_1}^2}\right)\right)\end{aligned} \tag{4.5}$$

The probability weight corresponding to the set of slip-spring orientations is proportional to the second exponential in eqn (4.5), which is in the form of a probability weight of a reflected random walk from anchor position $a_{j,y}$ to slip-link position $s_{j,y}$. Analogous to Likhtman's original slip-spring model [94], integrating over all possible anchor positions in the channel leads to a probability distribution for the complete set of real chain beads that is unchanged with respect to the model without slip-links, since the partition function of a reflected random walk inside a channel is conserved irrespective of the walk start position. Figure 4.2 verifies that the surface normal mean square end-to-end distances of segments comprising m bonds, $\langle {u_{m,\perp}}^2\rangle$, match the model without slip-springs, at all points in the channel.

The virtual-spring potential, $U_Z(\{\boldsymbol{s}^Z\},\{\boldsymbol{a}^Z\},y_w)$, is a simple and natural choice that conserves the static behaviour of the modified-Rouse model. If the additional term, eqn (4.4), is neglected, the asymmetry of slip-spring orientations near the surface changes the distribution of real chain orientations. For an alternative approach that counteracts such an

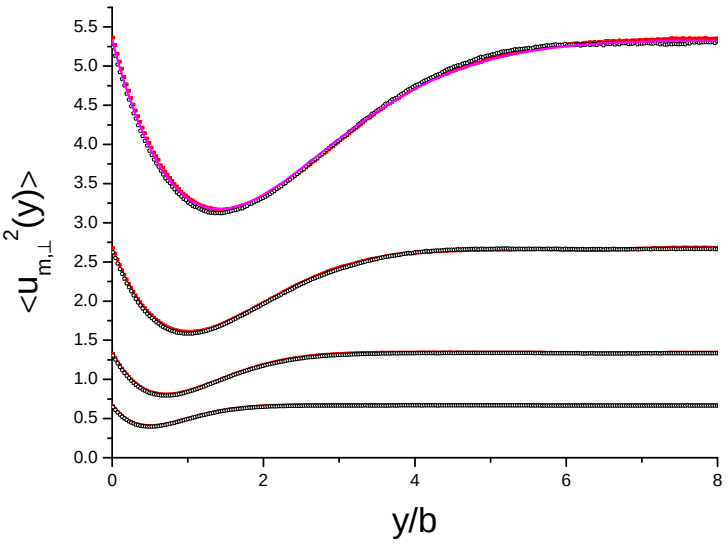

Figure 4.2: Surface normal mean square end-to-end distances of segments, using segments consisting of $m = 2, 4, 8$, and 16 bonds, as a function of segment start bead position with respect to a surface, y. Black open circles: modified-Rouse model (no slip-springs); red squares: slip-spring model using $N_e^{SS} = 4$ and $N_s = 0.5$; green line: analytic solution [148] for $m = 16$. Both models, with and without slip-springs, use chains with $N = 32$ bonds.

asymmetry see Masnada et al. [105].

Model implementation

In order to create the initial configuration of the modified slip-spring model, the first bead of each chain is placed with wall normal position inside the channel according to a uniform distribution. Then the chains are grown by generating bond vectors according to a Gaussian distribution with zero mean and variance b^2. If a generated bead is placed outside of the channel then its position is reflected in the surface plane that it has crossed. This procedure results in a set of chain orientations sampling the distribution Ψ, eqn (4.5). Following the generation of the set of bead positions, a bead is selected from all beads in the channel with equal probability. If the selected bead is currently unoccupied then a slip-link is placed on it. The corresponding slip-spring anchor position is selected by making a displacement relative to the position of the slip-link according to a Gaussian distribution with zero mean and variance $N_s b^2$. If the anchor is outside of the channel then this position is reflected in the surface plane that it crossed. This leaves a set of anchor and slip-link positions sampling the distribution Ψ, eqn (4.5). This system preparation is

completed when there are $\texttt{round}(N_{ch}N/N_e^{SS})$ slip-springs in total in the channel, where N_{ch} is the number of chains in the slip-spring simulation. By construction the density of slip-links and anchors is uniform across the channel.

Slip-links may only exist at the position of chain beads. Slip-link dynamics are given by discrete moves according to a Metropolis-Hastings algorithm [96] satisfying detailed balance. Slip-link jump attempts are made only to adjacent beads with equal probability: $\Delta i = \pm 1$, although in principle it would be possible to choose $|\Delta i| \geq 1$, where Δi is an integer specifying the change in bead index following a slip-link jump. The acceptance probability of the jump attempt is given by:

$$P_{\text{accept}} = \begin{cases} 1, & \Delta U_{SS} \leq 0 \\ \exp(-\Delta U_{SS}/T), & \Delta U_{SS} > 0 \end{cases} \tag{4.6}$$

where ΔU_{SS} is the change in the chain potential, eqn (4.3), due to the Monte-Carlo move.

A slip-spring does not contribute to the system potential once it has left a chain end bead. This means that a slip-spring occupying an end-bead has a 50% chance of being deleted every jump attempt. When a slip-link is deleted from a chain end, a new end-bead is selected from amongst all the chain end-beads in the channel with equal probability irrespective of the bead's position in the channel. If the selected end-bead is unoccupied a new slip-link is created on it. The total number of slip-springs in the channel is then fixed for all time at $\texttt{round}(N_{ch}N/N_e^{SS})$.

We use a slip-spring model comprising $N = 26$ bonds to fit observables of the KG MD system comprising chains of $n = 256$ bonds so that the mapping ratio is $n/N \approx 9.85$. We use the parameter values $N_s = 0.5$ and $N_e^{SS} = 4$ following earlier work [169]. A finer mapping may be used to get a better fit of observables at early time [154]. However this would be computationally expensive and unnecessary since we are interested in the dynamics at $t > \tau_e$. It is found that fine graining the slip-spring model by increasing proportionally N, N_s, and N_e^{SS}, makes very little difference to the dynamics at $t \gtrapprox \tau_e$ for all observables investigated. For an investigation of the segmental dynamics at $t < \tau_e$, and details of the model dynamics for the real chain beads, see chapter 2.

The channel width is chosen to be identical in units of $\sqrt{\left\langle \boldsymbol{R}_e{}^2 \right\rangle_{\text{bulk}}}$ to the KG MD system ($L_c \approx 3.4\sqrt{\left\langle \boldsymbol{R}_e{}^2 \right\rangle_{\text{bulk}}}$). The time-step used is $\Delta t = 0.01\tau_0$ where

$$\tau_0 = \xi b^2/T \tag{4.7}$$

refers to the time unit used by Zhu et al.[180]. Following Zhu [179] the frequency of slip-link jump attempts used is $f^{SS} = 100\tau_0^{-1}$ - i.e. a jump attempt every computational time-step interval. For bulk chains it is already known [169] that the slip-spring model time unit mapped from the KG MD model is $\tau_0 = 3370\tau_{\text{LJ}}$ using the chosen parameters, which is very similar to τ_e.

Constraint release

Slip-links model the effect of constraints on the selected chain resulting from all the other chains in the melt. Since the other chains relax on the same time scale as the selected chain, the resulting constraints get destroyed and reorganized also on this time scale. This effect is called constraint release and can be implemented into the model by pairing up slip-links. If slip-links are paired then when one slip-link is deleted from a chain end a corresponding paired slip-link is also deleted and a move is attempted to regenerate the paired slip-link on any bead of any chain in the channel with equal probability. In a single-chain model it only matters that the distribution of constraint release events is accurate. We observe that the distribution of slip-spring lifetimes is approximately independent of the channel position of the slip-spring when constraint release is switched off. In view of the simplicity of the resulting model, we follow the original approach of randomly pairing slip-links without consideration of the existence of confining surfaces. In appendix E the small differences in the slip-spring lifetime distributions as a function of the slip-spring position in the channel are investigated in detail when constraint release is switched off.

Density profile

Figure 4.3 plots the bead density profile near a reflective surface using the KG MD model. The density oscillates near the surface but the mean density is very similar to the bulk

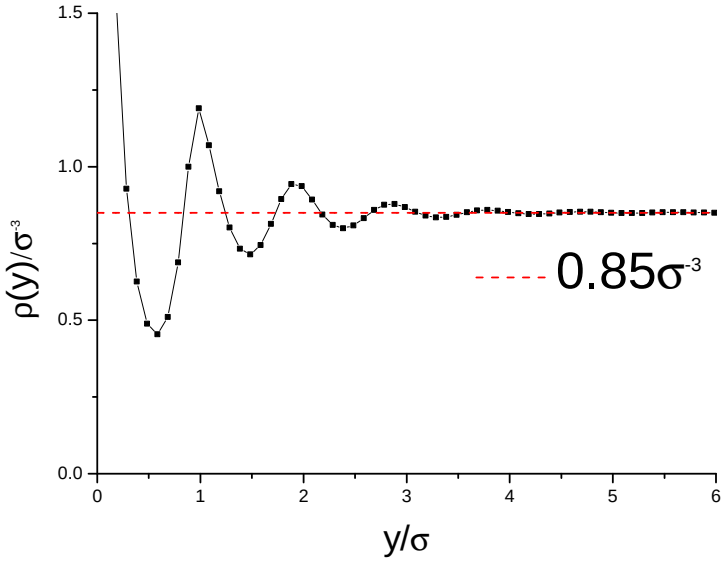

Figure 4.3: Bead density profile near a flat reflective surface using the KG MD model with $n = 256$ bonds per chain.

value of $0.85\sigma^{-3}$. Similar behaviour has been observed using more realistic simulations of a polymer melt in contact with structured flat surfaces. For example, Daoulas et al. [32] studied a united atom model of monodisperse polyethylene (PE) melts in contact with a graphite surface, spanning a decade of molecular weights up to chains consisting of 400 carbon atoms (the crossover to entanglement dominated dynamics occurs at around 156 Methyl groups (C_{156}) [58]). Lee et al. studied an all atom simulation of a polystyrene melt in contact with a graphite surface [92]. In both cases no notable depletion in mass density was observed at the surfaces. For simplicity, we therefore assume a constant bead density for the modified slip-spring model proposed here. If compressibility effects are found to be important, they could be taken into account, as for example they have been in the multi-chain slip-spring model of Ramirez-Hernandez et al. [134].

Chain dynamics: comparison to the KG MD model

Chains are categorized into channel regions of wall normal width $L_c/12 \approx 0.28\sqrt{\left\langle \boldsymbol{R}_e{}^2 \right\rangle_{\text{bulk}}}$ at $t' = 0$, depending on the distance, y_{cm}, from the chain centre of mass to the nearest wall at that time. For example, chains in the $j = 0$ region closest to the surface satisfy $y_{\text{cm}} <$

$0.28\sqrt{\left\langle \boldsymbol{R}_e{}^2 \right\rangle_{\text{bulk}}}$ at $t' = 0$, whereas chains in the $j = 1$ region satisfy $0.28\sqrt{\left\langle \boldsymbol{R}_e{}^2 \right\rangle_{\text{bulk}}} < y_{\text{cm}} < 0.56\sqrt{\left\langle \boldsymbol{R}_e{}^2 \right\rangle_{\text{bulk}}}$. For ideal bulk chains the mean square radius of gyration satisfies $\left\langle \boldsymbol{R}_g{}^2 \right\rangle = \left\langle \boldsymbol{R}_e{}^2 \right\rangle /6$ [141]. This means that the chains located in the two regions closest to the surface may be expected to be less entangled than bulk chains according to previous work [21, 170], since such chains are located within approximately one radius of gyration from the surface. Since the channel is symmetric we improve statistics by averaging opposing regions.

We investigate time correlation functions of form:

$$\begin{aligned} F_j(t) &= \left\langle \frac{\sum_{i=1}^{N_{ch}} \Theta(y^i_{cm}(0) - \mathcal{Y}_j)\Theta(\mathcal{Y}_{j+1} - y^i_{cm}(0)) \int_0^{t_{\max}-t} f^i(t'+t) f^i(t') dt'}{\sum_{i=1}^{N_{ch}} \Theta(y^i_{cm}(0) - \mathcal{Y}_j)\Theta(\mathcal{Y}_{j+1} - y^i_{cm}(0))(t_{\max} - t)} \right\rangle \\ &= \langle f(t) f(0) \rangle_{j, t_{\max}-t} \end{aligned} \tag{4.8}$$

where $f^i(t')$ is a function of the complete set of monomer positions of the ith chain, $\{\boldsymbol{r}^{n+1}\}^i$, at time t'. The Heaviside step function is denoted by $\Theta(y)$; $\mathcal{Y}_j$ indicates the surface normal position at which the jth region begins: for instance $\mathcal{Y}_0$ denotes the position of the surface. The surface normal centre of mass position of the ith chain at $t' = 0$ is $y^i_{cm}(0)$.

In words, eqn (4.8) is a time average of the time-correlation $f(t)f(0)$, taken with duration $t_{\max} - t$, averaged over all chains whose centre of mass lie in the jth region at the beginning of the time average: $t' = 0$. For brevity, in the following we use the shorthand notation $\langle f(t) f(0) \rangle_{j, t_{\max}-t}$ to represent such a time average, as indicated by the second equality in eqn (4.8).

The correlation functions were calculated for a total time duration of $t_{\max} = 2.4\tau_{\text{F}}$ for both slip-spring and KG MD models. Over this time period, for both models the centre of mass positions of chains in the first two surface regions move a distance normal to the surface of approximately the region width on average. The mean density of chains is similar in every region. We compare the slip-spring model using the parameters: $N = 26$, $N_s = 0.5$ and $N_e^{SS} = 4$, with the KG MD model using $n = 256$. All the parameters of the slip-spring model have been determined and we keep them fixed throughout, so there is no freedom for any adjustments in all of the following comparison between the slip-spring and MD models.

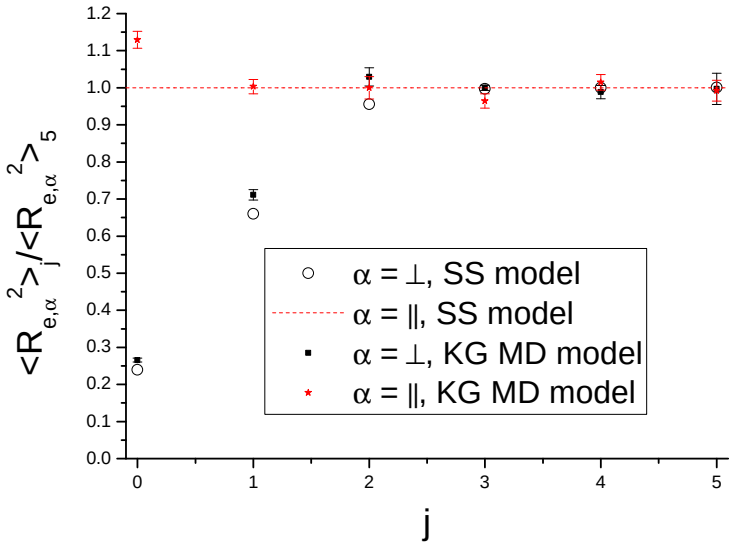

Figure 4.4: Mean square end-to-end distances of chains in the $\alpha = \parallel, \perp$ directions normalized by the centre channel value: $\left\langle {R_{e,\alpha}}^2 \right\rangle_j / \left\langle {R_{e,\alpha}}^2 \right\rangle_5$. Channel regions are selected depending on the chain centre of mass position. Error bars correspond to the KG MD model; error bars are not plotted for the slip-spring model since they are smaller than the size of the symbols.

Chain end-to-end vector correlation function

Before investigating the dynamical end-to-end vector correlation function we first compare the mean square end-to-end distances of chains in each channel region. The system is invariant with respect to a swap of the surface parallel dimensions $\hat{\boldsymbol{x}}$ and $\hat{\boldsymbol{z}}$. Therefore we average over both dimensions for relevant observables, indicated by the parallel indices, $\parallel$. Figure 4.4 plots the mean square chain end-to-end distance for chains with centre of mass position in the jth channel region in both the surface normal and parallel directions ($\alpha = \parallel, \perp$), $\left\langle {R_{e,\alpha}}^2 \right\rangle_j$, normalized by the centre channel value, $\left\langle {R_{e,\alpha}}^2 \right\rangle_5$. The two models agree quite well with regard to this purely static quantity. In the surface normal direction the mean square end-to-end distance is much smaller in the $j = 0$ and $j = 1$ regions compared to in the channel centre. For the slip-spring model the surface parallel end-to-end distance profile is uniform, whereas for the KG MD model there is a weak swelling in the $j = 0$ region which has been discussed previously [78].

Figure 4.5 compares normalized time correlation functions of the chain end-to-end vector in the surface parallel direction, $\Phi_{j,\parallel}(t)$, for chains located in the $j = 0$ and $j = 5$ (centre

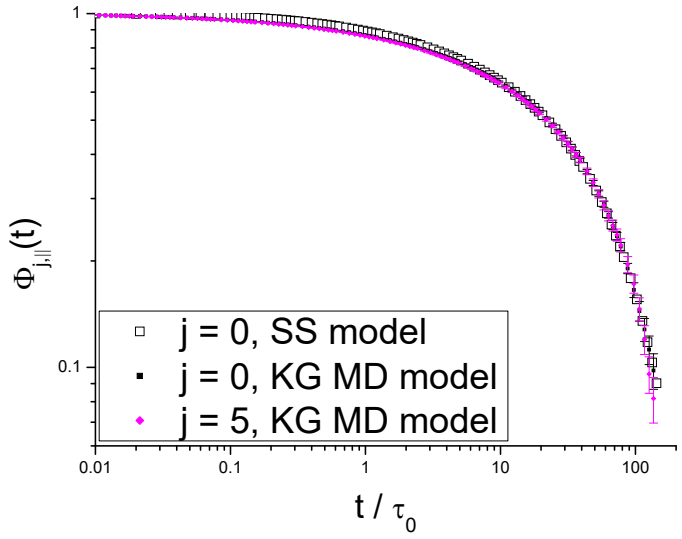

Figure 4.5: Normalized end-to-end vector correlation functions in the surface parallel direction, $\Phi_{j,\parallel}(t)$. The time unit, τ_0, is given by eqn (4.7), and $\tau_0 \approx \tau_e$. Error bars correspond to the KG MD model.

channel) regions. The normalization is made with respect to the value of the end-to-end correlation function at $t = 0$: $\left\langle {R_{e,\parallel}}^2 \right\rangle_{j,t_{\max}}$. Note that $\left\langle {R_{e,\alpha}}^2 \right\rangle_{j,t_{\max}}$ are dynamical observables that depends on $t_{\max}$. This case corresponds to $f(t) = R_{e,\parallel}(t)/\sqrt{\left\langle {R_{e,\parallel}}^2 \right\rangle_{j,t_{\max}}}$ in eqn (4.8). There is no discernible channel dependence for this observable using the slip-spring model which agrees very well with the KG MD model.

Figure 4.6a plots the end-to-end vector correlation function in the surface normal direction normalized by the centre channel value of the end-to-end vector correlation function at $t = 0$: $\left\langle {R_{e,\perp}}^2 \right\rangle_{5,t_{\max}}$. This case corresponds to $f(t) = R_{e,\perp}(t)/\sqrt{\left\langle {R_{e,\perp}}^2 \right\rangle_{5,t_{\max}}}$ in eqn (4.8). There is qualitative agreement between the models. Also good quantitative agreement is found up until region $j = 1$. But in the $j = 0$ region nearest to the surface the slip-spring model does not accurately predict the value of $\left\langle {R_{e,\perp}}^2 \right\rangle_{0,t_{\max}} / \left\langle {R_{e,\perp}}^2 \right\rangle_{5,t_{\max}}$ that is found using the KG MD model. The disagreement, approximately 20%, is worse than for the purely static quantity, $\left\langle {R_{e,\perp}}^2 \right\rangle_0 / \left\langle {R_{e,\perp}}^2 \right\rangle_5$ (see figure 4.4), for which the disagreement is approximately 10%.

Figure 4.6b plots $\Phi_{j,\perp}(t)$: the end-to-end vector correlation function in the surface normal direction normalized by $\left\langle {R_{e,\perp}}^2 \right\rangle_{j,t_{\max}}$. Figure 4.6b reveals a progressively faster relaxation

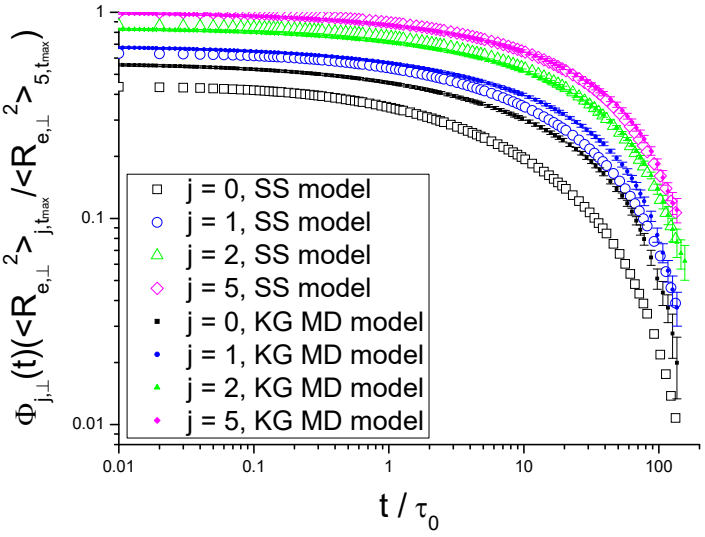

(a)

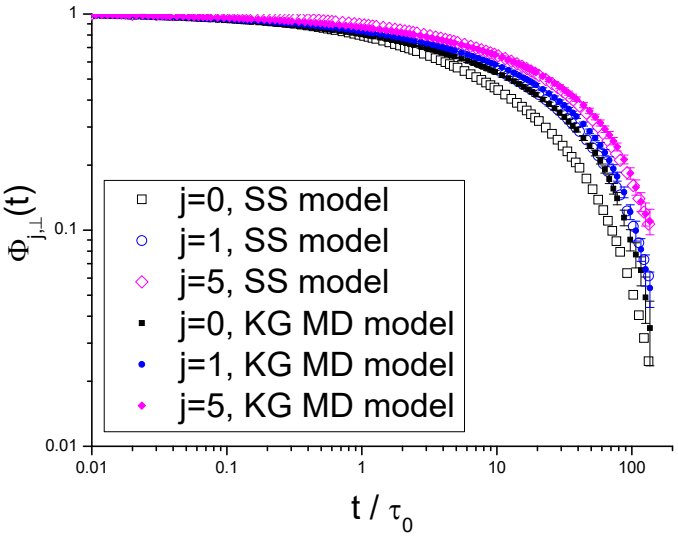

(b)

Figure 4.6: End-to-end vector correlation functions normalized by **(a)** $\left\langle {R_{e,\perp}}^2 \right\rangle_{5,t_{\max}}$ **(b)** $\left\langle {R_{e,\perp}}^2 \right\rangle_{j,t_{\max}}$. Open and filled symbols correspond to the slip-spring and KG MD models respectively. The time unit, τ_0, is given by eqn (4.7), and $\tau_0 \approx \tau_e$. Error bars correspond to the KG MD model.

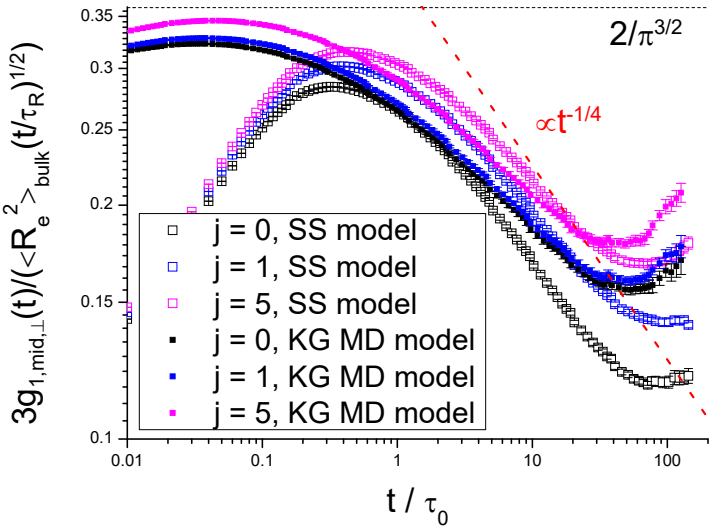

Figure 4.7: Mid-monomer mean square displacement in the surface normal direction, normalized to reveal the sub $\sqrt{t}$ time-dependence for $t > \tau_0$. The time unit, τ_0, is given by eqn (4.7), and $\tau_0 \approx \tau_e$. Open and filled symbols correspond to the slip-spring and KG MD models respectively. An estimated Rouse time, τ_R, for this chain length is found by scaling from the Rouse time for chains consisting of $n = 64$ bonds found in chapter 2 ($\tau_R = 23.5\tau_0$ for $n = 256$). The black dotted line is $2/\pi^{3/2}$ (continuous limit Rouse model prediction of this observable for $\tau_N < t < \tau_R$, where τ_N is the relaxation time of the fastest Rouse mode [96]). The red dashed line is proportional to the reptation model [39] prediction at $\tau_e < t < \tau_R$

as the surface is approached. The slip-spring model describes this accelerated relaxation rather accurately except for the region closest to the wall ($j = 0$). In this region there is a notably faster relaxation using the slip-spring model with respect to the KG MD model for this observable.

The mid-monomer mean square displacement in the surface parallel direction is strongly dependent on the choice of surface structure and thermostat friction constant [78]. However this is not the case for the same observable in the surface normal direction, $g_{1,\mathrm{mid},\perp}(t)$, so that a more meaningful comparison with the slip-spring model can be made for this case. Figure 4.7 plots $g_{1,\mathrm{mid},\perp}(t)$ in a normalized form which reveals its sub $\sqrt{t}$ scaling for $\tau_0 \lessapprox t \lessapprox \tau_R$, where τ_R is an estimated Rouse time for this chain length (see the caption of figure 4.7). For chains that are not influenced by the surface, this deviation from the $\sqrt{t}$ scaling that is predicted by the Rouse model is associated with topological effects. For $t \gtrapprox \tau_0$ and $j \geq 1$, the slip-spring model matches the KG MD model quite well, and as the surface is approached the mid-monomer diffusion becomes progressively slower using both models. However, using the KG MD model, the mid-monomer diffusion in the $j = 0$ region is only very slightly less than in the $j = 1$ region. For the slip-spring model the drop in diffusion rate from the $j = 1$ region to the $j = 0$ region is considerably larger. Since the KG MD mid-monomers are more mobile than the slip-spring prediction in the immediate proximity of the surface ($j = 0$), this may appear to suggest a decreased degree of entanglement. However the opposite conclusion could be made if we only looked at the surface normal end-to-end vector relaxation, figure 4.6. Note also that for $g_{1,\mathrm{mid},\perp}(t)$ a similar behavior was observed using non-entangled chains (see figure 2.11): very close to the surface KG MD chains consisting of $n = 64$ bonds have a faster mid-monomer diffusion than the (non-entangled) modified-Rouse prediction.

Further work is needed to investigate the origin of the wall-mediated effects leading to the discrepancies in the perpendicular relaxation and mid-monomer mean square displacement very close to the surface.

Chain bond orientation correlation function

A shear component of the chain bond orientation tensor involving the direction normal to the surface is:

$$O_{\parallel\perp}(t) = \sum_{i=0}^{n-1} \Big(r_{i+1,\parallel}(t) - r_{i,\parallel}(t)\Big)\,(r_{i+1,\perp}(t) - r_{i,\perp}(t)) \tag{4.9}$$

where n is the number of bonds in a chain. Eqn (4.9) matches the definition used by Cao and Likhtman [24]. It makes no difference whether we normalize the bond vectors by their length or not, since the bond lengths are very quickly equilibrated in our simulation. Figure 4.8a plots the chain bond orientation auto-correlation functions, $\bar{A}_j(t)$, which use $f(t) = O_{\parallel\perp}(t)/n$. This observable is found to be sensitive to the presence of confining walls up to distances of approximately one radius of gyration ($j = 0, 1$), while regions further away ($j \geq 2$) behave very similarly to the centre channel ($j = 5$). We observe that the proximity to a confining surface accelerates the relaxation of the bond auto-correlation function for sufficiently long times ($t \gtrsim 100\tau_{\mathrm{LJ}}$). This trend is qualitatively captured by the slip-spring model, although generally the relaxation in this intermediate time scale is generally overemphasized by the slip-spring model. Nevertheless, for $t \gg \tau_e$ the KG MD curves are simultaneously well described by the slip-spring model both near the surface and in the centre channel. However, the agreement between the two models is less good for $j = 0$ at $t \approx \tau_e$ compared to the other two regions. Note that it is not possible to simultaneously fit both the chain mean square end-to-end distance and bond orientation moment, $\bar{A}_j(0)$, of a slip-spring model to the KG MD model, even in the bulk. This is due to the effect of chain-swelling, which the ideal chain slip-spring model does not describe (see 2.2.1). Figure 4.8b compares the ratios $\bar{A}_0(t)/\bar{A}_5(t)$ and $\bar{A}_1(t)/\bar{A}_5(t)$, using the slip-spring plots in figure 4.8a in addition to plots corresponding to longer chains ($N = 104$) with $N_s = 0.5$ and $N_e^{SS} = 4$ held fixed. For chains nearer the surface $\bar{A}_j(0)$ is smaller. In addition, as discussed above, the decay of correlations is faster near the surface at $t < \tau_e$, such that the ratios in figure 4.8b are non-negligibly less than unity for both $j = 0$ and $j = 1$ regions at $t > \tau_e$. The ratios are larger using the longer slip-spring model chains. This appears unsurprising since in units of the mean bond length the longer chains have a centre of mass position further from the surface compared to the shorter chains, and will

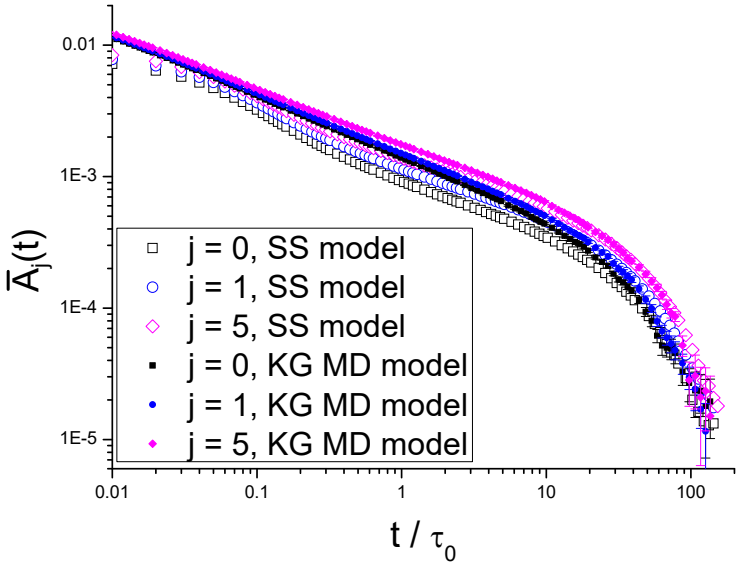

(a)

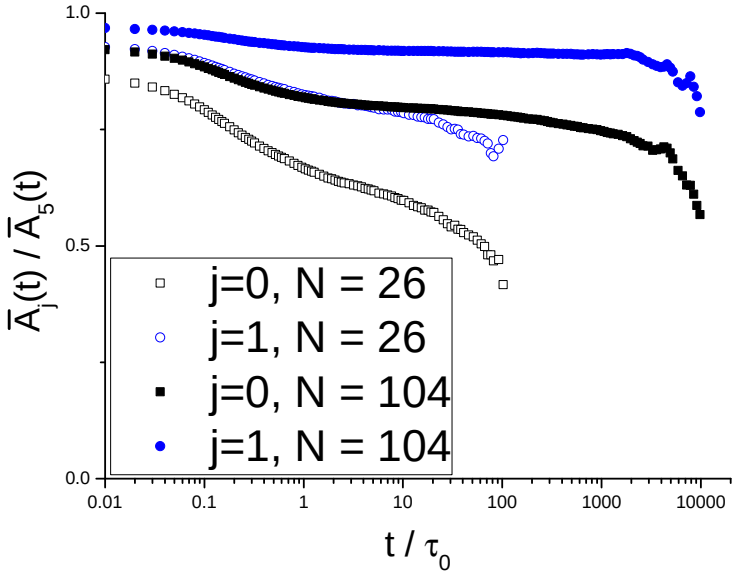

(b)

Figure 4.8: (**a**) Bond orientation correlation functions, $\bar{A}_j(t)$. Error bars correspond to the KG MD model. (**b**) Ratios of the bond orientation correlation functions using the slip-spring model, $N_e = 4$ and $N_s = 0.5$. Black: $\bar{A}_0(t)/\bar{A}_5(t)$; blue: $\bar{A}_1(t)/\bar{A}_5(t)$. Open squares use $N = 26$. Filled stars use $N = 104$. The KG MD plots here calculate eqn (4.9) using coarse-grained segments comprising 4 bonds (although this is not important: the result is proportional to the case of microscopic bonds. The coarse-grained case is chosen for the plot simply because better statistics were available). The time unit, τ_0, is given by eqn (4.7), and $\tau_0 \approx \tau_e$

.

correspondingly have a lower proportion of bonds that are near the surface.

The plateau modulus is often defined theoretically [39] as the value of the linear shear stress relaxation function at τ_e: $G(\tau_e)$ (also see [97] for a discussion of the relation between this theoretical definition and experimental definitions of the plateau modulus). The Stress Optical Rule (SOR) can be used to relate $G(t)$ to the total system bond shear orientation correlation function, $S(t)$, which includes cross-chain bond correlations [24]. $S(t)$ is defined (following the notation of Cao and Likhtman [24]) as:

$$\begin{aligned} S(t) =& \frac{N_b}{T} \sum_{l=1}^{N_{ch}} \sum_{m=1}^{N_{ch}} \frac{1}{N_b^2} \left\langle O_{\parallel\perp}^l(t) O_{\parallel\perp}^m(0) \right\rangle \\ =& A(t) + C(t) \end{aligned} \tag{4.10}$$

where $N_b = N_{ch} n$ is the total number of bonds in the system, and $A(t)$ and $C(t)$ are the auto-chain and cross-chain contributions to $S(t)$:

$$\begin{aligned} A(t) =& \frac{N_b}{T} \sum_{l=1}^{N_{ch}} \frac{1}{N_b^2} \left\langle O_{\parallel\perp}^l(t) O_{\parallel\perp}^l(0) \right\rangle = \frac{N_b}{T N_{\text{reg}}} \sum_{j=0}^{N_{\text{reg}}-1} \bar{A}_j(t) \\ C(t) =& \frac{N_b}{T} \sum_{l=1}^{N_{ch}} \sum_{m=1, m\neq l}^{N_{ch}} \frac{1}{N_b^2} \left\langle O_{\parallel\perp}^l(t) O_{\parallel\perp}^m(0) \right\rangle \end{aligned} \tag{4.11}$$

where N_{reg} is the total number of distinct regions comprising the fluid (in our case $N_{\text{reg}} = 6$). The SOR states that $G(t) \propto S(t)$. For bulk systems it has been demonstrated that at around τ_e [24, 106] the cross-chain and auto-chain contributions have a similar magnitude (and form), $C(\tau_e) \approx A(\tau_e)$. This is true for a variety of blends of linear chains [24] such that $G(\tau_e)$ becomes a function of $A(\tau_e)$, and we may write $G(\tau_e) = \beta A(\tau_e)$ with some generality, where β is constant for a range of blend composition. However the behaviour of cross-chain correlations in confinement could in principle be different from a corresponding bulk system: see e.g. [31], and see chapter 3 for an investigation of cross-chain correlations in confinement using non-entangled systems. If the SOR is valid for a confined polymer melt and we observe the same relationship: $A_{\text{confined}}(\tau_e) \approx C_{\text{confined}}(\tau_e)$, as for bulk melts, the relation $G(\tau_e) = \beta A(\tau_e)$ may be further generalized to confined systems. Figure 4.8 would then suggest that the plateau modulus may be lower for a confined system compared to a

bulk melt. It may then appear plausible that the prediction of figure 4.8b could explain part of the drop in the plateau modulus observed by Weir et al. [170]. Note however that this analysis doesn't take into account the influence of surface adsorbed chains that may have slower segmental relaxation at $t < \tau_e$ [78] which could actually increase the plateau modulus. If N_e^{topo} is unchanged in confinement then the relationship of the plateau modulus with N_e^{topo} may be different from a corresponding bulk relation.

It was demonstrated in section 2.3 that the zeroth Rouse mode (centre of mass) motion of KG MD model chains is quite highly dependent upon the value of the thermostat friction used. This is due to the importance of momentum conservation for Hydrodynamic Interactions (HI) [48]. Appendix B.3 also demonstrates that the centre of mass diffusion coefficient in a direction parallel to the surface also depends strongly on surface structure (whether the surface reflects momentum: flat reflective, or not: roughened lattice surface), even beyond the Rouse time, using short chains comprising $n = 64$ bonds. As a result, it may not be straightforward or necessarily meaningful to compare zeroth mode motion in slip-spring model simulations to that of the KG MD model, since the HI and surface structure effects are not described by the single-chain model. In contrast, higher mode auto-chain correlation functions (i.e. not dependent on cross-chain correlations) are very weakly, if at all, dependent on the boundary structure or thermostat friction. Therefore it is natural that we first investigated the behaviour of observables that depend only on non-zero Rouse modes, such as the chain end-to-end vector and bond orientation auto-correlation functions, and compared the results to KG MD using a flat reflective surface and a Langevin thermostat with the most commonly used friction constant in the literature that allows for a large time-step.

Conclusion

We have investigated a KG MD model of a polymer melt weakly confined in a channel with flat reflective boundaries. No discernible confinement effect was found for the terminal relaxation time of the end-to-end vector correlation function in the surface parallel direction for chains with different centre of mass positions relative to a surface. Despite this we

find that the auto-chain bond shear orientation correlation functions for chains in different regions depend on the distance of the chains to the confining wall by a non-negligible amount at $t > \tau_e$. We proposed a minimal and parameter-free extension of a well-known slip-spring model [94] to include confinement effects via the modified-Rouse model that was presented in chapter 2. For simplicity, we assume a uniform density of slip-springs in the channel. Despite its simplicity, at $t \gg \tau_e$, both the bond orientation and the normalized surface parallel end-to-end vector correlation functions were simultaneously quite well described by the single-chain model. However the single-chain model agreed less well with the MD simulation for the surface normal end-to-end vector correlation function and mid-monomer mean square displacement, $\Phi_{j,\perp}(t)$ and $g_{1,\mathrm{mid},\perp}(t)$ respectively. Modifications of the proposed confined slip-spring model for an improved comparison of $\Phi_{0,\perp}(t)$ and $g_{1,\mathrm{mid},\perp}(t)$ is left for future work.

The simulation results do not support the picture of strong disentanglement at flat surfaces in weak confinement that has sometimes been suggested in the past [21]. The reasonably good agreement between the MD model and slip-spring model suggests that further such comparison using longer chain lengths could be fruitful, and may be used to provide a more precise measure of any disentanglement (or lack there of) at the flat surface.

The behaviour of the auto-chain bond orientation correlation function, using the slip-spring model with a uniform density of slip-links in the channel, suggests that the experimentally observed plateau modulus could be lower in confined melts even when there is no drop in topological interactions.

Chapter 5

Non-equilibrium sliding plate simulations of surface disentanglement

This chapter investigates the phenomenon of shear-flow induced disentanglement between chains that are not adsorbed on the surface and those that are permanently adsorbed (grafted) to the surface. We are particularly interested in the influence of the disentanglement on the experimental stick-slip phenomena introduced in section 1.0.4. A non-equilibrium Molecular Dynamics (MD) simulation in the sliding plate geometry (also known as simple planar Couette flow) is performed.

Introduction

The literature has primarily focused on two mechanisms that may explain macroscopic surface slip in entangled polymer melts. The first mechanism is chain desorption from the surface above a critical stress [60]. The second mechanism is flow induced surface disentanglement between adsorbed and non-adsorbed chains, thought to be the result of a coil-stretch transition of the adsorbed chains [167]. In addition, the action of a low molecular weight species in a polydisperse sample containing a high molecular weight species has been investigated [142]. Here we focus on the phenomenon of shear-flow induced surface disentanglement. Although this work focuses on surface disentanglement, in general different mechanisms for slip may occur concurrently: e.g. desorption and disentanglement. However, advances in the functionalization of surfaces with grafted molecules [89, 29, 30] may mean that even simple models of permanently grafted chains have direct experimental

applicability. Eliminating the desorption mechanism entirely may be desirable for certain applications, warranting more detailed investigation of this ideal case, for which much theoretical attention has focused. The system that we consider consists of so-called T chains that are permanently end-grafted (tethered) to the surfaces at regular positions, in addition to free, so-called F chains. The grafting density is at the limit of the 'mushroom' regime whereby adjacent T chains only very weakly overlap.

This chapter is organized as follows. In section 5.2 we survey the current state of the literature, focusing on theoretical models for the surface disentanglement. The aim of the present work is to critically examine some of the assumptions made in the theoretical models using state of the art MD simulations. In section 5.3 we introduce the MD model and methods. Z1 Primitive Path Analysis (PPA) [76, 84, 147] is employed to characterize the topological state of the fluid both at equilibrium and at high Weissenberg numbers. There is much evidence for a binary picture of entanglements [46, 99, 25, 23]. In line with this picture, we are particularly interested in identifying the number and behavior of topological interactions between T and F chains away from equilibrium. We study the locations of topological interactions between different primitive paths, both in space and along the primitive path contours. We examine the correlations between primitive paths that are generated by the Z1 algorithm, the configurations of the corresponding bead-spring chains, and the rheological properties of the fluid. In section 5.4 the main results are presented and discussed. In section 5.5 final conclusions are made.

2. Survey of theoretical descriptions of surface disentanglement and slip in polymer melts

Theoretical scaling models describing the surface disentanglement were primarily developed by Brochard, de Gennes, and co-workers [19, 5, 6, 20]. They considered a simple model using the low grafting density limit whereupon a deformed T chain may increase the number of F chains it entangles with, and resultantly also increases the surface shear friction force, providing that the surface-normal diameter, D, of the stretched 'cigar' conformation remains larger than a bulk entanglement 'tube' diameter: $D > a_0$. Then once

$D < a_0$, the T chain experiences a complete disentanglement from the F chains. This leads to a sudden reduction of the shear friction force, and resultantly the strongly deformed chain relaxes rapidly and re-entangles with the bulk. The primary prediction was then of a 'marginal regime' where the stress remains constant for a range of applied shear-rates or slip velocities corresponding to $D \approx a_0$.

The first experimental observation of a marginal regime was made by Migler et al. [115], in a study in which the surface was specially treated to reduce the F chain adsorption. Soon, further experiments exploring temperature [166] and molecular weight [167] dependence concluded that under many conditions the most important mechanism for a sudden onset of slip is disentanglement between adsorbed and non-adsorbed chains. For an accessible review of some seminal experiments investigating surface slip in polymer melts see Léger et al. [104].

Later scaling models were essentially more detailed variations of the original Brochard—de Gennes theory, aiming to describe several different observed scaling regimes. The higher grafting density cases were also considered [20]. Ajdari et al. [5] employed the analogy of a single T chain with one end tethered to a nano-particle that is pulled through a melt. Contour length fluctuations [118] were assumed to aid relaxation of bond orientation far away from the T chain end, such that it was postulated that the deformation leads to a trumpet-shaped T chain conformation. Above a critical pull velocity, the narrow cylinder part of the trumpet crosses over to a diameter below the entanglement length. The contribution to the friction force acting on the fluid from this section of the chain contour is greatly reduced compared to the entangled section. Mhetar and Archer developed a similar scaling model based on the same ideas [114]. All of the scaling models are based upon a concurrent T chain alignment and consequent disentanglement between T and F chains. These models also assume that the F chains remain unperturbed from their equilibrium conformations: it has been demonstrated experimentally [18] that the onset of slip can occur at small Weissenberg numbers with respect to the F chain terminal relaxation time, such that the conformations of F chains are only weakly perturbed with respect to quiescence. Since many polymer melts shear-thin, any bulk deformation is expected to decrease the degree of slip following surface disentanglement compared to instances where

a coil-stretch transition of T chains occurs at a negligible bulk Weissenberg number.

Following the scaling models, adaptations of bulk tube models [112, 119, 56] were made, forming constitutive relations at the surface and in the bulk [71, 158]. In these models the surface constitutive relation is coupled to a bulk constitutive relation via stress balance and an additional diffusion of the tube contour due to convective constraint release [56] of the F chains. The tube model of Tchesnokov et al. [158] is based on the bulk GLaMM (Graham, Likhtman, Milner, McLeish) model [56]. In the surface region the shear stress is set equal to the product of an interfacial modulus G_{I0} with the mean tube segment shear orientation S^I_{xy} of T chains: $\sigma_{xy} = G_{I0} S^I_{xy}$. In their notation the interfacial modulus is $G_{I0} = 2k_{\mathrm{B}}T\psi^0_{\mathrm{BT}}/a_0^3$, where ψ^0_{BT} is the volume fraction of entanglements that involve F and T chains which depends upon the grafting density within the model, T is the temperature, k_{B} Boltzmann's constant, and a_0 is the mean spatial distance between entanglements, which is often considered equal to the equilibrium tube diameter. These models also considered a range of grafting densities from sparsely grafted 'mushroom' chains to the dense brush. The model of Tchesnokov et al. [158] was compared with experimental data which used a range of well controlled grafting densities [41]. As a comparison, Hoy and Grest [63] have examined entanglements between T and F species for a range of grafting densities above the Gaussian mushroom regime but below the dry brush regime, using MD simulations and PPA. Interestingly, although (i) the model of Tchesnokov predicts a sudden onset of slip, and (ii) the characteristic height of the surface region (found from the T chain surface normal height) is a quantity that is employed in the computation of the slip length, the key parameters controlling the effects of surface entanglements are independent upon the tube deformation: the surface modulus, G_{I0}, and the fraction of T chain entanglements that are due to F chains (ϕ_Z in [158]). The construction of the Joshi et al. [71] model is analogous in this respect. This means that these models imply the same assumption for the number of entanglements in T chains under strong shear as the one applied in the GLaMM model [56] for deformed F chains: the number of entanglements increases in proportion with the primitive path length of the chain (the tube diameter is assumed to be held fixed). Therefore, in the surface tube models, surface disentanglement is not explicitly modeled: these models assume that the coil-stretch transition precedes

disentanglement. Instead, the initial slip is apparently due to the surface alignment of the T chains which is accelerated due to a limited convective constraint release mechanism [71] acting on the T chains from the F chains. It is also notable that the higher relaxation modes of the T chains, which do not depend on entanglements but become important once the chains are stretched, do not contribute to the stress in the interfacial tube models. However these models do include a contribution to the tube relaxation due to chain stretch via the tube retraction rate. In contrast the more detailed bulk GLaMM model does include the higher mode contributions to the stress.

Clearly it is desirable to examine the physical assumptions used in these various models. One limitation of experimental methods is that it is difficult to probe in detail what is happening on a molecular level at the surface, although recently Chennevière et al. [30] have been able to examine the change in the T chain monomer density profile following deformation, using a well defined end-grafted system. An alternative means of investigation is via computer simulation. In recent years simulation studies [139, 40, 178, 69, 79] have sought to examine in detail the molecular mechanisms which contribute to slip in entangled melts. A notable case is the work by Zhou et al. [178], where they found that adsorbed chains may slip across a smooth surface whilst remaining adsorbed, with the surface friction describing this process being dynamic: the total surface slip then depends upon a competition between disentanglement and this additional mechanism. Very recently Jeong et al. [69] have studied in more detail this phenomenology, identifying three flow regimes, universally valid at different molecular weights. For example, the fast flow regime is characterized by the tumbling motion of adsorbed chains which can lead to complete desorption. The majority of such simulation studies have used systems with partially adsorbing boundaries. One exception is a recent paper by Korolkovas et al. [79] that compared a coarse-grained simulation model of the collapse of permanently grafted brushes immersed in a dense polymer solution to corresponding experiments using two types of brushes. A degree of universality describing the brush collapse was found.

To isolate the coil-stretch phenomena from other mechanisms, and to examine the ideas and assumptions made in the various theoretical descriptions, we here consider an idealized simulation consisting of T chains that are permanently end-grafted to the surface,

immersed in a melt of F chains with the same molecular weight and chemistry. Although the scaling models are not quantitative, and the tube models are probably not applicable to the molecular weights we are able to simulate, we can examine some of the principles they are based on. In particular we consider some main questions:

(i) Is the general picture of the scaling models correct? I.e. is there a disentanglement associated with the coil-stretch transition?

(ii) Irrespective of the relationship between T chain orientation and effective surface friction, do the scaling models accurately describe the evolution of the T chain orientation with respect to shear-rate; are the stretched T conformations cigar-like or trumpet-like?

(iii) What is the correlation of any observed 'disentanglement' with surface friction and slip length?

3. Simulation details and equilibration methods

A schematic representation of the simulation system is given by Fig. 5.1. We use the confined Kremer-Grest (KG) bead-spring model [81] and parameters for flexible chains as in previous chapters, which is very similar to other models in the literature [13, 3]. The simulation comprises $N_\mathrm{F} + N_\mathrm{T} = 676$ linear chains, each consisting of $n = 256$ Finitely Extensible Nonlinear Elastic (FENE) bonds, in the sliding plate geometry. The majority, $N_\mathrm{F} = 628$ F chains, have two free ends. The top and bottom walls each carry 24 T chains, permanently adsorbed by one end to them, giving $N_\mathrm{T} = 48$ such T chains in total. The grafting density of the T chains is chosen as $\rho_g = 0.00625\sigma^{-2} \approx 2.8\rho_g^*$, where we define the overlap grafting density $\rho_g^* = 1/\langle \boldsymbol{R}_{e,\mathrm{bulk}}{}^2 \rangle = 0.0022\sigma^{-2}$ for this chain length, where σ is the Lennard-Jones length, and $\boldsymbol{R}_{e,\mathrm{bulk}}$ denotes the end-to-end vector of a n-chain in the bulk whose mean squared norm is actually very close to the one we find for F chains in the channel center. The same is true for all quantities to be discussed. For this reason we are going to label center channel quantities throughout by 'bulk'. Lennard-Jones units time and mass we denote by τ_LJ and m_b, respectively.

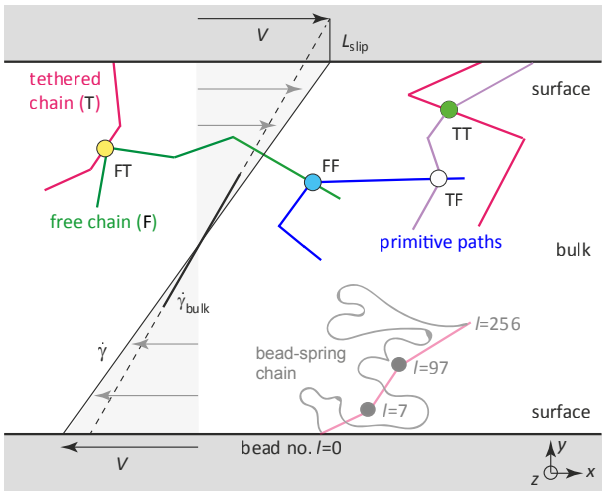

Figure 5.1: Schematic of the simulation system confined between planar walls, subjected to shear. An example bead-spring T chain conformation is represented by the wavy gray curve. Its primitive path is represented by the red lines that are connected at the locations of kinks in the primitive path (gray circles). Two shear rates $\dot{\gamma}$ and $\dot{\gamma}_{\text{bulk}}$ as well as wall speed V and slip length L_{slip} are specified. Several A $\in$ {F,T} chain primitive paths are shown. Examples of the four possible types of AB kinks on A chains due to a B chain are represented: **(a)** FF (cyan), **(b)** FT (yellow), **(c)** TT (green), and **(d)** TF (white).

The grafted beads are located in a regular pattern using a two-dimensional slice of the Face Centered Cubic (FCC) lattice with miller indices (111), such that opposing surfaces have reflection symmetry. The grafting density is sufficiently low such that the chains are still in the 'Gaussian' (reflected random walk) regime; i.e. the T chains do not stretch significantly; therefore the grafting density that we investigate corresponds roughly with the recent experimental work of Chennevière et al. [30]. For this grafting density, we can use a previously establish protocol [78] to generate initial configurations of F and T chains: the F chains have a uniform start bead distribution everywhere in the channel; then, for both F and T chains, conformations are generated according to a fixed mean equilibrium bond length (0.97σ) and a bond angle distribution that is similar to the bulk equilibrium distribution, under the boundary constraint. The simulation box has dimensions $L_x \approx 4\langle \boldsymbol{R}_{e,\text{bulk}}{}^2 \rangle^{1/2}$, $L_y \approx 3L_x/4$, and $L_z \approx L_x/2$. The simulation box is periodic in $\hat{\boldsymbol{x}}$ and $\hat{\boldsymbol{z}}$ directions and bounded by reflective surfaces with normal unit vector $\hat{\boldsymbol{y}}$, so that the channel width is $L_c = L_y = 60.7\sigma$. We use the Verlet algorithm [9] for integrating the equations of motion. For the Verlet algorithm, reflective surfaces are implemented in the following way: if a monomer crosses the surface at the current

time then both the current and previous positions of the monomer are reflected in the surface plane. The unit vector coinciding with the surface velocity is $\hat{\boldsymbol{x}}$. It was shown in chapter 3 that in the presence of surface grafted T chains, many important equilibrium dynamic properties of a non-entangled melt weakly confined in a channel by two surfaces are close to invariant using a range of boundary potentials. In the following section it will be verified that the center channel rheology of the entangled system we study is consistent with a corresponding simulation using periodic boundaries.

Some additional equilibration steps are necessary in this more entangled system, following the procedure of Cao and Likhtman [22]: initially we prepare a system that is half the final simulation size in the velocity direction with dimension $L_x \approx 2\langle \boldsymbol{R}_{e,\mathrm{bulk}}{}^2 \rangle^{1/2}$ while L_y and L_z remain unaltered. Initially we use soft non-bonded and harmonic bonded potentials which allow bond-crossing events. This set of soft interaction potentials has been termed 'soft MD' [96]. We have previously demonstrated that in the presence of a flat reflective surface the soft MD model has very similar static properties to the KG model [81]. Simulations using the soft MD model ran for several rotational relaxation times [39] of the T species, as determined from the longest relaxation mode from a spectrum fitted to the end-to-end vector correlation function. Following this the potentials were switched to the KG model using a 'push-off' over the first Lennard-Jones time, τ_{LJ}. The system then runs for a rotational relaxation time of the T species under the KG potential, $\tau_{\mathrm{T}} \approx 10^6 \tau_{\mathrm{LJ}}$. Then every chain in the system is cloned; the cloned chains are displaced with respect to their parents by $L_x\hat{\boldsymbol{x}}$, and the box $\hat{\boldsymbol{x}}$ dimension is reset to $2L_x$. Following this, the final double sized system runs for another τ_{T} before any shear deformation is applied. In the non-equilibrium simulations we employ a Langevin thermostat which only acts in the neutral, $\hat{\boldsymbol{z}}$, vorticity direction, and is applied uniformly across the channel. The thermostat friction is $\xi_{\mathrm{MD}} = 0.5 m_b/\tau_{\mathrm{LJ}}$. For steady-state shear simulations, steady state observations begin τ_{T} after the shear is switched on. It is validated that the transient stress following the stepped-shear has reached steady-state beyond the overshoot at this time, and that the primitive path data appears time-independent.

All computations were performed using a GPU 'device' except for on-the-fly data analysis performed on the CPU 'host'. The program was coded using Nvidia's CUDA

platform [143]. For details of the core GPU MD code that we use see [10]. The code was extended for the present purpose to also allow for the simulation of non-periodic systems, including T chains and explicit surface deformation. Further technical details regarding the GPU code, including details of consistency checks with a corresponding CPU code, are given in appendix F.

Each steady state simulation ran for approximately six months, corresponding to approximately $10^7\tau_{\mathrm{LJ}}$ or $10\,\tau_{\mathrm{T}}$ at an integration time step of $\Delta t = 0.01\tau_{\mathrm{LJ}}$ using a single k10 GPU and single CPU. The duration was sufficiently long to get small error bars for the static Z1 analysis, taken using many system snapshots. Error bars are generated under the assumption that snapshots separated by intervals of τ_{T} are uncorrelated. For other dynamic observables it was not possible to construct error bars in this way since only a single observation was made over the entire simulation duration. An improvement, allowing for the construction of error bars, would have been to make, for example, ten separate observations each lasting $\approx \tau_{\mathrm{T}}$. However, the duration of observation was sufficiently long to give a clear qualitative picture of the shear-rate dependence of all observables investigated.

4. Results and discussion

As illustrated in Fig. 5.1, the fluid deformation is generated by displacing the grafted beads of the T chains. The opposing velocities at which grafted beads on the top and bottom walls are displaced are V and $-V$ respectively. The speed of each wall is $V = \dot{\gamma}L_c/2$, where $\dot{\gamma}$ is the channel average shear-rate, which from now on is referred to as the applied shear-rate. Due to the inhomogeneous nature of the fluid, an inhomogeneous shear-rate profile is developed such that in the center channel the 'bulk' shear-rate, $\dot{\gamma}_{\mathrm{bulk}}$, is generally different from the applied shear-rate, $\dot{\gamma}$. We define $\dot{\gamma}_{\mathrm{bulk}}$ from the gradient of a straight line fitted to the monomer velocity profile in the channel center.

Entanglements are frequently taken to be binary interactions between different chains [117]. We recognize that a kink in the final conformation of a primitive path is in some way dependent on all original positions of the monomers of all chains. However we may still identify the secondary primitive path whose final proximity directly led to the kink. This

pairing introduces a binary picture of entanglements which in the following we exploit in order to examine primitive path interactions between different chain species: T and F. Figure 5.1 illustrates the four possible types of binary interactions which lead to a kink on a primitive path that we say is *due* to the proximity of a different primitive path (self-entanglements are ignored by Z1). A kink on a T primitive path is due to the path meeting either another T path (TT kink) or a F path (TF kink). Likewise, a kink on a F primitive path is due to the path meeting either another F path (FF kink) or a T path (FT kink).

We define a F chain Weissenberg number using the bulk shear-rate: $\mathrm{Wi_F} = \dot{\gamma}_{\mathrm{bulk}}\tau_{\mathrm{F}}$, where $\tau_{\mathrm{F}} = 2.5 \times 10^5 \tau_{\mathrm{LJ}}$ is the rotational relaxation time of the F chains ($n = 256$), which is defined from the longest Maxwell mode of a spectrum fitted to the end-to-end vector correlation function of F chains. The mean rotational relaxation time of all F chains in the channel is very similar to that of chains in the center of a channel without T chains (see chapter 4), or that of a system of F chains using periodic boundaries. An alternative definition of the longest relaxation time, as used in previous work with which we may compare results [12], fits a single stretched exponential to the normalized end-to-end vector correlation function and then calculates the area under the curve. This integral is then equated with the relaxation time, which it coincides with exactly in the case of a single exponential. Both definitions give the same τ_{F} within a relative error of $\approx 5\%$ for this KG simulation. We also define a T chain Weissenberg number using the applied shear-rate: $\mathrm{Wi_T} = \dot{\gamma}\tau_{\mathrm{T}}$. The rotational relaxation time of the T chains, τ_{T}, is related to τ_{F} by $\tau_{\mathrm{T}} \approx 4\tau_{\mathrm{F}}$ for this chain length, matching the ratio found using shorter completely non-entangled chains [78]. Table 5.1 gives the corresponding values of the shear-rates and Weissenberg numbers for each simulation. See Fig. 5.2 for an illustration of a small part of a primitive path network, including only those chains whose proximity results in a kink on the primitive path of a single selected (red) T chain ($\mathrm{Wi_T} = 9.6$, $\mathrm{Wi_F} = 1.8$). In Fig. 5.2, the real space positions of the primitive path kinks are consistent with the areas of high overlap of the pervaded volumes of the chains involved in the kink.

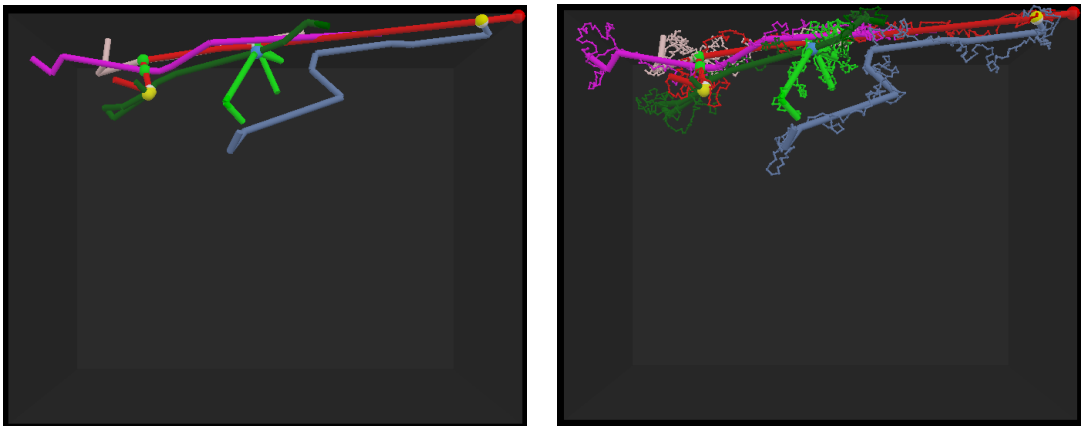

(a) (b)

Figure 5.2: **(a)** Unfolded primitive paths of all chains that are entangled with a single selected T chain (red), found using the Z1 algorithm. **(b)** Same as (a), decorated with the position of every bead in all of the chains prior to the Z1 algorithm. For illustrative purposes the primitive path conformations are placed inside a box with the same dimensions as the simulation box. There are two other T chains (beige and magenta) 'entangled' with the selected (red) chain. There are also three F chains (dark green, green, and blue) entangled with the selected chain. The red sphere represents the tethered end of the red chain/primitive path. Other spheres represent primitive path kinks which involve any two of the selected chains. The color code is consistent with other figures — TT: green sphere, TF: white sphere (hiding behind yellow spheres), FF: cyan sphere, FT: yellow sphere. Note that there is a topological interaction in this portion of the network that does not directly involve the red chain: indicated by the cyan sphere FF kink). The snapshot is from a simulation using $\dot{\gamma} = 9.6 \times 10^{-6} {\tau_{\mathrm{LJ}}}^{-1}$ ($\mathrm{Wi_T} = 9.6, \mathrm{Wi_F} = 1.8$).

$\dot{\gamma}\tau_{\mathrm{LJ}}$	Wi_{T}	$\dot{\gamma}_{\mathrm{bulk}}\tau_{\mathrm{LJ}}$	Wi_{F}
2.4×10^{-6}	2.4	2.64×10^{-6}	0.66
4.8×10^{-6}	4.8	4.56×10^{-6}	1.14
9.6×10^{-6}	9.6	7.20×10^{-6}	1.80
2.5×10^{-5}	25	1.45×10^{-5}	3.625
1×10^{-4}	100	6.50×10^{-5}	16.25
1×10^{-3}	1000	7.70×10^{-4}	192.5
1×10^{-2}	10000	8.50×10^{-3}	2125

Table 5.1: Table giving the correspondence between the applied shear-rate, $\dot{\gamma}$, the T chain Weissenberg number, $\mathrm{Wi}_{\mathrm{T}} = \dot{\gamma}\tau_{\mathrm{T}}$, the bulk shear-rate, $\dot{\gamma}_{\mathrm{bulk}}$, and the F chain Weissenberg number, $\mathrm{Wi}_{\mathrm{F}} = \dot{\gamma}_{\mathrm{bulk}}\tau_{\mathrm{F}}$.

Center channel (*bulk*) rheology

Here we investigate the center channel ('bulk') rheology. Figure 5.3a shows a snapshot of all primitive path conformations, folded in the simulation box at equilibrium. T chain primitive paths are all red whereas the primitive paths of F chains are all blue. Cyan spheres represent FF kinks whereas yellow spheres represent FT kinks. TT and TF kinks are not represented. At equilibrium there is a small number of T primitive paths which reach the center channel. However once the F chains have become moderately oriented by the flow (e.g. at $\mathrm{Wi}_{\mathrm{F}} = 16.25$: see Fig. 5.3b) all T chains (primitive paths) are completely located immediately at the surfaces. Generally the center channel consists almost exclusively of F chains under all flow conditions.

The end-to-end unit vector of a chain is denoted by $\hat{\boldsymbol{k}}$. We define an orientation order parameter depending on the α component of $\hat{\boldsymbol{k}}$, averaged over chains of species A $\in$ {F,T} with chain start bead at a distance y from the surface as:

$$S_{\alpha}^{\mathrm{A}}(y) = \left\langle P_2\left(\hat{k}_{\alpha}\right)\right\rangle_{y}^{\mathrm{A}} \tag{5.1}$$

Here $P_2(x) = (3x^2 - 1)/2$ is the second Legendre polynomial. S_{α}^{A} is bounded by 1, corresponding to perfect alignment, whereas $S_{\alpha}^{\mathrm{A}} = 0$ indicates isotropy. Figure 5.4 plots the orientation order parameter for the end-to-end unit vector of the F chains projected onto the flow direction, $S_{x}^{\mathrm{F}}(y)$, at different applied shear-rates. Overall only mild spatial

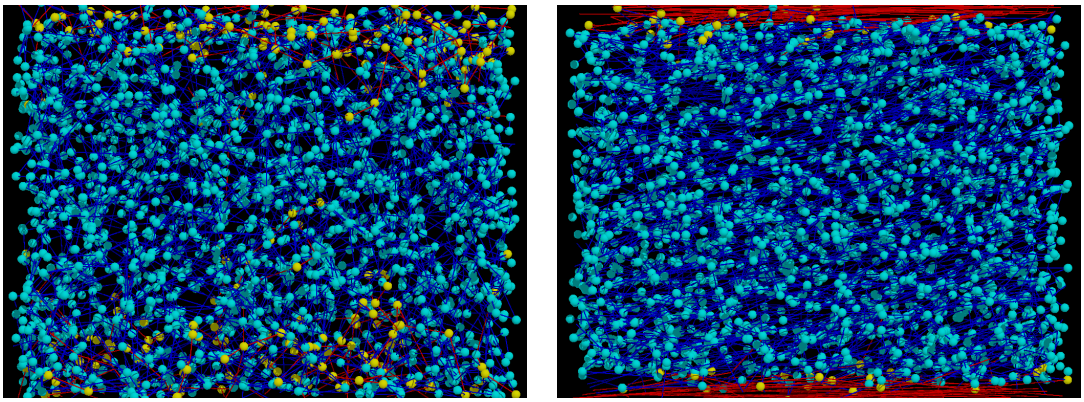

(a) Equilibrium (b) $\mathrm{Wi_T} = 100$, $\mathrm{Wi_F} = 16.25$

Figure 5.3: Snapshot of the complete set of folded primitive paths in the simulation box at **(a)** equilibrium; **(b)** $\dot{\gamma} = 10^{-4}{\tau_{\mathrm{LJ}}}^{-1}$ ($\mathrm{Wi_T} = 100, \mathrm{Wi_F} = 16.25$). Red lines: T chain primitive paths; blue lines: F chain primitive paths. Kinks in the primitive paths of F chains are indicated by spheres. Cyan spheres: kinks due to the proximity of another F chain (FF kinks); yellow spheres: kinks due to the proximity of a T chain (FT kinks).

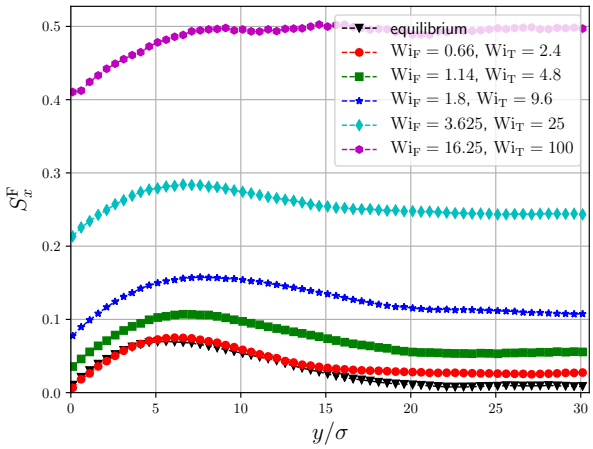

Figure 5.4: Flow orientation order parameter of F chains, eqn (5.1), as a function of the distance, $y \in [0, L_c/2]$, from the position of the chain start (an end) bead to the nearest wall. Different plots correspond to different flow conditions (see the legend).

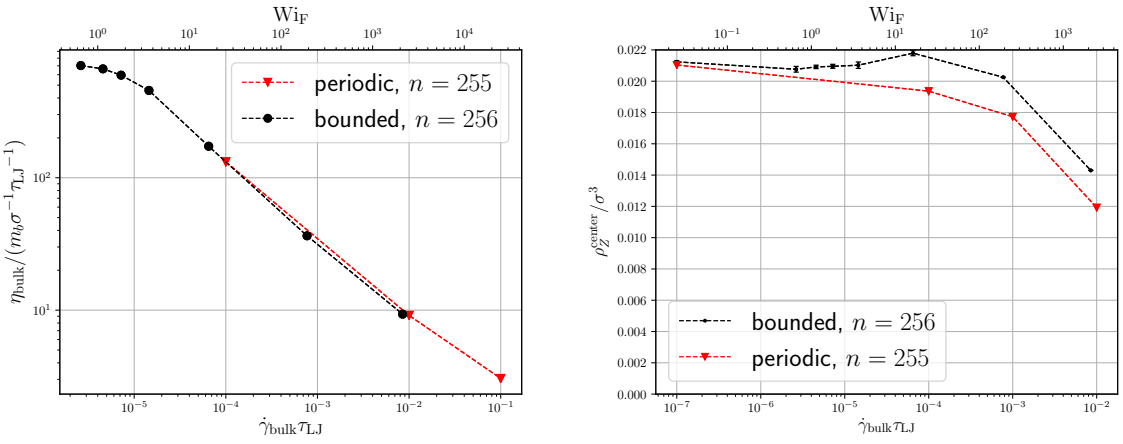

(a) (b)

Figure 5.5: **(a)** Channel center (black circles), and reference true bulk (red triangles), viscosity as a function of bulk shear-rate. Using the final four black points we determine the power law: $\eta_{\text{bulk}} \propto \dot{\gamma}_{\text{bulk}}^{-\mathcal{N}}$, with $\mathcal{N} = 0.61$ compared to $\mathcal{N} = 0.6$ in previous non-equilibrium MD investigations of the KG model using periodic boundaries [83]. The red data points correspond to a periodic (true bulk) simulation using the SLLOD algorithm [44] and an almost identical molecular weight ($n = 255$). **(b)** Kink density in the channel center (black circles with error bars - kinks are at least 25σ from the surface) and in reference true bulk (red triangles) as a function of bulk shear-rate. Note that the available densities at equilibrium are plotted at $\dot{\gamma}_{\text{bulk}} = 10^{-7}{\tau_{\text{LJ}}}^{-1}$.

dependence of $S_x^{\text{F}}(y)$ is observed; in equilibrium and at low shear-rates there is a weak wall-induced orientation over a distance of approximately $\langle {\boldsymbol{R}_{e,\text{bulk}}}^2 \rangle^{1/2}$. Figure 5.4 shows that the F chains only undergo moderate orientational ordering after the coil-stretch transition of T chains ($\text{Wi}_{\text{F}} \gtrapprox 1.8$, $\text{Wi}_{\text{T}} \gtrapprox 9.6$) (see Fig. 5.11a for the orientation order parameter of T chains). Despite this, at $\text{Wi}_{\text{F}} \gtrapprox 1$ there is already a non-negligible bulk shear-thinning which has an important influence on the degree of surface slip. The bulk shear-thinning acts against the effect of surface chain disentanglement with regard to surface slip. Figure 5.5a plots the bulk viscosity (defined from the shear-rate in the channel center as $\eta_{\text{bulk}} = \sigma_{xy}/\dot{\gamma}_{\text{bulk}}$) against the bulk shear-rate. The shear stress, σ_{xy}, is uniform across the channel and was found using the method of planes [160]. The monomeric velocity profiles are plotted in Fig. 5.6.

Figure 5.5a is consistent with existing data for the non-linear rheology of the KG model under periodic boundary conditions - as a comparison see Fig. 1a of Kröger and Hess [83] (the density is set slightly lower - $0.84\sigma^{-3}$ in the cited paper). Fitting a power-law relation

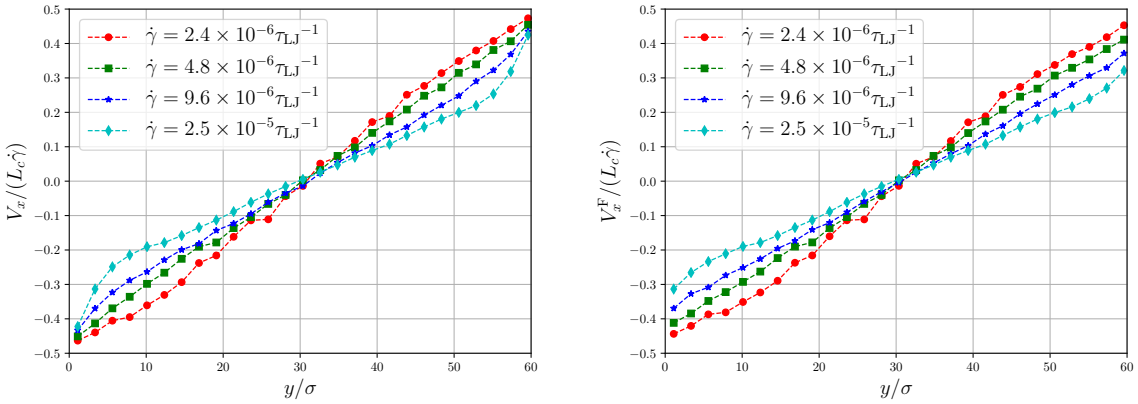

(a) (b)

Figure 5.6: Mean velocity profiles of **(a)** all monomers, V_x, and **(b)** only monomers forming F chains, V_x^{F}. The profiles give the mean velocity in the flow gradient direction normalized by the difference in the top and bottom plate velocities, $L_c\dot{\gamma}$, as a function of the monomer position within the channel, y. A selection of velocity profiles are included, corresponding to applied shear-rates which span the T chain coil-stretch transition.

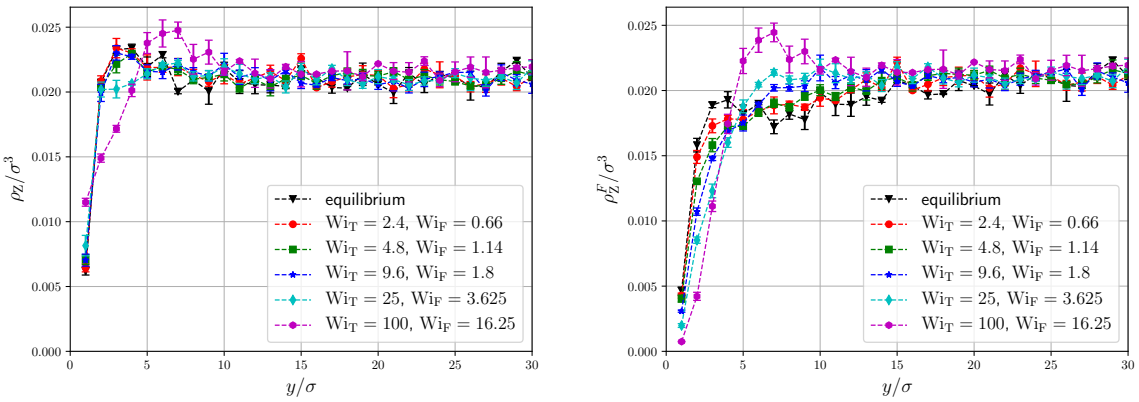

(a) (b)

Figure 5.7: **(a)** Channel density profile of all kinks, $\rho_Z(y)$. **(b)** Channel density profile of all kinks on F paths, $\rho_Z^{\mathrm{F}}(y)$.

$\eta_{\text{bulk}} \propto \dot{\gamma}_{\text{bulk}}^{-\mathcal{N}}$ using the largest four shear-rate data points available, determines an exponent $\mathcal{N} = 0.61$, in close agreement with the earlier study [83] using a true bulk system. It is noted that for $\dot{\gamma}_{\text{bulk}} \gtrsim 0.01{\tau_{\text{LJ}}}^{-1}$ the size of F chains in the flow direction can be greater than the box dimension which may lead to finite-size effects at such very fast deformation rates.

Next, we investigate 'entanglements' of F and T chains using the Z1 algorithm [76, 147] for the PPA analysis. The uppermost curve in Fig. 5.5b plots the spatial density of kinks in the channel center (only kinks at a distance greater than 25σ from the surface contribute), ρ_Z^{center}, as a function of bulk shear-rate. Figure 5.5b shows that the density of kinks drops by only approximately $5-10\%$ between $\dot{\gamma} \approx 1 \times 10^{-4}{\tau_{\text{LJ}}}^{-1}$ and $\dot{\gamma} \approx 1 \times 10^{-3}{\tau_{\text{LJ}}}^{-1}$ whilst the bulk viscosity has dropped by a factor of approximately $10^{-0.61} \approx 0.25$ (75% decrease). The kink data may be compared with an alternative atomistic model [12], which gives a drop in kink density of $\approx 20\%$ at only $\text{Wi}_{\text{F}} \approx 10$. The notable drop of ρ_Z^{center} in Fig. 5.5b occurs at a delay of an order of magnitude in Wi_{F} with respect to the atomistic model, despite a qualitative agreement in the shear-rate dependence of viscosity as a function of Wi_{F} between the models. From Fig. 5.4 we also see that in the channel center the F chain order parameter is $S_x^{\text{F}} \approx 0.5$ at $\text{Wi}_{\text{F}} = 16.25$ which matches very closely to the atomistic simulation at a similar Weissenberg number (see figure 7b of [12]). Channel profiles for the densities of (a) all kinks, $\rho_Z(y)$, and (b) only kinks on free chains, $\rho_Z^{\text{F}}(y)$, are plotted in Fig. 5.7. The profile of $\rho_Z(y)$ remains unchanged over the range of shear-rates characterizing the T chain coil-stretch transition.

The lack of a direct correlation between the viscosity and the number of kinks per chain at low Wi_{F} in the current simulation appears as a warning against generally correlating the number of kinks with viscosity away from equilibrium. It encourages further investigation into the general rheological significance of the number of kinks per chain away from equilibrium even for true bulk systems. We leave detailed considerations of the bulk case for future work, and in the following sections we instead concentrate on investigating more closely the qualitative changes in the characteristics of kinks involving F and T chains as a function of applied shear-rate. We can note at least that Fig. 5.14d shows that the kinks are only slightly more concentrated at the ends of F chains at $\text{Wi}_{\text{F}} = 16.25$ compared to

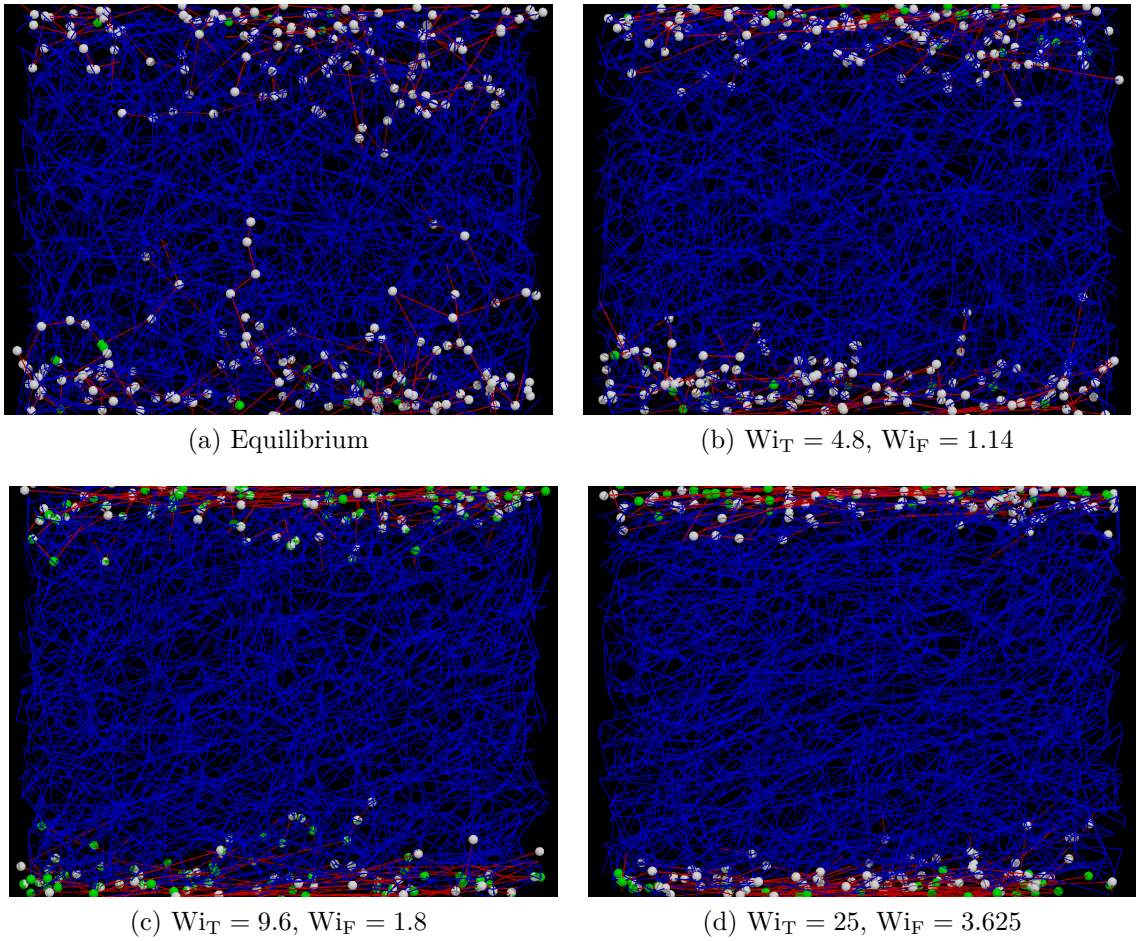

(a) Equilibrium

(b) $\mathrm{Wi_T} = 4.8$, $\mathrm{Wi_F} = 1.14$

(c) $\mathrm{Wi_T} = 9.6$, $\mathrm{Wi_F} = 1.8$

(d) $\mathrm{Wi_T} = 25$, $\mathrm{Wi_F} = 3.625$

Figure 5.8: Snapshots of the complete set of primitive paths in the simulation box, using steady state shear simulations over a range of (**a**)–(**d**) four different flow-rates characterizing the T chain coil-stretch transition. Red lines: T chain primitive paths; blue lines: F chain primitive paths. Kinks in the primitive paths of T chains are indicated by spheres. White spheres: kinks due to the proximity of F chains (TF kinks); green spheres: kinks due to the proximity of T chains (TT kinks).

at equilibrium; suggesting perhaps that the flow induced alignment of F chains is more important for bulk shear-thinning than this measure of topological interactions.

Interface region behavior

Figure 5.8 shows snapshots of all primitive path conformations in the simulation box, using a range of flow conditions characterizing the T chain coil-stretch transition. T chain primitive paths are red whereas the primitive paths of F chains are blue. Figure 5.9 plots the root mean square of the T chain end-to-end vector projected onto the flow

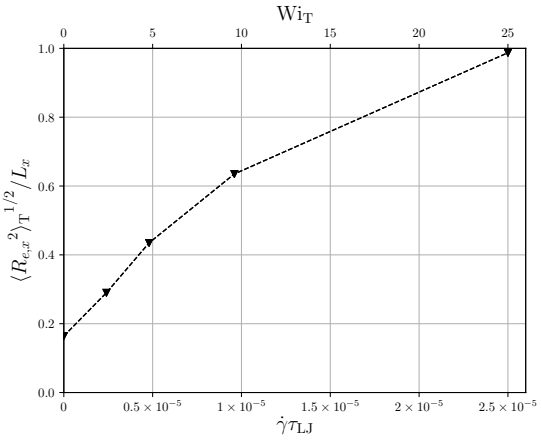

Figure 5.9: Root mean square of the end-to-end vector projected onto the flow direction for T chains, $\langle R_{e,x}^2 \rangle_\mathrm{T}^{1/2}/L_x$, normalized by the box length, L_x. Beyond an applied shear-rate of approximately $\dot{\gamma} = 2.5 \times 10^{-5} {\tau_\mathrm{LJ}}^{-1}$ ($\mathrm{Wi_T} = 25$) the size of T chains can be greater than the box length, meaning that finite-size effects may eventually occur.

direction, at different applied shear-rates. At shear-rates greater than approximately $\dot{\gamma} = 2.5 \times 10^{-5} {\tau_\mathrm{LJ}}^{-1}$ (Fig. 5.8) the T chains are so strongly deformed that it is possible for them to directly interact with their mirror images. As a result there may be some finite-size effects in the surface region behavior at such rates. The box dimension was chosen to avoid such issues at the most relevant range of shear-rates that characterize the coil-stretch transition. Figure 5.10 plots the shear-rate dependence of the mean numbers of kinks, (i) in a T chain primitive path due to the proximity of a F chain, $\langle Z_\mathrm{TF} \rangle$; (ii) in a F chain primitive path due to the proximity of a T chain, $\langle Z_\mathrm{FT} \rangle$; (iii) in T due to T, $\langle Z_\mathrm{TT} \rangle$; and (iv) in F due to F, $\langle Z_\mathrm{FF} \rangle$. At equilibrium, $\langle Z_\mathrm{TF} \rangle + \langle Z_\mathrm{TT} \rangle \approx \langle Z_\mathrm{FT} \rangle + \langle Z_\mathrm{FF} \rangle$: the mean number of kinks in T chains is almost identical to that of F chains.

In Fig. 5.11a three orientation order parameters (S_α^T, $\alpha = x, y, z$) for the corresponding components of the end-to-end unit vector of the T chains are plotted as a function of applied shear-rate. We defined S_α^T already in eqn (5.1). The chain alignment in the flow direction is already characterized by orientation parameter $S_x^\mathrm{T} \approx 0.9$ at $\mathrm{Wi_F} = 1.8$ ($\mathrm{Wi_T} = 9.6$), so that the T chain flow alignment occurs before any strong deformation of F chains. Fig. 5.10 shows that $\langle Z_\mathrm{TF} \rangle$ and $\langle Z_\mathrm{FT} \rangle$ begin to decrease as soon as the T chain begins to orient. $\langle Z_\mathrm{TT} \rangle$ initially begins to increase and then stagnates beyond the coil-stretch transition. Figure 5.12a plots the corresponding bead density profiles for the T chain

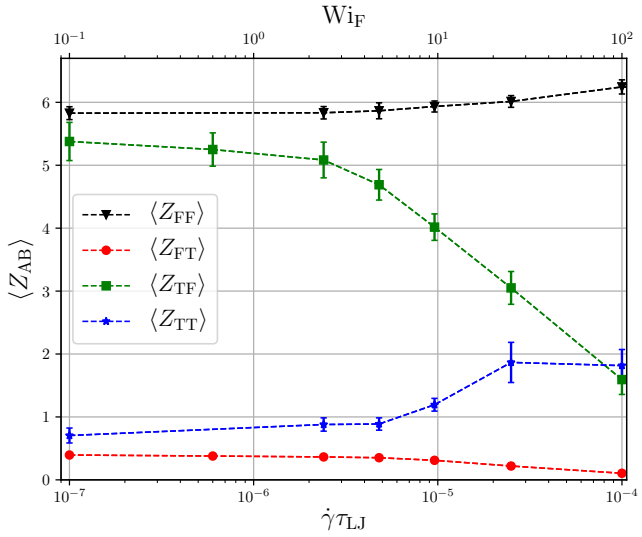

Figure 5.10: Mean number of different types of kinks existing on a T or F chain primitive path as a function of applied shear-rate. $\langle Z_{AB} \rangle$ stands for mean the number of kinks on A chains due to the proximity of a B chain, averaged over all A chains in the channel.

species, which may be compared with recent experimental results for the same observable [30]. The transition from isotropy to flow alignment (coil-stretch transition) takes place over a much more narrow range of shear-rates for the T chains compared to the F chains (Fig. 5.4), but it does not coincide with any sudden large drop in the number of kinks involving F and T chains which would be expected for complete interfacial disentanglement as assumed in the earliest scaling model [19]. For the interfacial disentanglement, the early scaling models emphasized the importance of the surface normal component of the T chain dimension rather than the angle of the end-to-end vector with respect to the surface. Figure 5.11b plots the root mean square of the end-to-end vector projected onto directions normal to the flow. For the largest shear-rates considered, the root mean square of the end-to-end vector projected in the surface normal direction is similar to the root mean square of the end-to-end vector of a bulk segment with entanglement bond number, N_e, at equilibrium (taking for example 8σ as a modest estimate for the root mean square of the entanglement segment end-to-end vector corresponding to $N_e \approx 40$ [64, 99]). Therefore we are clearly within the scaling regime for surface disentanglement of Brochard and De Gennes. The gradual drop in TF kinks (surface 'disentanglement') apparent in Fig. 5.10 is consistent with the assumptions of the more detailed scaling models [5, 6, 114].

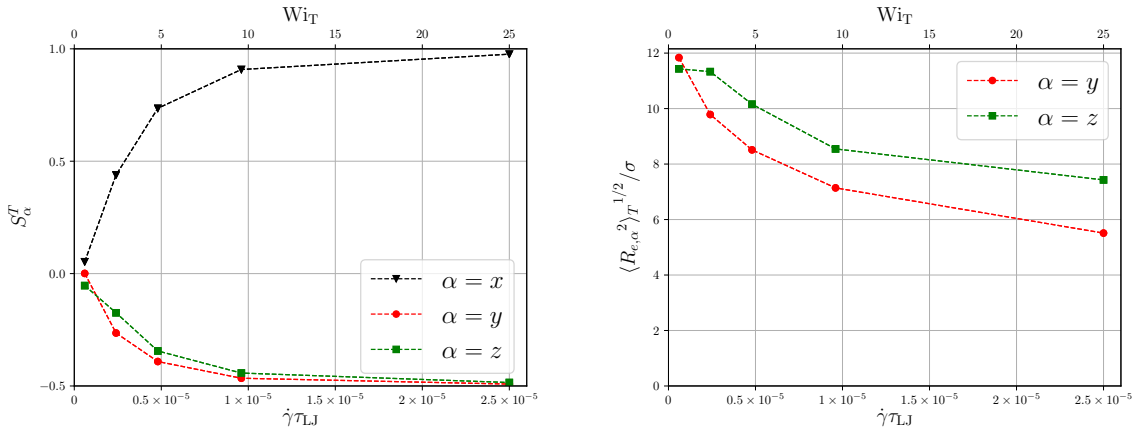

(a) (b)

Figure 5.11: (**a**) Directional orientation order parameters of the end-to-end unit vector of T chains, S_α^{T}, versus applied shear-rate; (**b**) Root mean square of components of the end-to-end vectors of T chains normal to the velocity field, i.e., in flow gradient $\hat{\mathbf{y}}$ and vorticity $\hat{\mathbf{z}}$ directions, versus applied shear-rate.

Figure 5.13 plots the root mean square of the components of end-to-end vectors of T chain sub-segments comprising $\Delta\ell = 32$ bonds, as a function of the index ℓ of the first monomer in the sub-segment. From Fig. 5.13a we see that the stretching of the T chains leads to trumpet like conformations, as predicted by Ajdari et al. [5]. Following this observation it is natural to ask whether this anisotropic degree of deformation corresponds with a non-uniform occupational density of kinks along the T chain primitive path contour. To address this question first we must define a contour parameter for the primitive path.

Kink densities as a function of the primitive path contour variable

At the beginning of the Z1 algorithm [84, 76, 147], kinks are located at the positions of the interior chain beads. Together with the two 'ghost nodes' occupying the end bead positions, which remain fixed in space and conserved throughout the algorithm, the kinks are more generally 'nodes'. At the beginning of the algorithm there are then $n+1$ nodes and $n-1$ kinks in each primitive path. Each node is initially assigned a contour label, given by the index of the bead that coincides with the node. As the algorithm progresses many nodes disappear as the chain contour length is reduced. When nodes are displaced

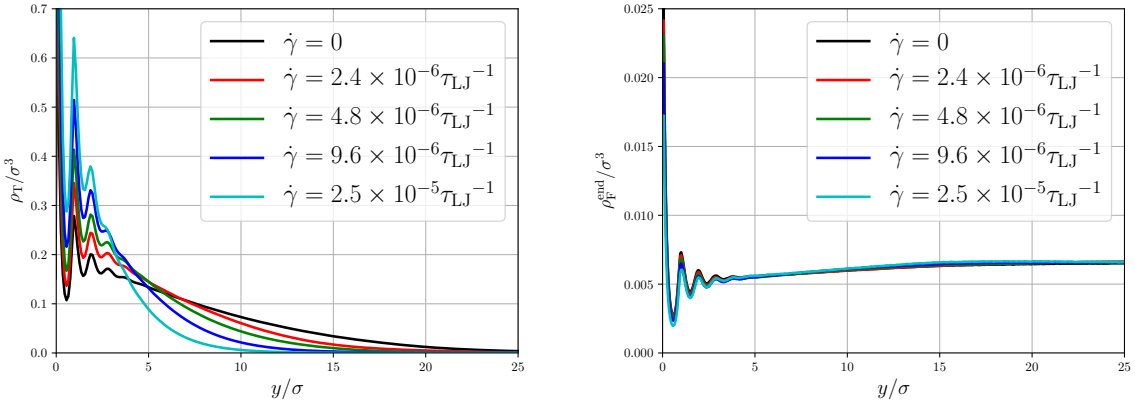

(a) (b)

Figure 5.12: (**a**) Tethered bead number density, $\rho_T(y)$; (**b**) Number density of end beads of F chains, $\rho_F^{end}(y)$. Both observables are given as a function of the distance to the surface, y, at different applied shear-rates spanning the T chain coil-stretch transition.

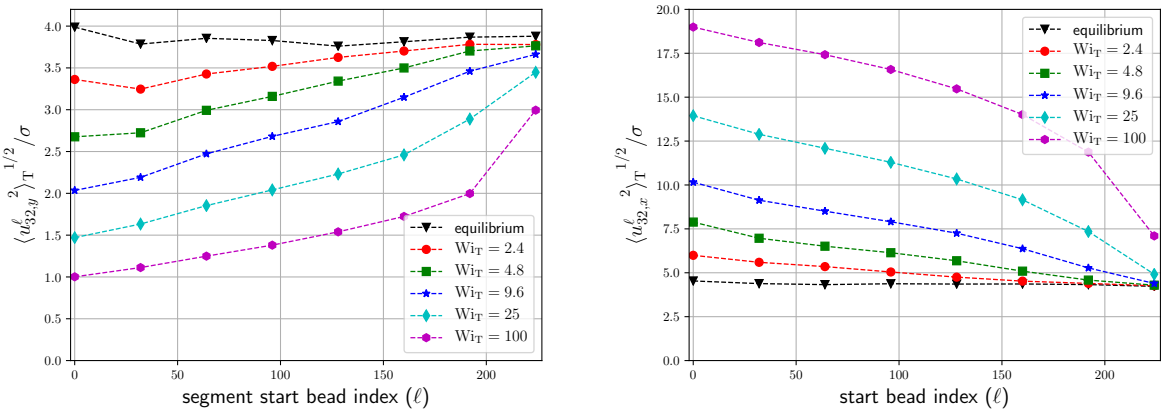

(a) (b)

Figure 5.13: Root mean square of components of the end-to-end vector of sub-segments comprising $\Delta\ell = 32$ bonds in the T chain, as a function of the index ℓ of the first monomer in the sub-segment. The grafted sub-segment starts at monomer $\ell = 0$ and the final sub-segment starts at monomer $\ell = n - \Delta l = 224$. Data shown for several applied shear-rates.

in space they keep the contour label that they were initially assigned. When a primitive path is shortened, new nodes may be created on the chain contour (see Ref. [84]). If a new node is created such that it becomes the jth node along the chain contour, then it is assigned a contour label, ℓ_j, intermediate between ℓ_{j-1} and ℓ_{j+1}:

$$\ell_j = \ell_{j-1} + (\ell_{j+1} - \ell_{j-1}) \frac{|\boldsymbol{s}_j - \boldsymbol{s}_{j-1}|}{|\boldsymbol{s}_{j+1} - \boldsymbol{s}_j| + |\boldsymbol{s}_j - \boldsymbol{s}_{j-1}|} \tag{5.2}$$

where $\boldsymbol{s}_j$ is the jth node position in space. Note that this means that ℓ_j is not necessarily an integer. When the Z1 algorithm is finished the final set of *kink* contour labels, $\{\ell^Z\}\backslash\{\ell_0, \ell_{Z+1}\}$, in each chain is recorded. Here Z is the final number of kinks in a primitive path. Note that the ghost node contour labels, $\{\ell_0 = 0, \ell_{Z+1} = n\}$, are excluded from the set of kinks. We can examine the progressive drop in the mean number density of kinks along the primitive paths using the sets of contour labels. A contour label is bounded by the start and end values the contour variable may take: $0 \leq \ell \leq n$. It may be located on a F or T chain, and to prevent any confusion we occasionally use ℓ_{F} and ℓ_{T} for contour positions on T and F chains, respectively. We are interested in exploring the possibility of correlations between the density of kinks at different values of the contour variable, the real chain orientations, and the corresponding flow behavior. We note that alternative parameterizations of the primitive path contour are possible, and it would be desirable to examine whether such alternatives give similar qualitative results for kink occupational densities. The most easily accessible alternate definition is the arc length of the primitive path considered as a polygon in space, where the information about original beads is completely ignored.

Entanglements are frequently interpreted as binary interactions between different chains [117]. Kinks in the network of primitive paths do not always fit this picture: it is possible that a kink occurs in a primitive path due to the proximity of a straight part of another primitive path, although it is also possible that a kink on one path can be associated with a corresponding kink on another path. The total number of kinks on all F primitive paths in the system that are due to T paths is $N_{\mathrm{F}}\langle Z_{\mathrm{FT}}\rangle = N_{\mathrm{F}} \int_0^n d\ell_{\mathrm{F}} \, \langle z_{\mathrm{FT}}(\ell_{\mathrm{F}})\rangle$. Here $\langle z_{\mathrm{FT}}(\ell_{\mathrm{F}})\rangle$ is an occupational density of kinks around contour position ℓ_{F} in a F chain primitive path

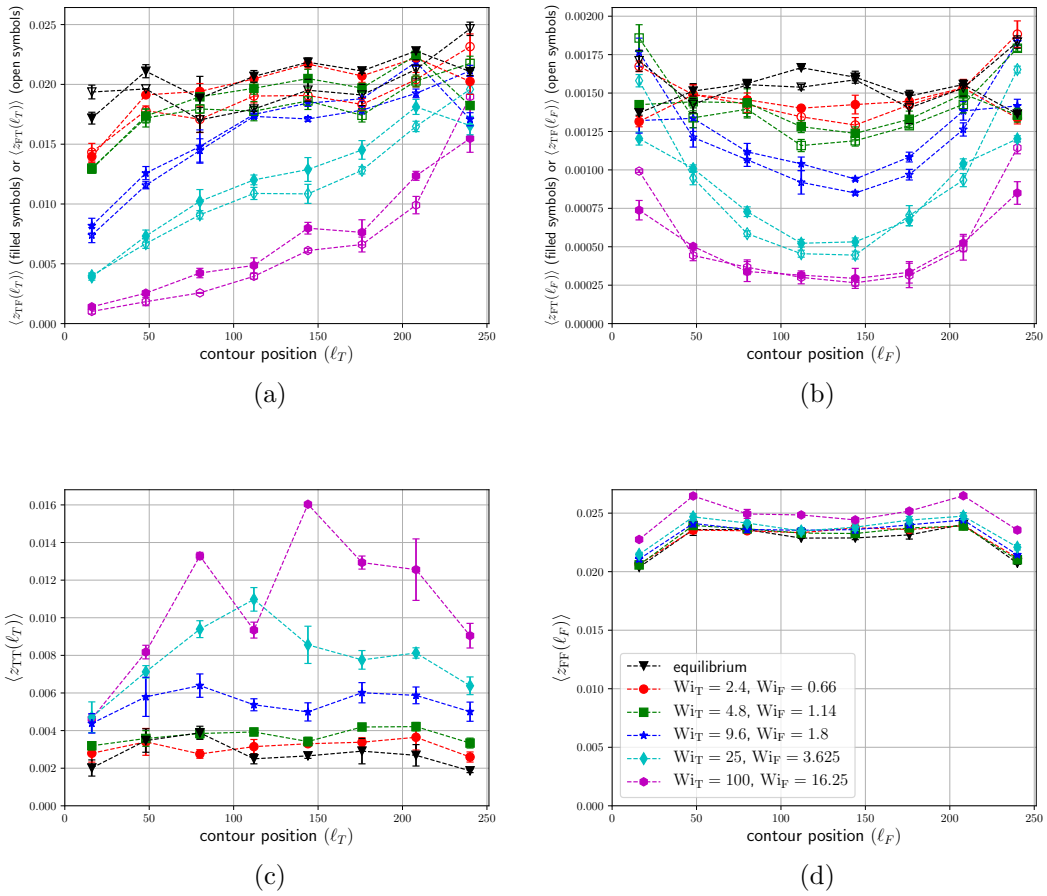

Figure 5.14: Mean local occupational densities of kinks $\langle z_{\mathrm{AB}}(\ell)\rangle$ for all possible combinations A,B $\in$ {F,T} and $\ell \in \{\ell_{\mathrm{F}}, \ell_{\mathrm{T}}\}$ along primitive path contours, averaged over primitive path segments with size $\Delta\ell = 32$ (to avoid a certain noise level). Different symbols (and colors) correspond to different applied shear-rates, specified in (d). While $\langle z_{\mathrm{AB}}(\ell_{\mathrm{A}})\rangle$ characterizes the amount of kinks on contour location ℓ_{A} on A due to the presence of B, $\langle z_{\mathrm{AB}}(\ell_{\mathrm{B}})\rangle$ characterizes the amount of kinks on A due to the presence of contour location ℓ_{B} on B. **(a)** Entanglements on T chains due to F chains, $\langle z_{\mathrm{TF}}(\ell_{\mathrm{T}})\rangle$ (filled symbols), in comparison with $\langle z_{\mathrm{FT}}(\ell_{\mathrm{T}})\rangle$ (open symbols). These two densities would perfectly agree with each other for strictly binary contacts made of two kinks on different chains. **(b)** Entanglements on F chains due to T chains: $\langle z_{\mathrm{FT}}(\ell_{\mathrm{F}})\rangle$ in comparison with $\langle z_{\mathrm{TF}}(\ell_{\mathrm{F}})\rangle$. **(c)** Entanglements on T chains due to T chains: $\langle z_{\mathrm{TT}}(\ell_{\mathrm{T}})\rangle$, and **(d)** as (c) for F chains.

due to the proximity of part of a T chain primitive path. Upon analyzing the shortest path network resulting from Z1, we associate each kink with a unique contour variable label for the part of a secondary primitive path whose proximity led to the kink, whether or not this contour label corresponds to the position of a kink. We define $\langle z_{\mathrm{FT}}(\ell_{\mathrm{T}})\rangle$ as an occupational density of instances in which the proximity of a T path at contour variable around ℓ_{T}, to a F chain path, resulted in a kink on the F chain path. Since for every FT kink (on F due to T) there is a corresponding T path whose proximity caused the kink we have: $N_{\mathrm{F}}\langle Z_{\mathrm{FT}}\rangle = N_{\mathrm{F}}\int d\ell_{\mathrm{F}}\,\langle z_{\mathrm{FT}}(\ell_{\mathrm{F}})\rangle = N_{\mathrm{T}}\int d\ell_{\mathrm{T}}\,\langle z_{\mathrm{FT}}(\ell_{\mathrm{T}})\rangle$. We also define $\langle z_{\mathrm{TF}}(\ell_{\mathrm{T}})\rangle$ as an occupational density of kinks around contour position ℓ_{T} in a T chain primitive path due to the proximity of part of a F chain primitive path. This density satisfies $\int d\ell_{\mathrm{T}}\,\langle z_{\mathrm{TF}}(\ell_{\mathrm{T}})\rangle = \langle Z_{\mathrm{TF}}\rangle$. We plot $\langle z_{\mathrm{TF}}(\ell_{\mathrm{T}})\rangle$ and $\langle z_{\mathrm{FT}}(\ell_{\mathrm{T}})\rangle$ in Fig. 5.14a, which shows that they both have very similar density profiles at all shear-rates, in agreement with a binary picture of entanglements. Note however that in general $\langle z_{\mathrm{FT}}(\ell_{\mathrm{T}})\rangle$ is larger than $\langle z_{\mathrm{TF}}(\ell_{\mathrm{T}})\rangle$ near to the F ends of primitive paths.

At equilibrium, Fig. 5.14a shows that the density of TF kinks is close to uniform along the contour, with only a small drop near the T end (the contour variable corresponding to the tethered end is $\ell = 0$). Kinks are no longer distributed equally along the contour of T chains under (strong enough) shear. The contour positions from which kinks due to F chains are lost from T paths under shear, with respect to at equilibrium, correlate with the contour positions of the T chain sub-segments which have a decreased size normal to the surface (see Fig. 5.13a). However it does not appear clear from this data whether the drop in kinks is only a function of chain segment orientation or whether it also depends on the position of the segment relative to the surface; i.e. would the situation change for a T chain pulled through a melt far from the surface? Figure 5.15 plots the mean surface normal position of the ℓth bead of T chains.

Figure 5.14b plots the contour occupational densities of kinks along the primitive path of F chains that are due to the proximity of a T chain, $\langle z_{\mathrm{FT}}(\ell_{\mathrm{F}})\rangle$, at different applied shear-rates. We find that as the T chain aligns with the surface there is an increasing relative probability of forming a kink near the end of a nearby F chain with respect to forming one near the center of the F chain. The end bead density profile of F chains, plotted

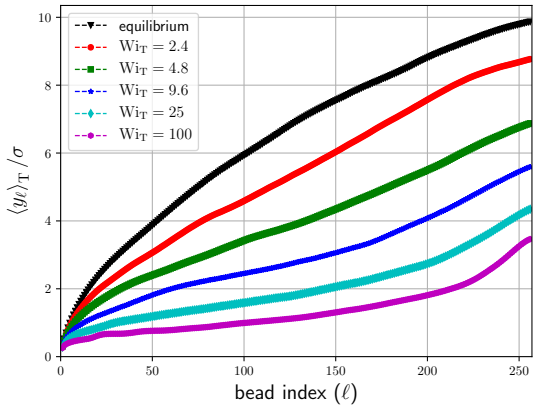

Figure 5.15: Mean surface normal position, $\langle y_\ell \rangle_\mathrm{T}/\sigma$, of the ℓth bead of T chains at different applied shear-rates.

in Fig. 5.12b, is found to be approximately independent of shear-rate: the distribution of chain ends is largely unchanged with respect to at equilibrium for all shear-rates of interest. An excess of end beads within a monomer size from the surface, followed by a corresponding depletion until a distance of approximately the molecular size from the surface, has been theoretically predicted by Matsen and Mahmoudi [108], using a system completely made up of F chains. We find that this characterizes the end density plot well (Fig. 5.12b), although it is difficult to immediately discern the excess at the surface from the plots due to the oscillations in bead density. It can be immediately verified that the mean end bead density of F chains within a molecular distance from the surface, $\langle \boldsymbol{R}_{e,\mathrm{bulk}}{}^2 \rangle^{1/2} \approx 17.5\sigma$, approximately matches the channel center value: the excess and depletion cancel one another. It is expected that an excess in the end segment density of F chains at the surface will lead to an enhanced constraint release rate of F chains acting on T chains as the T chain becomes aligned against the surface.

Figure 5.14d plots the contour occupational density of kinks on F paths due to other F paths averaged over the whole channel, $\langle z_\mathrm{FF}(\ell_\mathrm{F}) \rangle$. The integral of this quantity over the complete contour satisfies $\int d\ell \, \langle z_\mathrm{FF}(\ell_\mathrm{F}) \rangle = \langle Z_\mathrm{FF} \rangle$. Unlike FT kinks (Fig. 5.14b), there is little difference in the contour density profiles for FF kinks over the range of shear-rates characterizing the T chain coil-stretch transition. Figure 5.14c plots the contour occupational density of kinks on T paths due to other T paths, $\langle z_\mathrm{TT}(\ell_\mathrm{T}) \rangle$. At equilibrium

$\langle z_{\mathrm{TT}}(\ell_{\mathrm{T}})\rangle$ is roughly uniform across the path contour. At shear-rates beyond the coil-stretch transition the profile becomes increasingly non uniform.

A uniform density of entanglements along the chain contour is frequently assumed in theoretical models [94] even away from equilibrium [56, 158]. Our results in this section suggest that this assumption is incorrect for the entangled interfacial chains if we directly associate primitive path kinks with entanglements. Figure 5.14d indicates that this assumption is more appropriate for FF kinks, although preliminary results at faster rates indicates some decrease in kink density in the contour center for F chains. This may be the first time that the density of primitive path kinks as a function of contour position has been investigated for a system of linear KG chains, although a contour density plot of an alternative measure of entanglements has been given by Likhtman and Ponmurugan at equilibrium [100], which is qualitatively similar to Fig. 5.14d. Recently the kink density along the primitive paths of lamellae forming block copolymers has also been investigated [135].

Slip length and surface friction

A common measure of the amount of slip of fluid flow past a confining wall is the 'slip length', which is usually defined as [104, 19] (Fig. 5.1)

$$L_{\mathrm{slip}} = \frac{V_s}{\dot{\gamma}_{\mathrm{bulk}}} \tag{5.3}$$

where V_s is the 'slip velocity'. In the context of transport theory, the slip velocity is used as a boundary condition for fluid flow and denotes the (extrapolated) fluid velocity at the (effective) wall. For the present case of a polymer melt bounded by a surface with polymers grafted to it, the precise location of such an effective wall is not clear. In addition, different definitions of V_s and $\dot{\gamma}_{\mathrm{bulk}}$ have been suggested in the literature which focus more on the dynamics near the wall [104, 132]. We will later investigate eqn (5.3) using different definitions for V_s, but $\dot{\gamma}_{\mathrm{bulk}}$ is fixed throughout this work. It is calculated from fitting a straight line to the velocity profile in the channel center (c.f. Figs. 5.1 and 5.6).

At low Reynolds numbers, the planar Couette geometry enforces a balance of shear

stresses in the channel: $V_s\xi_s = \dot{\gamma}_{\text{bulk}}\eta_{\text{bulk}}$, where ξ_s is a surface friction coefficient and the bulk viscosity, η_{bulk}, is given in Fig. 5.5a. We may define the surface friction coefficient from information extracted from the simulation via

$$\xi_s = \eta_{\text{bulk}}/L_{\text{slip}} \tag{5.4}$$

At this point we can consider how the interpretation of ξ_s depends on our definition of V_s. If the friction force, $V_s\xi_s$, acts between the permanently grafted T chains and the F chains, one choice is to define V_s from the F chain monomeric velocity profile, Fig. 5.6b, using the data point closest to the surface. We denote this F monomer slip velocity by V_s^{F}. The slip length found using eqn (5.3) with $V_s = V_s^{\text{F}}$ is plotted in Fig. 5.16b (red circles).

For other systems with only partially adsorbing surfaces (different from the current case), it is clear that chain desorption may influence the surface friction far from equilibrium. In such a case it would seem more natural that the slip velocity is defined from the velocity profile of all monomers, Fig. 5.6b. We denote such a total monomer slip velocity by V_s^{all}. Experimentally this is naturally how the slip velocity is defined [115, 104, 61]. The slip length defined using eqn (5.3) with $V_s = V_s^{\text{all}}$ is plotted in Fig. 5.16b (green squares). For shear-rates spanning the coil-stretch transition ($\text{Wi}_{\text{T}} < 25$), the slip length found using V_s^{all} increases at a weaker rate compared to the slip length found using V_s^{F}. This is unsurprising since with increasing shear-rate the monomers that are located immediately at the surface are progressively more likely to be part of a T chain, travelling at the surface velocity. For the current case of a simulation using reflective surfaces and permanently grafted T chains this choice for the slip velocity seems inappropriate.

So far we have considered two definitions of the slip velocity, V_s^{F} and V_s^{all}; the first may be judged more appropriate for non-adsorbing surfaces with permanently grafted T chains, and the second more appropriate for partially adsorbing surfaces. A possible criticism of both choices is that they depend only on information of the fluid locally at the surface, even though it could be argued that the surface friction force acts via the adsorbed chains which are extended objects in space. Considering the permanently grafted case, T chains are extended from the surface but move with the surface velocity. We could then

interpret the T chains as part of the 'wall', so that the 'wall' extends beyond the surface. How then is it appropriate to define the slip velocity via the fluid velocity immediately at the surface when the 'wall' is an object which extends beyond this point? Certainly we may observe that at the very lowest shear-rate in Fig. 5.6, deviations from the channel center linear velocity profile extend until approximately a molecular size from the surface. This consideration suggests an alternative definition for a slip velocity immediately at the surface, using an extrapolation of the velocity profile from the channel center:

$$V_s^{\text{extrap}} = \frac{L_c}{2}(\dot{\gamma} - \dot{\gamma}_{\text{bulk}}) \tag{5.5}$$

In this case the slip length, eqn (5.3), becomes

$$L_{\text{slip}}^{\text{extrap}} = \frac{L_c}{2}\left(\frac{\dot{\gamma}}{\dot{\gamma}_{\text{bulk}}} - 1\right) \tag{5.6}$$

The black triangles in Fig. 5.16b correspond to this definition of the slip length. It gives very similar values during the coil stretch transition to the definition which uses V_s^{F}. However at the lowest shear-rates it drops more rapidly and becomes negative, since the extrapolated velocity reaches zero inside the fluid. In Fig. 5.16a the ratio $\dot{\gamma}_{\text{bulk}}/\dot{\gamma}$ that is used in eqn (5.6) is plotted as a function of applied shear-rate. For all three definitions of the slip length, as the T chain orients the slip length increases before the bulk shear-thinning regime is entered whereupon the slip length decreases.

Using eqn (5.4) three different friction coefficients can be found from the three definitions of slip velocity (slip length) that we have considered. The idea that any of the three can be interpreted unambiguously as a surface friction is highly questionable. Bearing this warning in mind we choose to comment only on the qualitative correlations between the friction coefficients and the state of the fluid under different flow conditions. The three definitions of the surface friction, corresponding to the three definitions of slip length (Fig. 5.16b) are plotted in Fig. 5.16c as a function of applied shear-rate. The most rapid drop in surface friction universally occurs before $\dot{\gamma} = 9.6 \times 10^{-6}\tau_{\text{LJ}}$, during the coil-stretch transition, at the beginning of the drop in TF kinks (Fig. 5.10). Figure 5.14 shows that, although only a relatively small proportion of the TF kinks are lost by $\dot{\gamma} = 9.6 \times 10^{-6}\tau_{\text{LJ}}$,

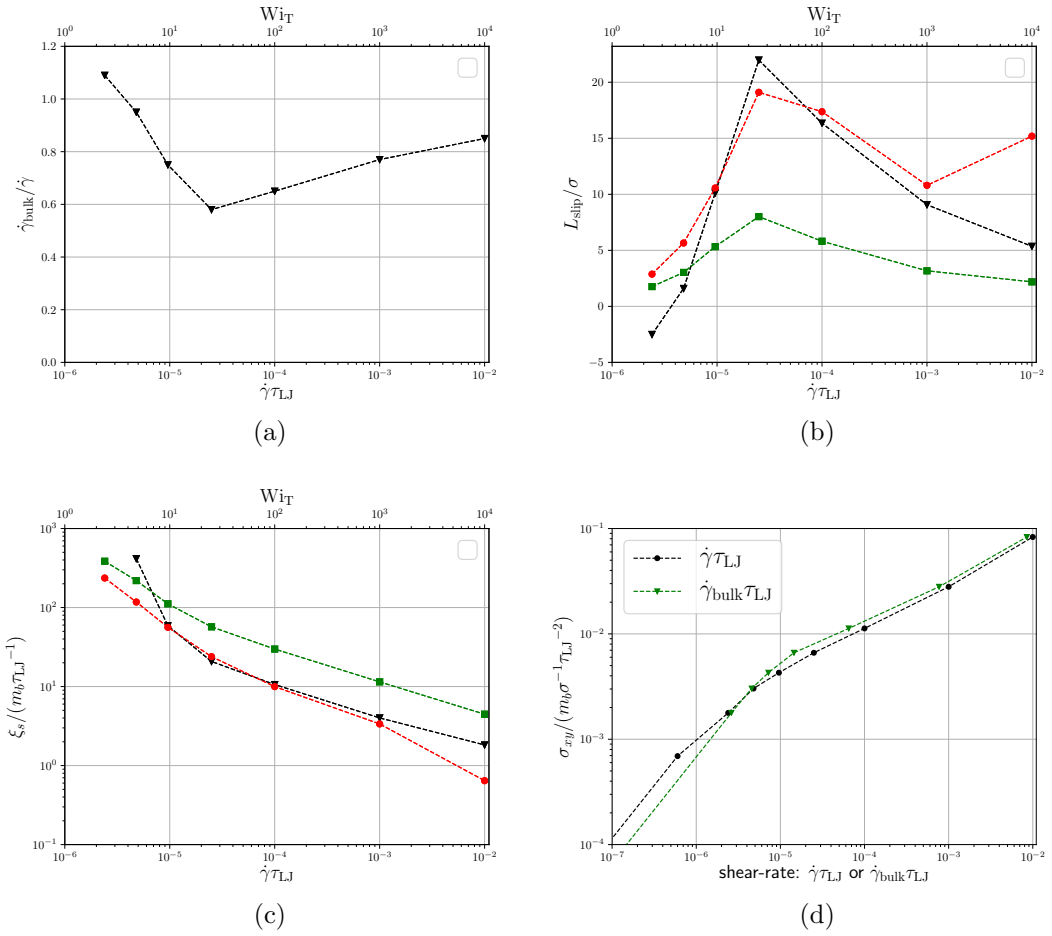

Figure 5.16: Various functions of applied shear-rate: **(a)** Ratio of shear-rates: $\dot{\gamma}_{\text{bulk}}/\dot{\gamma}$. **(b)** Slip length: Red circles: $L_{\text{slip}} = V_s^{\text{F}}/\dot{\gamma}_{\text{bulk}}$, where V_s^{F} is found from the F monomer velocity profile at the surface, Fig. 5.6b. Green squares: $L_{\text{slip}} = V_s^{\text{all}}/\dot{\gamma}_{\text{bulk}}$, where V_s^{all} is found from the total monomer velocity profile at the surface, Fig. 5.6a. Black triangles: slip length extrapolated from the center channel velocity profile, eqn (5.6). **(c)** Surface friction found from eqn (5.4), using the three different definitions of the slip length in **(b)** (and the same color/marker code). **(d)** Film flow curves: shear stress plotted against either the applied or bulk shear-rate.

those which are lost were almost exclusively located in the half of the T contour closest to the T end, or the center contour for the case of F chains. The friction defined using the extrapolated slip velocity, eqn (5.5), fails strongly in its interpretation as a surface friction at the lowest shear-rate ($\dot{\gamma} = 2.4 \times 10^{-6}\tau_{\mathrm{LJ}}$). At this shear-rate the friction coefficient is negative since the extrapolated velocity at the surface is greater than the wall velocity. Finally Fig. 5.16d shows that the effects of bulk shear thinning and surface slip are too weak to lead to a non-monotonic flow curve, so that at this chain length stable dynamical behavior is expected across the film. In Fig. 5.16d the black circles correspond to the experimentally observable flow curve, whereas green triangles corresponds to the flow curve in terms of the bulk shear-rate. The two plots are quite similar because the degree of slip is relatively small.

5. Conclusion

We have performed non-equilibrium shear flow simulations of a mildly entangled polymer melt which have both tested existing ideas regarding surface disentanglement and revealed new phenomena. If the number of kinks in primitive paths is in some way correlated with the number of 'entanglements' (even away from equilibrium), the simulations validate the idea of a surface disentanglement resulting from the coil-stretch transition of T chains.

In addition to a quantitative drop in TF kinks during the coil-stretch transition of T chains, Fig. 5.14a suggests the possibility of a drop in the rheological significance of TF kinks, due to the increased relative probability that kinks in T primitive paths that are due to the close proximity of F paths have a contour position near the free end of the T path following surface alignment. This effect has been postulated already [5]. We also identified a new mechanism that may also reduce the rheological significance of TF kinks, resulting from the higher density of F chain end segments in the immediate proximity of the surface (Fig. 5.12b). Following the coil-stretch transition, the end segment excess correlates with an increased relative occupational density of F chain primitive path kinks, that are due to the proximity of a T primitive path, near contour ends (Fig. 5.14b). This may lead to a faster F chain constraint release rate acting on the T chains.

Different definitions of a dynamic surface friction, $\xi_s(\dot{\gamma})$, were investigated. In all cases the surface friction decreases most rapidly during the coil-stretch transition (see Fig. 5.16c), even though, as seen in Fig. 5.10, the actual drop in TF kinks over this shear-rate range is quite low. However such kinks that are lost may be highly rheologically significant for reasons we discussed in detail. We find that in the non-linear flow regime the density of kinks does not necessarily correlate with dynamic viscosity in the bulk. It would be interesting to investigate the behavior of dynamic definitions of entanglements [100, 99] away from equilibrium, and their relation to primitive path kinks, even for true bulk chains. At equilibrium, the survival probability of 'long lived close contacts' has been demonstrated to be proportional to the linear stress relaxation function [23]. However such dynamic measures of entanglements are computationally expensive to investigate for non-equilibrium cases.

A marginal regime in which the fluid stress does not increase with increasing applied shear-rate is not observed here. This might be due to the relatively weakly entangled chain length. However the same mechanisms leading to slip that we have identified here may remain relevant for polymer melts of much higher (and more experimentally relevant) molecular weights. The conclusions made here may therefore be used in the future to inform theoretical models for surface rheology.

Chapter 6

Thesis conclusions and outlook

This thesis has closely examined the behaviour of simple multi-chain Molecular Dynamics models of a polymer melt confined in a channel. A particular effort has been made to examine the robustness of the behaviour of such confined films with respect to changes in surface structure and the time-scale over which momentum is conserved during the simulation (chapter 3). In addition, probing the effects of changing the monomer density would be a further important test that could be made in the future. The monomer density used in this thesis, $\rho \approx 0.85\sigma^{-3}$, was primarily chosen for the reason that it is the most commonly used value in the literature. In the seminal 1990 Kremer-Grest paper reasons of a practical nature are given for this choice [81]:

From these preliminary studies for small N, we determined that $\rho = 0.85$ was an appropriate density to work at. We wanted to work at high density so the tube diameter would be small, yet we needed to have reasonable relaxation times for chains which would allow us to equilibrate the system in a few million time-steps. This turned out to be $\rho = 0.85$.

However it has been suggested that the KG MD model is most realistic using a higher monomer density of $\rho \approx 1.15\sigma^{-3}$ [101]:

'*One can now ask the question: which simulation density corresponds to the usual polymer melts such as polystyrene, polyisoprene or polybutadiene? It is germane to note that for all these polymers experimental G' and G'' always cross each other at ω_{cross} around $1/\tau_e$, and G'' exceeds G' at frequency $10\omega_{cross}$ by a factor between 1.9 and 2.15 (e.g., $tan\delta(\omega_{cross})-2$).*

However, the storage and loss moduli from the standard Kremer-Grest model (Figure 4) do not cross each other and go parallel with a slope around $1/2$*. This behavior does not change significantly for stiffer chains (see next section). The only way to rectify this is to increase the density. In fact, the system with the density* $\rho = 1.15$ *produces a shape of* G' *and* G'' *very similar to the experimental one. However, it is more expensive to simulate.*'

If we were to investigate such a higher density it is feasible that the dynamic behaviour on the time-scales of interest would become yet more strongly dependent upon the particular choice of surface structure. More generally, the physical relevance of the confined Kremer-Grest model examined in this thesis can only be confirmed via further comparison with more detailed simulation and experiment: the conclusions of this thesis are limited to the extent that our 'fundamental' model is a realistic choice. Nevertheless, we have built a reasonable understanding of the particular KG MD model that we considered:

Chapter 2 began by investigating the single-chain dynamics of low-molecular weight non-entangled melts. It was found that the Rouse model description of mean single-chain bulk dynamics could be extended in a modified form for chains that are weakly confined, and that, apart from the centre of mass motion, the single-chain dynamics are almost invariant to the degree of surface roughness on a monomeric scale.

Chapter 3 then investigated inter-chain cooperative dynamics, and the influence of the surface structure on global film properties. In contrast to mean single-chain dynamics, the cross-chain contributions to the film average bond orientation correlation function depend strongly on the particular surface structure. In addition, it was only when using arguably the most realistic model for the boundary, that which used roughened lattice beads, that time correlations of the film stress were found to be almost invariant with respect to the choice of thermostat friction constant. An important lesson learnt from these results is that due care must be taken with regards to the choice of boundary structure when performing such confined simulations. It was also found that in the presence of chains that are permanently end-grafted to the surface, the melt behaviour became

much more invariant to the surface structure generally. Whether or not the perfectly flat boundary case is physically realistic remains to be seen. Future work could investigate the corresponding behaviour at a free surface. Such work could shed light on the strong effects of confinement that have recently been observed in the presence of a free surface [89].

In chapter 4 we fitted single-chain observables of the fundamental MD model using weakly entangled chains to a single-chain slip-spring model applicable at the flat surface. It was found that the terminal relaxation time of chains (defined using the surface parallel end-to-end vector correlation function) is almost identical at the surface and in the channel centre, using both the multi-chain and slip-spring models. This observation is not consistent with the prediction made in some works [21], of a much weaker degree of entanglement near the flat surface, but is consistent with a Primitive Path Analysis that predicts only a small depletion layer of primitive path kinks within a distance of approximately a single 'tube' diameter from the surface. One limitation of this investigation was the relatively short and weakly entangled chain lengths considered.
Despite similar terminal relaxation behaviour, it was found that the ratio of the bond orientation auto-correlation function at the surface with respect to at the channel centre was less than unity at $t > \tau_e$. This suggested that in confinement it may be inappropriate to use the same plateau modulus dependent definition of N_e that is used in the bulk (most commonly eqn (D.6)). In the future it would be interesting to investigate the influence of the surface on entanglement dynamics for less flexible polymers. How does a surface induced nematic ordering influence the 'tube' near the surface?

Chapter 5 investigated the phenomenon of shear-flow induced surface chain disentanglement, that occurs during a coil-stretch transition of surface end-grafted chains. For simplicity flat boundaries were used. The non-equilibrium simulation used a grafting density in units of the overlap density that matched closely to a particular case of the non-entangled system considered in chapter 3. For the non-entangled case we concluded that the equilibrium stress correlation function was largely independent of the particular surface topography in the presence of the grafted chains. However it was not explicitly

verified that the same conclusion could be made for the higher molecular weight case from chapter 5. It was verified that the centre channel dynamic shear viscosity matched closely to that of a corresponding bulk system using periodic boundaries.

For polymer melts of much higher (and more experimentally relevant) molecular weights compared to the one simulated in chapter 5, the degree of wall slip may be much larger, and even lead to a marginal regime in which the fluid stress does not increase with increasing applied shear-rate. However the same mechanisms leading to slip that were postulated in chapter 5 may remain relevant for such cases. The results of the non-equilibrium simulation may be used in the future to guide the construction of theoretical models for surface rheology. It would also be interesting to perform identical simulations where the moving grafts are located in a plane inside the bulk. Comparison with the results of chapter 5 could then shed light on the importance of the surface proximity for the disentanglement.

Appendices

Appendix A

Modified-Rouse model

Random walk boundary value problem

The propagator $G_n(y_1, y_0)$ for a discrete random walk in one of three dimensions, beginning at position y_0, reaching y_1 in n steps with step-length l satisfies:

$$G_n(y_1, y_0) = \frac{G_{n-1}(y_1 - l, y_0)}{6} + \frac{G_{n-1}(y_1 + l, y_0)}{6} + \frac{4G_{n-1}(y_1, y_0)}{6} \tag{A.1}$$

Using the initial condition $G_0(y_1, y_0) = \delta(y_1 - y_0)$, we get $G_n(y_1, y_0) = \Omega_n(y_1, y_0)/\tilde{\Omega}_n$ where $\Omega_n(y_1, y_0)$ is the number of walks (partition function) between y_0 and y_1 with n steps and $\tilde{\Omega}_n$ is the total number of walks with n steps and fixed start position in a system whereby at each step there are six distinct moves with a 100% survival probability. In the limit $n \to \infty$, $l \to 0$, from eqn (A.1) the propagator diffusion equation in the wall normal direction is found:

$$\frac{\partial G_n(y_1, y_0)}{\partial n} = \frac{l^2}{6} \frac{\partial^2 G_n(y_1, y_0)}{\partial {y_1}^2} \tag{A.2}$$

We seek the solution of eqn (A.2) which satisfies reflective boundary conditions at $y_1 = 0, L_c$:

$$\left. \frac{\partial G_n(y_1, y_0)}{\partial y_1} \right|_{y_1 = 0, L_c} = 0 \tag{A.3}$$

in the limit $L_c \to \infty$. Using this boundary condition, the total number of walks inside the channel is always conserved and equal to $\tilde{\Omega}_n$, so that the propagator must be a probability under the initial condition that the walk began at y_0.

The general solution of eqn (A.2) subject to reflective boundaries at 0 and L_c is well

known, consisting of $2m$ solutions with eigenvalues λ_m:

$$\sum_m \left(B_m \cos\left(\sqrt{\lambda_m} y_1\right) + D_m \sin\left(\sqrt{\lambda_m} y_1\right)\right) \exp\left(-{\sigma_1}^2 \lambda_m/2\right) \tag{A.4}$$

where ${\sigma_1}^2 = b^2/3 = l^2 n/3$. b is the characteristic length scale of the random walk. Applying the boundary conditions enforce $D_m = 0$, and $\lambda_m = \left(\frac{\pi m}{L_c}\right)^2$: $\quad m = 0, 1, 2, 3, ..., \infty$. Now we apply the initial condition: $G_0(y_1, y_0) = \delta(y_1 - y_0)$:

$$\delta(y_1 - y_0) = \sum_m B_m \cos\left(\sqrt{\lambda_m} y_1\right) \tag{A.5}$$

Then the B_m are found as:

$$B_m = \frac{2}{L_c} \int_0^{L_c} dy_1 \cos\left(\sqrt{\lambda_m} y_1\right) \delta(y_1 - y_0) = \frac{2}{L_c} \cos\left(\sqrt{\lambda_m} y_0\right) \tag{A.6}$$

The complete solution is then:

$$\sum_{m=0}^{\infty} \frac{2}{L_c} \cos\left(\sqrt{\lambda_m} y_0\right) \cos\left(\sqrt{\lambda_m} y_1\right) \exp\left(-{\sigma_1}^2 \lambda_m/2\right) = \sum_{m=0}^{\infty} f(m) \tag{A.7}$$

From eqn (A.7), $f'(m) \to 0$ as $L_c \to \infty$ over the whole range of m. Resultantly, in the limit $L_c \to \infty$, $f(m)$ is a constant over any finite interval, and the sum, eqn (A.7), may be equated with the following integral:

$$\begin{aligned} &\lim_{L_c \to \infty} \frac{2}{L_c} \int_0^{\infty} dm \, \cos\left(\sqrt{\lambda_m} y_0\right) \cos\left(\sqrt{\lambda_m} y_1\right) \exp\left(-{\sigma_1}^2 \lambda_m/2\right) = \\ &\lim_{L_c \to \infty} \frac{1}{L_c} \int_0^{\infty} dm \, \left(\cos\left(\sqrt{\lambda_m}(y_1 + y_0)\right) + \cos\left(\sqrt{\lambda_m}(y_1 - y_0)\right)\right) \exp\left(-{\sigma_1}^2 \lambda_m/2\right) \end{aligned} \tag{A.8}$$

Rewriting this integral in the following form:

$$\int_0^{\infty} dU \, \cos(aU) \exp\left(-U^2\right) = \frac{\sqrt{\pi}}{2} \exp\left(-\frac{a^2}{4}\right) \tag{A.9}$$

and evaluating, leads to the solution for the propagator (conditional probability):

$$\lim_{L_c \to \infty} P(y_1 | y_0, L_c) = \frac{1}{\sqrt{2\pi {\sigma_1}^2}} \exp\left(-\frac{(y_1 - y_0)^2}{2{\sigma_1}^2}\right) + \frac{1}{\sqrt{2\pi {\sigma_1}^2}} \exp\left(-\frac{(y_1 + y_0)^2}{2{\sigma_1}^2}\right) \tag{A.10}$$

Translating the coordinates such that the surface position is translated to y_w, we find a general expression in terms of unbounded random walk probability weights:

$$\begin{aligned} P(y_1|y_0, y_w) &= P(y_1|y_0) + P(\bar{y_1}|y_0) \\ &= \frac{1}{\sqrt{2\pi{\sigma_1}^2}} \exp\left(-\frac{(y_1 - y_0)^2}{2{\sigma_1}^2}\right) + \frac{1}{\sqrt{2\pi{\sigma_1}^2}} \exp\left(-\frac{(-\tilde{y_1} - \tilde{y_0})^2}{2{\sigma_1}^2}\right) \end{aligned} \tag{A.11}$$

where $\tilde{y}_i = y_i - y_w$.

Conformational free energy of a reflected random walk

We now assume that near a flat surface the probability distribution for positions of the start and end beads of polymer chain sub-segments in the canonical ensemble at arbitrary temperature T coincides with a reflected random walk. We give temperature in units of k_B. Then a conformational free energy may be defined for the polymer chain. The partition function, $\Omega(\boldsymbol{R}_i, \boldsymbol{R}_{i-1}, y_w)$, for a three dimensional random walk from $\boldsymbol{R}_{i-1}$ to $\boldsymbol{R}_i$ in the presence of a reflective surface at position y_w, can be written in terms of a sum of the probabilities of unbounded random walks of bond vector $\boldsymbol{Q}_i = \boldsymbol{R}_i - \boldsymbol{R}_{i-1}$ and bond vector from $\boldsymbol{R}_{i-1}$ to the reflection of $\boldsymbol{R}_i$ in the $y = y_w$ plane, $\bar{\boldsymbol{Q}}_i$:

$$\Omega(\boldsymbol{R}_i, \boldsymbol{R}_{i-1}, y_w) = (P(\boldsymbol{Q}_i) + P(\bar{\boldsymbol{Q}}_i))\tilde{\Omega} \tag{A.12}$$

where $\tilde{\Omega}$ is the total number of walks with fixed start. Therefore the thermodynamic potential (conformational free energy) may be defined up to a constant as:

$$U(\boldsymbol{Q}_i, \bar{\boldsymbol{Q}}_i) = -T \log(P(\boldsymbol{Q}_i) + P(\bar{\boldsymbol{Q}}_i)) \tag{A.13}$$

Identifying the symmetric (bonded) part of the potential as $-T\,\log(P(\boldsymbol{Q}_i)) = \frac{k}{2}\boldsymbol{Q}_i \cdot \boldsymbol{Q}_i$, where $k = T/{\sigma_1}^2$, eqn (A.13) can be written as a sum of bonded and non-bonded potentials:

$$U(\boldsymbol{Q}_i, \bar{\boldsymbol{Q}}_i) = -T\left(\log(P(\boldsymbol{Q}_i)) + \log\left(1 + \frac{P(\bar{\boldsymbol{Q}}_i)}{P(\boldsymbol{Q}_i)}\right)\right) \tag{A.14}$$

The bond vectors may be resolved into components parallel to and normal to the surface: $\boldsymbol{Q}_i = \boldsymbol{Q}_{i,\parallel} + (y_i - y_{i-1})\hat{\boldsymbol{e}}_\perp; \quad \bar{\boldsymbol{Q}}_i = \boldsymbol{Q}_{i,\parallel} + (-\tilde{y}_i - \tilde{y}_{i-1})\hat{\boldsymbol{e}}_\perp$. Since $\boldsymbol{Q}_i$ and $\bar{\boldsymbol{Q}}_i$ only differ in the wall normal direction, the quotient in eqn (A.14) is:

$$\begin{aligned}\frac{P(\bar{\boldsymbol{Q}}_i)}{P(\boldsymbol{Q}_i)} &= \exp\left(-\frac{((-\tilde{y}_i - \tilde{y}_{i-1})^2 - (y_i - y_{i-1})^2)}{2{\sigma_1}^2}\right) \\ &= \exp\left(-\frac{2\tilde{y}_i\,\tilde{y}_{i-1}}{{\sigma_1}^2}\right)\end{aligned} \tag{A.15}$$

Therefore the thermodynamic potential up to a constant is:

$$U(\boldsymbol{Q}_i, \bar{\boldsymbol{Q}}_i) = \frac{k}{2}\boldsymbol{Q}_i \cdot \boldsymbol{Q}_i + A(y_i, y_{i-1}, y_w) \tag{A.16}$$

where the wall contribution is:

$$A(y_i, y_{i-1}, y_w) = -T\log\left(1 + \exp\left(-\frac{2\tilde{y}_i\tilde{y}_{i-1}}{{\sigma_1}^2}\right)\right) \tag{A.17}$$

The additional thermodynamic force on particle i in the wall normal direction can now be calculated:

$$-\frac{\partial A(y_i, y_{i-1}, y_w)}{\partial \tilde{y}_i} = -\frac{\exp\left(-\frac{2\tilde{y}_i\tilde{y}_{i-1}}{{\sigma_1}^2}\right)}{1 + \exp\left(-\frac{2\tilde{y}_i\tilde{y}_{i-1}}{{\sigma_1}^2}\right)} 2k\tilde{y}_{i-1} \tag{A.18}$$

In the case of absorbing boundary condition, the partition function for a chain beginning at $\boldsymbol{R}_{i-1}$ and ending at $\boldsymbol{R}_i$ has to be zero when either bead is at the surface. This is satisfied with the propagator $G_n(y_1, y_0) = P(\boldsymbol{Q}_i) - P(\bar{\boldsymbol{Q}}_i)$ [173]:

$$\Omega(\boldsymbol{R}_i, \boldsymbol{R}_{i-1}, y_w) = (P(\boldsymbol{Q}_i) - P(\bar{\boldsymbol{Q}}_i))\tilde{\Omega} \tag{A.19}$$

Resultantly, the corresponding wall potential has a singularity at $\tilde{y}_i, \tilde{y}_{i-1} = 0$:

$$B(y_i, y_{i-1}, y_w) = -T \log\left(1 - \exp\left(-\frac{2\tilde{y}_i\tilde{y}_{i-1}}{{\sigma_1}^2}\right)\right) \tag{A.20}$$

End-to-end vector correlation function of a dumbbell tethered at a reflective surface

The probability distribution of the end-to-end vector of a reflected walk in the surface normal direction, eqn (A.11), becomes a reflected-Gaussian for $y_0 = y_w$. Resultantly, when modelling the wall grafted chain using a single dumbbell, the potential reduces to the simple harmonic form, $U(y_1) = k/2(y_1 - y_w)^2$, such that the mean square end-to-end distance of the whole chain (dumbbell) is related to the spring constant via the equipartition theorem as: $\langle (y_1 - y_w)^2 \rangle = T/k$. Setting $y_w = 0$, the first two moments of the half Gaussian end bead distribution are:

$$\begin{aligned} \langle y_1 \rangle &= \sqrt{2{\sigma_1}^2/\pi} \\ \left\langle {y_1}^2 \right\rangle &= {\sigma_1}^2 \end{aligned} \tag{A.21}$$

Knowing these moments, we only need to calculate the equilibrium correlation function of the end bead vector:

$$\langle y_1(t) y_1(0) \rangle = \int_0^\infty dy_1' y_1' \Psi_{\text{eq}}(y_1') \int_0^\infty dy_1 \, y_1 G_t(y_1, y_1') \tag{A.22}$$

in order to solve the dumbbell end-to-end vector correlation function $\Phi_{\text{db},\perp}(t)$:

$$\Phi_{\text{db},\perp}(t) = \frac{\langle y_1(t) y_1(0) \rangle - \langle y_1 \rangle^2}{\langle {y_1}^2 \rangle - \langle y_1 \rangle^2} \tag{A.23}$$

$\Psi_{\text{eq}}(y_1')$ is the equilibrium distribution function of the end position and $G_t(y_1, y_1')$ is the propagator of an end bead with position y_1' at time 0 and position y_1 at time t, corre-

sponding to the system described by the Langevin dynamics:

$$\frac{dy_1}{dt} = \frac{1}{\xi}\left(-\frac{\partial U}{\partial y_1} + f^r(t)\right) \tag{A.24}$$

supplemented with a reflective boundary; where ξ is the free bead friction and $f^r(t)$ is a white-noise random variable with zero mean and variance $2\xi T$. The propagator satisfies the Smoluchowski equation:

$$\frac{\partial G_t(y_1, y_1')}{\partial t} = \frac{1}{\xi}\frac{\partial}{\partial y_1}\left(T\frac{\partial G_t(y_1, y_1')}{\partial y_1} + \frac{\partial U}{\partial y_1}G_t(y_1, y_1')\right) \tag{A.25}$$

Using the potential, $U(y_1) = (k/2){y_1}^2$, eqn (A.24) becomes the Ornstein-Uhlenbeck process. Then the solution of eqn (A.25) over the unbounded domain, $(-\infty, \infty)$, is [39]

$$\tilde{G}_t(y_1, y_1') = \frac{1}{\sqrt{2\pi\sigma(t)^2}}\exp\left(-\frac{\left(y_1 - y_1'\exp(-t/\tau_{\mathrm{db},\|})\right)^2}{2\sigma(t)^2}\right) \tag{A.26}$$

where $\sigma(t) = \sigma_1\sqrt{1-\exp(-2t/\tau_{\mathrm{db},\|})}$ and $\tau_{\mathrm{db},\|} = \xi/k$ is the relaxation time of the unbounded system. We seek the solution of the propagator under a reflective boundary condition:

$$\left.\frac{\partial G_t(y_1, y_1')}{\partial y_1}\right|_{y_1=0} = 0 \tag{A.27}$$

Due to the symmetry of the harmonic potential, we can construct the solution, $G_t(y_1, y_1')$, satisfying eqn (A.25) and the reflective boundary condition, eqn (A.27), from the solution $\tilde{G}_t(y_1, y_1')$, as:

$$G_t(y_1, y_1') = \tilde{G}_t(y_1, y_1') + \tilde{G}_t(-y_1, y_1') \tag{A.28}$$

Using this propagator, an arbitrary probability distribution becomes the equilibrium half-Gaussian distribution for $t \to \infty$:

$$\begin{aligned}\Psi_{\mathrm{eq}}(y_1) &= \lim_{t\to\infty}\int_0^\infty dy_1'\left(\tilde{G}_t(y_1, y_1') + \tilde{G}_t(-y_1, y_1')\right)\Psi_0(y_1') \\ &= 2\left(\frac{1}{\sqrt{2\pi{\sigma_1}^2}}\exp\left(-\frac{{y_1}^2}{2{\sigma_1}^2}\right)\right)\end{aligned} \tag{A.29}$$

$\Psi_0(y_1')$ is the occupational probability density for the particle at position y_1' at an initial time when the distribution may not have reached equilibrium. Now eqn (A.22) may be written as:

$$\langle y_1(t)y_1(0)\rangle = \int_0^\infty dy_1' y_1' \Psi_{\rm eq}(y_1') \int_0^\infty dy_1\, y_1 \left(\tilde{G}_t(y_1, y_1') + \tilde{G}_t(-y_1, y_1')\right) \tag{A.30}$$

Evaluating the integrals in eqn (A.30) leads to $\Phi_{\rm db,\perp}(t)$, eqn (2.15), via eqn (A.23).

Evaluation of eqn (A.30)

We define the time dependent normalization part of the propagator, eqn (A.26), as $z(t)$:

$$z(t) = \sqrt{\frac{1}{2\pi\sigma(t)^2}} \tag{A.31}$$

The spatially dependant part is:

$$v(y_1, y_1') = \exp\left(-\frac{\left(y_1 - y_1' \exp(-t/\tau_{\rm db,\|})\right)^2}{2\sigma(t)^2}\right) \tag{A.32}$$

We take $z(t)$ outside of the inner integral in eqn (A.30) and then evaluate the inner integral:

$$\int_0^\infty dy_1\, y_1 (\underline{v(y_1, y_1')} + v(-y_1, y_1')) \tag{A.33}$$

First (underlined) term in expression (A.33)

We first consider the underlined term in expression (A.33). Making a change of variables, defining $u = y_1 - y_1' \exp(-t/\tau_{\rm db,\|})$, this term becomes:

$$\int_0^\infty dy_1\, y_1 v(y_1, y_1') = \int_{-y_1' \exp(-t/\tau_{\rm db,\|})}^\infty du \left(u + y_1' \exp\left(-\frac{t}{\tau_{\rm db,\|}}\right)\right) \exp\left(-\frac{u^2}{2\sigma(t)^2}\right) \tag{A.34}$$

We separate the right side of eqn (A.34) into two parts, denoting part $a1$ as:

$$\int_{-y_1' \exp(-t/\tau_{\rm db,\|})}^\infty du\, y_1' \exp\left(-\frac{t}{\tau_{\rm db,\|}}\right) \exp\left(-\frac{u^2}{2\sigma(t)^2}\right) \tag{A.35}$$

and part $b1$ as:

$$\int_{-y_1' \exp(-t/\tau_{\mathrm{db},\parallel})}^{\infty} du\, u \exp\left(-\frac{u^2}{2\sigma(t)^2}\right) \tag{A.36}$$

Second ('mirror') term in expression (A.33)

We now make a different change of variables, defining $u = -y_1 - y_1' \exp(-t/\tau_{\mathrm{db},\parallel})$. Then the second part of expression (A.33) becomes:

$$\int_0^{\infty} dy_1\, y_1 v(-y_1, y_1') = \int_{-y_1' \exp(-t/\tau_{\mathrm{db},\parallel})}^{-\infty} du \left(u + y_1' \exp\left(-\frac{t}{\tau_{\mathrm{db},\parallel}}\right)\right) \exp\left(-\frac{u^2}{2\sigma(t)^2}\right) \tag{A.37}$$

We separate the right side of eqn (A.37) into two parts, denoting part $a2$ as:

$$-\int_{-\infty}^{-y_1' \exp(-t/\tau_{\mathrm{db},\parallel})} du\, y_1' \exp\left(-\frac{t}{\tau_{\mathrm{db},\parallel}}\right) \exp\left(-\frac{u^2}{2\sigma(t)^2}\right) \tag{A.38}$$

and part $b2$ as:

$$-\int_{-\infty}^{-y_1' \exp(-t/\tau_{\mathrm{db},\parallel})} du\, u \exp\left(-\frac{u^2}{2\sigma(t)^2}\right) \tag{A.39}$$

Part a inner integrals

Now we move onto evaluating the integrals for the sum of parts $a1$ and $a2$, i.e. we sum expressions (A.35) and (A.38), forming a total part a integral (substituting: $q = y_1' \exp(-t/\tau_{\mathrm{db},\parallel})$):

$$\begin{aligned}
&q \int_{-q}^{\infty} du\, \exp\left(-\frac{u^2}{2\sigma(t)^2}\right) - q \int_{-\infty}^{-q} du\, \exp\left(-\frac{u^2}{2\sigma(t)^2}\right) \\
&= q \left(\int_0^{\infty} du\, \exp\left(-\frac{u^2}{2\sigma(t)^2}\right) + \int_{-q}^{0} du\, \exp\left(-\frac{u^2}{2\sigma(t)^2}\right)\right) \\
&\quad - q \left(\int_{-\infty}^{0} du\, \exp\left(-\frac{u^2}{2\sigma(t)^2}\right) - \int_{-q}^{0} du\, \exp\left(-\frac{u^2}{2\sigma(t)^2}\right)\right) \\
&= 2q \int_{-q}^{0} du\, \exp\left(-\frac{u^2}{2\sigma(t)^2}\right)
\end{aligned} \tag{A.40}$$

Making a change of variables, $u' = u/\left(\sqrt{2}\sigma(t)\right)$, the part a integral is evaluated:

$$2q\int_{-\frac{q}{\sqrt{2}\sigma(t)}}^{0} du'\,\sqrt{2}\sigma(t)\exp\left(-u'^2\right) = \sqrt{2\pi}q\sigma(t)\ \mathrm{erf}\left(\frac{q}{\sqrt{2}\sigma(t)}\right) \tag{A.41}$$

where $\mathrm{erf}(x)$ denotes the error function.

Part b inner integrals

Using the substitution: $p = u^2$ both part $b1$, expression (A.36), and part $b2$, expression (A.39), become:

$$\int_{y_1'^2\exp(-2t/\tau_{\mathrm{db},\parallel})}^{\infty} dp\frac{1}{2}\exp\left(-\frac{p}{2\sigma(t)^2}\right) \tag{A.42}$$

We then evaluate twice expression (A.42):

$$\begin{aligned}
&\int_{y_1'^2\exp(-2t/\tau_{\mathrm{db},\parallel})}^{\infty} dp\exp\left(-\frac{p}{2\sigma(t)^2}\right)\\
&= \left[-2\sigma(t)^2\exp\left(-\frac{p}{2\sigma(t)^2}\right)\right]_{y_1'^2\exp(-2t/\tau_{\mathrm{db},\parallel})}^{\infty}\\
&= 2\sigma(t)^2\exp\left(-\frac{y_1'^2\exp(-2t/\tau_{\mathrm{db},\parallel})}{2\sigma(t)^2}\right)
\end{aligned} \tag{A.43}$$

Outer integrals

Inserting eqn (A.43) and eqn (A.41), the correlator, eqn (A.30), becomes:

$$\begin{aligned}
\langle y_1(t)y_1(0)\rangle = 4z'(t)\sigma(t)^2\int_0^{\infty} dy_1'\,y_1'\exp\left(-\left(\frac{\exp(-2t/\tau_{\mathrm{db},\parallel})}{2\sigma(t)^2}+\frac{1}{2{\sigma_1}^2}\right)y_1'^2\right)+\\
2z'(t)\sigma(t)\sqrt{2\pi}\exp\left(-\frac{t}{\tau_{\mathrm{db},\parallel}}\right)\int_0^{\infty} dy_1'\,y_1'^2\ \mathrm{erf}\left(\frac{y_1'\exp(-t/\tau_{\mathrm{db},\parallel})}{\sqrt{2}\sigma(t)}\right)\exp\left(-\frac{y_1'^2}{2{\sigma_1}^2}\right)
\end{aligned} \tag{A.44}$$

where $z'(t)$ has absorbed the constant terms from the equilibrium distribution:

$$z'(t) = z(t)z(\infty) = \left(2\pi{\sigma_1}^2\right)^{-1}\left(1-\exp(-2t/\tau_{\mathrm{db},\parallel})\right)^{-1/2} \tag{A.45}$$

Making a change of variables, defining $u = y_1'^2$, the first term in eqn (A.44) can be evaluated:

$$2z'(t)\sigma(t)^2 \int_0^\infty du \exp\left(-L(t)u\right) = \left[\frac{-2z'(t)\sigma(t)^2}{L(t)} \exp(-L(t)u)\right]_0^\infty = \frac{2z'(t)\sigma(t)^2}{L(t)} \tag{A.46}$$

where:

$$L(t) = \frac{\exp(-2t/\tau_{\mathrm{db},\parallel})}{2\sigma(t)^2} + \frac{1}{2{\sigma_1}^2} \tag{A.47}$$

The second term in eqn (A.44) may be readily evaluated using Maple™[1] (alternatively see [121]). This leads to the final solution for the end-to-end vector correlation function with respect to the origin:

$$\langle y_1(t) y_1(0)\rangle = \frac{2\,T}{k\pi}\left(\arctan\left(\mathrm{e}^{-\frac{t}{\tau_{\mathrm{db},\parallel}}} \frac{1}{\sqrt{1-\mathrm{e}^{-2\frac{t}{\tau_{\mathrm{db},\parallel}}}}}\right)\mathrm{e}^{-\frac{t}{\tau_{\mathrm{db},\parallel}}} + \sqrt{1-\mathrm{e}^{-2\frac{t}{\tau_{\mathrm{db},\parallel}}}}\right)$$

Subtracting the mean and normalizing gives eqn (2.15).

Modified-Rouse model - large N limiting behaviour

As the number of bonds in a chain diverges, $N \to \infty$, the functional form of $\Phi_\perp(t)$ for a surface tethered-chain converges at a similar rate as for the surface parallel case, which is described by standard Rouse theory. In figure A.1, $\Phi_\perp(t)$ and $\Phi_\parallel(t)$ are compared for $N = 1, 2, 4, 8, 16, 32$. For each plot the time axis is normalized by the corresponding longest system relaxation time $\tau_{1,\alpha}$, which in the surface parallel direction is [93]:

$$\tau_{1,\parallel} = \frac{\xi b^2}{12T \sin^2\left(\frac{\pi(1/2)}{2(N+1/2)}\right)} \tag{A.48}$$

In the surface normal direction $\tau_{1,\perp}$ is found by assuming that the relationship:

$$\frac{\tau_{1,\perp}}{\tau_{1,\parallel}} = \frac{\tau_{\mathrm{db},\perp}}{\tau_{\mathrm{db},\parallel}} = \frac{1}{2} \tag{A.49}$$

[1] Version 18

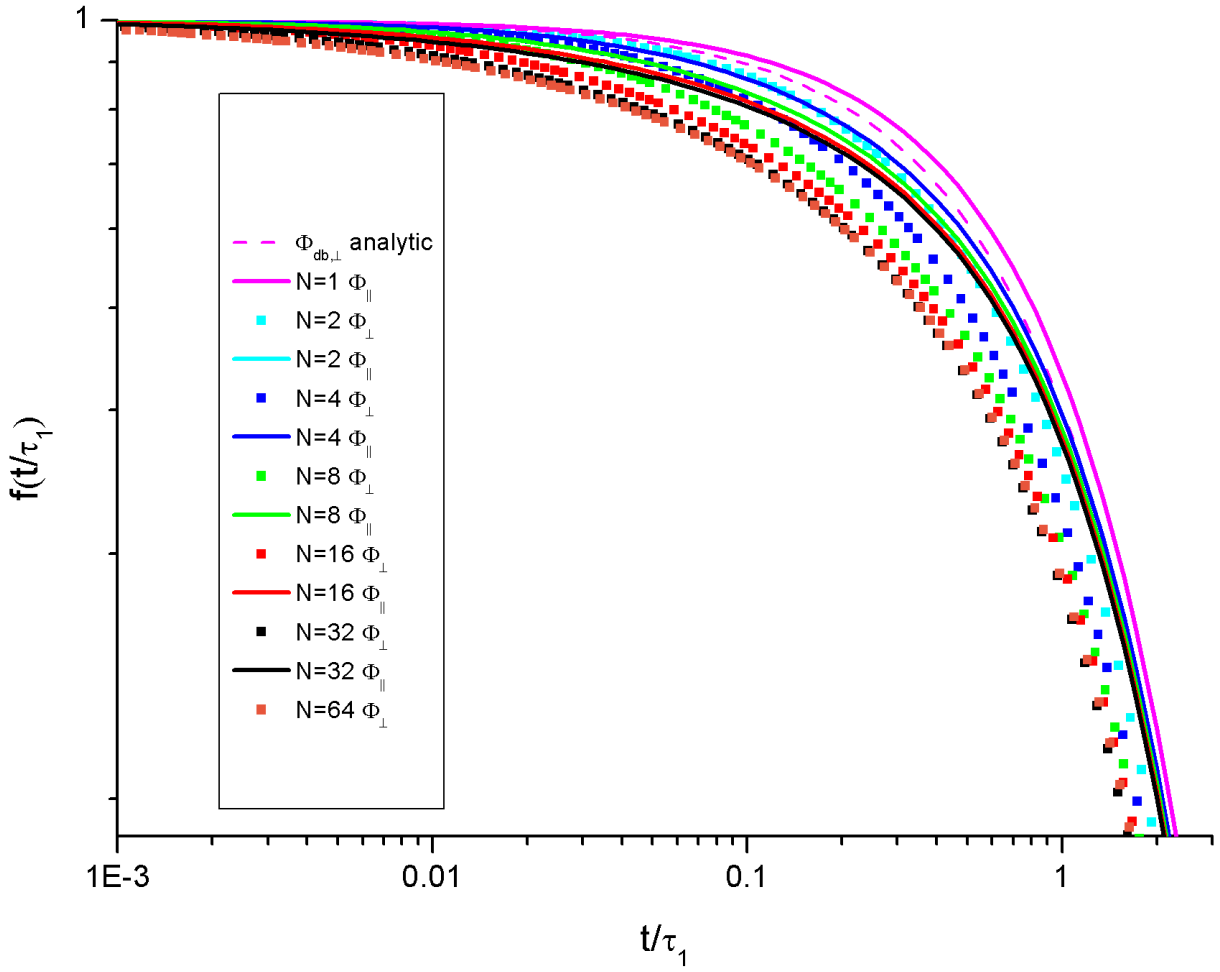

Figure A.1: Comparison of wall normal (symbols) and parallel (lines) components of $\Phi_\alpha(t)$ for a chain modelled using different numbers of bonds. Both directions give converged behaviour beyond $N \approx 32$. Time axes are normalized by the longest relaxation time in the corresponding direction.

is valid for all N. From figure A.1 it is apparent that the changes in the form of $\Phi_\perp(t)$ as N increases from $N = 1$ are greater than in the unbounded direction. This can be largely attributed to a decrease of the relative weight of the longest Rouse mode amplitude which does not dominate $\Phi_\perp(t)$ as much as it does $\Phi_\parallel(t)$. In general, the amplitudes of the modes strongly differ from the wall parallel direction. The first five Rouse mode amplitudes of reflected random walks beginning at the surface are plotted and compared to KG MD in figure 2.8.

Rouse cross-mode correlation functions for a surface tethered chain

Since in a confined system the Rouse coordinates are no longer normal modes, their cross-correlations are no longer zero. Here we simply present the qualitative behaviour of cross-mode correlations within the modified-Rouse model of a surface tethered chain (this qualitative behaviour is shared by KG MD), and show that the relative importance of cross-mode correlations is small compared to auto-correlations.

A general characteristic of the Rouse coordinates of a reflected random walk beginning at the surface is that the covariances, $\langle X_{p,\perp} X_{q,\perp}\rangle - \langle X_{p,\perp}\rangle \langle X_{q,\perp}\rangle$, are negative. This is an observation we make for all cases considered and is not generally proven. Since the mode covariances coincide with the amplitudes of the cross-mode correlation functions:

$$C_{pq,\perp}(t) = \langle (X_{p,\perp}(t) - \langle X_{p,\perp}\rangle)(X_{q,\perp}(0) - \langle X_{q,\perp}\rangle)\rangle \tag{A.50}$$

these functions are increasing. Figure A.2 shows that the magnitude of the sum over all first mode covariances quickly converges to a effectively constant value as N is increased. This value is more than seven times smaller than the variance of the first mode. The relative importance of cross-correlations is a decreasing function of p.

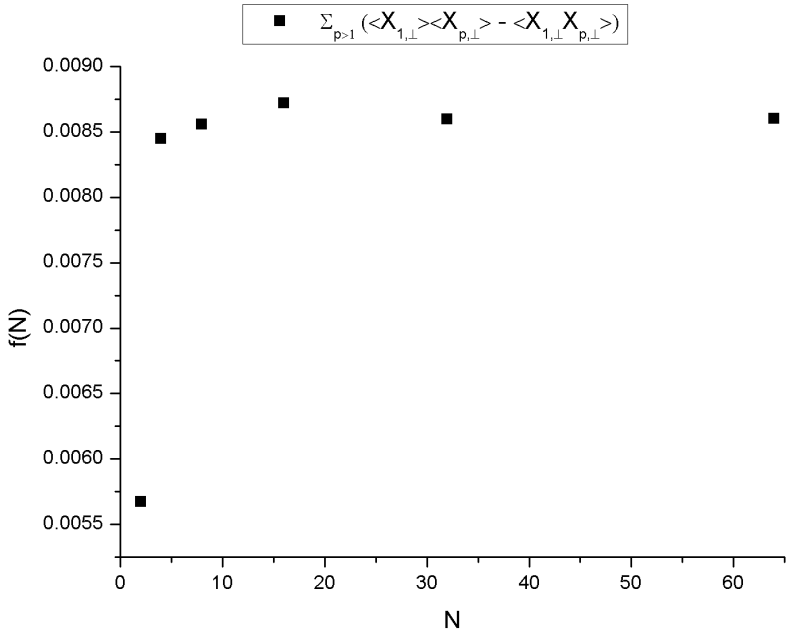

Figure A.2: Negative of the sum over all first mode covariances as a function of the number of bonds in a chain, normalized by the bulk chain mean square end-to-end distance in one direction.

Appendix B

KG MD model

Surface nematic interaction and enhanced chain swelling near the surface

In this section we investigate the weak additional swelling in the chain dimension that is apparent in figure 2.6, where it was found that the surface parallel mean square end-to-end distance of complete chains comprising $n = 64$ bonds is around 10% larger for KG MD chains beginning with one end at the surface, compared to in the channel centre. We partially attribute this swelling to the influence of the surface on short range nematic ordering. We consider a nematic order parameter of chain sub-segments comprising $m = 4$ bonds. The nematic order parameter is:

$$S_{4,\parallel}(y) = \left\langle P_2\left(\hat{k}_{4,\parallel}(y)\right)\right\rangle \tag{B.1}$$

where $\hat{k}_{4,\parallel}$ is a parallel component of the unit vector of a coarse-grained bond corresponding to a chain segment consisting of 4 bonds. $P_2(x) = \frac{3x^2-1}{2}$ is the second Legendre polynomial, and the averages are performed over bins centred at position $y = \Delta y(j+1/2)$ for $j = 0, 1, 2, 3, ...$; where Δy is the bin width. Each sub-segment is binned depending on the distance from the wall of the sub-segment end-bead position. It is necessary to use coarse-grained segments since for $m < 4$ the wall ordering obscures the trend near to the surface. In figure B.1 we plot the nematic order parameter, $S_{4,\parallel}(y)$, as a function of the centre bin position. The decay in $S_{4,\parallel}(y)$ occurs over a distance $\approx 2\sigma$ from the surface, which is similar to an approximate blob length for the Kremer-Grest chains. For semi-

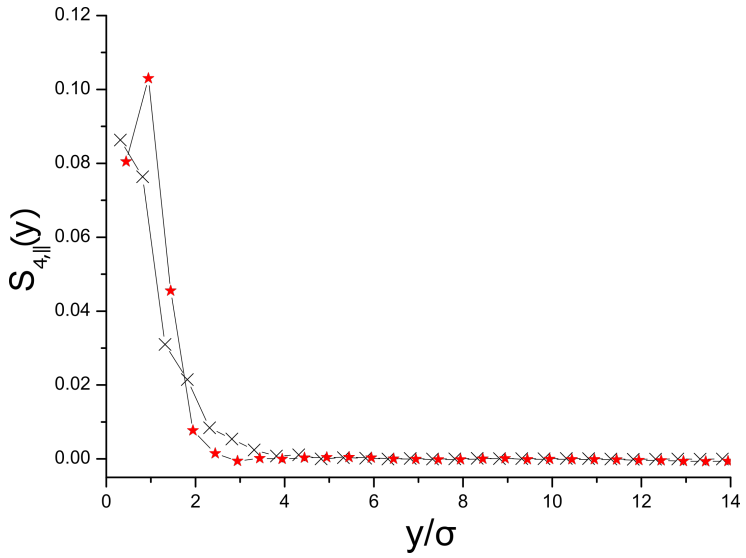

Figure B.1: Nematic order parameter, eqn (B.1), for chain sub-segments comprising $m = 4$ bonds. Binned by sub-segment end-bead position. Red stars: KG MD; black crosses: soft MD.

flexible polymers the nematic ordering persists over a longer interval [177]. The nematic order parameter corresponding to soft MD chains, also plotted in figure B.1, is no greater than KG MD at the surface. The higher density of ends immediately at the surface [108] is also expected to influence the surface normal square internal distance profiles in some way.

We can briefly consider whether contributions to chain swelling due to long range correlations [27] should be expected, and whether any effect should scale with chain length. In weak confinement, the distance separating the confining walls is a minimum of 3 times the equilibrium chain end-to-end distance. For chains with $n = 64$ this corresponds to 30 times the bead diameter, or approximately 20 blob lengths using the definition of a blob length as the long chain asymptotic Kuhn length [113], b, which for the Kremer-Grest model is $b \approx 1.5\sigma$. For the bond-fluctuating model, film average bulk-like behaviour was found for thicknesses larger than 5 blob lengths (see Cavallo et al. [27]). Essential two-dimensional behaviour was observed for ultra-thin films of thicknesses up to one blob size. Nevertheless, we consider a conjecture[1] that for chains with centre of mass within a blob length of the surface, long-ranged correlations may be similar to a thin slit (the

[1] due to an anonymous reviewer of [78]

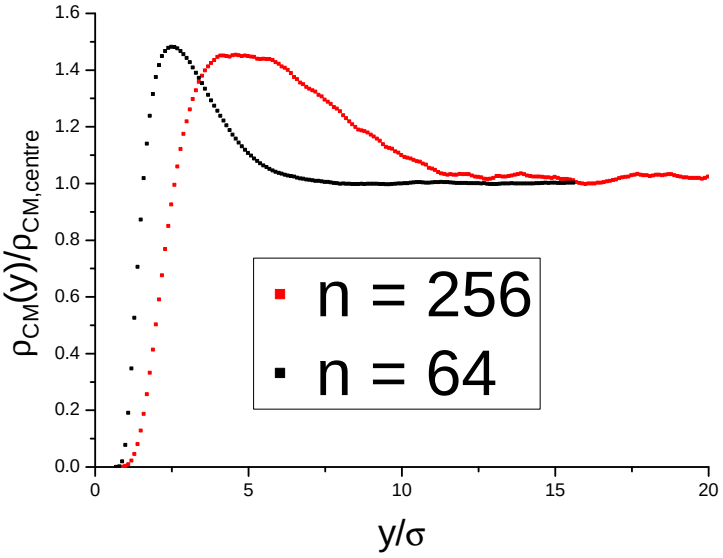

Figure B.2: Chain centre of mass volume density, $\rho_{\mathrm{CM}}(y)$, as a function of the distance from the centre of mass to the surface, y (normalized by the centre channel value). KG MD model at $n = 64$ and $n = 256$.

ratio of surface parallel square end-to-end distance in the slit with respect to in bulk is a growing logarithmic function of chain length [27]). A simple consideration suggests that this conjecture cannot lead to the conclusion that the degree of swelling of an average surface chain will scale with chain length in a similar way to the slit case: the distance from the surface of the centre of mass of surface chains scales with the bulk radius of gyration [144]. This means that, although following the conjecture: longer chains within a blob length of the surface will be more swollen with respect to their bulk dimension, the number of such chains becomes vanishingly small. As an example illustrating this, the centre of mass volume density normalized by its bulk value is plotted for chains of either $n = 64$ or $n = 256$ bonds in figure B.2. Considering that the blob length of KG MD chains is around 1.5σ, assuming the conjecture mentioned above, the logarithmic correction to chain size should be important for $n = 64$, and therefore possibly accounts for some of the swelling we observe. However if we look at longer chains, already at $n = 256$ it is apparent that only a very small number of chains have centre of mass within a blob length from the surface, and the argument that the logarithmic correction should be more important for longer chains breaks down.

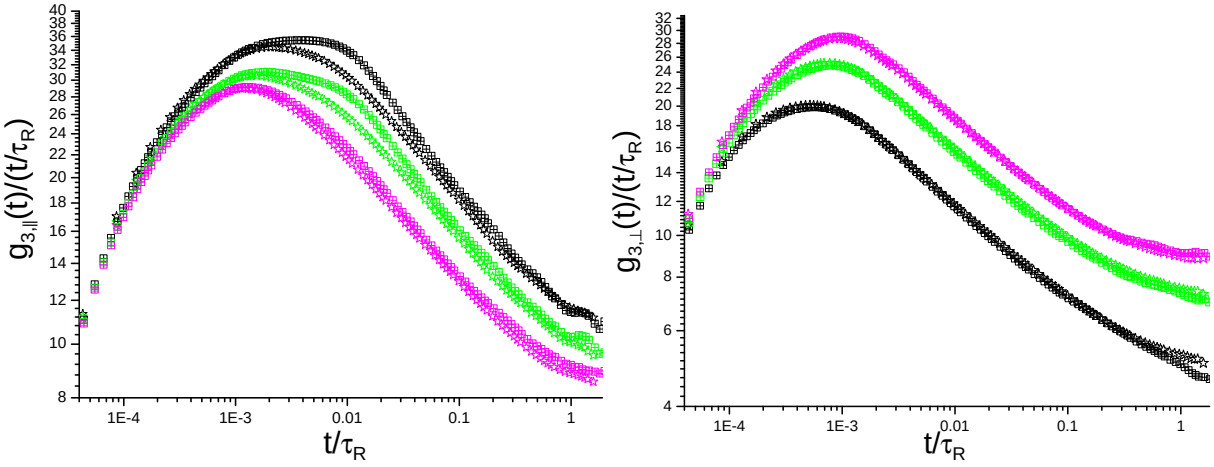

(a) $g_{3,\parallel}(t)/(t/\tau_R)$ (b) $g_{3,\perp}(t)/(t/\tau_R)$

Figure B.3: Centre of mass diffusion rate in directions (**a**) parallel, $g_{3,\parallel}(t)/(t/\tau_R)$, and (**b**) normal $g_{3,\perp}(t)/(t/\tau_R)$, to the surface. Black: $y_{\rm cm} < 0.25\sqrt{\langle \boldsymbol{u}_{\rm bulk}{}^2\rangle}$; green: $0.5\sqrt{\langle \boldsymbol{u}_{\rm bulk}{}^2\rangle} < y_{\rm cm} < 0.75\sqrt{\langle \boldsymbol{u}_{\rm bulk}{}^2\rangle}$; magenta: $1.25\sqrt{\langle \boldsymbol{u}_{\rm bulk}{}^2\rangle} < y_{\rm cm}$. Open stars are low friction KG MD with Langevin thermostat ($\xi_{\rm MD} = 0.05 m_b/\tau_{\rm LJ}$) with $\tau_{R,\xi_{\rm MD}=0.05} = 0.86\tau_{R,\xi_{\rm MD}=0.5}$. Open boxes with crosses are lowest friction KG MD with Langevin thermostat ($\xi_{\rm MD} = 0.01 m_b/\tau_{\rm LJ}$) with $\tau_{R,\xi_{\rm MD}=0.01} = 0.84\tau_{R,\xi_{\rm MD}=0.5}$

Centre of mass motion: $\xi_{\rm MD} \to 0$ limit

Figure B.3 plots the centre of mass mean square displacement both parallel, figure B.3a, and perpendicular, figure B.3b, to the surface, including plots corresponding to the Langevin thermostat using friction constants $\xi_{\rm MD} = 0.05 m_b/\tau_{\rm LJ}$ and $0.01 m_b/\tau_{\rm LJ}$. In order to clearly show the different diffusion regimes, the time dependent diffusion rates, $g_3(t)/(t/\tau_R)$, are plotted. For times shorter than the Rouse relaxation time there is a super-diffusive regime, followed by a sub-diffusive regime, before entering normal diffusion beyond the Rouse time. As mentioned in section 2.2, the low thermostat friction constant ($\xi_{\rm MD} = 0.05 m_b/\tau_{\rm LJ}$) produced results very similar to yet lower values, and therefore it represents well the limit $\xi_{\rm MD} \to 0$. In the parallel direction the lowest Langevin friction model shows a small additional feature at the crossover from super-diffusion to sub-diffusion compared to the lowest value of the friction used in section 2.2.

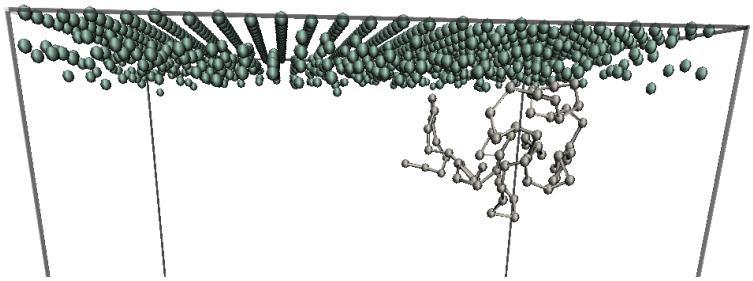

Figure B.4: Example random surface lattice configuration with $Var = 0.3\sigma$.

Influence of surface roughness on centre of mass motion in polymer melts

Here it is shown that the viscoelastic-hydrodynamic behaviour and variable diffusion rate occurring for the surface parallel centre of mass motion in confined systems (see section 2.3) depends strongly on the degree of surface roughness. Although for the case primarily investigated, a perfectly smooth flat wall, the centre of mass diffusion rate was faster near the surface with respect to the channel centre, the opposite is true using explicit particle walls which are roughened. The surface is formed from particles which are displaced randomly normal to the surface plane (with respect to an FCC lattice - figure 1.5), according to a normal distribution with variance: $Var = 0.15\sigma$ (medium roughness: figure B.5a), or $Var = 0.3\sigma$ (high roughness: figure B.5b). An example lattice is shown in figure B.4 with $Var = 0.3\sigma$. The Lennard-Jones potentials of the lattice use the same cutoff distance as the fluid Lennard-Jones interaction which is $r_c = 2^{1/6}\sigma$. The lattice particles have fixed positions and only interact with fluid particles. For the most rough surface, the opposite phenomenology as compared with the perfectly flat surface is found: the diffusion rate is slower closer to the surface. At medium roughness the rate of diffusion is close to constant across the channel. Interestingly, using the low thermostat friction ($\xi_{\mathrm{MD}} = 0.05m_b/\tau_{\mathrm{LJ}}$) generally leads to faster diffusion at all points in the channel with respect to the periodic simulation rate. This phenomenon is largely masked when the high thermostat friction coefficient ($\xi_{\mathrm{MD}} = 0.5m_b/\tau_{\mathrm{LJ}}$) is used. Also, perhaps counter-intuitively, the fastest average channel diffusion appears to occur, not using perfectly smooth walls, figure 2.10, but using

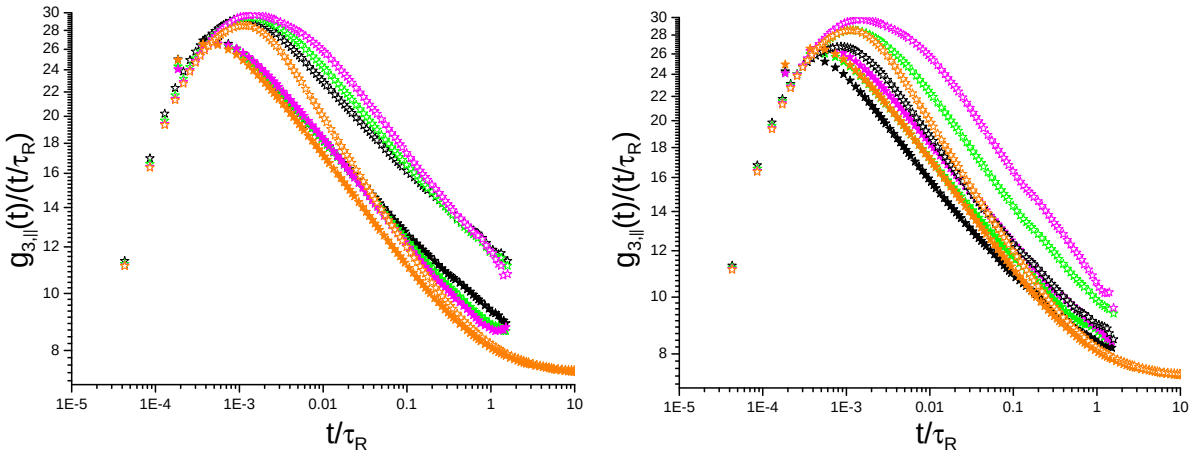

(a) Medium roughness $Var = 0.15\sigma$

(b) High roughness $Var = 0.3\sigma$

Figure B.5: Centre of mass diffusion rate in directions parallel, $g_{3,\parallel}(t)/(t/\tau_R)$, to the surface using explicit particle walls which are placed randomly in the surface normal direction according to a normal distribution with variance, (**a**) $Var = 0.15\sigma$, or (**b**) $Var = 0.3\sigma$. Black: $y_{\text{cm}} < 0.25\sqrt{\langle \boldsymbol{u}_{\text{bulk}}{}^2 \rangle}$; green: $0.5\sqrt{\langle \boldsymbol{u}_{\text{bulk}}{}^2 \rangle} < y_{\text{cm}} < 0.75\sqrt{\langle \boldsymbol{u}_{\text{bulk}}{}^2 \rangle}$; magenta: $1.25\sqrt{\langle \boldsymbol{u}_{\text{bulk}}{}^2 \rangle} < y_{\text{cm}}$; orange: periodic boundaries for reference. Filled stars are Langevin thermostat with friction constant $\xi_{\text{MD}} = 0.5 m_b/\tau_{\text{LJ}}$. Open stars use $\xi_{\text{MD}} = 0.05 m_b/\tau_{\text{LJ}}$, with $\tau_{R,\xi_{\text{MD}}=0.05} = 0.86\tau_{R,\xi_{\text{MD}}=0.5}$. KG MD model.

the medium roughness case, figure B.5a, where the diffusion rate is almost uniform across the channel. In addition, the behaviour using thermal walls (following Priezjev [130]) has been tested and the qualitative aspects of the roughness dependence are not altered in this case.

Appendix C

Fluctuation Dissipation Theorem (FDT)

Often [39, 28], a FDT is formulated for the mean relaxation of a system observable, A, following the application of a constant mechanical field, h, that was switched on in the distant past and switched off at $t = 0$. The FDT states that the relaxation function describing this process is identical to the equilibrium time-correlation function between A and another variable, B, that is conjugate to the field.

When the field is initially switched on the dynamics are controlled by the new system potential $\tilde{\mathscr{U}} = \mathscr{U}(\{\boldsymbol{r}^{n+1}\}) - hB(\{\boldsymbol{r}^{n+1}\})V$ where $\mathscr{U}$ is the unperturbed system potential. That $\tilde{\mathscr{U}}$ is linear in h indicates that the response is assumed to be weak, higher order terms are neglected. In general, immediately following the field being switched on the system will be away from equilibrium under the new system potential such that it takes a finite amount of time for the system to respond to the perturbation completely. Here we consider dynamics within the canonical ensemble. Before the field is switched on the probability distribution is:

$$\psi_{\text{eq}}(\{\boldsymbol{r}^{n+1}\}) = \frac{\exp(-\mathscr{U}(\{\boldsymbol{r}^{n+1}\})/T)}{\int \exp(-\mathscr{U}(\{\boldsymbol{r}^{n+1}\})/T)} \tag{C.1}$$

Following the application of the field for a long time the new probability distribution is:

$$\psi(\{\boldsymbol{r}^{n+1}\}) = \frac{\exp(-\tilde{\mathscr{U}}/T)}{\int \exp(-\tilde{\mathscr{U}}/T)} \tag{C.2}$$

Eqns (C.1) and (C.2) imply that once the field is switched on the system remains under isothermal conditions. In a realistic case the mechanical potential is dissipative and results in the conversion of work into heat. This effect may be counteracted in the case of computer simulation using a thermostat. For details of such issues including consideration of realistic systems where the isothermal approximation is accurate see Evans and Morriss [44]. In the case of a steady shear material deformation, the mean material shear stress, $B = \sigma_{xy}$, is conjugate to the shear-rate field, $h = \dot{\gamma}$ [44]. Instead of steady shear flow we can consider a simpler idealized case avoiding dissipation whereby a deformation, $\gamma = \dot{\gamma}dt$, is made in the limit $dt \to 0$. As shown in e.g. Doi and Edwards [39] (principle of virtual work 3.7.5) at the coarse-grained level of description, for such an instantaneous deformation $B = \sigma_{xy}$ is conjugate to the deformation, $h = \gamma$.

We now consider the relaxation after the field is switched off. At this time the system propagator switches to the field free propagator so that the mean of the observable $A(t)$ at time t after the field is switched off becomes ($\langle\rangle$ designates mean values under the equilibrium zero-field distribution):

$$\begin{aligned}\langle A(t)\rangle_h &= \int\{d\boldsymbol{r}'^{n+1}\}\int\{d\boldsymbol{r}^{n+1}\}A(\{\boldsymbol{r}^{n+1}\})G_t(\{\boldsymbol{r}^{n+1}\},\{\boldsymbol{r}'^{n+1}\})\psi\{\boldsymbol{r}'^{n+1}\}\\ &= \int\{d\boldsymbol{r}'^{n+1}\}\int\{d\boldsymbol{r}^{n+1}\}A(\{\boldsymbol{r}^{n+1}\})G_t(\{\boldsymbol{r}^{n+1}\},\{\boldsymbol{r}'^{n+1}\})\times\\ &\quad\frac{\exp\left(-\mathscr{U}(\{\boldsymbol{r}'^{n+1}\})/T\right)\exp\left(-(-hB(\{\boldsymbol{r}'^{n+1}\})V/T)\right)}{\left[\int\{d\boldsymbol{r}'^{n+1}\}\exp\left(-\mathscr{U}(\{\boldsymbol{r}'^{n+1}\})/T\right)\right]\left\langle\exp\left(-(-hBV/T)\right)\right\rangle}\\ &= \left\langle A(t)\frac{\exp\left(hB(0)V/T\right)}{\langle\exp\left(hBV/T\right)\rangle}\right\rangle\end{aligned} \tag{C.3}$$

Where $A(t) = \int\{d\boldsymbol{r}^{n+1}\}A(\{\boldsymbol{r}^{n+1}\})G_t(\{\boldsymbol{r}^{n+1}\},\{\boldsymbol{r}'^{n+1}\})$ is the mean value of A at time t given phase space point $\{\boldsymbol{r}'^{n+1}\}$ was occupied at time 0, and where $G_t(\{\boldsymbol{r}^{n+1}\},\{\boldsymbol{r}'^{n+1}\})$ is the propagator from $\{\boldsymbol{r}'^{n+1}\}$ at time 0 to $\{\boldsymbol{r}^{n+1}\}$ at time t. The linear FDT is derived by expanding to linear order:

$$\frac{\exp\left(hB(0)V/T\right)}{\langle\exp\left(hBV/T\right)\rangle} \approx 1 + h(B(0) - \langle B\rangle)V/T \tag{C.4}$$

Whereby we get the standard linear response result:
$\langle A(t)\rangle_h = \langle A\rangle + h\,\langle A(t)(B(0) - \langle B\rangle)\rangle\, V/T$. If $\langle B\rangle = 0$ then:

$$\frac{\langle A(t)\rangle_h - \langle A\rangle}{h} = \frac{V}{T}\,\langle A(t)B(0)\rangle \tag{C.5}$$

In the case of interest - instantaneous shear deformation - the field is $h = \gamma$; if we are interested in the stress response: $A = B = \sigma_{xy}$, we find that the non-equilibrium stress relaxation function following an instantaneous non-dissipative mechanical deformation matches the equilibrium shear stress time correlation function, eqn (3.15). If A is instead a local stress we get that the local stress relaxation function is given by eqn (3.16).

Appendix D

'Entanglement' measures

The successful 'tube' theories describing entangled dynamics in polymer melts were formulated in terms of the analogy with a single free chain moving in a fixed network. Within this formulation, the most important concept is the 'primitive path' of the free chain, defined as [39]:

'the shortest path connecting the two ends of the chain with the same topology as the chain itself relative to the obstacles' (of the network).

Clearly this definition is only meaningful if 'obstacle' is well defined. In dynamical models of polymer melts the constraints are defined by the collective motion of every polymer on time-scales $\tau_e < t < \tau_d$, where τ_e is the equilibration time and τ_d is the disengagement time. For a given set of initial three-dimensional chain conformations with fixed ends there is generally no unique solution for the set of primitive paths [84]. Nevertheless many methodologies for finding primitive path networks, which share common characteristics and are quite robust with respect to small changes in initial conditions, have been made using computer simulation. Everaers et al. [45] were the first to define a primitive path object within a polymer melt simulation, defined as the contour of the chain which results from making all bonded forces attractive. Under this condition all chains simultaneously minimize their energy whilst satisfying the constraints of fixed ends and the non-bonded interactions which prevent bond-crossings. Note however that this minimum energy protocol differs from the minimum length definition of the primitive path. Later methods, such as the 'Z' ('Z1') method of Kröger [84], define the primitive path directly via a min-

imization of chain contour lengths - a zero temperature method, which, unlike the energy minimization method, does not allow fluctuations that can increase chain contour lengths during the procedure. We now consider how relevant information is extracted from such primitive path objects, particularly under confinement.

Generalized 'S-coil' entanglement measure

Let us now assume that the primitive path is composed of bond vectors that are uncorrelated, and with mean length $\langle |\boldsymbol{Q}| \rangle$. This assumption is valid in all cases of interest here. The mean primitive path contour length is then:

$$\langle l_{pp} \rangle = \langle |\boldsymbol{Q}| \rangle \, N_{pp} \tag{D.1}$$

where N_{pp} is the number of distinct bond vectors forming the primitive path, which is assumed to be fixed. N_e is the mean number of fundamental chain bonds separating topological constraints in the long chain limit, the 'entanglement length':

$$N_e = \lim_{n \to \infty} \frac{n}{\langle Z \rangle} \tag{D.2}$$

where $\langle Z \rangle$ is the mean number of entanglements (topological constraints) in a chain. One well used general estimator for N_e is given by the ratio of the numbers of fundamental bonds and primitive path bonds:

$$\mathscr{N}_e(n) = n/N_{pp} \tag{D.3}$$

Since by definition the primitive path consists of straight lines connecting topological constraints under the additional constraint that the end positions of the primitive path are fixed and match the end positions of the fundamental chain, if topological constraints don't exist at the chain ends then one natural definition for the number of entanglements is: $\langle Z \rangle = N_{pp} - 1$. In this case, as for any other reasonable relationship between N_{pp} and

$\langle Z \rangle$, the estimator, eqn (D.3), satisfies:

$$\lim_{n\to\infty} \mathscr{N}_e(n) = N_e \tag{D.4}$$

It is at this point that we define a particular class of entanglement estimators by the shared characteristic that they make the following 'S-coil assumption':

S-coil assumption: *The primitive path bond orientation probability distribution is known.* Eqn (D.3) *may be written in terms of* $\langle l_{pp} \rangle$ *and* $\langle \boldsymbol{u}^2 \rangle$, *where* $\boldsymbol{u}$ *is the chain end-to-end vector.*

The case usually considered is that the primitive path is an unbounded random-walk with fixed step length a_{pp}, satisfying $a_{pp} = \langle \boldsymbol{u}^2 \rangle / \langle l_{pp} \rangle = {a_{pp}}^2 N_{pp} / a_{pp} N_{pp}$. Often a_{pp} is also equated with the 'tube diameter' parameter (referred to as a_0 in Doi and Edwards). The tube diameter may be more generally defined via a relation with the mean square displacement of a chain segment at the equilibration time: $a_0 = \sqrt{g_1(\tau_e)}$.
Then the N_e estimator, eqn (D.3), may be written:

$$\mathscr{N}_e(n) = n \frac{\langle \boldsymbol{u}^2 \rangle}{\langle l_{pp} \rangle^2} \tag{D.5}$$

Eqn (D.5) is called the 'classical S-coil' estimator, which is generally a function of the number of bonds, n, in a chain. It has been shown that, for a large set of different monodisperse entangled polymer melts with varying degrees of flexibility [161], eqn (D.5) gives a good prediction of the most commonly used rheological definition of entanglement length that is found experimentally via the definition of the bulk plateau modulus from the tube model [64, 52]:

$$G_N^0 = \frac{4\rho T}{5 N_e} \tag{D.6}$$

where ρ is the monomer density, T is the temperature and G_N^0 is the plateau modulus, which is defined theoretically [39] as the value of the linear response stress relaxation function at the equilibration time, τ_e. There is a factor of 4/5 in eqn (D.6) with respect to the stress modulus used for rubber networks that accounts for the relaxation occurring

prior to τ_e. This factor has been derived in several different ways (see Doi and Edwards: section 7.5.3 [39] and references) and its validity has been scrutinized (see Likhtman and McLeish [97]). It is worthwhile to note that eqn (D.6) currently has no analogue for confined systems.

Since the accuracy of the assumption of random walk chain statistics in the bulk depends upon the chain length, as already discussed in chapter 2, the resulting value of $\mathscr{N}_e(n)$ for small n has corresponding errors with respect to the asymptotically long chain limit N_e. There are also additional finite n errors that follow from the fixing of the ends. Since it is desirable to have an accurate measure for the entanglement molecular weight of asymptotically long chains using results of shorter chains which may be more easily simulated, Hoy et al. [64] developed modified estimators which converge at a faster rate to the $n \to \infty$ limit. One frequently employed modified version of eqn (D.5) is the modified S-coil estimator:

$$\mathscr{N}_e(n) = n \left(\frac{\left\langle {l_{pp}}^2 \right\rangle}{\langle \boldsymbol{u}^2 \rangle} - 1 \right)^{-1} \tag{D.7}$$

'S-coil' type measures under confinement

Why precisely is it assumed that the primitive path has a random-walk conformation for bulk melts? In the simple case that constraints always exist on the chain contour and have a well defined single length-scale separating them, we can think of the primitive path as simply being a coarse-grained version of the real chain, such that we could define a primitive path model from a chain model using eqn (1.32). Or less exactly we may approximate that the primitive path simply shares the same form of probability distribution for its connector vectors as the real chain model. This leads us to imagine that the primitive path of a random-walk is also a random-walk. For a random-walk chain under confinement it would then follow that its primitive path should be another random walk under the same confinement. Eqn (D.5) may only be generally equated with eqn (D.3) when the primitive path satisfies bulk random walk statistics. Apparently this has sometimes not been taken into account in the literature, e.g. see [73, 74, 165], where eqn (D.5) was applied to various confined cases instead of more meaningful applications of the S-coil assumption that we

now discuss.

If we are interested in fitting a data-set for a dynamical observable of a fundamental model (e.g. KG MD) using a coarse-grained model which includes topological constraints that exist on the coarse-grained chain, then it is natural to assume that the statistics of the primitive path object of the fundamental model are identical to the statistics of the constraints in the coarse-grained model. It is up to us to pick a coarse-grained model that is a good fit for static and dynamical behaviour of the fundamental model. As an example, the constraints for the case of the slip-spring model are slip-links that are only defined along the real chain contour.

Now we consider the case that the primitive-path is a *weakly* confined reflected-random walk, i.e. $L_c \to \infty$. For a random-walk on a lattice beginning with one end at fixed distance y from the reflective surface, the value of $\langle \boldsymbol{u}^2 \rangle$ is (in the continuous limit):

$$\left\langle \boldsymbol{u}(\nu)^2 \right\rangle = \frac{(2 + w(\nu)) N_{pp} {a_{pp}}^2}{3} \tag{D.8}$$

where $w(\nu) = \left\langle u_\perp(\nu)^2 \right\rangle / \left\langle u_\perp(\infty)^2 \right\rangle$, which is given by eqn (2.23) using $\nu = y/\sqrt{2N_{pp}{a_{pp}}^2/3}$. $w(\nu)$ is bounded below by $\approx 3/5$ so that the minimum in the mean square end-to-end distance for a primitive path near the surface is $\langle \boldsymbol{u}^2 \rangle_{\text{min}} \approx 13 N_{pp} {a_{pp}}^2/15$. This means that for such a reflected random walk, the estimator, eqn (D.5), underestimates the maximum value of the general estimator, eqn (D.3), by a factor of $\approx 13/15$. Although this factor is quite small, under *strong* confinement $\langle \boldsymbol{u}^2 \rangle_{\text{min}} \to 2N_{pp}{a_{pp}}^2/3$ for a random walk approaching the 2D limit: $L_c \to 0$.

We can also consider a primitive-path whose statistics match those of the discrete modified-Rouse model. This model is relevant since it corresponds with the statistics of the slip-links in the slip-spring model in chapter 4. In this case the bond length is not fixed but satisfies a reflected Gaussian distribution, such that the mean bond length becomes a channel position dependent quantity. The distribution for the wall normal component of the bond vector is given by eqn (2.4). The primitive path bond vectors then generally satisfy $\langle |Q| \rangle^2 \leq {a_{pp}}^2$ where ${a_{pp}}^2 = \langle {\boldsymbol{u}_{\text{bulk}}}^2 \rangle / N_{pp}$. In this case $\langle l_{pp} \rangle$, eqn (D.1), is also over-predicted by $a_{pp} N_{pp}$ for a modified-Rouse chain near the surface, except in the limit:

$a_{pp} \to 0, N_{pp} \to \infty$ (in this continuous limit the modified-Rouse (reflected Gaussian) primitive path has the contour length of a true random walk).

These observations are made to demonstrate that reasonable definitions of N_e estimators under confinement using the S-coil assumption are generally different from eqn (D.5), and are far from straightforward to calculate.

Appendix E

Probability distributions of slip-spring lifetimes

Here we investigate probability distributions of the lifetimes of slip-springs using the slip-spring model that is presented in chapter 4. Here, as in section 4.4 we use the parameters: $N = 26$, $N_e^{SS} = 4$, and $N_s = 0.5$. However in this section all results are generated with constraint release switched off. The model runs for several relaxation times before any measurements are made such that all slip-spring lifetimes contributing to a distribution have slip-links that were initially created on a chain end. We define the lifetime of a given slip-spring as the difference between the time it was deleted and the time it was created:

$$\tau_{SS} = t_{\text{delete}} - t_{\text{create}} \tag{E.1}$$

Figure E.1 plots four probability distributions of slip-spring lifetimes, corresponding to slip-springs with an anchor whose position in the surface normal direction relative to a nearest surface, y_a, falls within one of four regions. Note that this plot is a normalized probability plot. The majority of lifetimes ($\approx 98 - 99\%$) satisfy $\tau_{SS} < 1$ ('blinking slip-springs') such that their contribution is not visible in figure E.1. The mean lifetime of slip-springs binned by anchor position is the same for each region. The virtual-spring force, found from eqn (4.3), differs from its bulk form when a slip-spring is located within a distance of order $\sqrt{N_s}b$ from the surface. Figure E.1 shows that there is a small change in the lifetime distribution for anchors located within $\approx 2\sqrt{N_s}b$ from a surface. For anchors

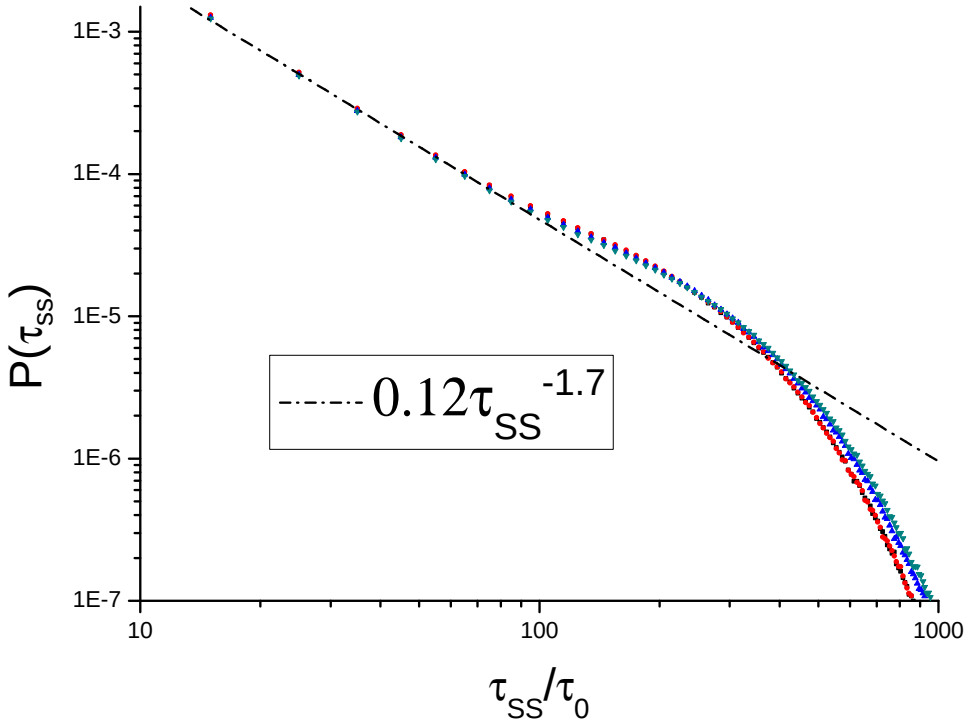

Figure E.1: Probability distributions of the slip-spring lifetime, τ_{SS}, for slip-springs with surface normal anchor position, y_a, in different regions relative to the surface. The regions have a surface normal width of $L_c/24 = 1.04\sqrt{N_s}b$. Black squares: $y_a < 1.04\sqrt{N_s}b$; red circles: $1.04\sqrt{N_s}b < y_a < 2.08\sqrt{N_s}b$; blue triangles: $2.08\sqrt{N_s}b < y_a < 3.12\sqrt{N_s}b$; olive triangles: centre channel region.

satisfying $2.08\sqrt{N_s}b < y_a < 3.12\sqrt{N_s}b$ (blue triangles), already the distribution of slip-spring lifetimes is very similar to that of slip-springs located in the channel centre (olive triangles). Figure E.2 plots probability distributions of slip-spring lifetimes which depend on the centre of mass position of the chains that the slip-spring had occupied at the time of its deletion. Figure E.3 plots the mean for each distribution in figure E.2, in addition to the distributions of other regions in the channel that were not included in figure E.2. The mean lifetime as a function of chain centre of mass position at the time of deletion is not uniform across the channel. However it is apparent from figure E.5 that the density of chains corresponding to the data-point closest to the surface in figure E.3, that shows a marked increase in slip-spring lifetime with respect to the other regions, is low.

The most notable difference in slip-spring behaviour across the channel is characterised by figure E.4, which plots the mean lifetime of slip-springs that are deleted by passing through a different end to the one upon which they were created, $\langle \tau_{SS} \rangle_{\text{switch}}$. For this quantity the

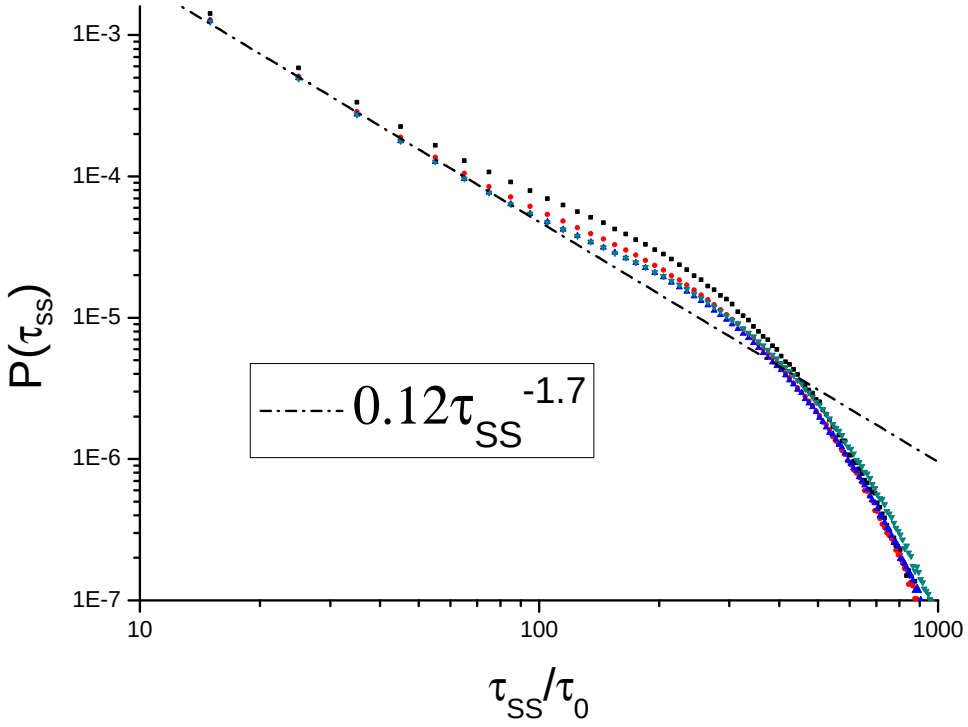

Figure E.2: Probability distributions of the slip-spring lifetime, τ_{SS}, for slip-springs binned by the surface normal centre of mass position, y_{cm}, of chains occupied by the slip-spring at the time of slip-spring deletion, into different regions relative to the surface. The regions have a surface normal width of $L_c/24 = 1.04\sqrt{N_s}b \approx 0.14\sqrt{\left\langle \boldsymbol{R}_{\mathrm{e,bulk}}{}^2 \right\rangle}$. Black squares: $y_{\mathrm{cm}} < 1.04\sqrt{N_s}b$; red circles: $1.04\sqrt{N_s}b < y_{\mathrm{cm}} < 2.08\sqrt{N_s}b$; blue triangles: $2.08\sqrt{N_s}b < y_{\mathrm{cm}} < 3.12\sqrt{N_s}b$; olive triangles: centre channel region.

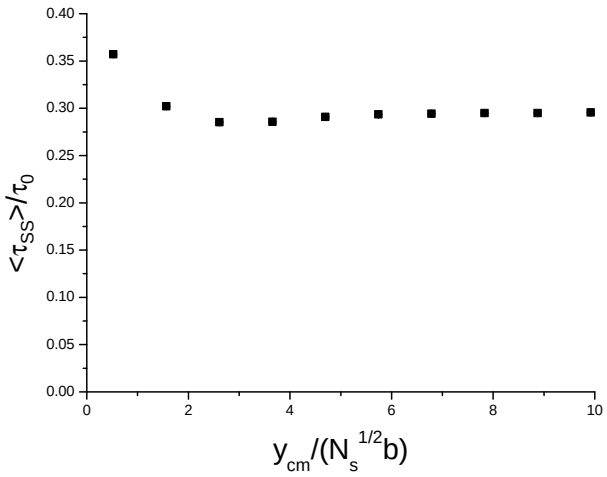

Figure E.3: Mean lifetime of all slip-springs, $\langle \tau_{SS} \rangle$, in a region in which the centre of mass of the occupied chain is located at the time of deletion. Plotted verses the mid-point of the region.

behaviour is very similar whether slip-springs are binned by their anchor position or the chain centre of mass position at the time of deletion. $\langle \tau_{SS} \rangle_{\text{switch}}$ becomes progressively shorter approaching the surface for $y_a < 3\sqrt{N_s}b$. Such a chain end switching event may often correspond with a displacement of the chain centre of mass of order the chain size, and correspondingly $\langle \tau_{SS} \rangle_{\text{switch}}$ is expected to roughly represent a reptation time. For this reason the centre of mass motion near the surface should be faster than far from the surface. We do indeed find that the centre of mass mean square displacement in the surface parallel direction is approximately $5-10\%$ greater at $t \approx \langle \tau_{SS} \rangle_{\text{switch}}$ for chains very close to the surface with respect to those in the channel centre. We do not find that this factor increases, nor that the behaviour of the distributions, figures E.1 and E.2, changes, if N is increased whilst fixing N_e^{SS} and N_s. Therefore, since all differences in slip-spring behaviour across the channel are rather small, we consider it reasonable to not introduce constraints on which slip-springs in the channel may be paired. When constraint release is switched on the small differences in the slip-spring lifetime distributions discussed here almost completely disappear.

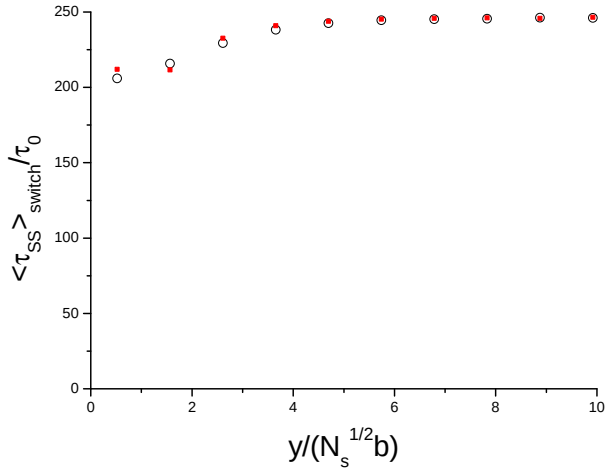

Figure E.4: Mean lifetime of slip-springs that cross ends, $\langle \tau_{SS} \rangle_{\text{switch}}$. Open circles: binned by anchor position; red squares: binned by chain centre of mass position. Plotted verses the mid-point of the region that the slip-spring is binned into.

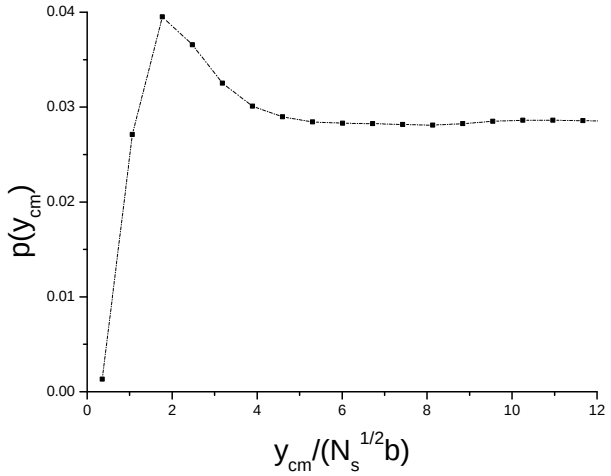

Figure E.5: Chain centre of mass occupational probability near a surface, $N = 26$.

Appendix F

Surface slip simulations: testing the GPU code

The GPU code that was employed in chapter 5 has been validated at equilibrium via comparison of both static and dynamic observables with pre-existing CPU code. In addition, a preliminary shear study using short chains is presented here. The flow set-up is identical to that described in chapter 5. Figure F.1a compares the steady-state monomer velocity profiles for a small system comprising surface tethered and free chains with $n = 64$ bonds, using either the CPU or GPU codes. The results are clearly in close agreement. It is also found that the relative error in film stress using the GPU code with respect to the CPU code is less than 1% in the simulation corresponding to figure F.1.

There is one important difference between the GPU and CPU applications. The GPU code uses single floating point arithmetic for updating particle positions. The choice of single floating point numbers vastly reduces computation time using the Nvidia Tesla $K10$ architecture. The use of single floats also allows for more efficient use of the GPU 'texture' memory cache [143], such that if possible the use of single floats is favourable. However, this drop in precision leads to a small increase in numerical errors and can therefore lead to an increase in temperature if the thermostat is not duly adjusted. The temperature profile corresponding to the flow profile, figure F.1a, is shown in figure F.1b. Note that this temperature profile is also representative of the same simulations under equilibrium conditions (The shear-rate is far too weak to influence the temperature profile in all cases considered in chapter 5 using the chosen thermostat conditions and time-step). There is the possibility of either decreasing the time-step or increasing the thermostat friction

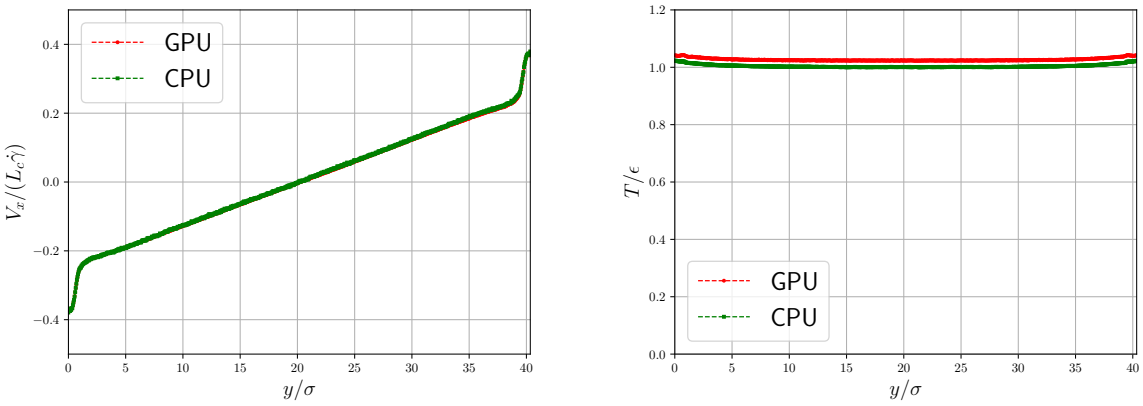

(a) (b)

Figure F.1: CPU/GPU code comparison at applied shear-rate $\dot{\gamma} = 5 \times 10^{-3}{\tau_{\mathrm{LJ}}}^{-1}$ using chains with $n = 64$.
(a) Bead velocity in the flow direction.
(b) Temperature profiles.

constant in order to remove the small additional deviations from a uniform temperature profile, $T/\epsilon = 1$. Since the small difference between CPU and GPU temperature profiles in figure F.1b leads to no discernible differences in all observables of interest, and taking into account computational limitations, the choice is instead made to leave the simulation conditions as they are. The influence of the existing deviation from a uniform temperature profile at the surface using the CPU code has already been shown to be negligible via comparison with lower time-steps using equilibrium observables. Thus we keep the time-step $\Delta t = 0.01\tau_{\mathrm{LJ}}$, and the thermostat friction constant, $\xi_{\mathrm{MD}} = 0.5m_b/\tau_{\mathrm{LJ}}$.

A more important issue with using single floats arises for the shear simulations of the $n = 256$ system considered in chapter 5. In that case the shear-rates of interest are sufficiently small such that the precision necessary to deform the melt every time-step is not available using single floats. Instead the deformations can be separated by larger time intervals. The interval between deformations in the simulations using $n = 256$ is $10\tau_{\mathrm{LJ}}$, equivalent to every 1000 computational time-steps. This time interval is short compared to the characteristic chain relaxation times probed by the deformation. GPU simulations using such 'staccato' displacements have been compared with corresponding CPU simulations which make displacements every time-step whilst conserving the mean deformation

rate. At the relatively high applied shear-rates: $\dot{\gamma} = 2.5 \times 10^{-5} {\tau_{\mathrm{LJ}}}^{-1}$ and $\dot{\gamma} = 1 \times 10^{-4} {\tau_{\mathrm{LJ}}}^{-1}$, there are no discernible differences between the two deformation methods for all observables investigated. It has also been validated that such a protocol at the shear-rates of interest does not lead to deviations from the equilibrium temperature profile.

Bibliography

[1] Thanks to Jean-Louis Barrat for pointing this out.

[2] http://www.openmp.org/.

[3] B. C. Abberton, W. K. Liu, and S. Keten. Anisotropy of Shear Relaxation in Confined Thin Films of Unentangled Polymer Melts. Macromolecules, 48:7631–7639, 2015.

[4] J. L. Adams, S. M. Fielding, and P. D. Olmsted. The interplay between boundary conditions and flow geometries in shear banding: Hysteresis, band configurations, and surface transitions. J. Non-Newt. Flu. Mech., 151(1-3):101–118, 2008.

[5] A. Ajdari, F. Brochard-Wyart, P.-G. De Gennes, and L. Leibler. Slippage of an entangled polymer melt on a grafted surface. Physica A, 204(1):17–39, 1994.

[6] A Ajdari, F. Brochard-Wyart, C. Gay, P. G. De Gennes, and J. Viovy. Drag on a Tethered Chain Moving in a Polymer Melt. Journal de Physique II, 5(4):491–495, 1995.

[7] R. L. C. Akkermans and W. J. Briels. Coarse-grained dynamics of one chain in a polymer melt. J. Chem. Phys., 113(15):6409–6422, 2000.

[8] Giuseppe Allegra, Guido Raos, and Michele Vacatello. Theories and simulations of polymer-based nanocomposites: From chain statistics to reinforcement. Prog. Polym. Sci., 33:683–731, 2008.

[9] M. P. Allen and D. J. Tildesley. Computer Simulation of Liquids. Oxford Science Publications, 1987.

[10] D. Amin. Computational and theoretical modelling of self-healable polymer materials. PhD thesis, 2016.

[11] Rolf Auhl, Ralf Everaers, Gary S. Grest, Kurt Kremer, and Steven J. Plimpton. Equilibration of Long Chain Polymer Melts in Computer Simulations. J. Chem. Phys., 119:12718, 2003.

[12] C. Baig, V. G. Mavrantas, and M. Kröger. Flow Effects on Melt Structure and Entanglement Network of Linear Polymers: Results from a Nonequilibrium Molecular Dynamics Simulation Study of a Polyethylene Melt in Steady Shear. Macromolecules, 43:6886–6902, 2010.

[13] J. Baschnagel and F. Varnik. Computer simulations of supercooled polymer melts in the bulk and in confined geometry. J. Phys.: Condens. Matter, 17:R851, 2005.

[14] Windsor Bisbee, Jian Qin, and Scott T. Milner. Finding the Tube with Isoconfigurational Averaging. Macromolecules, 44:8972–8980, 2011.

[15] W. B. Black and M. D. Graham. Wall-slip and polymer melt flow instability. Phys. Rev. Lett., 77(5):956–959, 1996.

[16] H. Bodiguel and C. Fretigny. Viscoelastic Properties of Ultrathin Polystyrene Films. Macromolecules, 40:7291–7298, 2007.

[17] V. A. H. Boudara and D. J. Read. Periodic "stick-slip" transition within a continuum model for entangled supramolecular polymers. Journal of Rheology, 62(249), 2018.

[18] P. E. Boukany and S-Q. Wang. Exploring Origins of Interfacial Yielding and Wall Slip in Entangled Linear Melts during Shear or after Shear Cessation. Macromolecules, 42:2222–2228, 2009.

[19] F. Brochard and P. G. De Gennes. Shear-Dependent Slippage at a Polymer/Solid Interface. Langmuir, 81:3033–3037, 1992.

[20] F. Brochard, C. Gay, and P. G. De Gennes. Slippage of polymer melts on grafted surfaces. Macromolecules, 29:377–382, 1996.

[21] H. R. Brown and T.P. Russell. Entanglements at Polymer Surfaces and Interfaces. Macromolecules, 29(2):798–800, 1996.

[22] J. Cao and A. E Likhtman. Simulating Startup Shear of Entangled Polymer Melts. ACS. Macro. Lett., 4(12):1376–1381, 2015.

[23] J. Cao and Z. Wang. Microscopic Picture of Constraint Release Effects in Entangled Star Polymer Melts. Macromolecules, 49(15):5677–5691, 2016.

[24] Jing Cao and Alexei E Likhtman. Time-dependent orientation coupling in equilibrium polymer melts. Phys. Rev. Lett., 104(20):207801, 2010.

[25] Jing Cao, Jian Qin, and Scott T. Milner. Simulating Constraint Release by Watching a Ring Cross Itself. Macromolecules, 47:2479–2486, 2014.

[26] Jing Cao, Jian Qin, and Scott T. Milner. Finding Entanglement Points in Simulated Polymer Melts. Macromolecules, 48:99–110, 2015.

[27] A. Cavallo, M. Müller, J. P. Wittmer, A. Johner, and K. Binder. Single chain structure in thin polymer films: corrections to Flory's and Silberberg's hypotheses. Journal of Physics: Condensed Matter, 17(20):S1697–S1709, 2005.

[28] D. Chandler. Introduction to Modern Statistical Mechanics. Oxford University Press, 1987.

[29] Wei-Liang Chen, Roselynn Cordero, Hai Tran, and Christopher K Ober. 50th Anniversary Perspective: Polymer Brushes: Novel Surfaces for Future Materials. Macromolecules, 50:4089–4113, 2017.

[30] A. Chennevière, F. Cousin, F. Boué, E. Drockenmuller, K. R. Shull, L. Léger, and F. Restagno. Direct Molecular Evidence of the Origin of Slip of Polymer Melts on Grafted Brushes. Macromolecules, 49:2348−2353, 2016.

[31] Yoon-Kyoung. Cho, H. Watanabe, and S. Granick. Dielectric response of polymer films confined between mica surfaces. J. Chem. Phys., 110(19):9688, 1999.

[32] K C Daoulas, V A Harmandaris, and V G Mavrantzas. Detailed Atomistic Simulation of a Polymer Melt/Solid Interface: Structure, Density, and Conformation

of a Thin Film of Polyethylene Melt Adsorbed on Graphite. Macromolecules, 38: 5780–5795, 2005.

[33] P. G. De Gennes. Mechanics of liquids. C. R. Acad. Sci. Paris, 288 B(219), 1979.

[34] P. G. De Gennes. Scaling Concepts In Polymer Physics. Cornell University Press, 1979.

[35] P. G. De Gennes. Conformations of Polymers Attached to an Interface. Macromolecules, 13:1069–1075, 1980.

[36] S. R. de Groot and P. Mazur. Non-Equilibrium Thermodynamics. North Holland Publication Company, 1962.

[37] Morton. M. Denn. Extrusion Instabilities and Wall Slip. Annu. Rev. Fluid Mech., 33:265–287, 2001.

[38] D. I. Dimitrov, A. Milchev, and K. Binder. Local Viscosity in the Vicinity of a Wall Coated by Polymer Brush from Green–Kubo Relations. Macromolecular Theory and Simulations, 17:313–318, 2008.

[39] M. Doi and S. F. Edwards. The Theory of Polymer Dynamics. Clarendon Press, 1986.

[40] J. R. Dorgan and N. A. Rorrer. Molecular Scale Simulation of Homopolymer Wall Slip. Phys. Rev. Lett., 110:176001, 2013.

[41] E. Durliat, H. Hervet, and L. Léger. Influence of grafting density on wall slip of a polymer melt on a polymer brush. Europhys. Lett., 38(5):383–388, 1997.

[42] A. Einstein. On the movement of small particles suspended in stationary liquids required by the molecular-kinetic theory of heat. Annalen der Physik, 17:549–560, 1905.

[43] E. Eisenriegler, K. Kremer, and K. Binder. Adsorption of polymer chains at surfaces: Scaling and Monte Carlo analyses. J. Chem. Phys., 77(12):6296–6320, 1982.

[44] D. J. Evans and G. Morriss. Statistical mechanics of nonequilibrium liquids. Cambridge, 2008.

[45] R. Everaers, S. K. Sukumaran, G. S. Grest, C. Svaneborg, A. Sivasubramanian, and K. Kremer. Rheology and Microscopic Topology of Entangled Polymeric Liquids. Science, 303(5659):823, 2004.

[46] Ralf Everaers. Topological versus rheological entanglement length in primitive-path analysis protocols, tube models, and slip-link models. Phys. Rev. E., 86:022801, 2012.

[47] J Farago, H Meyer, J Baschnagel, and A N Semenov. Hydrodynamic and viscoelastic effects in polymer diffusion. Journal of Physics: Condensed Matter, 24(28): 284105–284115, 2012.

[48] J. Farago, H. Meyer, J Baschnagel., and A. N. Semenov. Mode-coupling approach to polymer diffusion in an unentangled melt. II. The effect of viscoelastic hydrodynamic interactions. Phys. Rev. E., 85:051807, 2012.

[49] J. Farago, A. N. Semenov, H. Meyer, J. P. Wittmer, A. Johner, and J. Baschnagel. Mode-coupling approach to polymer diffusion in an unentangled melt. I. The effect of density fluctuations. Phys. Rev. E., 85:051806, 2012.

[50] N. F. Fatkullin, T. M. Shakirov, and N. A. Balakirev. Why does the rouse model fairly describe the dynamic characteristics of polymer melts at molecular masses below critical mass? POLYMER SCIENCE SERIES A, 52(1):72–81, 2010.

[51] J. D. Ferry. Viscoelastic properties of polymers. Wiley, 1980.

[52] L. J. Fetters, D. J. Lohse, D. Richter, T. A. Witten, and A. Zirkel. Connection Between Polymer Molecular-Weight, Density, Chain Dimensions, and Melt Viscoelastic Properties. Macromolecules, 27:4639, 1994.

[53] P. J. Flory. Principles of Polymer Chemistry. Cornell University Press, 1953.

[54] A. Galuschko, M. Lang, T. Kreer, and J. U. Sommer. Monte Carlo Simulation of Thin Film Polymer Melts. Soft Materials, 12:S49–S55, 2014.

[55] Herbert Goldstein. Classical Mechanics. Addison-Wesley Publishing Company, 1980.

[56] R. S. Graham, A. E. Likhtman, T. C. B. McLeish, and S. T. Milner. Microscopic theory of linear, entangled polymer chains under rapid deformation including chain stretch and convective constraint release. J. Rheol., 47:1171, 2003.

[57] S. Granick and Hsuan-Wei Hu. Nanorheology of Confined Polymer Melts. 1. Linear Shear Response at Strongly Adsorbing Surfaces. Langmuir, 10:3857–3866, 1994.

[58] V A Harmandaris, V G Mavrantzas, D N Theodorou, M Kröger, J Ramirez, H C Öttinger, and D Vlassopoulos. Crossover from the Rouse to the Entangled Polymer Melt Regime: Signals from Long, Detailed Atomistic Molecular Dynamics Simulations, Supported by Rheological Experiments. Macromolecules, 36:1376–1387, 2003.

[59] S. G. Hatzikiriakos. Wall slip of molten polymers. Prog. Polym. Sci., 37(3):624, 2012.

[60] S.G. Hatzikiriakos, C. W. Stewart, and D. M. Dealy. Effect of Surface coatings on Wall Slip of LLDPE. Intern. Polymer Processing VIII, 8:3033, 1993.

[61] M Henot, A. Chennevière, E. Drockenmuller, L Léger, and F Restagno. Comparison of the Slip of a PDMS Melt on Weakly Adsorbing Surfaces Measured by a New Photobleaching-Based Technique. Macromolecules, 50:5592–5598, 2017.

[62] Ji Xuan Hou, Carsten Svaneborg, Ralf Everaers, and Gary S. Grest. Stress Relaxation in Entangled Polymer Melts. Phys. Rev. Lett., 105:068301, 2010.

[63] R. S. Hoy and G. S. Grest. Entanglements of an End-Grafted Polymer Brush in a Polymeric Matrix. Macromolecules, 40:8389–8395, 2007.

[64] R. S. Hoy, K. Foteinopoulou, and M. Kröger. Topological analysis of polymeric melts: Chain length effects and fast-converging estimators for entanglement length. Phys. Rev. E., 80:031803, 2009.

[65] Hsuan-Wei Hu and Steve Granick. Viscoelastic Dynamics of Confined Polymer. Science, 258:1339–1342, 1991.

[66] P. Ilg, H. C. Ottinger, and M. Kröger. Systematic time-scale-bridging molecular dynamics applied to flowing polymer melts. Phys. Rev. E., 79:011802, 2009.

[67] Patrick Ilg, Vlasis Mavrantzas, and Hans Christian Öttinger. Multiscale Modeling and Coarse Graining of Polymer Dynamics: Simulations Guided by Statistical Beyond-Equilibrium Thermodynamics. In D. Gujrati Purushottam and Arkadii I. Leonov, editors, Modeling and Simulations in Polymers, volume 7. Wiley, 2009.

[68] J. H. Irving and J. G. Kirkwood. The Statistical Mechanical Theory of Transport Processes. IV. The Equations of Hydrodynamics. J. Chem. Phys., 18(817), 1950.

[69] S. Jeong, S. Cho, J. M. Kim, and C. Baig. Molecular mechanisms of interfacial slip for polymer melts under shear flow. J. Rheol., 61, 2017.

[70] Ronald G. Larson John M. Dealy. Structure and Rheology of Molten Polymers. Hanser, 2006.

[71] Y. M. Joshi, A. K. Lele, and R. A. Mashelkar. Molecular Model for Wall Slip: Role of Convective Constraint Release. Macromolecules, 34:3412–3420, 2001.

[72] J. T. Kalathi, S. K. Kumar, M. Rubinstein, and G. S. Grest. Rouse mode analysis of chain relaxation in homopolymer melts. Macromolecules, 47:6925–6931, 2014.

[73] A Karatrantos, N. Clarke, R. J. Composto, and K. I. Winey. Topological entanglement length in polymer melts and nanocomposites by a DPD polymer model. Soft Matter, 9:3877–3884, 2013.

[74] Argyrios Karatrantos, Russell J. Composto, Karen I. Winey, Martin Kröger, and Nigel Clarke. Entanglements and Dynamics of Polymer Melts near a SWCNT. Macromolecules, 45:7274−7281, 2012.

[75] Argyrios Karatrantos, Nigel Clarke, Russell J. Composto, and Karen I. Winey. Entanglements in polymer nanocomposites containing spherical nanoparticles. Soft Matter, 12:2567–2574, 2016.

[76] N. C. Karayiannis and M. Kröger. Combined Molecular Algorithms for the Generation, Equilibration and Topological Analysis of Entangled Polymers: Methodology and Performance. Int. J. Mol. Sci., 10:5054–5089, 2009.

[77] T. A. Kavassalis and J. Noolandi. New View of Entanglements in Dense Polymer Systems. Phys. Rev. Letts., 59:2674, 1987.

[78] J. Kirk and P. Ilg. Chain Dynamics in Polymer Melts at Flat Surfaces. Macromolecules, 50(9):3703–3718, 2017.

[79] Airidas Korolkovas, Cesar Rodriguez-Emmenegger, Andres Santos de los Pereira, Alexis Chennevière, Frédéric Restagno, Maximilian Wolff, Franz A. Adlmann, Andrew J. C. Dennison, and Philipp Gutfreund. Polymer brush collapse under shear flow. Macromolecules, 50:1215–1224, 2017.

[80] F. Kremer. Dynamics in Geometrical Confinement. Advances in Dielectrics. Springer, 2014.

[81] K. Kremer and G. S. Grest. Dynamics of entangled linear polymer melts: A molecular-dynamics simulation. J. Chem. Phys., 92:5057, 1990.

[82] M. Kröger. Simple models for complex nonequilibrium fluids. Physics Reports, 390: 453, 2004.

[83] M. Kröger and S. Hess. Rheological Evidence for a Dynamical Crossover in Polymer Melts via Nonequilibrium Molecular Dynamics. Phys. Rev. Lett., 85(5):1128, 2000.

[84] Martin Kröger. Shortest multiple disconnected path for the analysis of entanglements in two- and three-dimensional polymeric systems. Computer Physics Communications, 168(3):209–232, 2005.

[85] L. D. Landau and E. M. Lifshitz. Statistical Physics. Addison-Wesley Publishing Company, 1958.

[86] M. Lang, M. Werner, R. Dockhorn, and T. Kreer. Arm Retraction Dynamics in Dense Polymer Brushes. Macromolecules, 49(14):5190–5201, 2016.

[87] R. G. Larson. Constitutive Relations for Polymer Melts and Solutions. Butterworth Publishers, 1988.

[88] R. G. Larson. Oxford University Press, 1999.

[89] J. K. Lee, B. Akgun, Z. Jiang, S. Narayanan, and M. D. Foster. Altering surface fluctuations by blending tethered and untethered chains. Soft Matter, 13:8264–8270, 2017.

[90] N-.K. Lee, J. Farago, H. Meyer, J. P. Wittmer, J. Baschnagel, and S. P. Obukhov. Non-ideality of polymer melts confined to nanotubes. EPL, 93:48002, 2011.

[91] Nam-Kyung Lee, Diddo Diddens, Hendrik Meyer, and Albert Johner. Local Chain Segregation and Entanglements in a Confined Polymer Melt. Phys. Rev. Letts., 17: 067802(5), 2017.

[92] Sanghun. Lee, A. V. Lyulin, Curtis. W. Frank, and D. Y. Yoon. Interface characteristics of polystyrene melts in free-standing thin films and on graphite surface from molecular dynamics simulations. Polymer, 116:540, 2017.

[93] A. E. Likhtman. Short course: Entangled Polymer Dynamics. http://www.personal.reading.ac.uk/~sms06al2/short_course.

[94] A. E. Likhtman. Single-Chain Slip-Link Model of Entangled Polymers: Simultaneous Description of Neutron Spin−Echo, Rheology, and Diffusion. Macromolecules, 38 (14):6128–6139, 2005.

[95] A. E Likhtman. Whither tube theory. J. Non-Newt. Fluid. Mech., 157(3):158–161, 2009.

[96] A. E. Likhtman. Viscoelasticity and molecular rheology. In K. Matyjaszewski and M. Müller, editors, Polymer Science: A Comprehensive Reference, volume 10, page 133. Elsevier B.V, 2012.

[97] A. E. Likhtman and T. C. B. McLeish. Quantitative Theory for Linear Dynamics of Linear Entangled Polymers. Macromolecules, 35:6332–6343, 2002.

[98] A. E. Likhtman and A. N. Semenov. An advance in the theory of strongly segregated polymers. Europhysics Letters, 51(3):307–313, 2000.

[99] A.E. Likhtman. The tube axis and entanglements in polymer melts. Soft Matter, 10:1895–1904, 2014.

[100] Alexei E Likhtman and M Ponmurugan. Microscopic Definition of Polymer Entanglements. Macromolecules, 47:1470−1481, 2014.

[101] Alexei E. Likhtman, Sathish K. Sukumaran, and Jorge Ramirez. Linear Viscoelasticity from Molecular Dynamics Simulation of Entangled Polymers. Macromolecules, 40(18):6748–6757, 2007.

[102] Y-H Lin. Number of Entanglement Strands per Cubed Tube Diameter, a Fundamental Aspect of Topological Universality in Polymer Viscoelasticity. Macromolecules, 20:3080–3083, 1987.

[103] G. Luengo, Franz-Josef. Schmitt, R. Hill, and J. Israelachvili. Thin Film Rheology and Tribology of Confined Polymer Melts: Contrasts with Bulk Properties. Macromolecules, 30:2482–2494, 1997.

[104] L Léger, H Hervet, G Massey, and E Durliat. Wall slip in polymer melts. J. Phys: Condens. Mat., 9:7719–7740, 1997.

[105] E. Masnada, S. Merabia, M. Couty, and J-L. Barrat. Entanglement-induced reinforcement in polymer nanocomposites. Soft Matter, 9:10532–10544, 2013.

[106] Yuichi Masubuchi, Ankita Pandey, Yoshifumi Amamoto, and Takashi Uneyama. Orientational cross correlations between entangled branch polymers in primitive chain network simulations. J. Chem. Phys., 147:184903, 2017.

[107] M. W. Matsen. Investigating the dominant corrections to the strong-stretching theory for dry polymeric brushes. J. Chem. Phys., 121:1938–1948, 2004.

[108] M. W. Matsen and P. Mahmoudi. Segregation of chain ends to the surface of a polymer melt. The European Physical Journal E, 37(8):78, 2014.

[109] G. B. McKenna. Commentary on rheology of polymers in narrow gaps. Eur. Phys. J. E., 19:101–108, 2006.

[110] T. C. B. McLeish. Rheology of linear and branched polymers, page 79. Scottish Graduate Textbook Series. IOP, 2000.

[111] T. C. B. McLeish. Tube theory of entangled polymer dynamics. Adv. Phys., 51(6): 1379–1527, 2002.

[112] D. W. Mead and R. G. Larson. Macromolecules, 31:7895–7914, 1998.

[113] H Meyer, J P Wittmer, T Kreer, P Beckrich, A Johner, J Farago, and J Baschnagel. Static Rouse Modes and Related Quantities: Corrections to Chain Ideality in Polymer Melts. Eur. Phys. J. E, 26:25–33, 2008.

[114] V. Mhetar and L. A. Archer. Slip in Entangled Polymer Solutions. Macromolecules, 31(19):6639–6649, 1998.

[115] K. B. Migler, H. Hervet, and L. Léger. Slip Transition of a Polymer Melt under Shear Stress. Phys. Rev. Lett., 70(3):283–290, 1993.

[116] S. T. Milner. Polymer Brushes. Science, 251(4996):905–914, 1991.

[117] S. T. Milner. Predicting the Tube Diameter in Melts and Solutions. Macromolecules, 38:4929, 2005.

[118] S. T. Milner and T. C. B. Mcleish. Reptation and contour-length fluctuations in melts of linear polymers. Phys. Rev. Letts., 81(3):725–728, 1998.

[119] S. T. Milner, T. C. B. McLeish, and A. E. Likhtman. J. Rheol., 45(2), 2001.

[120] C. Mischler, J. Baschnagel, and K. Binder. Polymer Films in the Normal-Liquid and Supercooled State: A Review of Recent Monte Carlo Simulation Results. Adv. Coll. Int. Sci., 94(1-3):197–227, 2001.

[121] E. W. Ng and M. Geller. A Table of Integrals of the Error Functions. J. Res. Nat. Bur. Standards. - B. Math. Sci., 73B(1), 1969.

[122] Anoosheh Niavarani and Nikolai V Priezjev. Slip boundary conditions for shear flow of polymer melts past atomically flat surfaces. Phys. Rev. E., 77:041606, 2008.

[123] W G Noid, Jhih-Wei Chu, Gary S Ayton, and Gregory A Voth. Multiscale coarse-graining and structural correlations: connections to liquid-state theory. J. Phys. Chem. B., 111(16):4116–4127, 2007.

[124] W. G. Noid, G. S. Ayton, S. Izvekov, and G. A. Voth. The Multiscale Coarse-Graining Method, page 21. CRC Press, 2009.

[125] W. Paul and G. D. Smith. Structure and dynamics of amorphous polymers: computer simulations compared to experiment and theory. Reports on Progress in Physics, 67(7):1117–1185, 2004.

[126] W. Paul, G. D. Smith, D. Y. Yoon, B. Farago, S. Rathgeber, A. Zirkel, L. Willner, and D. Richter. Chain motion in an unentangled polyethylene melt: A critical test of the rouse model by molecular dynamics simulations and neutron spin echo spectroscopy. Phys. Rev. Lett., 80(11):2346–2349, 1998.

[127] J. Peanasky, L. L. Cai, and S. Granick. Nanorheology of Confined Polymer Melts. 3. Weakly Adsorbing Surfaces. Langmuir, 10:3874–3879, 1994.

[128] E. A. J. F. Peters and Th. M. A. O. M. Barenbrug. Efficient Brownian dynamics simulation of particles near walls. I. Reflecting and absorbing walls. Phys. Rev. E., 66:056701, 2002.

[129] N. V. Priezjev. Effect of surface roughness on rate-dependent slip in simple fluids. J. Chem. Phys., 127(14):144708, 2007.

[130] N. V. Priezjev. Shear rate threshold for the boundary slip in dense polymer films. Phys. Rev. E., 80:031608, 2009.

[131] Nikolai V. Priezjev. Effect of surface roughness on rate-dependent slip in simple fluids. J. Chem. Phys., 127:144708, 2007.

[132] Nikolai V Priezjev and Sandra M Troian. Molecular origin and dynamic behavior of slip in sheared polymer films. Phys. Rev. Lett., 92(1):018302, 2004.

[133] J. Ramirez and A. E. Likhtman. http://www.reptate.com/.

[134] A. Ramirez-Hernandez, B. L. Peters, L. Schneider, M. Andreev, and J. D. Schieber. A multi-chain polymer slip-spring model with fluctuating number of entanglements: Density fluctuations, confinement, and phase separation. J. Chem. Phys., 146: 014903, 2017.

[135] A. Ramirez-Hernandez, B. L. Peters, L. Schneider, M. Andreev, J. D. Schieber, M. Müller, M. Kröger, and J. J. de Pablo. A detailed examination of the topological constraints of lamellae-forming block copolymers. Macromolecules, 51:2110–2124, 2018.

[136] Jorge Ramírez, Sathish K Sukumaran, Bart Vorselaars, and Alexei E Likhtman. Efficient on the fly calculation of time correlation functions in computer simulations. J. Chem. Phys., 133(15):154103, 2010.

[137] M. Reiner. The Deborah Number. Physics Today, 17(1):62, 1964.

[138] D. Reith, A. Milchev, P. Vernau, and K. Binder. Computer Simulation Studies of Chain Dynamics in Polymer Brushes. Macromolecules, 45:4381–4393, 2014.

[139] N. A. Rorrer and J. R. Dorgan. Molecular-scale simulation of cross-flow migration in polymer melts. Phys. Rev. E., 90:052603, 2014.

[140] P. E. Rouse Jr. A theory of the linear viscoelastic properties of dilute solutions of coiling polymers. J. Chem. Phys., 21:1272, 1953.

[141] Michael Rubinstein and Ralph H. Colby. Polymer Physics. Oxford University Press, Oxford, UK, 2003.

[142] S. M. Sabzevari, I. Cohen, and P. M. Wood-Adams. Wall Slip of Bidisperse Linear Polymer Melts. Macromolecules, 47:3154–3160, 2014.

[143] Jason Sanders and Edward Kandrot. CUDA by Example. Addison-Wesley, Upper Saddle River, NJ, 2010.

[144] J. Sarabadani, A. Milchev, and T. Vilgis. Molecular Dynamic Study of the Structure and Dynamics of Polymer Melt at Solid Surfaces. J. Chem. Phys., 141:044907, 2014.

[145] A. N. Semenov and A. Johner. Theoretical notes on dense polymers in two dimensions. Eur. Phys. J. E., 12(3):469–480, 2003.

[146] V. Sethuraman, D. Kipp, and V. Ganesan. Entanglements in Lamellar Phases of Diblock Copolymers. Macromolecules, 48:6321–6328, 2015.

[147] S. Shanbhag and M. Kröger. Primitive path networks generated by annealing and geometrical methods: Insights into differences. Macromolecules, 40:2897–2903, 2007.

[148] A. Silberberg. Distribution of Conformations and Chain Ends near the Surface of a Melt of Linear Flexible Macromolecules. J. Coll. Int. Sci., 90(1):86–91, 1981.

[149] M. K. Singh, P. Ilg, R. M. Espinosa-Marzal, M. Kröger, and N. D. Spencer. Polymer Brushes under Shear: Molecular Dynamics Simulations Compared to Experiments. Langmuir, 31(16):4798–4805, 2015.

[150] A. M. Skvortsov, F. A. M. Leermakers, and G. J. Fleer. Equivalence of chain conformations in the surface region of a polymer melt and a single Gaussian chain under critical conditions. J. Chem. Phys., 139(5):054907, 2014.

[151] K. A. Smith, M. Vladkov, and J-L. Barrat. Polymer Melt near a Solid Surface. Macromolecules, 38(2):571–580, 2005.

[152] M. Solar, L. Yelash, B. Virnau, K. Binder, and W. Paul. Polymer Dynamics in a Polymer-Solid Interphase: Molecular Dynamics Simulations of 1,4-Polybutadiene At a Graphite Surface. Soft Materials, 12(1):S80–S89, 2014.

[153] S S Sternstein and Ai-Jun Zhu. Reinforcement Mechanism of Nanofilled Polymer Melts As Elucidated by Nonlinear Viscoelastic Behavior. Macromolecules, 35: 7262–7273, 2002.

[154] S. K. Sukumaran and A. E. Likhtman. Modeling entangled dynamics: comparison between stochastic single-chain and multichain models. Macromolecules, 42(12): 4300–4309, 2009.

[155] S. K. Sukumaran, G. S. Grest, K. Kremer, and R. Everaers. Identifying the primitive path mesh in entangled polymer liquids. J. Pol. Sci. B: Pol. Phys., 43:917, 2005.

[156] D. M. Sussman. Spatial distribution of entanglements in thin free-standing films. Phys. Rev. E., 94:012503, 2016.

[157] D. M. Sussman, W-S. Tung, K. I. Winey, K. S. Schweizer, and R. A. Riggleman. Entanglement Reduction and Anisotropic Chain and Primitive Path Conformations in Polymer Melts under Thin Film and Cylindrical Confinement. Macromolecules, 47:6462–6472, 2014.

[158] M. A. Tchesnokov, J. Molenaar, J. J. M. Slot, and R. Stepanyan. A molecular model for cohesive slip at polymer melt/ solid interfaces. J. Chem. Phys., 122(21):214711, 2005.

[159] P. A Thompson and M. O Robbins. Shear flow near solids: Epitaxial ordering and flow boundary conditions. Phys. Rev. A., 41(12):6830–6837, 1990.

[160] B. D. Todd, D. J. Evans, and P. J. Daivis. Pressure tensor for inhomogeneous fluids. Phys. Rev. E., 52(2):1627–1638, 1995.

[161] Nariya Uchida, Gary S. Grest, and Ralf Everaers. Viscoelasticity and primitive path analysis of entangled polymer liquids: From f-actin to polyethylene. J. Chem. Phys., 128:044902, 2008.

[162] F. Varnik, J. Baschnagel, and K. Binder. Molecular dynamics results on the pressure tensor of polymer films. J. Chem. Phys., 113(10):4444, 2000.

[163] Fathollah Varnik and Kurt Binder. Multiscale modeling of polymers at interfaces. Int. J. Mat. Sci., 100(11):1494–1502, October 2009.

[164] Mihail Vladkov. Modeling interfacial effects on transport properties. PhD thesis, 2007.

[165] Mihail Vladkov and Jean-Louis Barrat. Local Dynamics and Primitive Path Analysis for a Model Polymer Melt near a Surface. Macromolecules, 40(10):3797–3804, 2007.

[166] S-Q. Wang and P. A. Drda. Superfluid-Like Stick-Slip Transition in Capillary Flow of Linear Polyethylene Melts. 1. General Features. Macromolecules, 29:2627–2632, 1996.

[167] S-Q. Wang and P. A. Drda. Macromolecules, 29:4115–4119, 1996.

[168] S-Q. Wang, S. Ravindranath, and P. E. Boukany. Homogeneous shear, wall slip, and shear banding of entangled polymeric liquids in simple-shear rheometry: A roadmap of nonlinear rheology. Macromolecules, 44:183–190, 2011.

[169] Z. Wang, A. E. Likhtman, and Ronald G. Larson. Segmental Dynamics in Entangled Linear Polymer Melts. Macromolecules, 45(8):3557–3570, 2012.

[170] M. P. Weir, D. W. Johnson, S. C. Boothroyd, R. C. Savage, R. L. Thompson, S. M. King, S. E. Rogers, K. S. Coleman, and N. Clarke. Distortion of Chain Conformation and Reduced Entanglement in Polymer–Graphene Oxide Nanocomposites. ACS. Macro. Lett., 5:430, 2016.

[171] J. P. Wittmer, H. Meyer, A. Johner, S. Obukhov, L. Mattioni, M. Müller, and A. N. Semenov. Long Range Bond-Bond Correlations in Dense Polymer Solutions. Phys. Rev. Lett., 93:147801, 2004.

[172] J. P. Wittmer, P. Beckrich, J. Johner, A. N. Semenov, S. P. Obukhov, H. Meyer, and J. Baschnagel. Why polymer chains in a melt are not random walks. EPL, 77 (5):56003, 2007.

[173] N. J. Woo, E. S. G. Shaqfeh, and B. Khomani. Effect of confinement on dynamics and rheology of dilute DNA solutions. I. Entropic spring force under confinement and a numerical algorithm. J. Rheol., 48(2):281–298, 2004.

[174] H. Yamakawa. Modern theory of polymer solutions. Harper & Row, 1971.

[175] L. Yelash, P. Virnau, K. Binder, and W. Paul. A slow process in confined polymer melts: layer exchange dynamics at a polymer solid interface. Phys. Rev. E., 82: 050801, 2010.

[176] J. E. Zabel. Deviations from chain ideality. PhD thesis, Université de Strasbourg.

[177] W. Zhang, E. D. Gomez, and S. T. Milner. Surface-Induced Chain Alignment of Semiflexible Polymers. Macromolecules, 49:963–971, 2016.

[178] X. Zhou, D. Andrienko, L. Delle Site, and K. Kremer. Dynamic surface decoupling in a sheared polymer melt. Europhys. Lett., 70:264–270, 2005.

[179] J. Zhu. Multiscale Computer Simulation Studies of Entangled Branched Polymers. PhD thesis, Department of Mathematics and Statistics, University of Reading, 2016.

[180] Jian Zhu, Alexei E Likhtman, and Zuowei Wang. Arm retraction dynamics of entangled star polymers: A forward flux sampling method study. Journ. Chem. Phys., 147:0044907, 2017.

[181] J. M. Ziman. Principles of the Theory of Solids. Cambridge University Press, 1964.

[182] H. C. Öttinger. Tools and examples for developing simulation algorithms. Springer, 1996.